

Classifying the High-Energy Sky with Spectral Timing Methods

Dissertation zur Erlangung des
naturwissenschaftlichen Doktorgrades
der Julius-Maximilians-Universität Würzburg

vorgelegt von
Annika Franziska Eleonore Kreikenbohm

aus Hannover

Würzburg 2018

Eingereicht am:
bei der Fakultät für Physik und Astronomie

- 1. Gutachter: Prof. Dr. Matthias Kadler
 - 2. Gutachter:
 - 3. Gutachter:
- der Dissertation

Vorsitzende(r):

- 1. Prüfer: Prof. Dr. Matthias Kadler
 - 2. Prüfer:
 - 3. Prüfer:
- im Promotionskolloquium

Tag des Promotionskolloquiums:

Doktorurkunde ausgehändigt am:

Abstract

Active galactic nuclei (AGN) are among the brightest and most frequent sources on the extragalactic X-ray and γ -ray sky. Their central supermassive blackhole generates an enormous luminosity through accretion of the surrounding gas. A few AGN harbor highly collimated, powerful jets in which are observed across the entire electromagnetic spectrum. If their jet axis is seen in a small angle to our line-of-sight (these objects are then called blazars) jet emission can outshine any other emission component from the system. Synchrotron emission from electrons and positrons clearly prove the existence of a relativistic leptonic component in the jet plasma. But until today, it is still an open question whether heavier particles, especially protons, are accelerated as well. If this is the case, AGN would be prime candidates for extragalactic PeV neutrino sources that are observed on Earth. Characteristic signatures for protons can be hidden in the variable high-energy emission of these objects. In this thesis I investigated the broadband emission, particularly the high-energy X-ray and gamma-ray emission of jetted AGN to address open questions regarding the particle acceleration and particle content of AGN jets, or the evolutionary state of the AGN itself. For this purpose I analyzed various multiwavelength observations from optical to gamma-rays over a period of time using a combination of state-of-the-art spectroscopy and timing analysis. By nature, AGN are highly variable. Time-resolved spectral analysis provided a new dynamic view of these sources which helped to determine distinct emission processes that are difficult to disentangle from spectral or timing methods alone.

Firstly, this thesis tackles the problem of source classification in order to facilitate the search for interesting sources in large data archives and characterise new transient sources. I use spectral and timing analysis methods and supervised machine learning algorithms to design an automated source classification pipeline. The test and training sample were based on the third XMM-Newton point source catalog (3XMM-DR6). The set of input features for the machine learning algorithm was derived from an automated spectral modelling of all sources in the 3XMM-DR6, summing up to 137200 individual detections. The spectral features were complemented by results of a basic timing analysis as well as multiwavelength information provided by catalog cross-matches. The training of the algorithm and application to a test sample showed that the definition of the training sample was crucial: Despite oversampling minority source types with synthetic data to balance out the training sample, the algorithm preferably predicted majority source types for unclassified objects. In general, the training process showed that the combination of spectral, timing and multiwavelength features performed best with the lowest misclassification rate of $\sim 2.4\%$.

The methods of time-resolved spectroscopy was then used in two studies to investigate the properties of two individual AGN, Mrk 421 and PKS 2004–447, in detail. Both

objects belong to the class of γ -ray-emitting AGN. A very elusive sub-class are γ -ray-emitting Narrow Line Seyfert 1 (γ -NLS1) galaxies. These sources have been discovered as γ -ray sources only recently in 2010 and a connection to young radio galaxies especially compact steep spectrum (CSS) radio sources has been proposed. The only γ -NLS1 on the Southern Hemisphere so far is PKS 2004–447 which lies at the lower end of the luminosity distribution of γ -NLS1. The source is part of the TANAMI VLBI program and is regularly monitored at radio frequencies. In this thesis, I presented and analyzed data from a dedicated multiwavelength campaign of PKS 2004–447 which I and my collaborators performed during 2012 and which was complemented by individual observations between 2013 and 2016. I focussed on the detailed analysis of the X-ray emission and a first analysis of its broadband spectrum from radio to γ -rays. Thanks to the dynamic SED I could show that earlier studies misinterpreted the optical spectrum of the source which had led to an underestimation of the high-energy emission and had ignited a discussion on the source class. I show that the overall spectral properties are consistent with dominating jet emission comprised of synchrotron radiation and inverse Compton scattering from accelerated leptons. The broadband emission is very similar to typical examples of a certain type of blazars (flat-spectrum radio quasars) and does not present any unusual properties in comparison. Interestingly, the VLBI data showed a compact jet structure and a steep radio spectrum consistent with a compact steep spectrum source. This classified PKS 2004–447 as a young radio galaxy, in which the jet is still developing.

The investigation of Mrk 421 introduced the blazar monitoring program which I and collaborator have started in 2014. By observing a blazar simultaneously from optical, X-ray and gamma-ray bands during a VHE outbursts, the program aims at providing extraordinary data sets to allow for the generation of a series of dynamical SEDs of high spectral and temporal resolution. The program makes use of the dense VHE monitoring by the FACT telescope. So far, there are three sources in our sample that we have been monitoring since 2014. I presented the data and the first analysis of one of the brightest and most variable blazar, Mrk 421, which had a moderate outbreak in 2015 and triggered our program for the first time. With spectral timing analysis, I confirmed a tight correlation between the X-ray and TeV energy bands, which indicated that these jet emission components are causally connected. I discovered that the variations of the optical band were both correlated and anti-correlated with the high-energy emission, which suggested an independent emission component. Furthermore, the dynamic SEDs showed two different flaring behaviors, which differed in the presence or lack of a peak shift of the low-energy emission hump. These results further supported the hypothesis that more than one emission region contributed to the broadband emission of Mrk 421 during the observations.

Overall, the studies presented in this thesis demonstrated that time-resolved spectroscopy is a powerful tool to classify both source types and emission processes of astronomical objects, especially relativistic jets in AGN, and thus provide a deeper understanding and new insights of their physics and properties.

Zusammenfassung

Aktive Galaxienkerne (active galactic nuclei, AGN) gehören zu den hellsten und häufigsten Quellen am extragalaktischen Röntgen- und Gammastrahlen Himmel. Das zentrale supermassive Schwarzes Loch erzeugt durch Akkretion des umgebenden Gases eine enorme Leuchtkraft. Einige AGN beherbergen stark kollimierte, leuchtstarke Jets die im gesamten elektromagnetischen Spektrum beobachtet werden. Betrachtet man Jets unter einem kleinen Winkel zu unserer Sichtlinie (diese Objekte werden Blazare genannt), kann die Jetemission die anderen Strahlungskomponenten des Systems überstrahlen. Die Synchrotronemission von relativistischen Elektronen und Positronen beweist eindeutig die Existenz einer leptonischen Plasmakomponente in Jets. Bis heute aber ist es offen, ob auch schwerere Teilchen, insbesondere Protonen, beschleunigt werden können. Wenn dies der Fall ist, wären AGN vielversprechende Quellen für extragalaktische PeV-Neutrino, die auf der Erde beobachtet werden. Charakteristische Signaturen von Protonen könnten in der variablen hochenergetischen Emission dieser Objekte verborgen sein. In dieser Arbeit untersuchte ich daher die Breitbandemission, insbesondere die hochenergetische Röntgen- und Gammastrahlung, von AGN mit Jets, um offene Fragen bezüglich der Teilchenbeschleunigung und des Teilcheninhalts von Jets in AGN oder dem evolutionären Zustand eines AGN selbst zu adressieren. Zu diesem Zweck analysierte ich mittels einer Kombination von hochmoderner Spektroskopie und Zeitreihen Analysemethoden verschiedener Wellenlängenbeobachtungen, die das Breitbandspektrum von optische bis Gammastrahlen zu verschiedenen Zeitpunkten abdeckten. Von Natur aus sind AGN sehr variabel. Die Kombination der zeitaufgelösten Spektroskopie lieferte somit eine neue dynamische Sicht auf diese Quellen, die dazu beitrug, unterschiedliche Emissionsprozesse zu bestimmen, die sich nur schwer von getrennten Spektral- oder Zeitreihen-Verfahren unterscheiden lassen.

Diese Arbeit behandelt zunächst das Problem der Quellenklassifikation, um die Suche nach interessanten Quellen in großen Datenarchiven zu erleichtern und neue variable Quellen zu charakterisieren. Ich nutze die Zeit- und Spektralanalyse Methoden sowie überwachte Machine-Learning Algorithmen, um eine automatisiertes Verfahren zur Quellklassifizierung zu entwerfen. Das Auswahl der Test- und Trainingsbeispiele basierte auf dem dritten XMM-Newton Punktquellenkatalog (3XMM-DR6). Die Attributen für den maschinellen Lernalgorithmus wurde aus einer automatisierten Spektralmodellierung aller Quellen in dem 3XMM-DR6 definiert, die 137200 individuelle Detektionen umfasst. Die spektralen Attribute werden durch Ergebnisse einer einfachen Zeitreihenanalyse sowie durch Multiwellenlängeninformationen ergänzt. Letztere ergaben sich aus den Abgleichen verschiedener Quellkataloge. Das Training des Algorithmus und die Anwendung auf die Testquellen zeigte, dass die Definition der Trainingsquellen für die Vorhersage von Quellklassen unbekannter Quellen entscheidend war. Obwohl das Trainingsset

mittels synthetischer Daten von Minderheitsquellklassen ausbalanciert wurde, prognostizierte der Algorithmus bevorzugt jene Quellentypen für nicht klassifizierte Objekte, die am häufigsten im ursprünglichen Trainings Set vorkamen. Im Allgemeinen zeigte der Trainingsprozess, dass die Kombination von Spektral-, Zeitreihen- und Multiwellenlängenattributen beim Klassifizieren einer großen Menge von unbekanntem Objekten mit der niedrigsten Fehlklassifizierungsrate von $\sim 2.4\%$ am besten war.

Die zeitaufgelösten Spektroskopie wurden in zwei zusätzlichen Studien an einzelnen außergewöhnlichen Quellen, Mrk 421 und PKS 2004–447, benutzt, um ihre Eigenschaften im Detail zu untersuchen. Beide Objekte gehören zu der Klasse von AGN, die Gammastrahlung emittieren. Eine sehr schwer fassbare Unterklasse sind sogenannte γ -emittierende Narrow Line Seyfert 1 (γ -NLS1) Galaxien. Gammastrahlung dieser Quellen wurden erst im Jahr 2010 entdeckt. Man vermutet eine Verbindung zu jungen Radiogalaxien, insbesondere zu kompakten Radioquellen mit einem steilen Radiospektrum (sog. Compact Steep Spectrum sources, CSS). Das einzige bestätigte γ -NLS1 auf der südlichen Hemisphäre ist bisher PKS 2004–447, die am unteren Ende der Helligkeitsverteilung von γ -NLS1 liegt. Die Quelle ist Teil des TANAMI VLBI-Programms und wird regelmäßig auf im Radiobereich beobachtet. In dieser Dissertation präsentiere ich Ergebnisse einer Multiwellenlängen-Kampagne von PKS 2004–447, die ich und meine Kollegen zwischen 2012 durchgeführt haben und die durch weitere Einzelbeobachtungen zwischen 2013 und 2016 ergänzt wurde. Ich konzentrierte mich auf die detaillierte Analyse der Röntgenemission und eine erste Analyse ihrer dynamischen Multiwellenlängen SED von Radio bis Gammastrahlung. Dank der dynamischen SED konnte ich zeigen, dass frühere Studien das optische Spektrum der Quelle falsch interpretierten, was zu einer Unterschätzung der hochenergetischen Emission führte und eine Diskussion über die Quellklasse entfaltete. In meiner Studie zeigte ich, dass die gesamten spektralen Eigenschaften konsistent durch Jetemission erklärt werden kann, die Synchrotronstrahlung und Inverse Comptonstreuung von beschleunigten Leptonen umfasst. Die Breitbandemission ist typischen Beispielen von Flachspektrum-Radio-Quasaren sehr ähnlich und weist im Vergleich keine ungewöhnlichen Eigenschaften auf. Interessanterweise zeigten die VLBI-Daten eine kompakte Jet-Struktur und ein steiles Radiospektrum, das mit den Eigenschaften von CSS verträglich ist. Dies klassifiziert PKS 2004–447 als junge Radiogalaxie, in der sich der Jet noch entwickelt.

Die Untersuchung von Mrk 421 führt das Blazar-Monitoring-Program ein, das ich und meine Mitarbeiter 2014 begonnen haben. Dabei werden Blazare während eines Strahlungsausbruchs im TeV Energieband gleichzeitig in den optischen, Röntgen- und Gammastrahlenbändern beobachtet. Das Ziel des Programms ist die Erzeugung von dynamischen SEDs von hoher spektraler und zeitlicher Auflösung zu ermöglichen. Das Programm nutzt dafür die dichte Überwachung von Blazaren im TeV Bereich durch das FACT-Teleskop. Seit 2014 sind drei markante Blazar Teil unseres Programms. 2015 zeigte eine unserer beobachteten Quellen, Mrk 421, einen moderaten Ausbruch im TeV Band und löste damit unser Programm zum ersten Mal aus. In dieser Arbeit habe ich unsere Beobachtungen im Optischen bis TeV Band dieser Quelle benutzt um eine erste zeitaufgelöste Spektroskopie der dynamischen SED dieser Quelle vorzunehmen. Die Analyse der Flussvariabilität in

unterschiedlichen Energiebändern bestätigte eine enge Korrelation zwischen der Röntgen- und TeV-Emission. Dies deutet darauf hin, dass diese Jetstrahlungskomponenten kausal verknüpft sind. Ich entdeckte, dass die Helligkeitsvariationen im optischen Band sowohl korreliert als auch antikorreliert mit der Strahlung im Röntgen- und Gammaband waren, was auf eine unabhängige Emissionskomponente hinwies. Darüber hinaus zeigten die dynamischen SEDs zwei unterschiedliche Verhalten bei Strahlungsausbrüchen, die sich im Vorhandensein oder Fehlen einer Verschiebung des niederenergetischen Emissionsmaximums unterschieden. Diese Ergebnisse unterstützen die Hypothese, dass während der Beobachtungen von Mrk 421 mehr als eine Emissionsregion zu dessen Breitbandemission beigetragen haben.

Die Studien in dieser Arbeit zeigen, dass die zeitaufgelöste Spektroskopie ein leistungsfähiges Werkzeug ist, um sowohl Quellentypen als auch die Emissionsprozesse einzelner Quellen zu klassifizieren und so ein tieferes Verständnis und neue Einblicke in die Physik und Eigenschaften astronomischer Objekte, insbesondere relativistischer Jets in AGN zu ermöglichen.

Contents

Abstract	i
Zusammenfassung	iii
1. Introduction	5
2. The variable High-Energy Sky	9
2.1. A changing source type distribution	9
2.2. A transient high-energy sky	17
2.3. The challenge of source identification and classification	21
2.4. Emission and Acceleration of High-energy Particles	23
2.4.1. Blackbody Radiation	24
2.4.2. Bremsstrahlung	24
2.4.3. Synchrotron Radiation	25
2.4.4. Inverse Compton Scattering	26
2.4.5. $\gamma\gamma$ Pair Production	27
2.4.6. Absorption processes	28
2.4.7. Particle Acceleration	29
3. The hot all-rounder: Active Galactic Nuclei	31
3.1. Overview of AGN unification	31
3.1.1. The building blocks of the central engine	32
3.1.2. Classes of γ -ray detected AGN	33
3.1.3. A unification model - not one to rule them all	37
3.2. Broadband emission spectrum of AGN	40
3.2.1. Nuclear emission and reprocessing	40
3.2.2. Characteristics of jet emission	41
3.2.3. Broadband variability of jetted-AGN	42
3.2.4. Leptonic and lepto-hadronic emission models	44
3.3. The physics of relativistic jets	45
3.3.1. Accretion and Eddington limit	46
3.3.2. Formation of relativistic jets	47
3.3.3. Jet collimation and acceleration	49
3.3.4. Relativistic effects	49

4. High-energy observations and data reduction	51
4.1. X-ray data	52
4.1.1. Focusing X-ray instruments	53
4.1.2. Coded-Mask instruments	54
4.1.3. The <i>XMM-Newton</i> satellite	55
4.1.4. The <i>Neil-Gehrels Swift</i> spacecraft	56
4.1.5. The <i>INTEGRAL</i> mission	57
4.2. γ -ray data	58
4.2.1. The <i>Fermi</i> Telescope	59
4.2.2. The small IACT: FACT	60
5. Spectroscopy and Timing Analysis Methods	63
5.1. Spectral fitting	63
5.2. Timing Analysis	65
6. The concept of machine learning	69
6.1. Supervised and Unsupervised Learning methods	70
6.2. To see no forest for the trees - the supervised Random Forest algorithm	72
6.2.1. Performance measures of the RF classifier	73
6.3. Handling of imbalanced training sets	77
6.4. Synthetic Minority Over-sampling Technique (SMOTE)	78
7. Taking source classification to the EXTraS level	81
7.1. The EXTraS project	82
7.2. Source classification with Random Forests	83
7.3. The 3XMM-DR6 catalog	83
7.4. Classification features	87
7.5. Randomized detection positions	93
7.6. Training an algorithm	93
7.7. Classification of the 3XMM-DR6 test sample	102
7.8. Classification of EXTraS transient sources	106
7.9. Summary and future work	108
8. Unveiling the nature of PKS 2004–447	113
8.1. Oh PKS 2004–447, what are thou?	113
8.2. The multiwavelength campaign	115
8.3. The X-ray view	116
8.4. The multiwavelength view of PKS 2004–447	133
8.5. The nature of PKS 2004–447	141
8.6. Summary and future work	145
9. Time-resolved high-energy emission in Mrk 421	147
9.1. The Blazar Monitoring Program	148
9.1.1. Long-Term Monitoring at TeV and X-ray energies	148

9.1.2.	Broadband target-of-opportunity observations	150
9.1.3.	The HBL Target Mrk 421	150
9.2.	Observations and data processing	153
9.2.1.	FACT data	153
9.2.2.	<i>Fermi</i> -LAT data	154
9.2.3.	<i>INTEGRAL</i> data	154
9.2.4.	<i>Swift</i> XRT data	155
9.2.5.	<i>Swift</i> UVOT data	156
9.3.	The long-term evolution of the X-ray spectrum	157
9.4.	Multiwavelength Variability and Correlation Studies	157
9.4.1.	Inter-band cross-correlation studies	159
9.5.	Time-resolved Spectral Energy Distributions of Mrk 421	164
9.6.	Discussion	169
9.6.1.	Interpretation in the context of leptonic jet scenarios	171
9.7.	Summary	174
10.	Summary and Conclusion	177
A.	EXTraS	181
A.1.	Automated fitting pipeline	181
A.2.	Spectral Model description	182
A.3.	Complete List of Classification Features	186
A.4.	Example Parameter Correlations for the Train, Test and Transient Sample	189
A.4.1.	Training sample	189
A.4.2.	Test sample	189
A.4.3.	Transient sample	189
A.5.	Complete list of EXTraS Transient sources	189
A.6.	Auxiliary class predictions of EXTraS Transient sources	204
B.	Mrk 421	207
B.1.	Spectral fit results of all Mrk 421 <i>Swift</i> observations.	207
B.2.	Complementary multiwavelength light curves	212
B.3.	Discussion: results in the context of hadronic jet scenarios	216
C.	Supplementary studies	219
C.1.	Extragalactic Neutrinos from jetted AGN	219
C.2.	X-ray emission from Young Radio Galaxies	221
C.2.1.	The discovery of the new young radio galaxy PMN J1603–4904	222
C.2.2.	Disentangling the extended X-ray emission of PKS 1718–649	224
C.3.	Mapping X-ray absorption in AGN and the local ISM	225
C.3.1.	Variable absorption in the radio-quiet AGN NGC 3227	226
C.3.2.	A 3D map of the local ISM: a <i>Gaia</i> and <i>XMM-Newton</i> synergy	226
	References	229

List of Figures	239
List of Tables	251
Acknowledgement	253

1. Introduction

High-energy astrophysics addresses the most energetic and violent processes in the Universe. The term 'high-energy' covers more than seven orders of magnitudes of the electromagnetic spectrum from X-rays up to TeV γ -rays. Such energetic radiation arises from astrophysical sources in a non-steady state through processes at very high temperatures (above 10^6 Kelvin), or highly energetic non-thermal phenomena. The fundamental emission processes responsible for the observed high-energy radiation are similar in different objects. But as the properties of the cosmic environments vary so does the interplay between these processes. Hence, observations in different points in time and energy of the same object may sample different dominating processes leading to different appearances. Consequently, the study of high-energy sources often requires a multiwavelength approach and the combination of imaging, spectroscopy, and time-domain measurements.

Due to the extreme environments that are tested, high-energy astrophysics touches various fields of research, for example the study of space-time anomalies (gravitational waves), particle physics (e.g., cosmic rays), or the search for signatures of dark matter and dark energy. The topics in this field of research are as diverse as the sources that can be observed at these high energies (see Table.2.1). For example, one of the oldest questions of modern astrophysics is the origin of high-energy cosmic rays. Cosmic rays are particles, i.e., leptons and hadrons, that reach Earth from anywhere beyond its atmosphere. The energy spectrum of these particles is an almost featureless power-law (see Fig.1.1, e.g., Hillas 2006; Kotera & Olinto 2011) reaching up to more than 10^{20} eV, the highest energy ever observed. The only features detected in the cosmic ray spectrum are the so-called "knee" at 5×10^{15} eV, the "ankle" at 10^{18} eV, and a cutoff at 10^{20} eV (referred to as GZK cut-off, see e.g., Zatsepin & Kuz'min 1966). Until now it is not understood how and where these astrophysical particles are accelerated to such enormous energies. How do they interact with cosmic background radiation? Furthermore, we lack knowledge about their spatial distribution, or their role in shaping galaxies and giant galaxy clusters over cosmic time. Because the Galactic magnetic field is not strong enough to constrain ultra-high energy cosmic rays (UHECR) in the Milky Way itself these particles must have extragalactic origins. Candidate sources range from compact objects, e.g., black holes or neutron stars, to explosions related to γ -ray bursts. The investigation of how and where those particles are accelerated to those extreme energies is one of the big challenges of high-energy astrophysics. The most promising acceleration mechanisms include the build up of plasma turbulence or shocks. Such processes are highly non-stationary or explosive and can yield extreme emission outbursts throughout the whole electromagnetic spectrum as the accelerated particles rapidly cool down, making the high-energy sky highly dynamic and transient.

It is well known that relativistic particles produce high-energy radiation when inter-

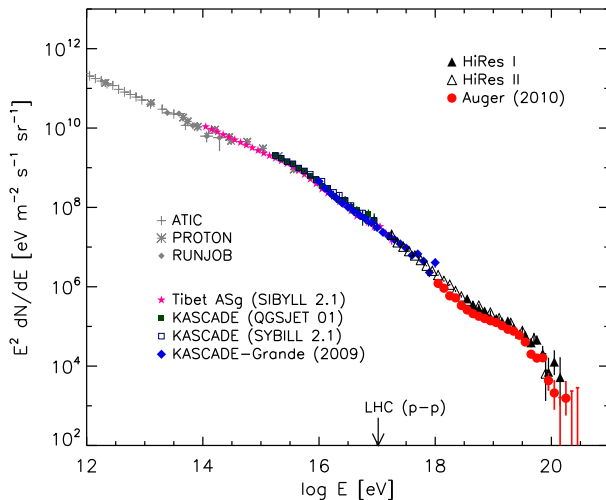


Figure 1.1: Cosmic ray particle spectrum (Kotera & Olinto 2011). The spectrum covers more than 8 orders of magnitude in energy and more than 24 orders of flux. A transition from Galactic to extragalactic cosmic rays is thought to be somewhere between $(10^{15} - 10^{18})$ eV.

acting with electromagnetic fields or matter. Consequently, high-energy photons are a significant tracers of relativistic particles and an indicator of their acceleration, transport, and interaction of energetic particles. That means, all astrophysical objects that emit hard X-ray and γ -ray radiation could be candidate sources for cosmic ray acceleration. Hence, identifying the origin of cosmic rays requires understanding the composition and processes at work in those candidate objects. To study them researchers make use of many multi-messengers observations, which include photons from the entire electromagnetic spectrum, cosmic rays itself, neutrinos, and since recently gravitational waves. Besides neutron stars and γ -ray bursts (GRB), Active Galactic Nuclei (AGN) are prime candidates for UHECR acceleration. Their high-energy emission up to several TeV as well as the presence of powerful collimated, relativistic outflows (jets) indicate extreme environmental conditions where processes that yield high-energy particles could take place. The present knowledge about the highest energy cosmic rays was mainly acquired from the two major experiments HiRes (Abbasi et al. 2009) and Auger (Abreu et al. 2010; Abraham et al. 2010). The angular distributions of the observed events exceeding 6×10^{19} eV was different in these two experiments: the HiRes data showed the isotropic distribution; the Auger data demonstrated a correlation with AGN. Crossmatching the distribution of cosmic rays events with AGN requires large source catalogs. Because of their hard non-thermal spectrum and high luminosity in the X-ray band, X-ray surveys of modern satellites are well suited to identify and locate AGN due to their high sensitivity and good angular resolution.

Accelerators of UHECR are also intriguing in the light of the latest reports by the ICECUBE observatory¹. Astronomers are searching for the origin of extragalactic PeV neutrinos since their first detection in 2011 and 2013 (e.g., Aartsen et al. 2013, 2017). Several claims for a directional correlation between high-energy detected AGN and neu-

¹<https://icecube.wisc.edu/>

trino events have been reported (e.g., Torres et al. 2003, and references therein). Among the problems of associating a single source with a neutrino event is the low number of detected neutrino events and the limited positional reconstruction. Their isotropic sky distribution suggests that most of them have an extragalactic origin. Many different scenarios for the astrophysical counterparts of ICECUBE neutrinos have been put forward, including blazars, star-forming galaxies, GRB, galaxy clusters, and high-energy Galactic sources (see e.g. Ahlers & Halzen 2015, and references therein, for a comprehensive discussion). So far, AGN with jets pointed in our direction are most promising candidate high-energy neutrino sources and their potential has been studied long before the ICECUBE detection (e.g. Mannheim 1995; Halzen & Zas 1997a; Mücke et al. 2003a; Padovani & Resconi 2014; Tavecchio & Ghisellini 2015). Kadler et al. (2016) showed that in principle the fluence of AGN is enough to produce the observed number of PeV neutrinos. In 2017, Lucarelli et al. (2017) discovered a gamma-ray flare of a new transient source AGL J1418+0008 in the data of the TeV AGILE detector which was positionally consistent with a the neutrino event ICECUBE-160731, reported on 2016 July 31 by the ICECUBE collaboration, and which took place between 1 and 2 days before the start the event. Based on an extensive catalog search for sources within the error regions of ICECUBE-160731 and AGL J1418+0008, the transient could be associated with the flaring high-energy peaked BL Lac TXS 0506+056. A detailed multiwavelength study of this source during different emission states could exclude a neighboring AGN as possible neutrino source and revealed that TXS 0506+056 may have undergone a hadronic flare that resulted in the neutrino event (Padovani et al. 2018).

These studies demonstrate the importance of large high-energy surveys in order to find possible counter parts of cosmic rays and neutrino events. Dedicated studies of the spectral composition and evolution of interesting individual sources are then required to investigate whether the sources are physically capable to accelerate proton.

Plan of the thesis

This work focuses on the classification of γ -ray AGN using multiwavelength information with special emphasis on spectral and timing analysis of high-energy observations. This includes a systematic source classification of X-ray sources using machine learning algorithms as well as detailed sources studies of selected γ -ray-emitting AGN in order to classify their emission spectrum. Chapter 2 serves as an introduction to the current observational understanding of the variable high-energy sky and outlines the importance and difficulties of source identification in multiwavelength campaigns. It also provides the theoretical background for production of high-energy radiation. Active Galactic Nuclei and the jet phenomenon are introduced in chapter 3. Chapter 4 describe which instruments and methods that were used to acquire and process X-ray and γ -ray data for this work. The concept of spectral and timing analysis as well as the machine learning algorithm used in this thesis are described in Chpt. 5 and 6, respectively. The results are divided into three chapters. Chapter 7 presents a study that was performed

in the context of the *EXTraS*² program. Together with Mirjam Örtel I developed an automated classification chain with the aim to give a first identification of unknown transient sources. The subsequent chapters focus on two selected γ -ray-emitting AGN: PKS 2004–447 (Chpt. 8), which is a peculiar source whose classification is still an open issue, and Mrk 421 (Chpt. 9), one of the closest and brightest flaring AGN. On both sources I performed multiwavelength monitoring campaigns. The results of each analysis is presented within each chapter. An overall summary and outlook is given chapter 10.

²Exploring the X-ray and Transient Sky, EXTraS

2. The variable High-Energy Sky

Unless stated otherwise information for this chapter is based on a number of reviews: A detailed overview on the characteristics of cosmic X-ray spectra is provided in Paerels & Kahn (2003), while Harris & Krawczynski (2006) review the X-ray emission of extragalactic jets, in particular. A good overview on γ -ray astronomy from the observational and instrumentation side is given by Funk (2015). For a review on TeV astronomy and the astrophysics of UHECR see, for example, Hinton & Hofmann (2009) and Kotera & Olinto (2011), respectively.

2.1. A changing source type distribution

A statistical overview of the objects in the sky is possible through surveys that scan the sky at different energies. Their sky images reveal a changing distribution of detected source types with the observed energy. Figures 2.1, 2.3, 2.4, and 2.5 show the sky images from different surveys and instruments from X-ray, soft GeV γ -rays and TeV γ -rays, respectively. Each distribution is shown in Galactic coordinates with the plane of the Milky Way as the horizontal axis and the Galactic center in the origin. Cosmic sources of high-energy radiation range from large scale structures such as galaxy clusters and distant active galactic nuclei (AGN) down to the smallest objects, i.e. stellar mass black holes, white dwarfs, or the sun. X-ray and γ -ray emission is seen in a large number of point sources whose spatial extensions are smaller than the resolution of modern instruments. In addition, there are large regions of diffuse emission whose origin is not yet fully understood. Significant contribution can certainly be attributed to unresolved background sources but also interactions of cosmic rays with the interstellar medium (ISM) play a role.

In the X-ray band from 1 keV up a few 100 keV, there is an unusually rich range of astrophysical processes because a fundamental shift from thermal to non-thermal sources and phenomena occurs in this energy range. The first soft X-ray imaging all-sky survey was performed with the *ROSAT* satellite (*ROSAT* all-sky survey, RASS, Voges et al. 1999) between 1990 and 1991 with a flux limit of 1.5×10^{-4} photons $\text{cm}^{-2} \text{s}^{-1}$. A revised version of the *ROSAT* source catalog (2RXS) has been recently published by Boller et al. (2016). It still provides the deepest and cleanest soft X-ray all-sky catalog. The *INTEGRAL* and *Swift*-BAT mission then provided valuable complementary observations in the hard X-ray range. At soft X-rays most bright objects are of local origin (from the Milky Way or the Magellanic Clouds) with a large fraction made up from flaring stars, white dwarfs (WD) and cataclysmic variables (CV). A large fraction of X-ray sources are binary systems in which a companion star transfers mass to a neutron star or stellar

mass black hole. Very bright and hard X-rays results from accretion onto the compact object, which is why these sources are called X-ray binary (XRB) systems. They are subdivided into low-mass (LMXRB) and high-mass X-ray binaries (HMXRB) depending on the mass of the companion star. Although they are among the brightest Galactic objects, their intrinsic luminosities are not sufficient to detect them in other galaxies with the sensitivity of current instruments.

Besides accretion in binary systems, X-ray emission can originate from emission of accelerated particles or novae explosions at the surface of accreting white dwarfs and cataclysmic variables (e.g., see Mukai 2017, for a recent review). Particle acceleration is also found to be the dominant driver of X-ray emission in extended supernova remnants (SNR) (see e.g., Allen et al. 1997; Bamba et al. 2000). The fast inner shells that were accelerated in the core collapse overtake the slower outer shells and induce shocks. Shocked particles are thought to release energy via thermal bremsstrahlung or inverse Compton radiation when interacting with surrounding photon fields or material. Due to their proximity these sources can be resolved with current instruments and characterized by extended emission (e.g., Lu & Aschenbach 2000). X-rays from supernovae (SN) itself arise from the nuclear reactions and subsequent down scattering within the outer shells of the star. The 2RXS detected 32 large extended regions with diffuse emission and embedded point sources, as well as extended sources which were mainly SNR and cluster of galaxies but also a few pulsar wind nebulae (PWN) and clusters of stars. The rest of the sources appear as point sources. Figure 2.2 shows the ROSAT image of the extended Vela SNR. Another large fraction of galactic sources are stars who besides thermal emission emit non-thermal X-rays through line-driven winds or due to magnetic activity (e.g., Güdel 2004).

The thermal component of hot material completely vanishes in the γ -ray sky. The smoothed counts maps averaged over 7 years of *Fermi-LAT* observations are shown in Fig. 2.3 with intensity color-coded from blue to white. The maps show the GeV γ -ray sky in two energy regimes: above 10 GeV and above 50 GeV up to 2 TeV. γ -rays are observed from any direction of the sky, with an isotropic background from unresolved sources. Its isotropy indicates that such sources are primarily extragalactic (see Fig. 2.4).

Furthermore, a bright band of diffuse γ -rays is seen in the Galactic plane and many discrete γ -ray sources, which are visible as bright point sources, can be observed against the isotropic extragalactic background and diffuse emission from the Milky Way. It turns out that the diffuse component is stronger for lower energies while individual sources dominate the sky at higher energies, in particular the TeV energy band. Part of the diffuse component is associated with cosmic ray interactions with the ISM in our Galaxy (e.g., Ackermann et al. 2012c). A prominent example are the *Fermi bubbles*, related to outflows from a region of the Galactic center (GC), which are visible across the whole energy band observed by *Fermi-LAT* (e.g., Su et al. 2010; Crocker & Aharonian 2011).

On Galactic scales, γ -rays have been detected from Solar system objects, such as the sun, the moon, and even thunderstorms on Earth. However, the largest classes of Galactic γ -ray sources are pulsars and their PWN. The rapidly rotating, magnetized neutron stars can generate strong electromagnetic fields which are able to accelerate particles in the

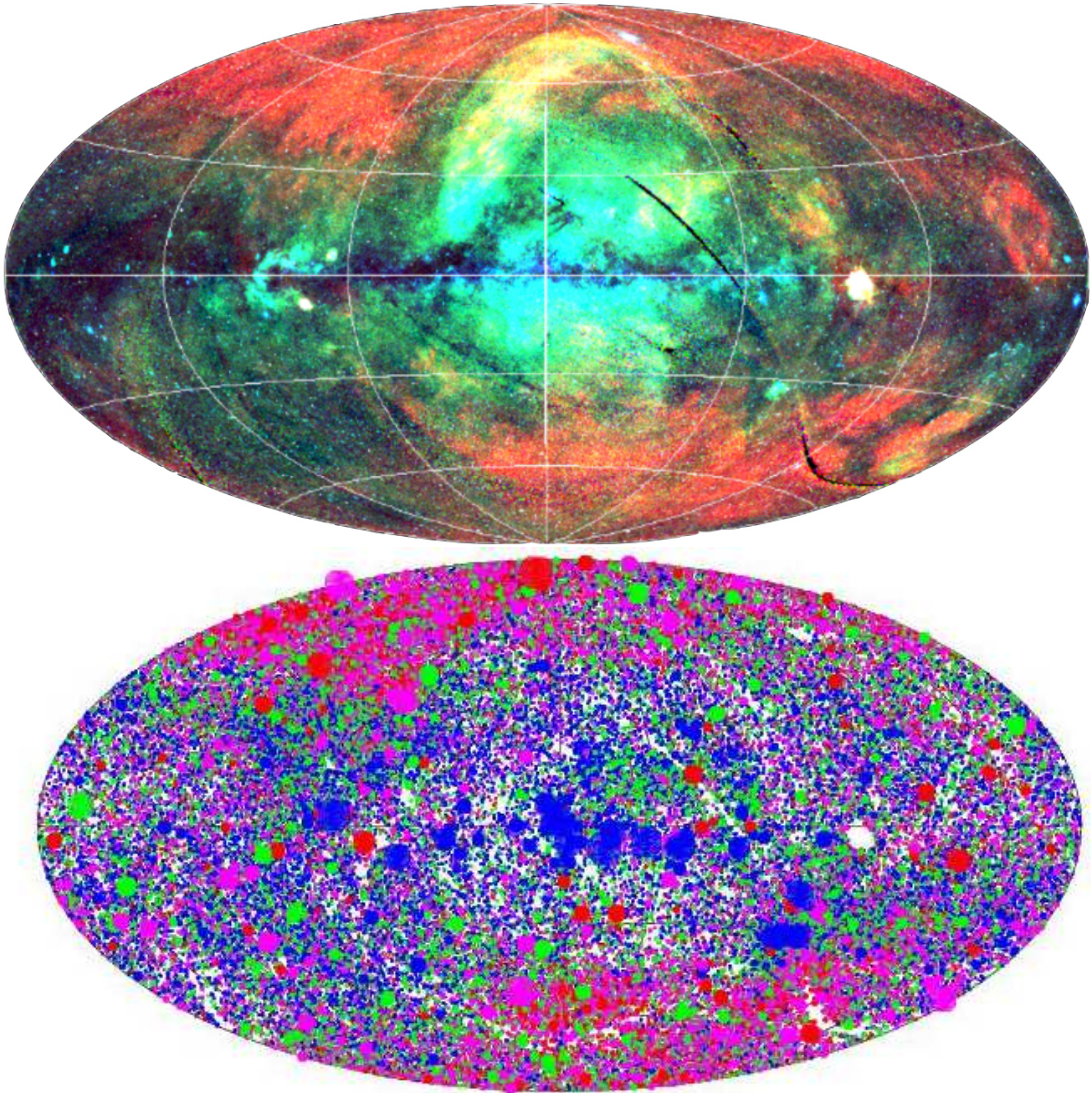


Figure 2.1.: Sky map of X-ray sources in Galactic coordinates and Hammer-Aitoff projection as observed by the *ROSAT* all-sky survey in the (0.1-2.4) keV range. *Top:* Distribution of diffuse emission (Credit: X-ray group at MPE, Germany). Colors represent the spectral shape from red (soft spectra) to blue (hard spectra). *Bottom:* Distribution of point sources in the Second *ROSAT* X-ray Source Catalog (2RXS, Boller et al. 2016). Color-code as in the top panel. The size of the point source symbols corresponds to the count rate. A large number of bright individual sources with hard spectra are found in the Galactic plane, indicating that at least part of the hard diffuse emission is induced by unresolved point sources (e.g., XRB). A large number of hard but faint sources are spread isotropically across the entire sky, produced by extragalactic objects (e.g., AGN). See text for more information.

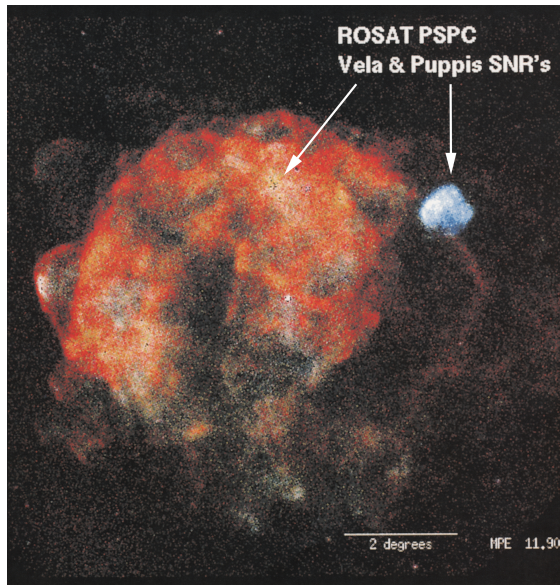


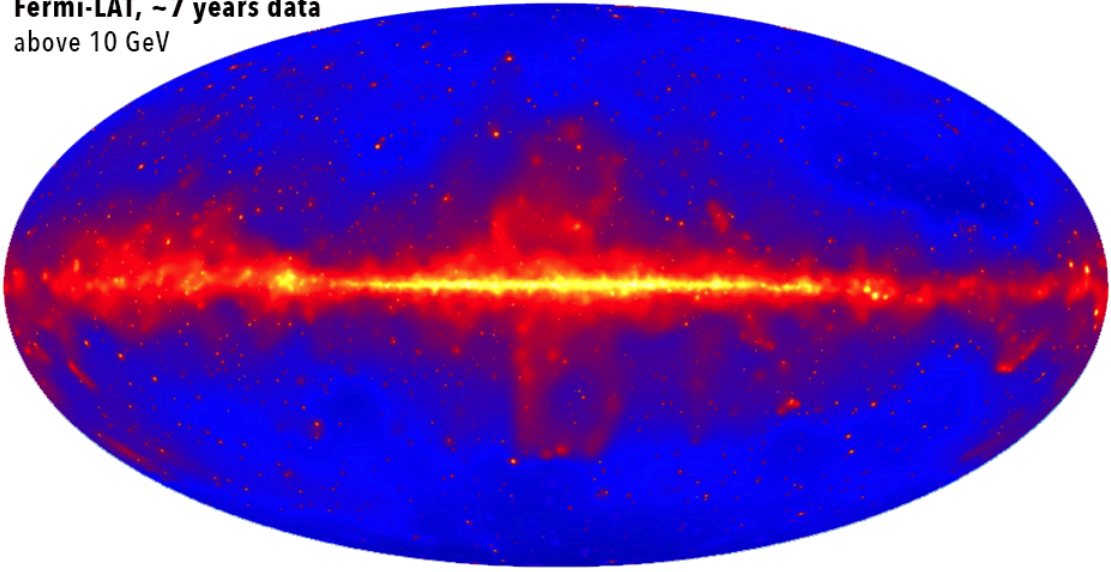
Figure 2.2: ROSAT image of two supernova remnants: the larger one is the Vela SNR at a distance of roughly 1,500 light years, and a smaller one, the Puppis SNR which is farther away from the sun and is visible as bright spot in the upper right corner. Image credit: Max-Planck-Institute for extraterrestrial physics (MPE), Germany.

"gap" regions within the magnetosphere to high enough energies that they can produce γ -rays, e.g., through curvature, synchrotron, and inverse Compton radiation (e.g., Bai & Spitkovsky 2010). Furthermore, pulsars produce strong particle outflows (jets) into their environments, creating their PWN. The shock fronts of these nebulae can also accelerate particles which interact with the ambient medium and produce γ -rays — similar to shock acceleration at the fronts of SNR. Interestingly, *Fermi*-LAT detected also four high-mass binaries systems (Acero et al. 2015). The nature of the companion star as well as particle acceleration and interaction processes in these systems are still unknown (see, e.g., Thompson 2010).

Of course, there is also contribution from isotropic extragalactic background emission in the Galactic plane as there is a large number of point sources that are isotropically distributed across the sky. The majority of extragalactic sources are AGN, blazars in particular (see Sect. 3.1.2). Indeed, there are only a handful of other extragalactic source types that have been observed: normal galaxies where γ -rays are produced through star formation (e.g., M31, starburst galaxies, or the small and large Magellanic clouds), galaxy clusters, and γ -ray bursts (GRB). The later are intense flashes of γ -rays which only last from a fraction of a second to minutes. Their respective isotropic luminosities of the order of 10^{51} erg s $^{-1}$, making GRB the most luminous objects in the sky. However, their nature is still unknown. The current paradigm suggests that they might result from extreme types of supernovae or the mergers of compact neutron stars or black holes binaries (see, e.g., Piran 2004). They are divided in long (>2 s) bursts which show longer afterglows in lower-energy bands, and short (<2 s) bursts. Whether there is a fundamental difference between these subgroups of bursts is still a matter of debate (e.g., Yamazaki et al. 2004). Both kinds were detected in the GeV sky.

These objects are also expected to show up in the very high energy (VHE) TeV γ -ray sky. So far, there is no firm detection of such an event. The main energy source of

Fermi-LAT, ~7 years data
above 10 GeV



50 GeV - 2 TeV

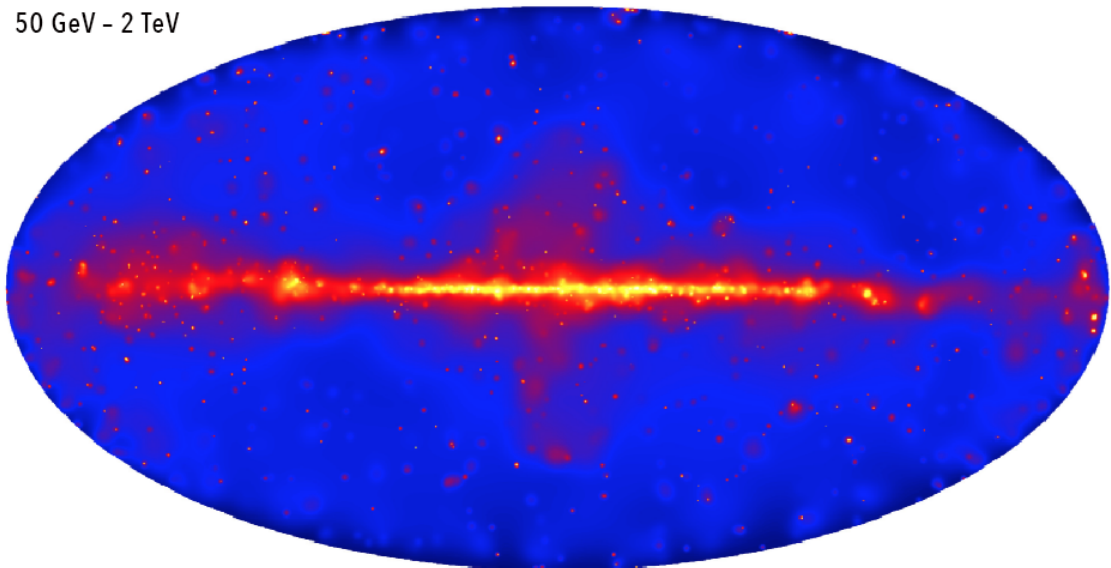


Figure 2.3.: Full sky maps of the γ -ray sky observed with *Fermi*-LAT averaged over 7 years. Colors represent the photon flux from blue (low) to yellow (high). *Top panel:* shows the photon distribution for energies above 10 GeV (Ajello et al. 2017). *Bottom panel:* shows the same for hard energies between 50 GeV – 2 TeV (Ackermann et al. 2016).

TeV objects appears to be bulk flow, such as relativistic jets and non-relativistic shocks, that cause high-energy particle acceleration. Theses processes transfer bulk motion into populations of relativistic particles. The properties of the TeV radiation is then determined by the convection, diffusion and cooling of these particles making TeV sources ideal

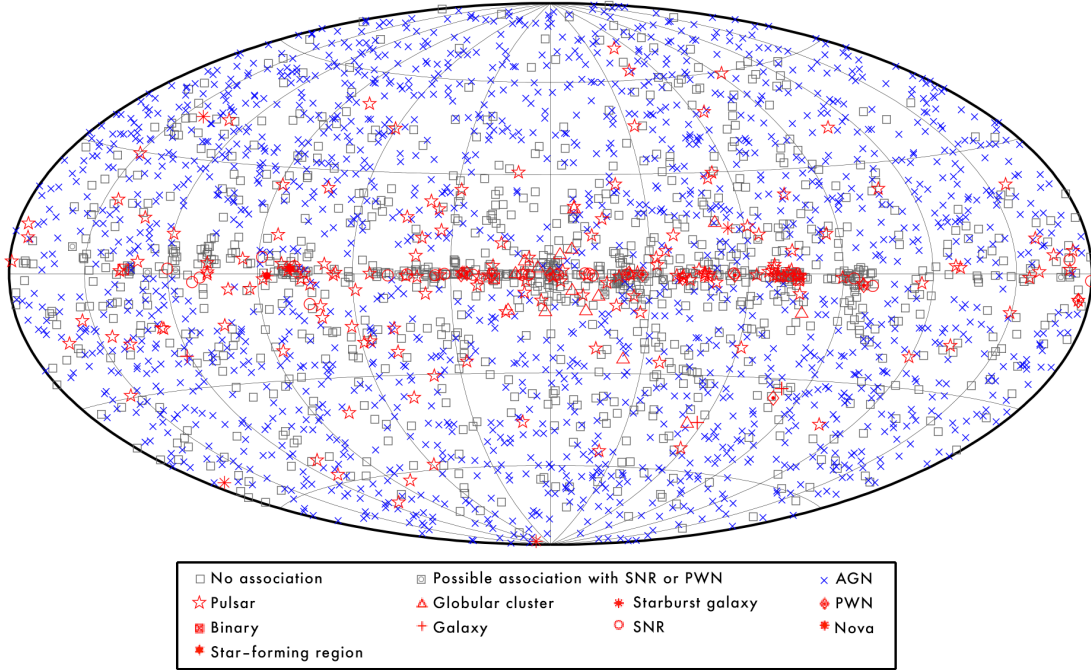


Figure 2.4.: Full sky map of γ -ray sources in the Third *Fermi*-LAT source catalog (3FGL, Acero et al. 2015). See text for more information.

tracers of high-energy particle interaction with the ambient medium. On one hand, the non-detection put constraints on the theoretical models for the processes that yield γ -ray bursts. On the other hand, the highly transient objects are very difficult to observe with current TeV observatories due to the fact that there is no survey mode observations yet. TeV γ -rays are observed indirectly by detecting their signatures in Earth's atmosphere in the form of optical Cherenkov light. Hence, large telescope arrays and a challenging effort of data processing are required to achieve high sensitivity and angular resolution. Pointed observations have been performed for sources that were known from observations in other wavelength bands and for which TeV emission is expected. At the time of writing, there are only a couple of 100 detected TeV sources which are summarized in the TeV catalog TeVCat¹. Figure 2.5 shows the sky distribution and object types of sources in TeVCAT. Also in this energy band, diffuse emission from the innermost part of the Galactic Center was detected, which supports the idea that γ -rays in this region are partially induced by cosmic rays (e.g., H. E. S. S. Collaboration et al. 2018). Quite often, there is a difference between the extension of X-ray and γ -ray emitting regions. A possible explanation may be that the cooling times of very high-energy electrons (~ 10 kys) are longer than for keV emitting electrons (~ 1 kys)². Thus, emission regions with TeV

¹TeVCat: <http://tevcat.uchicago.edu/>

²For example, a 1 TeV electron travels approximately 10^4 yrs before it interacts which is comparable to the lifetime of pulsars or young SNR.

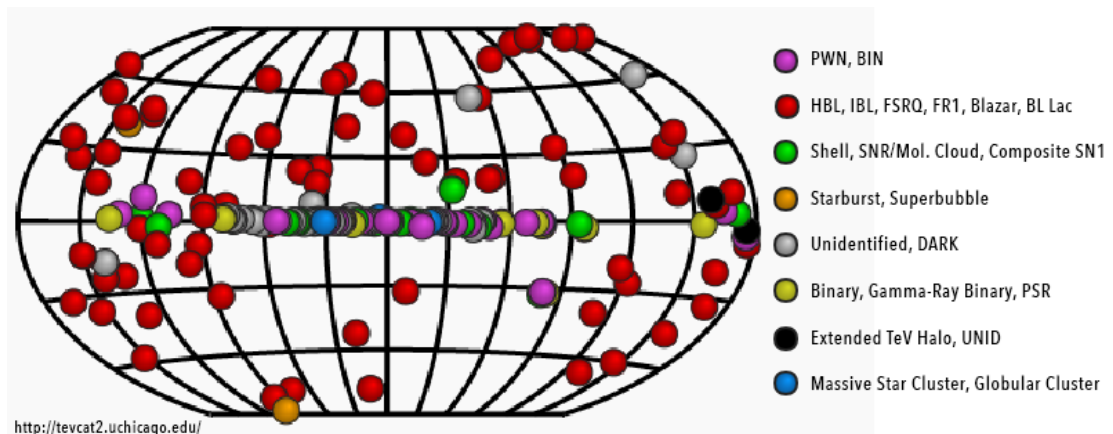


Figure 2.5.: Full sky map of VHE sources in the TeV catalog (TeVCat). See text for more information.

photons that accumulate over the object’s lifetime can extend up to 10 pc. For Galactic distances these objects appear extended. Among those, SNR are prime candidates for Galactic cosmic ray accelerators which produce particle energies up to 10^{17} eV. Their sky distribution concentrates on the Galactic plane. In TeV γ -ray observations SNR show evidence of interactions with molecular clouds. Shock acceleration is thought to take place where interacts with the cloud and/or surrounding medium which is supported by a strong spatial agreement of the γ -ray and X-ray emission regions.

The first γ -ray source that was detected by TeV observatories was the Crab nebula (see e.g., Weekes et al. 1989; Atoyan & Aharonian 1996). It is associated with a historical supernova recorded in 1054. The SN resulted in an pulsar which continuously emits a wind of magnetized plasma. The wind is expected to terminate in a standing shock where shock acceleration takes place. The high-energy emission is associated with electrons and positions from the pulsar wind which terminates in a shock when the pressure of the wind is balanced by the ambient medium (e.g., Rees & Gunn 1974). This region is referred to as pulsar wind nebula (PWN). PWN are close enough to be spatially resolved at lower energies, as well. However, the most abundant group of identified Galactic TeV sources are pulsars themselves. These objects show short and periodic emission whenever their jets are aligned with the line of sight (e.g., Aharonian et al. 2006a) which suggests that their high-energy emission is induced by these jets and their strong magnetic fields near the poles. Surprisingly, another group of Galactic sources are compact object binary systems (see e.g., Aharonian et al. 2006b; Albert et al. 2006), which are also detected in GeV γ -rays. These binaries are so-called *microquasars* because they feature accretion and jet formation similar to their giant counterparts in active galactic nuclei (Mirabel & Rodríguez 1994). Internal and external shocks in the jet can accelerate particles producing high-energy emission. In addition, the instabilities in the accretion process in microquasars produces high radiation densities of VHE photons (Mirabel & Rodríguez 1999). But also steady extended TeV γ -ray emission is possible if the particles escape

the production region inside the binary without significant energy loss.

Among extragalactic sources, AGN with relativistic jets are by far the most abundant source type in the GeV and TeV sky. Synchrotron and inverse Compton cooling of highly relativistic particles within these jets are responsible for the VHE emission. Most TeV AGN have already been detected by *Fermi*-LAT. Among those blazars are dominating the source population and only a few non-blazar AGN are observed (for example, M87, Aharonian et al. 2006c; Acciari et al. 2008; Albert et al. 2008). All TeV blazars are also strong radio and X-ray sources and suggest that there might be a common electron population. Other source types include starburst galaxies, which have enhanced supernova rates and a high gas densities, and galaxy clusters, where VHE γ -rays results result from a combination of particles (accelerated through accretion shocks that cool in the VHE band), the inter-cluster medium, supernovae, and AGN activity within the cluster. About one third of detected TeV and GeV sources are still unidentified. Because these sources carry the potential for new discoveries, one of the most important tasks in γ -ray astronomy is the identification of unknown sources with low-energy counterparts.

In summary, by comparing the different surveys a changing composition of objects depending on the observed energy band and telescope sensitivity can be observed. While pulsar and supernova remnants are prominent high-energy emitter within our galaxy, the extragalactic high-energy sky is dominated by AGN. Of the *ROSAT* source catalogs, only 10% were of extragalactic origin (mainly AGN), and 26% remained unidentified (Boller et al. 2016). The low fraction of extragalactic sources stems from the lower flux due to their distance which was below the sensitivity of the instruments. Deeper surveys of smaller regions of the sky were performed with pointed observation from the *ROSAT*, *XMM-Newton*, and *Chandra* satellite missions, where the X-ray instruments aboard *XMM-Newton* and *Chandra* operate between 0.3 keV to 10 keV. The 7-year *INTEGRAL*/IBIS all-sky hard X-ray survey (Krivonos et al. 2010) from (17–60) keV shows that there is still a large fraction of Galactic sources at energies above 10 keV (50% of the listed sources, of which 74% are XRB, 14% CVs, and 11% are of other Galactic types). But the fraction of extragalactic sources increased to 42% (of which 98% are AGN and 2% are galaxy clusters). Only 8% of the catalog were not identified yet. The dominance of extragalactic sources becomes larger towards higher observed frequencies: The *Fermi*-LAT 3FGL catalog at GeV (Acero et al. 2015) shows that $\sim 58\%$ of sources are extragalactic, of which 98% are AGN and only 9% are Galactic. A large fraction (one third) of γ -ray sources have not been identified or associated yet and it is an ongoing challenge to find low-energy counterparts for those sources as they harbor the opportunity for new discoveries. In TeV energies there are currently 207 known sources. The fractions of extragalactic sources comprise an even share of 36% for both Galactic and extragalactic objects. The remaining 28% which are mostly detected in the Galactic plane are unidentified. Table 2.1 lists which source types are most commonly observed at different energies.

2.2. A transient high-energy sky

The X-ray to VHE regime is the energy range where most of the extreme astrophysical behavior is taking place, e.g. cosmic acceleration, explosions and accretion onto black holes and neutron stars. Hence, it is not surprising that variability in both flux and spectral shape of an observed source is more the rule than the exception.

In the X-ray band, the Rossi X-ray Timing Explorer (RXTE, Bradt et al. 1993) was designed specifically to study the variability of X-ray sources on timescales from milliseconds to years. It operated from 1995 until early 2012. The spacecraft carried an all-sky monitor which observed 80% of the sky during a single orbit and provided new insights in the variable X-ray sky. Nowadays it is generally accepted that X-ray emission of most astrophysical objects is variable on all timescales and used as an important tool besides spectroscopy to gain information on the emission regions. An exception are large-scale structures, for example Galaxy Clusters, SNR, or some PWN, for which the dynamical timescale are much larger than the observing periods of current instruments. Therefore, their emitted radiation appears stationary. The study of X-ray variability has led to a deeper understanding of the structure and interactions of high-energy sources. The high temporal resolution of RXTE led to the first discovery of millisecond pulsations in highly magnetized pulsars (e.g., White & Zhang 1997). The detection of coherent X-ray pulsations during an X-ray flare (so-called *quasi-periodic oscillations*, QPOs) provided evidence that the magnetic field strength of the neutron star crust is correlated with the X-ray flux (e.g., Strohmayer et al. 1996; Strohmayer & Watts 2005). The study of strong and rapid variability also provided strong evidence that X-rays are emitted close to the central black hole in XRBs and AGN (e.g., Uttley et al. 2002).

In the γ -ray sky the *Fermi* satellite images the sky every three hours with the *Large Area Telescope*. Systematic variability analyses of the *Fermi*-LAT sky revealed that 20% to 30% of sources detected by *Fermi*-LAT showed variable emission on monthly timescales. For γ -rays above 100 MeV variability allows to separate individual sources from the dominant Galactic diffuse emission and the extragalactic isotropic diffuse emission. Due to their extension, these components vary on timescales much longer than observing periods and are considered stable over the duration of current satellite missions (Ackermann et al. 2013a; Abdollahi et al. 2017). Thus, by comparing the observed γ -ray photons in a given region and time interval with expected number from long-term average one can isolate the irregular and bursts-like sources in the sky. It turns out that the vast majority of the Galactic γ -ray sources are relatively persistent, i.e. being steady or having regular periodic variability. The later has been observed from pulsars and binary systems, e.g., HMXRB with a compact central object (neutron star or black hole) and a massive companion star (Aharonian et al. 2005a). Two examples of different pulse profiles from γ -ray detected pulsar are shown in Fig. 2.6. Flare-like variable γ -ray emission has only been established for a few Galactic sources. The second catalog of flaring γ -ray sources (2FAV) lists one pulsar (Papitto et al. 2014; Takata et al. 2014), three HMXRB, and a binary system with a Wolf-Rayet companion star (Cygnus X-3, Tavani et al. 2009).

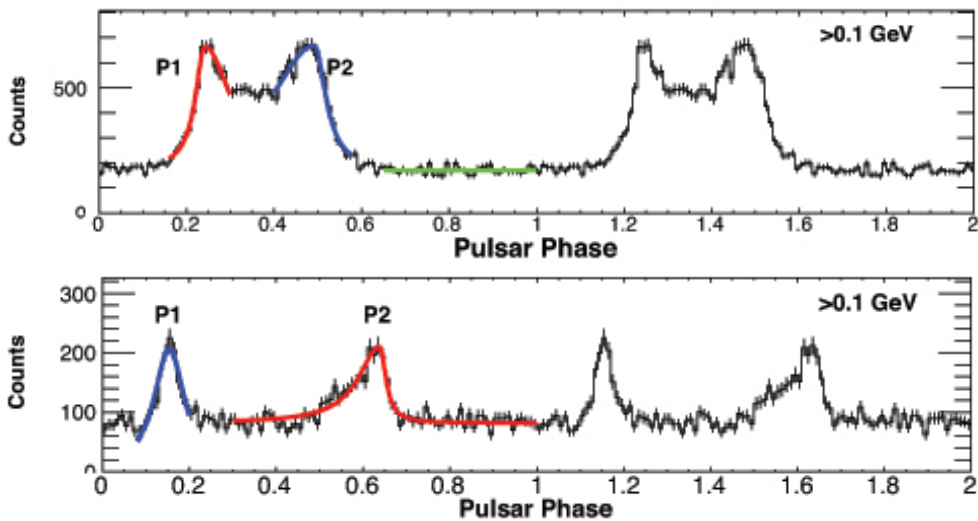


Figure 2.6.: Pulse profiles of the *Fermi*-LAT sources PSR J1709–4429 (top) and PSR J1952+3252 (bottom) for the full energy band above 0.1 GeV (Abdo et al. 2010d). Two pulsar rotation cycles are shown, and the fitting functions (thick solid lines) are superimposed on the light curves in the first cycle.

A surprising discovery was the detection of γ -rays associated with nova explosions (see Fig. 2.7, Abdo et al. 2010b). Nova are thermonuclear explosions on the surface of white dwarfs that are fueled by accretion of mass from a companion star. High-energy emission was expected in the form of X-rays from the shocked expanding gas of the nova shell. Then a γ -ray flare which was correlated with the detection of a bright optical nova explosion allowed the authors to associate the γ -ray source with the position of V407 Cyg: a binary system of a white dwarf with a red giant companion star. Nowadays, nova γ -rays are thought to arise as a consequence of shock acceleration and the interaction of the accelerated particles with the dense ambient medium or infrared radiation of the red giant. By now, five nova explosions have been detected by *Fermi*-LAT (Abdo et al. 2010a).

Another surprise was the detection of γ -ray flares from the Crab PWN (Abdo et al. 2011a) which was expected to be steady within a few percent. Within the first years of performance, *Fermi*-LAT detected several short γ -ray flares from the Crab PWN on days time scales. The short duration and large intensity increases suggested that these flares are emitted from small regions $\lesssim 0.1$ pc. The origin of these flares are still unknown. The radiation was identified as synchrotron radiation from relativistic particles of PeV energies. However, these scenarios challenged the models for particle acceleration at the termination shock. Current explanations suggest that plasma instabilities in the highly magnetized post-shock medium cause magnetic reconnection events (e.g., Lyutikov et al. 2018). An alternative scenario was proposed by Kirk & Giacinti (2017) who attribute the flares to changes in the mass load of the pulsar.

In contrast to Galactic sources, the extragalactic γ -ray sky is characterized by extreme

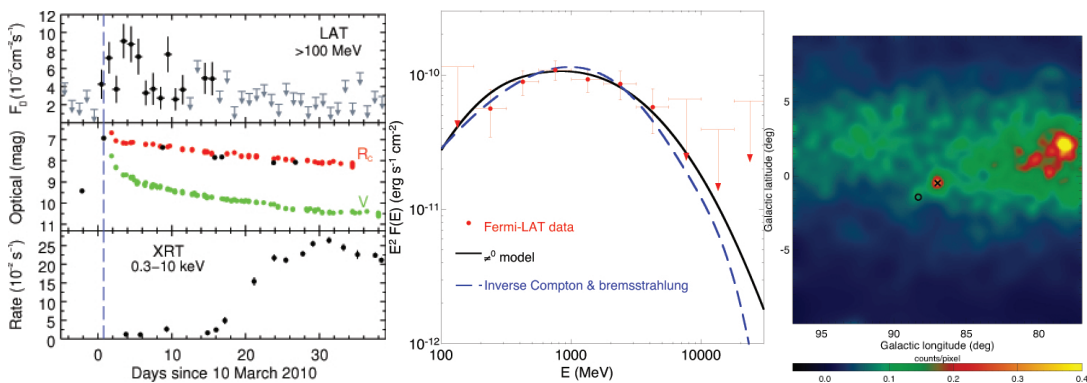


Figure 2.7.: First nova explosion detected at γ -rays from the symbiotic system V407 Cyg Abdo et al. (2010b). *Left panel:* γ -ray, optical R and V band, and X-ray light curves. The vertical lines marks the epoch of the optical nova detection. Correlated variability between the γ -ray and optical band confirmed the nova counterpart which was prior found via positional coincidence. *Middle panel:* *Fermi*-LAT 0.2–100 GeV spectrum of the γ -ray flare. The spectrum can be π^0 decay due to proton-proton interaction of shocked gas in the dense ambient medium or inverse Compton emission of electrons with the radiation of the companion star. X-rays are interpreted as thermal emission as a reaction to shock heating of the ambient medium. *Right panel:* *Fermi*-LAT γ -ray count map of the region around V407 Cyg averaged over 19 days after the nova optical explosion. The 'x' marks the position of V407 Cyg. The closest known γ -ray source is marked with a circle in an angular distance of $\sim 1.5^\circ$.

variability from GRB and AGN (e.g., Aharonian et al. 2009; Ackermann et al. 2011b). The systematic flare analysis for the 2FAV revealed a total of 4547 γ -ray flares associated with 518 variable γ -ray sources during the first 7 years of *Fermi*-LAT mission. The majority of γ -ray flares were associated with AGN, mostly blazars. Burst-like variability on timescales of a few minutes and days are detected. During these flares, AGN outshine brightest galactic sources by a factor of 10, despite their distance. The 2FAV found 2 non-blazar AGN, 14 GRB, 67 blazars of unknown type, 73 Bl lac objects, 253 FSRQ, 3 radio galaxies, and 3 NLS1). Only 77 objects (3%) remained unassociated. The low percentage demonstrates that counterparts of variable sources can be found more easily than for stable sources where the percentages lies at approximately 30%. The majority of unassociated flaring sources align along the Galactic equator, where the diffuse foreground emission is strongest and hinders the counterpart search. The variability behaviour that is observed at GeV γ -rays is similar to the transient properties of the TeV sky. Here, pulsed emission from pulsars and burst-like emission from AGN can be observed and provide the possibility to identify unknown sources.

Overall, researcher use the variable high-energy emission to put constraints on the emission models. Where are the production sites of high-energy radiation? What are the dominating processes for particle acceleration? For example, in the common paradigm of AGN, flux variations are driven by shocks within the jet plasma. However, the detection of extreme minute and sub-hour scale variability in the γ -ray emission of blazars challenge this interpretation. The shortest variability timescales (e.g., observed in CTA 102, IC

Table 2.1.: List of most commonly detected high-energy source types divided in galactic and extragalactic origin.

Source Type	X-rays	GeV γ -rays	TeV γ -rays	Reference
Galactic:				
Sun	✓	✓	x	(1,5)
Flare Stars	✓	✓	x	(1,7,11)
White dwarfs (WD)/ Novae	✓	✓	x	(1,3,8)
Neutron Stars (NS, isolated)	✓	x	x	(1)
Pulsars	✓	✓	✓	(1,2,3,4,12)
Binary Systems (BH/NS)	✓	✓	✓	(1,3)
Cataclysmic variables (CV)	✓	x	x	(1,8)
Supernovae (SN)	✓	x	x	(1)
Pulsar Wind Nebular (PWN)	✓	✓	✓	(1,2,3)
Supernova Remnants (SNR)	✓	✓	✓	(1,2,3,10)
SNR/Molecular clouds interaction	x	x	✓	(2)
Tidal disruption Events (TDE)	✓	x	x	(13)
Galactic diffuse emission	x	✓	✓	(1,2,3,9)
Isotropic diffuse emission	x	✓	x	(3)
Galactic Center (GC)	✓	✓	✓	(1,3,9)
γ -ray Bursts (GRB)	✓	✓	x	(6,7)
Extragalactic:				
Active Galactic Nuclei (AGN)	✓	✓	✓	(1,2,3)
Starburst Galaxies	✓	✓	✓	(2,3)
Galaxy Clusters	✓	✓	✓	(2,3)

References: (1) Boller et al. (2016); (2) Hinton & Hofmann (2009) (3) Acero et al. (2015); (4) Aharonian et al. (2006b); (5) Abdo et al. (2011b); (6) Paradijs et al. (2000); (7) Benz & Güdel (2010); (8) Mukai (2017); (9) H. E. S. S. Collaboration et al. (2018); (10) Weekes et al. (1989); (11) Ohm & Hoischen (2018); (12) Reynolds (2008); (13) Ulmer (1999)

Note: ✓ – detected; x – no detection yet

310, Mrk 501, and PKS 2155-304, see, Shukla et al. 2018; Aleksić et al. 2014a; Aharonian et al. 2007; Albert et al. 2007, respectively) are shorter than the light traveling times across the event horizon. This implies very compact emission regions at the region of jet formation. However, short-term variability and changes in the spectral behaviour of these sources imply that the emission region are located further away from the jet formation region, outside a region which is occupied by fast and dense rotating clouds. Otherwise, the γ -ray photon would interact with these clouds and produce electron and positron pairs (see Sect. 4.1.3). The origin of such extreme flares is still an open issue. Overall the search for the emission regions of GeV and TeV γ -ray emission in AGN jets is still not settled. Another unsolved but important issue is which objects have the potential to accelerate hadrons and hence, are sources of high-energy cosmic rays and neutrinos?

2.3. The challenge of source identification and classification

The ongoing surveys of the high-energy sky has led (and will continue to do so) to a tremendous increase in the known population of high-energy emitters. One of the great challenges in observing astronomy is therefore the identification and classification of newly detected sources, which promises to yield new discoveries.

There is no unique method to classify a source which was detected with a given instrument and whose class is unknown. The angular extension of a source in an observed image can give first hints on the object type. Most extragalactic sources appear as point sources for high-energy detectors (except for galaxy clusters, Snowden et al. 1995). On galactic scales, extended emission in the γ -ray bands is seen as a first hint for supernova remnants, pulsar wind nebulae or star forming regions.

In order to identify a new object one of the first steps is typically to search for counterparts in other wavelengths or instrument catalogs, e.g., via positional cross-matching. An association can provide additional information and help to clarify the source type. Positional cross-matching means that all objects within a defined angular distance from the coordinates of the unknown source are considered as candidate counterparts. The threshold angular distance is typically defined based on the spatial resolution and accuracy of the observing instruments (e.g., 1σ positional uncertainties).

For each candidate match one then estimates the probability that the candidate can be identified with the source of interest using statistical methods such as Bayesian or maximum likelihood ratios (e.g., de Ruiter et al. 1977; Sutherland & Saunders 1992, respectively). In principle, these methods test the probability of detection against the null-hypothesis that an object of given properties (e.g., a certain magnitude) can be detected by chance taking into account the local source density and background noise in a certain region of the sky. Consequently, in a region of high source density such as the Galactic plane, this method requires very good source localization. One of the biggest limitations of this approach is the different positional uncertainty of source determination for different instruments. For example, for the γ -ray instrument *Fermi*-LAT the typical radius of the 95% confidence level position uncertainty is of the order of $\sim 0.1^\circ$ (Abdo et al. 2010a). This region is large with respect to lower energy observatories and contains numerous stars, galaxies, X-ray, infrared, or radio sources. Compared to an observation of optical telescopes (e.g., HST) with an accuracy of an arcseconds a simple positional cross-match can result in a large number of counterpart candidates with spatially similar properties. Such cases require additional information to resolve this degeneracy. Often various catalogs are used, for example, to gain multiwavelength information on an unknown source. In this case, a chain of pairwise cross-matches are performed, i.e., the cross-matching of two catalogs at a time where the order of matches is defined using prior knowledge or assumptions. Unfortunately, this approach can yield different results depending on the order of the pairwise matching (e.g., Budavári & Szalay 2008).

Another approach is to use properties derived from the observation (e.g., spectral shape, the presence of periodic variability, etc.) to narrow down the counterparts based on assumptions on the spectral energy distribution or emission process of the object.

This method is particularly useful, if the goal of the cross-match is to find counterparts of a known source type. One can use assumptions on the expected SED and use spectral properties such as photometric information or color ratios, to find the best match. For example, Cool et al. (1995) cross-matched an X-ray selected sample of cataclysmic variables with optical images and used optical photometric information ($H\alpha$ emission excesses with respect to the R band) to find CVs among a sample of stars. In order to increase the number of high-mass X-ray binaries, Cohn et al. (2010) used series optical images to identify those stars which change their position and indicate binary systems.

The problem is that the association with a counterpart relies on our assumptions of the source properties. Hence, is it less likely to detect unknown or untypical object types. For example, the algorithm that is used in the computation of the *Fermi*-LAT catalogs, to find counterpart associations for the γ -ray sources, makes assumptions on the availability of sufficient energy within a candidate source, as well as whether a source type can sustain a plausible physical process to produce γ -ray emission. Hence, there are some source classes which are very unlikely to be associated with an *Fermi*-LAT detection, simply because do not expect to see them this instrument (Abdo et al. 2010a).

To test the nature of candidate high-energy counterparts correlations between emission in different energy bands can be helpful. The correlation between radio and γ -ray emission has been established in numerous studies (e.g., Padovani et al. 1993; Salamon & Stecker 1994; Taylor et al. 2007) and is motivated by the combination of the synchrotron and inverse Compton process in regions populated by highly energetic particles. Multi-frequency radio observations can therefore be used to identify high-energy emitters. For example, relatively high compact radio flux density and radio flat spectrum sources indicate an AGN-like nature (e.g., Mattox et al. 1997; Acero et al. 2013). Also high angular resolution radio follow-up observations, VLBI observations in particular, are useful to reveal the radio morphology of a gamma-ray source (e.g., Ackermann et al. 2011a; Petrov et al. 2013). But also other energy bands that are sensitive to thermal emission can be used to distinguish between different types, such as stars and extragalactic objects. Massaro et al. (2013) developed a method in order to identify AGN candidates among *Fermi*-LAT sources based on color-color diagrams of the infrared counterparts from the Wide-field Infrared Survey Explorer (WISE) resulting from positional cross-matches. They find that γ -ray emitting blazars (see Sect. 3.1.2) are confined within a well-defined region, referred to as *blazar strip*. Furthermore, in case of AGN, optical spectroscopy provides crucial information on, redshift, the properties of the host galaxy, or orientation of the system with respect to our line of sight.

Unambiguous identification with a counterpart can be retrieved if there is variable emission. Ray et al. (2012) discovered an unexpected large number of pulsars among unassociated γ -ray *Fermi*-LAT sources by searching for radio pulsations. Correlated emission outbursts that are observed at different wavelengths also provide significant identification. However, the identification via correlated emission is very difficult with respect to the observing schedule and time resolution of different instruments and satellites. To make it even more complicated, flares in different energy bands are not necessarily simultaneous due to different emission region sizes or opacities.

Statistical studies are performed to find characteristic observational properties that facilitate source classification. Recently, many investigations test the use of machine learning and deep learning algorithms to compute the most likely counterpart of an observed source (e.g., Salvato et al. 2018) or classify objects solely based on their spectral features in one band (e.g., Farrell et al. 2015; Ackermann et al. 2012b). Mirabal et al. (2012), for example, used the random forest machine learning approach to assign a probability that an unassociated *Fermi*-LAT source is an AGN based on its spectral and variability information. The clustering ability and possible application of complex classification schemes to large data sets demonstrate the potential benefit of this simple artificial intelligence. The usefulness of machine learning algorithms in order to discover new source classes or phenomena depends on their ability to detect outliers. In the end, the detection of source types in formerly unexpected radiation bands raise new puzzles and offer the opportunity to discover new insights in the physical processes of astronomical sources (e.g., the detection of variable emission in SNR, White dwarfs, O-type and B-Type stars (Fuhrmeister & Schmitt 2003), or the detection of gamma-ray emission in certain types of Seyfert galaxies (Abdo et al. 2009b).

2.4. Emission and Acceleration of High-energy Particles

A mixture of different radiative processes are at work in high-energy sources. These can be divided into thermal or non-thermal processes, depending on whether the emitting particle distribution follows a Maxwell-Boltzmann distribution or not. While the mechanisms to generate X-ray photons include both thermal and non-thermal processes, high-energy radiation above a few keV is mainly attributed to non-thermal processes involving accelerated charged particles (nuclei or electrons/positrons) and their interaction with ambient matter or radiation fields (e.g., Funk 2015).

Acceleration processes transfer energy from matter and electromagnetic fields into a population of relativistic particles which typically yields a power-law energy distribution (see Sect. 2.4.7). The properties of the observable high-energy emission is determined by the convection, diffusion and cooling of these particles as well as their interaction with electromagnetic fields. Therefore, especially in γ -ray astronomy, the production of high-energy emission allows to track the propagation of accelerated hadrons and leptons owing to magnetic fields or convection away from the acceleration site (see e.g., Funk 2015, for a review).

Primarily, the cooling of those particles is caused by synchrotron or inverse Compton radiation. Above energies of 511 keV also pair production can play an important role. One usually distinguished between leptonic and lepto-hadronic emission processes. While the cooling via synchrotron and inverse Compton emission is the same for both types, hadrons may also cool via particle decay or photo-hadron interaction. Secondary particles can be further accelerated and contribute to the radiation which adds to the complexity in the observed high-energy spectrum.

In the following I give a concise overview of the relevant processes for emission and absorption of high-energy radiation and is based on Longair (2011); Rybicki & Lightman

(1986); Boettcher et al. (2012) and detailed derivations and descriptions can be found in these works.

2.4.1. Blackbody Radiation

Thermal bodies such as stars radiate as black bodies where the spectrum is solely characterized by their surface temperature and modified by stellar atmospheric features (i.e., absorption lines). In some stars the surface temperature is higher than 10^6 K (e.g., isolated neutron stars Pires et al. 2015) and the blackbody continuum reaches into the X-ray band.

The intensity of the photon field that radiated by a black body with temperature T at a frequency ν is given by Planck's law,

$$I_{BB}(\nu) = \frac{2\pi}{c^2} \frac{h\nu^3}{\exp(-h\nu/k_B T) - 1}, \quad (2.4.1)$$

with the Planck constant h , the speed of light c , the Boltzman constant k_B . The bulk of emission is emitted at a peak frequency defined by Wien's displacement law

$$\nu_{\max} = 58.8 \frac{\text{GHz}}{\text{T}} T. \quad (2.4.2)$$

It is possible that different states of temperatures within the same system. In this case the thermal emission is composed of the superposition of several single blackbody spectra of different gas temperatures T . For example, such spectra are used to describe the interstellar dust emission (Planck Collaboration et al. 2014) or the emission of accretion disks in X-ray binaries or AGN (e.g., Shakura & Sunyaev 1973), where the disk shows a temperature gradient from the center to towards the edges.

2.4.2. Bremsstrahlung

In a hot gas with charged particles, e.g., electrons and nuclei, a single particle can be accelerated by another one through Coulomb interaction. The radiation of an accelerated particle then emits so-called *bremstrahlung* or *free-free emission*. This mechanism is frequently observed in supernova remnants (e.g., Bykov et al. 2000; Vink 2012), pulsar winds nebulae (e.g., Bednarek & Bartosik 2003; Martín et al. 2012), or from the intergalactic gas in clusters of galaxies (e.g., Cavaliere & Fusco-Femiano 1976). Although, usually the thermal emission of hot gas is a blend of a bremsstrahlung continuum and line emission (e.g., Seward & Charles 2010).

If particles are in a thermal equilibrium, their velocity distribution resembles the characteristic Maxwell distribution. The radiation from such particles due to thermal bremsstrahlung is a continuum with characteristic shape, solely determined by the temperature and density of the gas. The energy loss rate of a charged particle in a gas per unit volume dV and frequency bandwidth $d\nu$ is given by

$$\frac{dE}{dt dV d\nu} \propto n_e n_i Z^2 \sqrt{kT} e^{-\frac{h\nu}{kT}} g_{\text{ff}}, \quad (2.4.3)$$

with the gas temperature T , the density of the ions n_i and electrons n_e , the charge of the ions Z , the Boltzmann factor k , and the *Gaunt factor* g_{ff} for free-free emission, which accounts for quantum-mechanic corrections. The total radiated power by a gas of charged particles equals the integrate over the energy distribution of the particles. For gas temperature above 10^6 K the emission takes place mainly in the X-ray band.

Particles with non-thermal velocities that move at relativistic speed in a medium containing atoms or plasma can produce γ -ray photons via so-called relativistic bremsstrahlung. In this case the energy loss becomes proportional to the particle's energy (Rybicki & Lightman 1986) which can lead to a rapid cooling of high-energy particles moving in a hot densed gas.

2.4.3. Synchrotron Radiation

Charged particles that transfers a region containing a magnetic field will be accelerated due to the Lorentz force and thus emit *synchrotron radiation*. This process plays an important part in the radio to X-ray emission in radio-loud AGN (e.g., Böttcher 2007), but it is also observed in pulsar wind nebulae and supernova remnants (e.g., Fleishman & Bietenholz 2007; Bühler & Blandford 2014; Auchettl et al. 2014). In astronomical setting, high-energy synchrotron radiation is a strong indicator for the presence of very energetic particles that move at an angle to the magnetic field lines.

For a single particle of mass m , energy $E_p = \gamma mc^2$ that moves with velocity $\beta = v/c$ within a magnetic field of strength B , the energy loss due to synchrotron emission is

$$\frac{d\gamma}{dt} = -\frac{4}{3}c\sigma_T \frac{u_B}{m_e c^2} Z^4 \left(\frac{m_e}{m}\right)^3 \beta^2 \gamma^2 \quad (2.4.4)$$

with the Thomson cross section σ_T and the magnetic field energy density $u_B = B^2/8\pi$. Hence, for a given species of particles the loss rate is $\propto \gamma^2 B^2 \beta^2$ and scales with the mass of the particles as $\propto -m^3$. This means that for an accelerated proton to suffer from the same energy loss as an electron, its kinetic energy needs to be a factor $\left(\frac{m_e}{m}\right)^3 \sim 6.2 \times 10^9$ higher. Consequently, at the same kinetic energy leptons (e.g., electrons) are more efficient synchrotron radiators than hadrons (e.g., protons) due to their smaller mass.

For relativistically moving particles beaming effects transform the dipole emission of a single particle in its rest frame to a narrow emission cone in lab frame with an opening angle $\propto \gamma^{-1}$, where γ is the Lorentz factor of the particle. When this cone is pointed towards the observer, a short pulse is detected. Furthermore, if the magnetic field is aligned, the synchrotron radiation is strongly polarized. This characteristic can be used to study the magnetic field configurations in astrophysical objects (e.g., Neining 1992).

In general, a distribution of particles is observed. Commonly the assumed distribution is a non-thermal population of accelerated particles (e.g., electrons) with an energy distribution that follows a power-law distribution,

$$n(\lambda)d\lambda = n_0\gamma^{-p}d\lambda, \quad (2.4.5)$$

where p is the spectral index. The average power of synchrotron radiation then also yields an overall power law from the superposition of all individual particle spectra $P_\nu \propto \nu^{-\alpha}$. In the optically thin medium, the spectral index s related to the spectral index p of the particle energy distribution

$$\alpha_{syn} = -\frac{(p-1)}{2}. \quad (2.4.6)$$

Synchrotron photons can be absorbed by the same particles that caused their emission. This process is called *synchrotron self-absorption* (SSA). The effect can be seen in radio spectra of radio-loud AGN as a turn over at frequencies ν_t that corresponds to an optical depth of $\tau_{SSA} = 1$. For frequencies below ν_t the medium is optically thick for its own synchrotron radiation. In this case the synchrotron spectrum is independent of the particle index and evolves $\propto \nu^{5/2}$.

2.4.4. Inverse Compton Scattering

Compton scattering describes the interaction of a particle (e.g., electron) and a photon. In the traditional Compton effect, a photon scatters off a non-relativistic electron ($\gamma = 1$) and transfers energy to the later and the cooling of the photon is proportional to the photon energy. In case of an electron with energy γmc^2 that moves at relativistic speed, i.e., $\gamma \gg 1$, energy may be transferred in the opposite direction from the electron to the radiation field. This process is referred to as *inverse Compton (IC)* scattering.

IC emission is particularly important for explaining the high-energy emission in astronomical sources with large amounts of hot plasma, such as Pulsars or the circumnuclear region of black holes. In AGN or X-ray binaries, thermal Comptonization describes the inverse Compton scattering of optical thermal photons from an accretion disks with a hot electron gas (Rybicki & Lightman 1986).

The energy transfer from particles to photons is possible because of a Doppler shift of the scattering photons. In the rest frame of the particle, Compton scattering takes place and the photon transfers energy to the particle. However, in lab frame the scattered photon is Doppler shifted to higher energies. The energy gain of the scattered particle is $\propto -\gamma^2$ in the Thomson regime ($h\nu \ll \gamma mc^2$).

To first order, the energy loss rate of an electron that scatters on an isotropic radiation field is

$$\frac{d\gamma}{dt} = -\frac{4}{3}c\sigma_T \frac{u_{ph}}{m_e c^2} \gamma^2, \quad (2.4.7)$$

with the photon field energy density u_{ph} . When compared to Eq.(2.4.4), it is obvious that in the low-energy Thomson regime, this expression is analogous to that of synchrotron radiation. While the latter depends on the energy density of the magnetic field, the energy loss of the IC process depends on the energy density of the radiation field. Subsequently, for a power-law distribution of particles, the resulting spectral shape due to IC scattering can be approximated by a power law with a similar spectral index as

synchrotron radiation (e.g., Dermer & Schlickeiser 1993).

The efficiency of the IC process depends on the energy of the incident photon in the rest frame of the electron. As long as the photon energy is small compared to the rest-mass energy of the particle $h\nu \ll mc^2$, the Compton cross-section, which is also known as Klein-Nishima cross section, assumes a constant value and is asymptotic to the Thomson cross section σ_T . The scattering is elastic. However, for large photon energies $h\nu \gg mc^2$, the Compton cross section is reduced and the efficiency of the energy transfer is limited.

For example, an isotropic distribution of electron and target photons with a power-law energy distribution $n_e(\gamma) \sim \gamma^{-p}$ will generate IC spectra with spectral index

$$\alpha_{IC} = \frac{(p+1)}{2}. \quad (2.4.8)$$

In Klein-Nishima regime the IC spectrum steepens by $\Delta\alpha_{IC} \approx (p+1)/2$ and

$$n_{\gamma,KN}(\nu) \propto \nu^{-(p+1)}. \quad (2.4.9)$$

2.4.5. $\gamma\gamma$ Pair Production

In the γ -ray regime, the only relevant absorption process is $\gamma\gamma$ *pair production* (also called $\gamma\gamma$ absorption). This absorption component becomes relevant for compact emission regions or very high-energy γ -rays from sources at cosmological distances. While γ -rays in compact emission regions are absorbed by the same photon field, the later suffer from absorption of external radiation. In particular, the infrared and optical extragalactic background light (EBL, see Dwek & Krennrich 2013 for a review and references therein) from dust, young, star-forming galaxies, or stars in galaxies, affects γ -ray spectra of these astronomical objects.

Two photons of energy $\epsilon_1 = \frac{h\nu_1}{m_e c^2}$ and $\epsilon_2 = \frac{h\nu_2}{m_e c^2}$ can annihilate to produce an electron-positron pair if their energy is at least as high as the rest-mass of the two leptons. The threshold for this interaction is

$$\epsilon_1 \epsilon_2 \geq \frac{2}{1 - \mu}, \quad (2.4.10)$$

where $\mu = \cos \theta$ is the scattering angle between the photons. Subsequently, the smallest threshold is reached for head-on collisions where $\mu = -1$ and $\epsilon_1 \epsilon_2 \geq 1$. Likewise, the inverse process can happen and an e^-e^+ pair may annihilate to two γ -ray photons.

The effect of pair production on the spectral energy distribution of a radiation field depends on the location of the target photon field. If the absorbing target field lies outside the initial emission region, then $\gamma\gamma$ pair production leads to a simple exponential absorption term

$$I_\nu^{obs}(\epsilon) = I_\nu^{ini}(\epsilon) e^{-\tau_{\gamma\gamma}(\epsilon)}, \quad (2.4.11)$$

with the opacity $\tau_{\gamma\gamma}(\epsilon)$ of the target photon field. However, if the absorption occurs inside the emission region the effects on the spectral energy distribution of the primary

photon field will change the radiative transfer equation. The importance of pair production is often measured by the compactness parameter

$$l = \frac{L_\gamma \sigma_T}{4\pi R \langle \epsilon \rangle m_e c^3}, \quad (2.4.12)$$

with the γ -ray luminosity L_γ , the average photon energy $\langle \epsilon \rangle$, and the size of the emission region R .

The resulting electron-positron pairs will have equal Lorentz factors $\gamma_{e^\pm}^2 = \frac{1}{2}\epsilon_1\epsilon_2(1 - \mu)$ in the co-moving frame. If the primary and target photon field have a power-law distribution in energy the resulting energy distribution of the pairs will also be a power law with gradual cut-off at low and high energies due to the minimum and maximum photon energies.

Pion Production

If protons are accelerated they can interact with other protons or photons. The excited states can lead to pion production which produces a *hadronic cascade*.

$$p + p \rightarrow N + N + n_1(\pi^+ + \pi^-) + n_2(\pi^0), \quad (2.4.13)$$

where N can be a neutron or proton and $n_{1/2}$ are integers. The lifetime of neutral pions is only $\sim 10^{-16}$ s. Hence, they almost immediately decay into two γ -ray photons. However, the charged pions decay under the production of muons and neutrinos.

$$\pi^+ \rightarrow \mu^+ + \nu_\mu, \quad (2.4.14)$$

$$\pi^- \rightarrow \mu^- + \nu_\mu, \quad (2.4.15)$$

The muons further decay producing electrons, positrons and neutrinos in a cascade via

$$\mu^+ \rightarrow e^+ + \nu_e + \bar{\nu}_\mu, \quad (2.4.16)$$

$$\mu^- \rightarrow e^- + \nu_e + \bar{\nu}_\mu \quad (2.4.17)$$

The charged particles can lead to additional synchrotron or IC emission as thought to occur in some AGN jets. The expected of neutrinos would be unambiguous evidence for hadronic processes within an object.

2.4.6. Absorption processes

In general, observed emission in most energy bands is affected by absorption of some kind due to matter in the line of sight between Earth and the objects of interest. All X-ray observations are generally affected by photoelectric absorption from the interstellar medium (ISM) of our galaxy (e.g. Wilms et al. 2000). In addition, source intrinsic absorption occurs in many astronomical objects (Guainazzi et al. 2005; Bianchi et al. 2012).

While free-free absorption (the reverse process to bremsstrahlung) and synchrotron self-absorption are relevant processes in the low-energy bands such as radio, observations in high-energy astronomy are primarily affected by photoelectric-absorption in the X-ray band or pair production in the γ -ray band.

When an X-ray source is obscured by material in the line of sight, some photons will collide with individual atoms and nuclei in the obscuring medium. X-ray photons will be absorbed and excite or ionize the material. The transmitted beam will have fewer photons, however, the energy of the transmitted photons is not changed.

The observed X-ray flux is related to the intrinsic flux through the absorbing factor $e^{-\tau}$, where $\tau = \int a dl$ is the optical depth of the obscuring matter with absorption coefficient a along the path length l . In astronomy, the thickness of the absorbing medium is rarely known. The optical depth is therefore expressed in terms of the photo-electric cross-section σ and the number of atoms in a 1 cm^2 column between the observer and the source. The column density is generally expressed by the neutral hydrogen equivalent column density N_{H} . The optical depth for photons of energy E and passing a medium of column density N_{H} is then given by

$$\tau(E) = N_{\text{H}} \sum_{ij} A_i \sigma_{i,j}(E), \quad (2.4.18)$$

where A_i is the abundance of element i with respect to neutral hydrogen. Because $\sigma(E) \propto Z^3/E^{-3}$, absorption is greatest for low-energies photons and in high- Z materials.

Column densities in the ISM range from 10^{20} to 10^{22} atoms/cm $^{-2}$ (Planck Collaboration et al. 2014) which only affects the observed X-ray spectra below a few keV. More energetic photons pass the medium unaffected. In contrast, in circumnuclear material in AGN the column density can exceed 10^{24} atoms/cm $^{-2}$. In this case, the primary X-ray emission is fully absorbed below 10 keV and Compton scattering becomes important. The X-ray source may only be observed in scattered emission or at higher energies above 10 keV (e.g., Akylas et al. 2016).

2.4.7. Particle Acceleration

The emission of high-energy radiation is a tracer of accelerated particles up to the highest energies. Theoretical models for acceleration need to explain typically observed power-law spectra up to energies of $\sim 10^{20}$ eV similar to energies observed for cosmic rays. One of the most prominent acceleration mechanism is *second-order Fermi acceleration*, (Fermi 1949), also referred to as shock acceleration. In these processes relativistic particles interact with a turbulent magnetized plasma cloud which moves in opposite direction. Inside the cloud the particles experiences several elastic scattering processes. If the particle leaves the cloud in the opposite but parallel direction to the cloud it gains the energy

$$\frac{E_1 - E_0}{E_0} = \gamma_{\text{cl}}^2 (1 + \beta_{\text{cl}})^2 - 1 \equiv \mu, \quad (2.4.19)$$

where $\beta_{\text{cl}} = v_{\text{cl}}/c$ is the speed of the cloud and $\gamma_{\text{cl}} = (1 - \beta_{\text{cl}})^{-1/2}$ (Stanev 2004). Consequently, the energy gain is proportional to the square of the velocity of the cloud. The produced particle spectrum follows a power-law. A more efficient acceleration process is called *first order Fermi acceleration process* (or diffuse shock acceleration). Particles interact with non-relativistic shocks created by density discontinuities in the plasma. If a relativistic particle crosses the shock front its energy gain is proportional to velocity of the shock, $\mu \propto \beta_s$ (Longair 2011).

Particles may also be accelerated through *magnetic reconnection*. The former process is often used to explain particle acceleration in the coronae of stars (Gordovskyy et al. 2010) but it is also considered for ,e.g., acceleration of heavy nuclei in AGN (Giannios et al. 2010). Large amounts of energy is stored in magnetic fields. In case this field coincides with a plasma, this magnetic energy can be dissipated by heating the plasma through the reconnection of field lines.

Another acceleration process is thought to take place in the magnetosphere of neutron stars in pulsars. Although it may also play a role in black hole in AGN (Punsly 2001). Particles can be accelerated through the electric field in the gaps near the magnetic poles (*polar cap*) of the rotating neutron star, or in a region between open field lines and surfaces between the positive and negative charged region of the magnetosphere (outer cap model, Weekes 2003).

3. The hot all-rounder: Active Galactic Nuclei

The extragalactic high-energy sky is dominated by active galactic nuclei (AGN) which are the central core of galaxies that produce more radiation across the whole electromagnetic spectrum than the rest of the galaxy. Their extreme brightness is caused by phenomena connected to the accretion of matter onto supermassive black holes and their interaction with the host galaxy (see Sect. 3.1.1). The prevalence of high-energy emission in all types of AGN shows that strong gravity, extreme plasma conditions, and strong gravity, high-energy particle acceleration are common in these objects. AGN are unique laboratories for studying these phenomena, as well as, testing gravitational waves generation. The study of the nature of AGN and environments also contribute to the understanding of extragalactic cosmic ray origins, galaxy evolution, and cosmology.

The investigation presented in this thesis focuses on the high-energy emission of AGN that were selected because of their emission properties in the γ -ray band. Therefore, this chapter offers a concise overview of AGN types that are detected in γ -rays. In Sect.3.1, I will then summarize the general components of an AGN, followed by an introduction to the unification scheme. Section 3.3 deals with the physics of relativistic jets in AGN. Eventually, typical broadband emission of AGN is given in Sect.3.2. Comprehensive overviews on the classification and physics of AGN are given for example in Boettcher et al. (2012) and Meier (2012). Padovani et al. (2017) gives an excellent recent review on the observed emission properties of AGN across the whole electromagnetic spectrum as well as their unification. Unless stated otherwise, the following sections are strongly based in these references.

3.1. Overview of AGN unification

Phenomenologically, AGN display a wide variety of observational appearances resulting in various AGN classes and types. The large number of AGN classes used in the literature today coined the term "zoo of AGN" in which a single object may multiple type associations depending on the applied classification scheme. Table 3.1 lists AGN acronyms that are typically used in the literature, as well as a few types that are relevant to this thesis. A full version of this list is given in (Padovani et al. 2017). Detailed information on the AGN zoo can be found for example in Peterson (2009). A The unification model of AGN assumes that all type of AGN share the same central engine and different characteristics are caused by orientation or changes in only a small number of parameters.

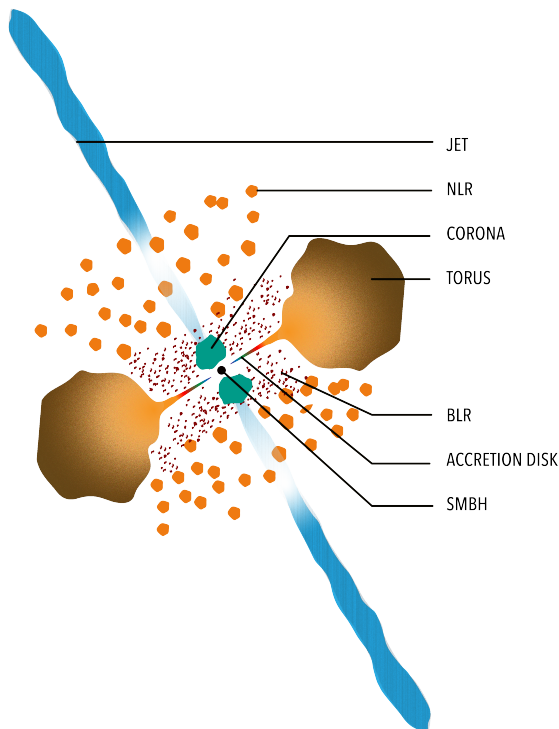


Figure 3.1: Schematic picture of an AGN. The scheme is highly simplified and relative sizes of individual components are not to scale. A SMBH in the center is surrounded by a rotating accretion disk. The combination of these components can launch a relativistic jets which is highly collimated. An X-ray corona, BLR, and NLR clouds are located above the disk, although their structure and distribution are still debated. A cold dense distribution of dust called torus obscures the central engine with large covering factors. Emission from the central regions can be reprocessed through scattering and Compton reflection. See text for more information on each component and the unified model of AGN.

3.1.1. The building blocks of the central engine

The center of all AGN is a rotating *supermassive black hole* (SMBH). Every black hole can be characterized by its mass and spin (e.g., Meier 2012). The mass of SMBH in AGN spans a wide range from $10^6 M_{\odot}$ to $10^{10} M_{\odot}$ (e.g. Peterson & Wandel 2000; Peterson et al. 2004; Calderone et al. 2013). The spin is typically parameterized by the dimensionless angular momentum a , $-1 \leq a \leq 1$, which measures the relative angular momentum J of the black holes with respect to the rotational energy of the hole $a = J(GM^2/c)^{-1}$ (Meier 2012). The SMBH is surrounded by a rotating accretion disk that extends from roughly 10^{-3} to 1 pc) and fuels the AGN via mass accretion (Salpeter 1964). Mass accretion is the most efficient mechanism to convert matter into energy and is 10 to 50 times more efficient than nuclear fusion. Hence, an active nuclei can shine more brightly than all the stars in the host galaxy itself.

In the standard picture, the energy release from matter that moves down the steep gravitational potential heats up the disk and is dissipated via thermal radiation in the form of a multi-temperature blackbody (Shakura & Sunyaev 1973; also see Sect. 2.4). This emission from the accretion disk is inverse Compton up-scattered (see Sect. 2.4) by hot electrons in the vicinity of the disk, giving rise to a non-thermal emission component in the X-ray band (Haardt & Maraschi 1993a; Titarchuk 1994; Dove et al. 1997). This region is often referred to as *X-ray corona*. The geometry and distance of the corona with respect to the accretion disk is debated (Matt et al. 1991; Fabian & Vaughan 2003; Dauser et al. 2013; Gonzalez et al. 2017). Several authors proclaim a tight connection

between the X-ray corona and the accretion flow (e.g., Steffen et al. 2006; Lusso & Risaliti 2016, and references therein). At a distance of roughly $r \sim 0.01\text{-}0.1$ pc resides the *broad line region* (BLR; e.g., Blandford & McKee 1982; Peterson & Wandel 2000). Fast rotating clouds of hot dense gas surround the accretion disk. The gas is ionized and accelerated through the strong gravitational potential of the SMBH. Observed broad emission lines from this region show typical gas velocities of a few 1000 km s^{-1} . Further out, the whole system enclosed by the *narrow line region* at $r \sim 100\text{-}1000$ pc (NLR, e.g., Evans et al. 1993; Congiu et al. 2017). This far out the gas clouds are colder and less dense. Emission lines from this region include forbidden transition (e.g., $[\text{O III}]\lambda 5007$, e.g., Schmitt et al. 2003) and exhibit much smaller line widths of a few 100 km s^{-1} . The classical unification model assumes the presence of a homogeneous, donut-shaped circumnuclear structure of hot and cold dust, called *torus* (e.g., Jaffe et al. 2004; Krolik 2007). In the classical view it is located in the plane of the accretion disk and extends from about $r \sim 1$ pc to ~ 10 pc, thus surrounding the BLR, corona, and accretion disk. Depending on the orientation of the torus to the line-of-sight, emission from the inner region is heavily absorbed or blocked. Hence, this structure is a critical component of the unification model. However, the geometric distribution and kinematics of the dusty material are still uncertain and strongly debated. Elitzur & Shlosman (2006) proposed a clumpy torus, which is supported by observed short-term variability of the absorbing column densities that cannot be attributed to changes in the intrinsic continuum emission (e.g. Elitzur & Shlosman 2006; Elitzur & Ho 2009; Markowitz et al. 2014; Beuchert et al. 2017). The structure of the torus and the covering factors of the obscuring material can differ significantly for different AGN and may be related to the accretion flow: a higher accretion rate yield a higher accretion luminosity with possible strong mass outflows leading to a receding torus (e.g., Lawrence 1991; Simpson 2005).

Another prominent radio-loud AGN phenomenon is the presence of highly collimated and relativistic outflows of plasma in AGN, called *jets*. The structure and inclination angle of the jet influences the observational phenomena, in particular in the radio and γ -ray band. Figure 3.2 show the powerful jet in the radio galaxy Centaurus A. The physical nature, such as the mechanism to launch a jet as well as their plasma composition are among of the open questions in AGN research today. Their extension can range from a few pc up to Mpc. However, the mechanism responsible for the collimation over such large distances are yet resolved. Furthermore, how the jet interacts with the interstellar medium in the environment of the AGN whether this interaction influences AGN and/or galaxy evolution is a hot topic modern astronomy. Sect.3.3 summarizes some basic aspects of relativistic jets in AGN.

3.1.2. Classes of γ -ray detected AGN

All types of AGN are typically observed as point sources on the X-ray sky, while only a smaller fraction are also known as gamma-ray emitters. The majority of extragalactic γ -ray detected sources are blazars, i.e., a class of AGN with relativistic jets where the angle of the jet axis with respect to our line of sight is small. Only a small number of different AGN types, so-called non-blazar AGN, have been detected in the γ -rays so

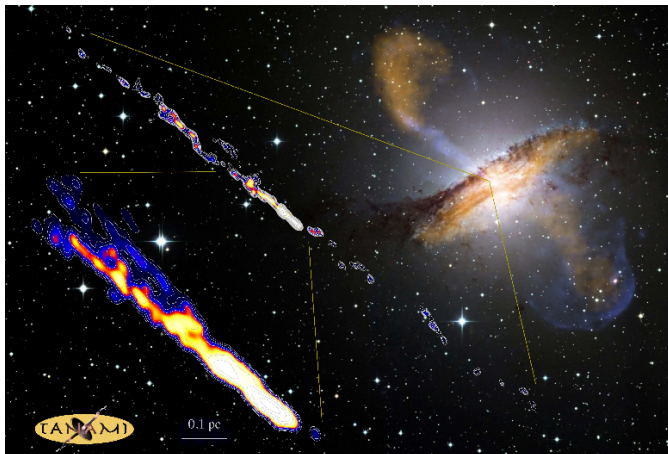


Figure 3.2: The optical HST image of the radio galaxy Centaurus A. The overlay of the radio emission shows a two-sided kpc scale structure of a powerful relativistic jet. Very long baseline interferometry allows to study jets on milliarcsecond resolution. The radio-structure of the highly collimated subparsec-scale jet of Cen A is shown in the inset images (Müller et al. 2011).

far which prevents extensive population studies. Only 2% of the third catalog of AGN detected between 0.1 GeV and 300 GeV by the *Fermi*-LAT instrument (Ackermann et al. 2015) are non-blazars and only four of such sources have been detected in the VHE TeV γ -ray band (Centaurus A, NGC 1275, M 87, and PKS 0625+35, see TeVCAT¹).

The investigation of individual objects of both non-blazar type compared to blazars can provide additional valuable insights on γ -ray emission sites and mechanisms of these AGN. In the following, I introduce the γ -ray detected AGN types.

Blazars

The *blazars* subclass is the most extreme and violent class of active galaxies showing strong, variable non-thermal continuum emission from radio to up to VHE γ -rays. In the radio to UV band this emission is strongly polarized. Their radio morphology show one-sided, core-dominated, and strongly foreshortened radio jets on (sub-) parsec scales at the highest spatial resolution (e.g., Ojha et al. 2010; Lister et al. 2016; Müller et al. 2018).

Blazars are divided into *BL Lac objects* (BL lacs) and *flat spectrum radio quasars*² (FSRQ) based on the existence of optical emission lines. BL lacs, named after the prototypical blazar BL Lacerta, lack or only show only weak lines. In contrast, FSRQ exhibit strong emission lines. Additionally, the radio jet power is stronger than in BL Lac objects. Blazars with additional high optical variability are called *optically violent variables* (OVV). This variability can lead to misclassification. For example, the prototype BL lac object BL lacerta itself exhibits optical emission lines during non-flaring periods (Vermeulen et al. 1995).

Despite being a minority among all AGN, blazars dominate the extragalactic high-energy sky. VLBI observations show that their continuum emission is strongly Doppler boosted and relativistically beamed, thus enhancing their luminosity (see Sect. 3.3).

¹TeV catalog: <http://tevcat.uchicago.edu/>

²Quasar is short for *quasi-stellar radio source*.

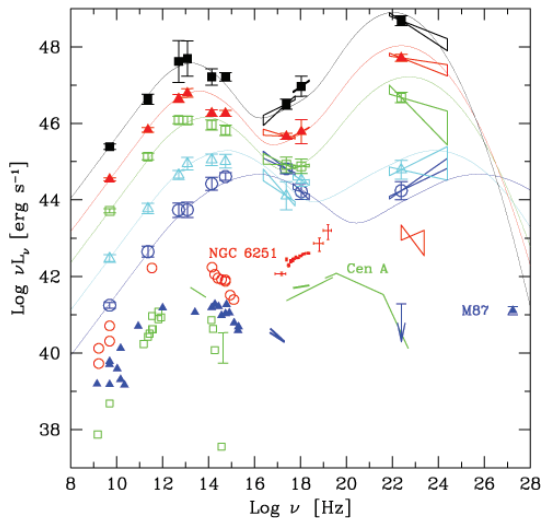


Figure 3.3: The blazar sequence refers to a correlation of the bolometric luminosity and synchrotron peak frequencies in the stationary broadband SED of blazars (Fossati et al. 1998). Also shown are three SEDs of γ -ray emitting non-blazars, Centaurus A, M 87, and NGC 6251, which show a similar spectral shape of their jet emission. The image taken from Ghisellini et al. (2005).

The broadband emission of blazars shows a characteristic double-hump shape (see e.g., Figs. 3.3 and 3.5) and exhibits strong variability at all wavelengths. A low-energy hump ranges from radio to UV/X-rays and a high-energy hump spans from X-rays up to γ -ray energies. The peak frequencies where these humps seem to be correlated with each other and with the bolometric luminosity of the source (e.g., Fossati et al. 1998; Ghisellini et al. 1998). This trend called *blazar sequence* (see Fig. 3.3) yields further subdivision of blazars with respect to their SED shape. Thus, BL lac objects are often subdivided based on the position of the peak frequency of their low-energy hump into low (LBL), intermediate (IBL), or high (HBL) frequency peaked BL lac object.

Seyfert galaxies and γ -loud Narrow Line Seyfert 1 galaxies

Seyfert galaxies are the most common class of AGN (Seyfert 1943). They were discovered based on their strong optical emission lines. These type of AGN are typically radio-quiet. All Seyfert galaxies show narrow optical emission lines. They are divided into type 1 and type 2 Seyfert galaxies, depending on the presence or absence of broad permitted Balmer lines in their optical spectrum (Antonucci 1993), e.g., the $\text{FWHM}(\text{H}\beta) \gtrsim$ a few 1000 km s^{-1} . In addition, type 1 Seyfert galaxies show stronger continuum emission than type 2 objects, which is not related to their host galaxy emission. In X-rays, type 2 objects present a high level of absorption and reprocessing of nuclear radiation, indicating large-scale absorbing material in the line of sight. Hence, in the X-rays, the expression type 1 and type 2 mostly refer to unobscured and obscured objects.

A subclass of Seyfert 1 galaxies has been defined by (Osterbrock & Pogge 1985): *Narrow-line Seyfert 1* (NLS1) galaxies are classified based on their optical spectrum. They show broad optical Balmer emission lines that are narrower than in ordinary Seyfert 1 objects. The primary criterion is $\text{FWHM}(\text{H}\beta) \leq 2000 \text{ km s}^{-1}$. In addition, the H β line is strong with respect to the forbidden [O III] $\lambda 5007$ line, given by flux ratio $[\text{O III}]/\text{H}\beta \leq 3$

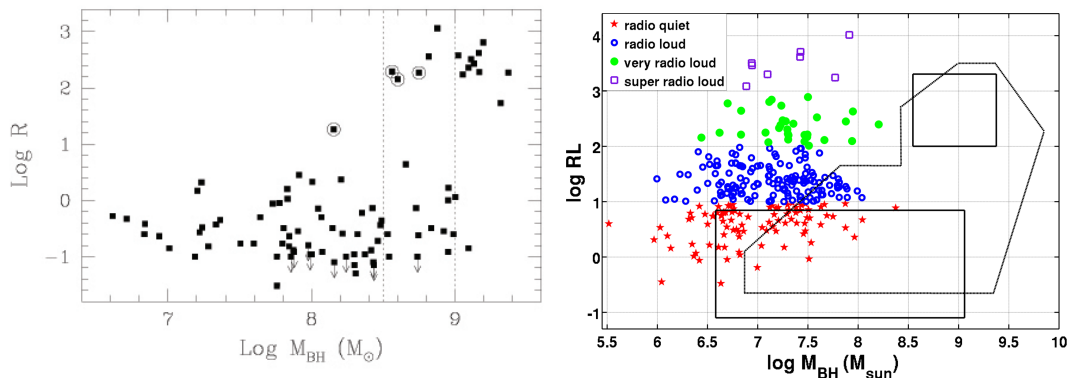


Figure 3.4.: Radio loudness as a function of AGN black hole mass. *Left panel* shows a sample of broad-line AGN (Laor 2000). The parameter space occupied by NLS1 is shown in the *right panel* (Järvelä et al. 2017).

(Osterbrock & Pogge 1985). The reason for such narrow lines is still unknown. Small Doppler widths can occur if the BLR in these objects is disk-like and viewed from extremely small inclination angles. An alternative scenario is based on the small black hole masses and high accretion rates observed in these objects. The masses are typically lower than in normal Seyfert 1 galaxies

These properties are typically accompanied by a strong Fe II emission line complex (Grupe 2004). Their X-ray properties are similar to those of normal Seyfert 1 galaxies. Except NLS1 exhibit stronger X-ray flux variability (see e.g., Grupe 2004; Kara et al. 2013) and a strong soft excess below 2 keV (Vaughan et al. 1999; Grupe 2004). Recent studies consider NLS1 as high-accretion rate objects with small black hole masses and thus in an earlier stage of evolution compared to other Seyfert galaxies (e.g., Mathur 2000; Järvelä et al. 2017; Grier et al. 2017).

Interestingly, 7% of known NLS1 galaxies show strong radio emission and can be classified as radio-loud (Komossa et al. 2006; Yuan et al. 2008). Among the population of radio-loud AGN, radio-loud NLS1 show lower black hole masses and high accretion rates than their broad-line counterparts (see Fig. 3.4). Furthermore, a small number of radio-loud NLS1 galaxies have been detected in γ -rays (Abdo et al. 2009c; Foschini 2012; D’Ammando et al. 2013b), hereafter referred to as γ -ray loud NLS1 or γ -NLS1. Although, up to 14 γ -NLS1 have been detected so far (Foschini et al. 2015; Paliya et al. 2018). The current 3LAC lists five γ -NLS1, including PKS 2004–447 which is investigated in Chpt. 8.

Radio Galaxies

These types of AGN show strong radio emission over several orders of magnitude in size on kpc and Mpc scales. Their large-scale radio structures can reach out to a few Mpc (e.g., Neeser et al. 1995). Radio galaxies are subdivided based on their radio morphology and surface brightness into Fanaroff-Riley (FR) I and II (Fanaroff & Riley 1974). FR I

radio galaxies have typical luminosities $< 10^{41} \text{erg s}^{-1}$ (at 178 MHz). They have slower, less collimated but strong two-sided jets, connected with radio lobes on each side. The more luminous FR II radio galaxies exhibit $> 10^{41} \text{erg s}^{-1}$ (at 178 MHz) and usually show powerful collimated one-sided jets extending from a bright compact central region. They show two well-defined radio lobes with hot spots on opposite sides of the compact centre.

In the optical band, radio galaxies are subdivided based on their emission line spectrum. They can be separated into *narrow-line RG* (NLRG) and *broad-line RG* (BLRG) similar to Type 1 and 2 Seyfert galaxies (see below). The main difference between Seyferts and RG is their radio luminosity with respect to their optical emission. The flux ratio of radio to optical flux defines the radio loudness R (Kellermann et al. 1989, 2016). RG have $R > 10$ and are called radio-loud, while Seyfert galaxies typically have $R < 10$ and are regarded as radio-quiet. The current third catalog of AGN detected between 0.1 GeV and 300 GeV by the *Fermi*-LAT instrument (3LAC, Ackermann et al. 2015) lists 14 radio galaxies, 11 FR I and 3 FR II, including famous radio sources such as Centaurus A (FR I), NGC 1275 (FR I), and 3C 111 (FR II).

Compact Steep Spectrum sources and GHz-peaked spectrum objects

Similar to radio galaxies *Compact Steep Spectrum* (CSS) and *GHz-peaked Spectrum* (GPS) objects are classified based on their radio spectrum and morphology (O’Dea 1998). It exhibits a turnover below ~ 1 GHz (CSS) or below (GPS). Their radio structure is enclosed within galactic scales $\lesssim 10$ kpc. Their radio structures are fully contained within the central regions of their host galaxies (< 1 kpc) and are thought to be the progenitors of the large-scale radio galaxies (lobes’ linear sizes of 10s–100s kpc). If the morphologic structure is symmetric, they are called, compact symmetric objects (CSO). These sources are typically referred to as young radio galaxies. Theoretical models have predicted γ -ray emission from these objects as their compact radio lobes contain large amounts of highly relativistic particles and are embedded in an environment rich in low-energy photons. The expected γ -ray variability time scales are substantially longer than those typically observed from blazars (Abdo et al. 2010c). It remains unclear which attributes make some young AGN γ -ray-loud.

3.1.3. A unification model - not one to rule them all

In the simplest unified scheme the only parameter to define the appearance of an AGN is the orientation of the observer relative to the axis symmetric torus (Antonucci 1993) and the jet axis (Urry & Padovani 1995). The model assumes a donut-shape circumnuclear torus in the plane of the accretion disk, as well as a jet axis perpendicular to the disk. The orientation is expressed by the inclination angle i , where objects viewed pole-on have $i \sim 0^\circ$ and those viewed edge-on $i \sim 90^\circ$. This concept could well explain the presence of broad emission lines from the BLR in Seyfert 1 galaxies where the line of sight is unobscured and the inner region (BLR, accretion disk) are visible. For type 2 objects, inclination angles are large and the direct view is likely blocked by circumnuclear gas and dust that is often imagined as being constrained to a torus shape. Emission from

the BLR or accretion disk are only indirectly or in polarized light. Shen & Ho (2014) suggested that also the line profiles and FWHM of optical Balmer lines (particularly $H\beta$) are good indicators for orientation. In case of radio-loud AGN, type 2 objects are associated with jets seen from the side (e.g., RG, SSRQ), while type 1 AGN have their jets pointed close to our l.o.s. (e.g, BL lacs, FSRQ). However, this classification based on orientation of obscuring material is incomplete. It cannot intrinsically explain the dichotomy between radio-loud and radio-quiet AGN, the existence of radio-loud NLS1, or the switching of type 1 Seyfert galaxies to type 2 and vice versa. Netzer (2015) show that the structure of AGN deviates from spherical symmetry and there is evidence that the dusty torus is not homogeneous. It can have a range of structures and covering factors. In addition, several studies found that the structure and emission properties of AGN can change with the efficiency of their accretion flow and excitation properties of surrounding gas (e.g., Gaspari et al. 2012; Wang 2015; Hambrick et al. 2011; Best & Heckman 2012). In a recent review Padovani et al. (2017) summarize that a more complete (though weaker) unification model needs to include the accretion rate, the torus covering factor, jet strength, host galaxy properties, and orientation effects. Most likely the deciding parameters cannot be interpreted as a clear separation of types but display a continuous distribution. Different classes of AGN sample different parts of this distribution.

A unified model must also include AGN evolution and co-evolution of the AGN and host galaxy to take into account all possible appearances. Radio jets and AGN feedback can influence the evolution of the host galaxy and vice versa (see e.g., Croton et al. 2006; Heckman & Best 2014). For example, Fabian (2012) link the formation of jets in the vicinity of a SMBH to the large-scale evolution of the host galaxy. The nuclear environment of the AGN is a highly dynamic open system and changes over time. Di Matteo et al. (2005) find that large amounts of gas in early formed galaxies and/or galaxy mergers can trigger AGN activity. Based on population studies, AGN can be divided into two distinct populations: radiative- or quasar-mode AGN and jet-mode AGN (e.g., Heckman & Best 2014). The former are associated with highly accreting black holes in excess of $\sim 1\%$ of the Eddington limit. They are primarily associated with less massive BHs which grow in high-density pseudo-bulges. AGN that are in jet-mode are associated with more massive black holes, with low accretion and low star-forming rates. Their host galaxies typically show (classical) bulges and are associated with elliptical galaxies. Hence, it is reasonable to assume that AGN show different properties because they are in a different evolutionary stage.

Table 3.1.: The AGN zoo: list of AGN types.

Acronym	Names	Main Properties	Main Classification Band
Quasar	Quasi-stellar radio source (originally)	radio source, optical emission lines	optical/radio
Sey1	Seyfert 1	RQ, $\text{FWHM} \gtrsim 1,000 \text{ km s}^{-1}$	optical
Sey2	Seyfert 2	RQ; $\text{FWHM} \lesssim 1,000 \text{ km s}^{-1}$	optical
QSO	Quasi-stellar object	Quasar-like, non-radio source	optical/radio
QSO2	Quasi-stellar object 2	High power Sey2	optical
RQ AGN	Radio-quiet AGN	$R_L \lesssim 100$	radio (optical)
RL AGN	Radio-loud AGN	$R_L \gtrsim 100$	radio (optical)
Type 1		unabsorbed l.o.s.	mainly optical/X-rays
Type 2		absorbed l.o.s.	mainly optical/X-rays
FR I	Fanaroff-Riley class I radio source	radio core-brightened	radio morphology
FR II	Fanaroff-Riley class II radio source	radio edge-brightened	radio morphology
BL Lac	BL Lacertae object	see Sect.3.1.2	-
Blazar	BL Lac and quasar	see Sect.3.1.2	-
Jetted AGN		with strong relativistic jets, *	-
Non-jetted AGN		without strong relativistic jets, *	-
CSS	Compact steep spectrum radio source	compact jet morphology, $\alpha_r > 0.5$	radio
CT	Compton-thick	$N_H \geq 1.5 \times 10^{24} \text{ cm}^{-2}$	IR/X-rays
FSRQ	Flat-spectrum radio quasar	RL AGN, $\alpha_r \leq 0.5$	radio
GPS	Gigahertz-peaked radio source	compact jet morphology, $\nu_{\text{radio,peak}} \lesssim 1 \text{ GHz}$	radio
HBL/HSP	High-energy cutoff BL Lac/blazar	$\nu_{\text{synch peak}} \geq 10^{15} \text{ Hz}$	SED
IBL/ISP	Intermediate-energy cutoff BL Lac/blazar	$10^{14} \leq \nu_{\text{synch peak}} \leq 10^{15} \text{ Hz}$	SED
LBL/LSP	Low-energy cutoff BL Lac/blazar	$\nu_{\text{synch peak}} < 10^{14} \text{ Hz}$	SED
NLS1	Narrow-line Seyfert 1	see Sect.3.1.2	optical

Note: The top part of the table relates to major/classical classes. The third column lists some of the main properties for orientation but note that in general these are too complex to be reduced to a single feature. The last column lists the energy band in which the classification is mainly/originally defined. * see Padovani et al. (2017)

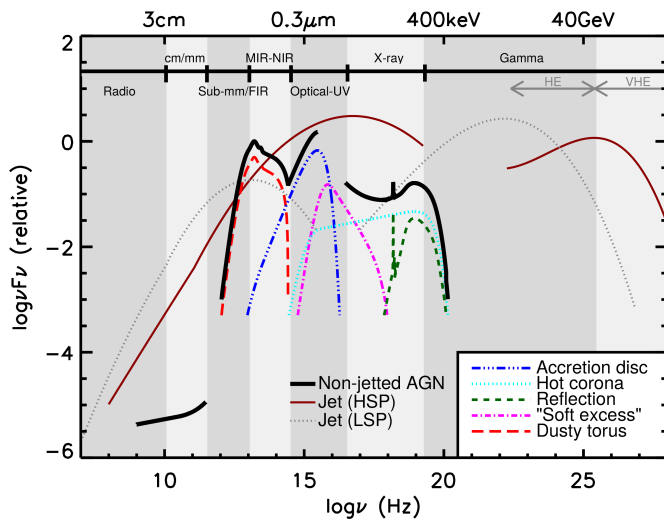


Figure 3.5: Illustration of emission component in the spectral energy distribution (SED) of jetted and non-jetted AGN. From Padovani et al. (2017), Fig. 1.

3.2. Broadband emission spectrum of AGN

AGN exhibit thermal and non-thermal emission across the whole electromagnetic spectrum. A multiwavelength (or multi-messenger) approach is therefore vital to study their radiative processes. Figure 3.5 illustrates the typical broadband spectral energy distribution (SED) observed in AGN in the typical $\nu f_\nu - \nu$ representation³, where f_ν is the flux density at frequency ν . In general, various component contribute to the emitted spectrum. In the unification of AGN all active nuclei share the same engine. But the relative contributions of these components depend on a of parameters such as the orientation of the AGN with respect to our line-of-sight, the efficiency of the accretion process, or the presence of a powerful relativistic jet.

3.2.1. Nuclear emission and reprocessing

All AGN show a large fraction of emission related to accretion processes (black solid lines, Fig. 3.5). In jetted AGN these components might be out-shined by jet emission depending on the angle to the line of sight. In the optical and UV band multi-blackbody radiation can be observed which may reach into the soft X-ray band (Sobolewska et al. 2004) and is commonly interpreted as direct emission from the accretion disk around the central SMBH. However, these energy bands (the UV band in particular) are strongly affected by photo-absorption and extinction causing attenuation of the accretion disk continuum as well as Doppler broadened fluorescent line emission through the reprocessing in the broad or narrow line region.

The intrinsic X-ray emission is characterized by a power-law from thermal Comptonization. The intrinsic power law is rarely observed directly but after being reprocessed in disk material or more distant gas, also involving GR effects when being reprocessed from the

³The νf_ν spectrum shows the amount of energy emitted per frequency decade.

innermost parts of the disk, close to SMBH. X-ray spectra thus often display characteristic signatures of reprocessing through neutral and relativistic Compton reflection (from the torus or accretion disk, see, e.g., Dauser et al. 2016 for a review), or photo-absorption (Guainazzi et al. 2005). The relative strength of these features vary significantly from source to source. In some AGN, particularly NLS1, the spectrum exhibits soft X-ray emission below 1 keV in excess of the primary power law from thermal Comptonization. This emission is often referred to as *soft excess*. The origin of this component is still debated. Current theories suggest that the soft excess is related to properties of the accretion disk. Crummy et al. (2006) associate soft excess emission to relativistically blurred emission lines from reflection of the primary emission off the innermost parts of the accretion disk. Done et al. (2012) argue that excess emission is a signature of thermal Comptonization of a more dense region. Interestingly, this component has been observed γ -ray NLS1 (e.g., D’Ammando et al. 2014a; Larsson et al. 2018). Whether the origin of this component is the same as in radio-quiet sources is still open. Recently, Kaufman et al. (2018) found that the soft excess can be explained by the bulk Comptonization of UV disk photons high-energy but sub-relativistic leptons which are not located in the corona but in shocked accreting plasma in a steady accretion flow at the ISCO or within a relativistic jet. The main modulation of the X-ray spectrum below 10 keV comes from photo-absorption (Wilms et al. 2000). The measured column densities are often in good agreement with absorption measured in the optical/UV band (Burtscher et al. 2016).

Strong absorption in the optical to soft X-ray regime ($N_{\text{H}} \sim 10^{24} \text{cm}^{-2}$) are often accompanied by an enhanced flux in the IR with respect to unabsorbed AGN (e.g., Shi et al. 2013; Treister et al. 2009; Alexander et al. 2008). The infrared band is sensitive to thermal emission from hot and cold dust residing outside the sublimation radius of the nucleus. This emission is thought to result from the reprocessing of the primary continuum that is absorbed by the dust of the putative torus. In addition, dust emission from star-forming regions of the host galaxy can contribute to the observed IR emission (e.g., Magnelli et al. 2012). So far, non-jetted AGN have not been detected in γ -rays (Ackermann et al. 2015) but they do exhibit radio emission. Although the radio fluxes are much fainter than for RL-AGN and contribution from the host galaxy (e.g., synchrotron radiation from SNR) may contaminate the spectrum. Whether non-jetted AGN carry (invisible or very faint) jets, which dissipate energy through different channels than radiation is not clear and subject of ongoing research.

3.2.2. Characteristics of jet emission

In AGN with strong relativistic jets (jetted or radio-loud AGN) the strong non-thermal emission associated with accelerated particles in the jet (solid red and dashed gray line, Fig. 3.5) dominated parts of the SED. In case of blazars the complete SED is dominated by Doppler boosted jet emission. Hence, the following focuses on the SED of blazars. In the $\nu f\nu$ representation blazar SED follow a characteristic double-hump structure with one hump at low energies extending from radio to X-rays is associated with relativistic electrons and positrons and the other one at high energies from X-rays to γ -rays.

Depending in the assumed particle populations in the jet plasma the origin of the high-energy hump is explained by IC scattering of relativistic electrons/positrons within the jet or a combination of proton synchrotron radiation and emission from secondary particle from hadronic interactions. While the SED of BL lacs is a featureless power-law, FSRQ often show an excess of thermal emission in the optical and UV band, the big blue bump (BBB). The BBB is assumed to be emission originating in the accretion disk (e.g., Elvis et al. 1994; Shang et al. 2005). Lawrence (2012) suggest additional contribution from reprocessed disk emission within the BLR.

Fossati et al. (1998) studied the SED of a complete sample of blazars. They found a correlation of the source luminosity and shape of the stationary SED, called *blazar sequence* (see Fig.3.3, see also Ghisellini et al. 1998). More luminous blazars show a lower synchrotron peak frequency than less luminous ones. Furthermore, the peaks of the low and high-energy hump are correlated and the whole SED is shifted in frequency depending on the bolometric luminosity of the source. Mechanism causing this sequence are still discussed. Some authors suggest that the sequence is caused by selection or variability effects (e.g., Finke 2013; Giommi et al. 2012a,b), while others even proclaim a physical difference between BL Lac objects and FSRQ (e.g., Meier 2012; Ghisellini et al. 1998). Although an object may follow the blazar sequence judging from their long-term averaged broadband spectrum. It can deviate in period of high activity and flares within a single object (Krauß et al. 2016).

3.2.3. Broadband variability of jetted-AGN

The observed jet emission is known to be variable on all frequencies which makes simultaneous observations important. In particular, jetted AGN emitting high-energy emission have been observed to show extreme variability (e.g., Sahakyan et al. 2018; Saito et al. 2013; Sobolewska et al. 2014). The variability timescales range from short variations, from hours to days, to longer variations on the scale of weeks and months. Rapid flux variability, often accompanied by spectral variations, on timescales down to a few minutes has been observed in blazars (e.g., Aharonian et al. 2007). Using rapid variability allows for the indirect probe of emission regions which are unresolved even by the highest VLBI angular resolution. The energy output during these extreme events often violate limits for transparency and as well as the Eddington accretion limit for isotropic emission and implies relativistic beaming effects (e.g., Maraschi et al. 1992a). Interestingly, a few objects at high inclination angles exhibit variability on timescales much smaller than the event horizon (Aleksić et al. 2014a).

The combination of high angular resolution radio observations and multiwavelength monitoring allows to study the relation between high-energy flares and structural changes in the jet. Flaring behaviour at high-energies is often accompanied by changes in the polarization which indicate changes in a highly order magnetic field (e.g., Abdo et al. 2010a). Dips in the X-ray light curve that were correlated with the ejection of a new radio components in VLBI images in the radio galaxies 3C 111 and 3C 120 could be explained by a connection of the accretion disk and the jet (Marscher 2006; Tombesi et al. 2012).

Often an outburst in one wavelength band is correlated with emission in another band

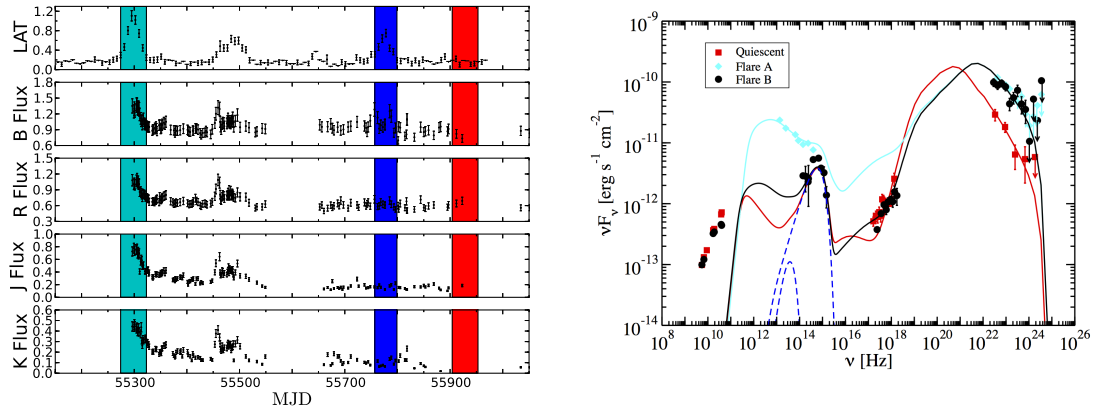


Figure 3.6.: Multiwavelength behaviour of the FSRQ PKS 2142–75 observed in 2011 (Dutka et al. 2013). *Left:* Long-term light curve in γ -ray and optical bands as observed with *Fermi*-LAT and SMARTS. The highlighted regions mark two γ -ray flaring events and one quiescent state showing different patterns of correlated emission. *Right:* Spectral energy distributions show very distinct shapes during the two γ -ray flaring states (blue and black points) and quiescent (red) periods.

(see Fig. 3.6, left panel). For example, Acciari et al. (2011a,b) found correlated variability in the light curves of the X-ray and TeV band in HBLs. Furthermore, Marscher et al. (2010) detected correlated emission between optical and γ -ray band in the FSRQ PKS 1510–089, while the radio was not correlated. The lack of correlation can be attributed to the fact that high-energy emission is produced in a compact region that is optically thick in the radio band. Another transient phenomenon are so-called "orphan flares", an outburst in a single emission band, which is not correlated with emission or observed in any other band (e.g., Krawczynski et al. 2004; Rani et al. 2013; Neronov et al. 2012). These examples show that the spectral evolution in time vary greatly from source to source and demonstrate the need for (quasi-) simultaneous observations of the broadband spectrum.

Such studies of multiwavelength variability and relationship between bands provide strong constraints on the underlying emission mechanisms and help to disentangle various contributions to the broad band spectrum. Simultaneous broadband spectra of different activity phases (flaring versus quiescent phases) provide insights in the spectral evolution during an outburst or variation (see Fig. 3.6), such as information on the relative contributions of individual emission components that helps to constrain jet emission models. Extensive (quasi-)simultaneous multiwavelength campaigns require the coordination of many different observatories with different spectral coverage and duty cycles. Insufficient spectral coverage can lead to the misidentification orphan flares because correlated emission is simply missed. Furthermore, variability timescale that can be detected with a specify instrument is limited by its sampling rate and sensitivity.

The physical mechanisms that drive fast large-amplitude flares are not yet understood.

The process of jet formation has impact on the steadiness of the jet. For example, modulations of the jet power output may cause plasma instabilities that cause large-amplitude variations in the X-ray and γ -ray emission from blazars (Spada et al. 2001; Tanihata et al. 2003). *Shock-in-jet* models (Blandford & Königl 1979a) are powerful to explain variable and correlated emission between different energy bands (e.g., Wagner & Witzel 1995a; Marscher & Gear 1985; Böttcher & Dermer 2010; Marscher 2014). In analogy to pulsar winds and supernova remnants the turbulent jets in AGN can experience changes in the local emissivity and activate flaring periods and particle acceleration due to shocks caused by instabilities within the jet flow or magnetic field. The signatures of such shocks depend on the nature of the shock. For example, shocks that compress the magnetic field configuration can lead to variability of the polarization degree and angle (e.g., Hughes 1985, Zhang 2016). However, the model has difficulties explaining ultra fast variability on timescales which imply emission regions smaller than the event horizon. Alternative models such as the *jet-in-jet* model are considered to explain such extreme phenomena (Aleksić et al. 2014a).

3.2.4. Leptonic and lepto-hadronic emission models

The radiation from a jet is thought caused by the transfer of energy to highly relativistic particles. These particles will lose energy through adiabatic or radiative cooling while moving down of the jet stream. Various models have been developed to explain the broadband emission of jets. These models can be separated into two families: leptonic and (lepto)-hadronic scenarios. It is generally accepted that the low-energy emission, ranging from radio band to the UV or soft X-rays band, results from synchrotron radiation of relativistic electrons and positrons within the jet plasma (Blandford 1972; Blandford & Königl 1979b; Sikora et al. 1994). Current SED models for jet emission differ in terms of jet composition, geometry of emission regions, and treatment of time evolution.

Leptonic models assume that electrons and positrons are responsible for the complete observed emission. The high-energy radiation is explained by inverse Compton scattering of either lower-energy synchrotron photons with relativistic electrons (synchrotron Self-Compton process, SSC, see e.g., Ghisellini et al. 2010a and references therein) or an external photon field (external Compton process, EC, e.g., Dermer et al. e.g., 1992; Sikora et al. e.g., 1994). Possible origins of seed photons are thermal photons from the accretion disk (Dermer & Schlickeiser 1994), the BLR or NLR (Ghisellini & Madau 1996), the cosmic microwave background (Harris et al. 2002), or even hot spots at kpc scales. Hadronic or lepto-hadronic scenarios are motivated by the presence of ultra relativistic protons ($E_p \sim 10^{20}$ eV) in the cosmic rays spectrum. They explore the possibility of that part of the kinetic energy of the jet can be transferred to accelerate protons within the jet plasma (see, e.g., Mannheim 1993; Reimer 2012; Böttcher et al. 2013, and references therein). Although, the acceleration of protons to these high energies require strong magnetic fields of several order of Gauss (Boettcher 2010; Mücke et al. 2003b). The high-energy emission in these scenarios stems from synchrotron of relativistic protons and emission from secondary emission from particles resulting from photo-pion production and photo-pair production processes (see Sect.2.4).

In the simplest case, the emission of low-energy synchrotron radiation and high-energy photons occurs within a single emission zone (so-called one-zone models). However, the detection of very rapid flares as well as uncorrelated emission in a single emission band (so-called orphan flares) display problems for single-zone models. Multi-zone models for different geometries and locations of the emission sites are being considered for both kind of scenarios. The leptonic model by Weidinger & Spanier (2015) considers a two-zone emission region with a spherical region embedded in a larger one. In contrast, Tavecchio & Ghisellini (2008) suggested a leptonic scenario with a cylindrical geometry, a fast inner spine and a slower outer sheath. Such models of a structured jet have been suggested to resolve the Doppler factor crisis, i.e., the observation of contradicting jet speeds in the radio and γ -ray band (e.g., Lyutikov & Lister 2010; Henri & Saug e 2006, and references therein). In the framework of a structured jet with a velocity gradient across the stream radio emission might come from a slow moving plasma and thus may not constrain the bulk motion of the fast moving jet component that is responsible for the high-energy emission. The deceleration jet model by Georganopoulos & Kazanas (2003) attempts to include differential motion with the jet.

SED models require a large number of parameters and are generally able to produce reasonable fits (e.g., B ottcher et al. 2013). Additional constraints must come from other diagnostic methods. The smoking gun evidence for hadronic processes in AGN jets is of course the identification of a blazar with the emission of a VHE neutrino which are created as a by-product of pion decay (e.g., Halzen & Zas 1997b; Kistler et al. 2014; Diltz et al. 2015; Petropoulou et al. 2015). Since ICECUBE has reported the detection of VHE neutrinos, scientist explore the possibility whether the origin of these neutrinos could be spatially connected to blazars (Aartsen et al. 2014; Kadler et al. 2016). Alternative constraints can be obtained from the analysis of broad band variability of blazars. More and more time-dependent models are being developed which can predict the expected multiwavelength light curves of jets which differ with respect to particle composition and geometry (e.g., Joshi & B ottcher 2011; Diltz et al. 2015; Weidinger & Spanier 2015; Zhang et al. 2016; Potter 2018). An example for an high-energy flare from internal shocks where the γ -rays are produced via external IC scattering is shown in Fig. 3.7 (B ottcher & Dermer 2010).

Most SED simulations suffer from the large dynamic range in size of the emission regions for radio and high energy data. Many SED models thus exclude the radio radiation which is emitted over a much larger region than X-rays and γ -rays. Spatially resolved SED models are still under development. Such model provide the possibility to derive radio morphologies (Richter & Spanier 2016). The combination of SED fitting and radio VLBI imaging can provide an alternative method to analyze emission processes in the jet.

3.3. The physics of relativistic jets

Collimated outflows are found in various astronomical objects from AGN and γ -ray bursts to objects on galactic scales such as microquasars, proto-stellar objects, or X-

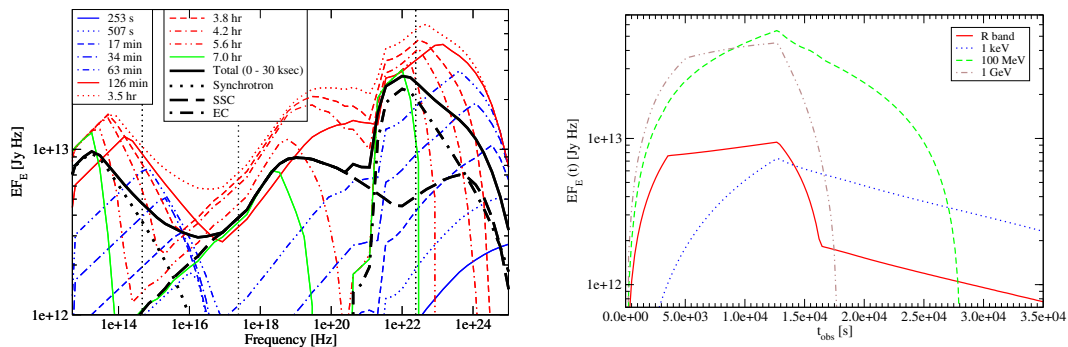


Figure 3.7.: Timing signatures from an internal shock model in blazars (Böttcher & Dermer 2010). The leptonic model includes synchrotron and SSC emission. High-energy photons are generated by IC scattering of relativistic photons with an external photon field. *Left:* Snapshot SEDs of the blazar flare at different time-steps. Solid curves show the SED resulting from averaging over an integration time of 30 ksec, representative of typical deep X-ray observation of a blazar. Dotted vertical lines indicate frequencies (R-band, 1 keV, 1 MeV, 100 MeV) at which light curves were extracted. *Right:* Light curves of the blazar flares at various energies resulting from the internal shock model. Images taken from Böttcher & Dermer (2010)

ray binaries. All these objects show clear evidence for ongoing accretion onto a central compact object (compact star or black hole), which suggest that disk accretion play an essential role in cosmic jet engines. Powerful relativistic jets in AGN are the most powerful ones observed on the largest scales. There are many open questions regarding AGN accretion, jet formation and collimation, particle composition and acceleration, and various emission components of AGN. This chapter summarizes some of the important aspects of relativistic jets.

3.3.1. Accretion and Eddington limit

In the simplest case, accretion of matter onto black hole is spherical accretion from a uniform reservoir of gas, called *Bondi accretion*. In reality, the distribution of accreting gas is nonuniform up to large distances from the black hole, which results in a net angular momentum of the in-falling matter. A rotating disk or torus will form as a result. The angular momentum of in-falling matter is transported outwards through viscosity within the disk (Shakura & Sunyaev 1973). The isotropic bolometric luminosity of an accretion disk is given by $L = \mu \dot{M} c^2$, with the accretion efficiency μ given by the radiated energy per unit of accreted mass. The density structure and geometry of the disk as well as the relative rotation of the black holes and accretion disk can affect the efficiency of the system (Boettcher et al. 2012, also see Fig.3.8). Accretion flows with inefficient radiative cooling are often called *advection dominated accretion disk* (ADAF, Narayan & Yi 1995b). Magnetohydrodynamic (MHD) simulations show that such ADAFs are capable of launching strong winds from the disk surface or even jets (e.g., Narayan & Yi 1995a; McKinney et al. 2012).

The radiation pressure from an accretion disk counteracts the gravitational potential.

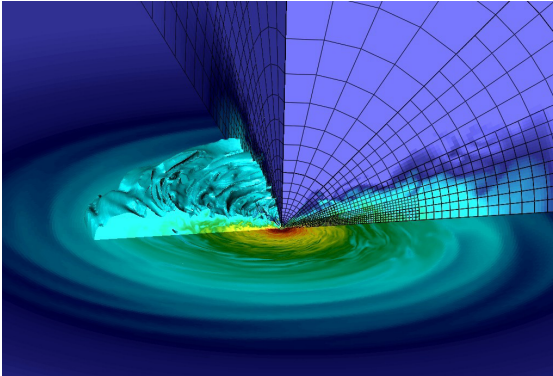


Figure 3.8: Example of the density structure in a turbulent thin accretion disk with a net vertical magnetic field from MHD simulations for CVs or proto-planetary disks (Zhu & Stone 2018). Magnetic flux diffusion and turbulence cause a filamentation of the disk surface and are capable of launching disk winds above the accretion disk corona.

The balance between these two forces defines the maximum isotropic bolometric luminosity of a black hole, called Eddington luminosity. For AGN, $L_{\text{Edd}} = 1.3 \times 10^{46} M_8$, where M_8 is the mass of the SMBH in units of one 10^8 solar masses. The accretion rate of a system is often expressed by the dimensionless accretion rate L/L_{Edd} . How the accretion rate affects jet formation is not yet understood. The paradigm that jets are launched in systems with low accretion rate (e.g., Marscher 2009) has been challenged by the discovery of powerful jets in NLS1, which typically accrete at high or even super-Eddington rates.

3.3.2. Formation of relativistic jets

A jet can be described as a fluid which contains relativistically moving particles, a magnetic field and/or Poynting flux. They are believed to be launched from accretion onto the SMBH insofar as gravitational or rotational energy are extracted from the accretion disk or black hole, respectively, which yields the acceleration of plasma along the rotational axis of the system. Currently, there are two scenarios, black hole-driven and accretion disk driven jets, which are thought to be capable to launch a relativistic jet. Both scenarios require highly magnetized accreting matter in the vicinity of the SMBH.

In the Blandford-Znajek process (BZ, Blandford & Znajek 1977), the jet extracts energy and angular momentum from the ergosphere of the central SMBH. The magnetic field confined in an accretion disk is twisted by spacetime rotation caused by the rotating black hole. Within the ergosphere, charged particles can be generated through pair production of accretion disk photons or potential gaps, similar to those in radio pulsars. This creates an magnetosphere in which plasma can be accelerated along the rotational axis similar to the Penrose process (Penrose 1969, also see Komissarov 2005 for observational studies). Blandford & Znajek (1977) derived the power of a slowly rotating black hole ($a \ll 1$) within a stationary magnetic field configuration. Later, numerical simulations confirmed that this mechanism also holds true for rapidly spinning black holes (see e.g., McKinney 2006; Tchekhovskoy et al. 2010; Komissarov 2001). The power extracted from the SMBH via BZ depends on the magnetic field flux of the disk field and the angular momentum of the SMBH. Figure 3.9 shows simulations by Tchekhovskoy et al. (2011) which show that this process can be very efficient in extracting energy of SMBH in case

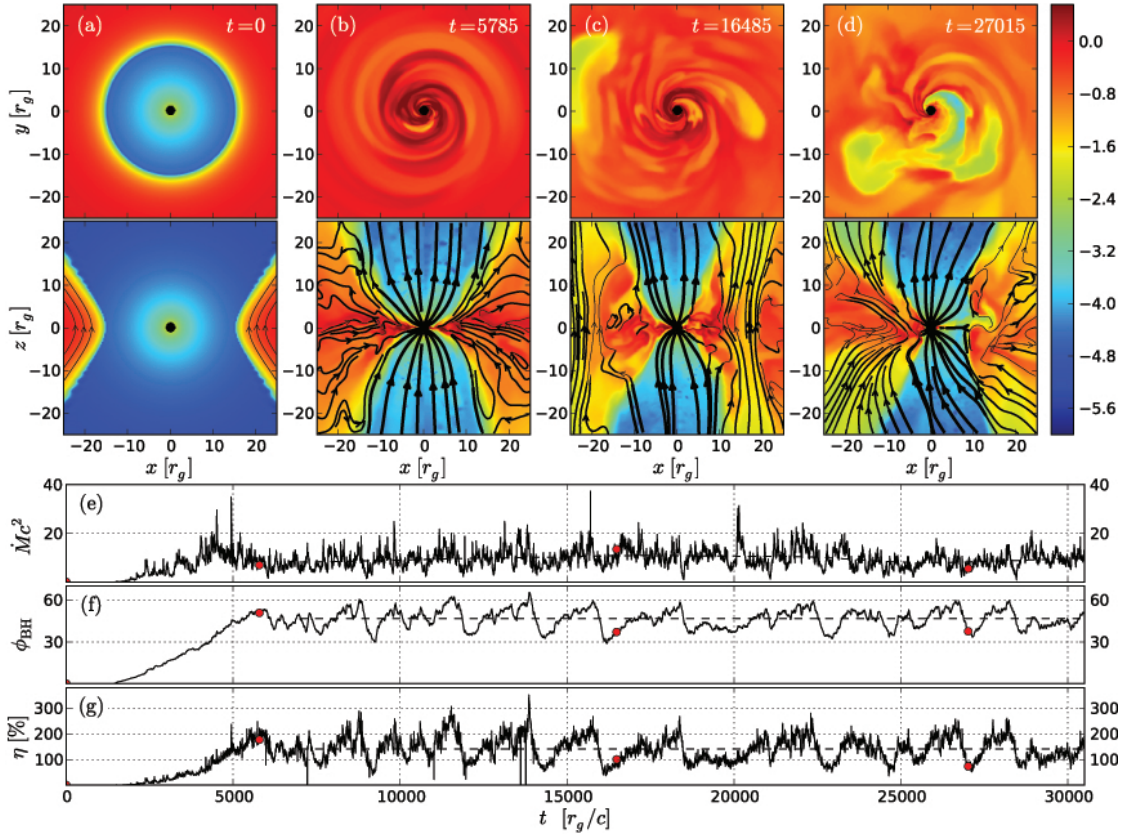


Figure 3.9.: GRMHD simulations by Tchekhovskoy et al. (2011) of a magnetically launched relativistic jet for a maximally rotating SMBH. *Panels a–d:* equatorial ($z = 0$, top rows) and meridional ($y = 0$, bottom rows) snapshots of the accretion flow at different points in time. The rest-mass density is indicated with color (red for high and blue for low values). Filled black circles shows the BH horizon, and black lines show magnetic field lines in the image plane. *Panels e–g:* time-evolution of the accretion rate (e), magnetic flux (f), and energy outflow efficiency μ (g). red circles indicate time at which snapshots were taken.

of highly magnetized accretion disks and high spin of SMBH.

An alternative scenario suggests that jets may also be formed by pure magnetodynamical processes at the inner regions of the accretion disk. In the Blandford-Payne process (BP, Blandford & Payne 1982) angular momentum is extracted via open field lines anchored in the accretion disk (e.g., Meier 2012). Strongly magnetized accretion disks extract and collimate plasma via magneto-centrifugal mechanisms that create relativistic, magnetically driven winds at the surface of the accretion disk (Uchida & Shibata 1985; Shibata & Uchida 1985; Pelletier & Pudritz 1992). This process is thought to be responsible for wind and jet launching in stellar mass black holes and proto-stellar objects (Meier 2012). However, recent theories and simulations favour the BZ process for jet formation in AGN because estimation of the SMBH spin are in better agreement with theoretical prediction (Boettcher et al. 2012).

3.3.3. Jet collimation and acceleration

AGN jets are highly collimated with small opening angles of a few degrees on pc scales (e.g., Junor & Biretta 1995). The collimation of jets extends several orders of magnitude up to Mpc scales. The process of confinement is not yet resolved. Lyubarsky (2011) suggest that the magnetic field and the ambient ram-pressure are essential components for the confinement.

Very long baseline interferometry (VLBI) with milliarcsecond spatial resolution allow for the investigation of jet morphology in the radio band on subparsec scales (e.g., Ojha et al. 2010; Müller et al. 2011; Lister et al. 2018; Müller et al. 2018). VLBI images show that jets are already highly collimated at these scales (Kovalev et al. 2007). The region of jet formation is thought to occur on scales close to the event horizon. Spatial resolution of a few tens of micro arcseconds are necessary to resolve structures on these scales, including the shadow of the SMBH. Significant progress to resolve such structures has been made on 1.3 mm VLBI observations with the Event Horizon Telescope (EHT; Doeleman et al. 2009, 2012; Akiyama et al. 2017).

Furthermore, the innermost regions of the jet are very compact and thus opaque to their own radiation due to absorption processes including synchrotron self-absorption (SSA), free-free absorption (FFA), pair production (see Sect. 2.4). Jet cores in VLBI images, thus, correspond to regions where the jet becomes optically thin.

Along the jet the specific plasma volume increases and adiabatic as well as radiative losses yield that the accelerated particles lose all their kinetic energy. Thus, there needs to be a mechanisms to further accelerate particles downstream and convert energy into the energy of the emitting particles. X-ray emitting electrons with Lorentz factors $\gamma \approx 10^7$ cool on the timescales of a few years. Thus, the interpretation of X-ray emission as synchrotron emission implies that the emitting region cannot be much larger than the electron acceleration regions. These lifetime-constraints are consistent with bright knots in the jet flow that can be associated with strong shocks. However, there are several jets of radio galaxies whose X-ray emission can be resolved and which show a quasi-continuous X-ray emission along the jet (for example in Centaurus A, Kataoka et al. 2006). Hence, particle acceleration in at least these sources must be rather spatially distributed than concentrated within a few bright knots.

Lyutikov & Blandford (2003) introduce a magnetically driven outflow in which the Poynting flux dominates the the kinetic and thermal energy fluxes. Alternatively, observed AGN jets could be kinetic energy dominated (Blandford & Rees 1974).

3.3.4. Relativistic effects

The following derivation is based on (Boettcher et al. 2012). Very long baseline interferometry revealed the relativistic nature of AGN jet. The high angular resolution of VLBI measurement allowed to resolved the proper motion of individual emission component ("knots") within AGN jets. Some knots appear to move faster than the speed of light (Lister et al. 2013; Asada et al. 2014). This phenomenon is called *superluminal motion* and is simple projection effect caused by the relativistic motion of the emission region

on the plane of the sky (Rees 1966). For a knot with speed with $\beta = v/c$ that moves along a jet that is oriented at a small angle θ_{LOS} with respect to our line of sight. The apparent speed β_{app} is

$$\beta_{\text{app}} = \beta \frac{\sin \theta_{\text{LOS}}}{1 - \beta \cos \theta_{\text{LOS}}}. \quad (3.3.1)$$

Another effect of relativistic motion is Doppler boosting. For example, this effect is responsible for the asymmetry of surface brightness between two opposite side of a jet or the presence of one-sided jets (e.g., M87 Acciari et al. 2009a). The photon frequency ν of an emission region with a bulk Lorentz factor $\Gamma = (1 - \beta^2)^{-1/2}$ moving at relativistic speed β in a small observed angle θ_{LOS} towards is Lorentz boosted by a factor

$$\delta = \frac{1}{\Gamma(1 - \beta \cos \theta_{\text{LOS}})}, \quad (3.3.2)$$

called *Doppler factor* δ and the observed frequency will be $\delta\nu$. For $\Gamma \gg 1$ the Doppler factor only depends on the combination of Γ and θ_{LOS} . Photons emitted in the backwards directions will be deboosted (redshifted) by a factor $\delta_{\text{back}} \approx 1/\Gamma$ (for $\Gamma \gg 1$) while photons emitted in the forward direction will be boosted (blueshifted) $\delta_{\text{for}} \approx 2\Gamma$ (for $\Gamma \gg 1$). Assuming photons are emitting isotropically in an emission region then half the photons beamed within a narrow cone of opening angle $\sim 1/\Gamma$ due to Doppler boosting. Doppler boosting has several effects on observed physical parameters. Observed fluxes and luminosities from AGN jets will be relativistically boosted,

$$L_{\text{obs}} = \delta^n L_{\text{em}}, \quad (3.3.3)$$

where L_{obs} and L_{em} are the observed and emitted luminosities, respectively. The exponent n depends on the spectral index α of the non-thermal spectrum and the geometry of the emission region. For an isolated spherical region $n = 3 - \alpha$, while a continuous jet yields $n = 2 - \alpha$ (Urry & Padovani 1995). Consequently, the without knowing δ and θ_{LOS} it is not possible to uniquely deduce the intrinsic luminosity and bulk Lorentz factor of a source and vice versa (Cohen et al. 2007). The flux amplification and Doppler factor depend on the viewing angle.

Doppler boosting can also explain rapid variability in blazars. In general, variability allows to estimate the size r of the emission region of observed radiation using causality arguments based on the speed of light,

$$r \leq c \cdot \Delta t_{\text{var}}^{\text{em}}, \quad (3.3.4)$$

with the variation timescale $\Delta t_{\text{var}}^{\text{em}}$ in the co-moving frame of the source. If the emission is Doppler boosted the variability timescales in the observer's frame is $\Delta t_{\text{var}}^{\text{obs}} = \Delta t_{\text{var}}^{\text{em}} \delta^{-1}$ with the Doppler factor δ . For example, Doppler boosting was used to solve the incompatible region size derived from γ -ray variability on timescales of days observed in 3C 279 and the size deduced from the requirement that the source has to be optically thin to its own radiation (Maraschi et al. 1992b).

4. High-energy observations and data reduction

To understand the processes concerning high-energy phenomena (e.g., particle acceleration in PWN or AGN jets, the nature of γ -ray bursts, etc.) it is necessary to study the multiwavelength and multi-messenger picture. The enormous range of frequencies from X-rays to high-energy γ -rays cannot be covered with a single instrument nor a single observation method. In order to observe the high energy sky we make use of different space- and ground-based observatories. Earth's atmosphere is not optically thin for all frequencies. Due to photoabsorption by oxygen molecules in the ionosphere direct observation of the above UV band requires instruments outside the atmosphere (Longair 2011). The detection of higher energetic photons also calls for different detection methods because they can easily penetrate matter and cannot be focused in the same way as optical photons. Soft X-ray telescopes onboard satellites such as *XMM-Newton*, *Chandra*, or *Swift* make use of focusing mirrors and charged-coupled devices (CCD) as detectors. In contrast, the *Swift*/BAT and instruments onboard *INTEGRAL* collect single photons at energies up to 100 keV using the coded mask method. The *Fermi*-LAT satellite detects MeV and GeV γ -ray photons by measuring the electron showers created by high-energy photons within a scintillator. An exception to direct observations above the atmosphere are ground-based Cherenkov telescopes (CT) which observe the TeV sky indirectly. This is due to the fact that the low photon flux of TeV γ -rays requires a large collecting area. A decisive difference to low-energy observations is that the high-energy flux is very low, thus, each of these instruments actually counts single photons. Hence, a detection event of a single photon is often called *count* and the so-called *count rate* refers to the photon rate of a source within a certain energy band.

In this Chapter I will introduce the observatories and instruments which were used in this thesis. Basic data reduction methods and extraction processes are given, while details on the extraction and use of data is presented in the respective analysis chapter. Many of the methods for data reduction and analysis have been described by Krauss (2016). Detection techniques are very different in various energy bands and the quantities in which the temporal, spatial and spectral information of an observed emission is stored varies from one instrument to another. In order to study source properties it is therefore necessary to calculate source fluxes, intensities, or source intrinsic luminosities. I will briefly describe how source fluxes for each instrument are derived in order to compute a broad band spectrum.

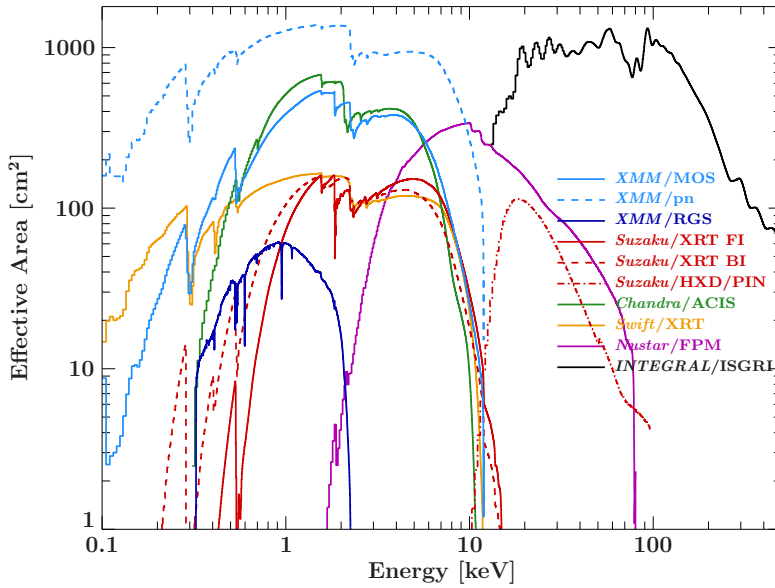


Figure 4.1: Comparison of the effective area for different X-ray satellite and instruments. Image credit: Beuchert (2017)

4.1. X-ray data

Currently there are several X-ray satellite missions, including *XMM-Newton* (Jansen et al. 2001), *Swift* (Burrows et al. 2005), *Suzaku* (Mitsuda et al. 2007), *Chandra* (Weiskopf et al. 2002), *NuSTAR* (Harrison et al. 2013), or *INTEGRAL* (Winkler et al. 2003). This thesis makes use of data acquired with *XMM-Newton*, *Swift*, *INTEGRAL*, *Fermi* and *FACT*. High-energy photons are essentially detected through ionization and the energy deposited by the resulting photo electrons. Detectors collect either the charge directly or the light emitted from recombination of ionized ions within the active material of the detector. The signal is then amplified and the time and amplitude of the event is recorded. There are many different detectors. Charge-coupled devices and scintillators are most important in modern satellites and shall be introduced briefly. Instruments sensitivity is expressed by the effective area A_{eff} . It includes the transmission and reflection efficiency of the mirrors as well as systematic effects reducing the number of detected photons due to detector components. As such the effective area is a function of X-ray photon energy. Fig. 4.1 shows the effective area of different X-ray satellites. The background consists of both instrumental background as well as unresolved X-ray sources (see Kreikenbohm 2013) For a detection of a source, the signal from this source must be significantly brighter than the background level. The significance can be expressed by the *signal-to-noise ratio* (snr). In X-ray astronomy, the number of detected photons is small such that small number statistics is valid. From Poisson statistics the $\text{snr} = C_s / \sqrt{C_s + C_B}$, with the source counts C_s and background counts C_B .

4.1.1. Focusing X-ray instruments

In order to study the emission from a given source and extract photons associated with a unique location on the plane of the sky it is essential to reconstruct the surface brightness distribution of the sky. Imaging instruments with CCD detectors consist of an array of pixels which allow to reconstruct an image of a focused beam of X-ray photons. Due to their penetration power X-rays cannot be focused with the same optic as used in optical astronomy. Instead, X-ray mirrors are grazing incident mirrors. If the incident angle is small X-rays reflect via total internal reflection. The critical angle for total X-ray reflection is

$$\theta_c = 5.6' \left(\frac{\rho}{1 \text{ g cm}^{-3}} \right)^{1/2} \frac{\lambda}{1 \text{ nm}}, \quad (4.1.1)$$

(Jackson et al. 1981). For a photon with wavelength $\lambda \sim 1 \text{ nm}$ this translates to $\theta_c \sim 1^\circ$. For angles larger than the critical angle, reflection drops substantially. The angle depends on the density of the reflecting medium as well as the photon energy. Fig.4.3 shows the light path of an X-ray photon within the *XMM-Newton* satellite. Mirrors in X-ray satellites are made of dense, high-Z material. Typically, gold (XMM) or iridium (Chandra) are used. The fixed critical angle defines the maximum photon energy that can be focused with these mirrors. In order to make focal length manageable two reflections are enforced by the combination of a parabolic and hyperbolic mirror, called Wolter type 1 configuration (Wolter 1952). This reduces the focal length to below $\sim 10 \text{ m}$. The nesting of many such mirrors increases the collecting area and thus efficiency of the instrument.

The focused X-ray beam can then be measured by the detector. For soft X-ray instruments, this is typically an assembly of *charge-coupled devices* (CCDs). A single CCD is an array of solid-state detectors (SSS) in which an X-ray photon ionizes atoms within the material in the detector. The SSS consists of a fully depleted pn-junction on a non-depleted p-type layer. The structure is shown in Fig.4.3. Originally, CCDs were used in optical astronomy and essentially work like a camera. The X-ray incident photon is absorbed within a potential well (pixel) of the CCD and excites several thousand electron-hole pairs in the base material (usually doped silicon). The charge which is proportional to its energy is deposited and stored there. After a recording time interval the charge of each pixel in the array is read out row by row at the edge of the chip. X-ray CCDs are read-out continuously which allows to detect individual photons. In normal mode, almost all pixels contain no charge except for a few which detected an X-ray photon. If a source is bright, more than one photon can hit a pixel during a single recording cycle. The recorded charge is then the sum of both photons. This effect is called *pile-up*. For photon rates larger than $\sim 0.01 \text{ counts/pixel/s}$ pile-up can lead to severe distortions of the X-ray spectrum and can lead to the rejection of events. The CCD image of such a bright source then shows a bright halo with a hole in its center. To reduce the effect of pile-up many X-ray instruments have various observing modes where only part of the CCD are read-out which essentially reduces the read-out time and thus increases the observable rate of a source. The energy resolution of CCDs depends by the

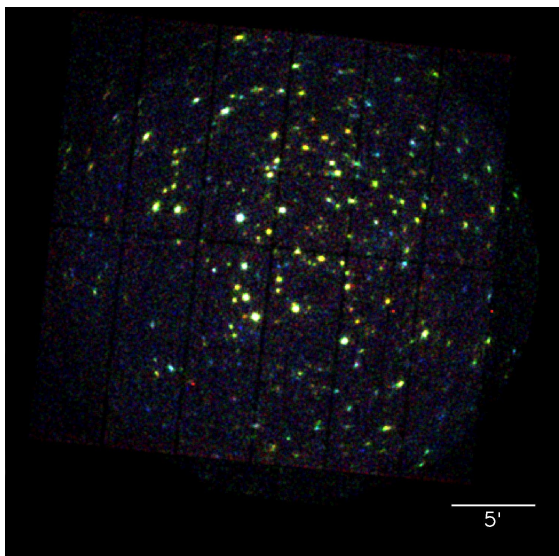


Figure 4.2: Sky image observed with the EPIC pn camera. Objects at large angular distance from the optical axis are distorted.

statistical fluctuations in the number of produced charges for a mono-energetic photon.

For a bright point source located in the focal axis of the telescope the image of the CCD detector shows a bright core and a faint broad halo. The size of this halo depends on the scattering of photons from small imperfections in the mirror. The surface brightness distribution of a point source in the image plane is described by the *point spread function* (PSF). The larger the distance of a source from the focal axis the stronger the distortion of the PSF (see Fig. 4.2).

4.1.2. Coded-Mask instruments

High-energy X-rays and γ -rays cannot be focused in the same manner as soft X-rays. An alternative method is to use coded mask instruments which in principal work like a pinhole camera with many pinholes. A coded mask is a sheet made of opaque and transparent elements that are arranged in a random pattern (see Fig.4.4, left panel). This mask is placed in front of a detector (usually a scintillator) and casts a shadow which can be interpreted as the folding of the coded mask pattern (see Fig.4.4, right panel) with the surface brightness distribution of the sky. Because the shadow is unique for each position on the sky the composite image can be decoded and the original sky image can be reconstructed in an iterative process.

There are different types of detectors that are able to measure photon energies up to several MeV. For example scintillation counters are crystals (mostly sodium ionide or caesium ionide) which effectively stop the photon and absorb its energy. Part of the photon energy is immediately re-emitted through scintillation and photo multiplier tubes detect the light pulse and register its arrival time. But semiconductor detectors such as silicon and germanium are also used in current missions. Often a second faster reacting scintillation counter (e.g., anti-coincidence detectors) surrounds the primary crystal in order to reject events from cosmic rays which may pass through the detector.

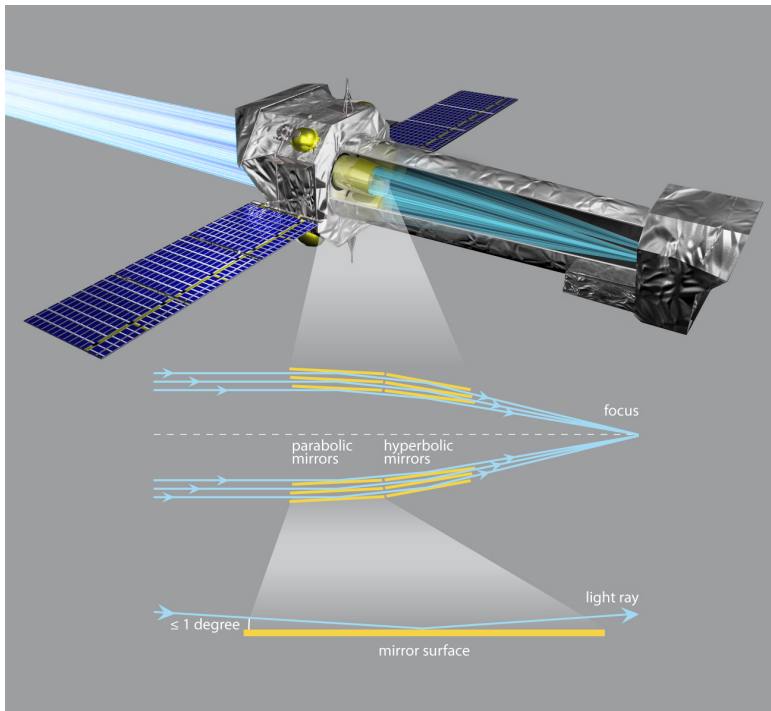


Figure 4.3: Light path of X-ray photons within the *XMM-Newton* satellite. Nested Wolter I mirrors focus X-ray photons via total reflection with a critical reflection index below $\sim 1^\circ$. Image credit: ESA / AOES Medialab

4.1.3. The *XMM-Newton* satellite

The European *X-ray Multi-Mirror* (*XMM-Newton*) mission was launched in 1999. It consists of three imaging detectors which provide a combination of instruments for high-snr imaging spectroscopy and high-resolution grating spectroscopy. The European Photo Imaging Cameras (EPIC) include the pn and two MOS (metal-Oxid-Semiconductor) cameras. In addition, there are two grating instruments, the Reflection Grating Spectrometer (RGS) with two cameras and an optical CCD (optical monitor, OM). Because the instruments can observe simultaneously *XMM-Newton* has played a crucial role in multiwavelength astronomy. For more details on the detectors see Jansen et al. (2001) and Kreikenbohm (2013).

XMM-Newton data was used in Chapters 7 and 8. Processed source and background spectra, as well auxiliary data for the *XMM-Newton* observations used in Chpt. 7 were provided by the EXTraS working group 2 (WP2) and is described in the EXTraS documentation¹. Reduction of the *XMM-Newton* data presented in Chpt. 8 was done based on the standard pipeline described on the ESA handbook² Kreikenbohm (also see 2013). In all observations, I used the data of all EPIC cameras. The following paragraph is taken verbatim from the data reduction section in Kreikenbohm et al. (2016). Observation data files (ODFs) were processed to create calibrated event lists and full frame images using standard methods with the *XMM-Newton* Science Analysis System (SAS

¹EXTraS WP2 doc: http://www.extras-fp7.eu/images/archive/EXTraS_WP2_docs.pdf

²*XMM-Newton* documents <https://www.cosmos.esa.int/web/xmm-newton/documentation>

Version 12). Source and background light curves were extracted for the (0.5–2) keV, (2–10) keV, and (0.5–10) keV energy ranges, adopting a circular extraction region with 30 arcsec radius for the source of interest. The background regions were chosen from a source-free circular region of the same radius on the same chip with similar distances to the readout nodes to ensure comparable background noise levels. Screening for flaring particle background was done using standard methods. The net exposure times are listed in Table 8.1. Source and background spectra were extracted for single and double event patterns from the filtered event lists. Response files were generated using RMFGEN and ARFGEN of the SAS software package.

4.1.4. The *Neil-Gehrels Swift* spacecraft

The *Swift* Gamma-ray Burst mission was launched in 2004 and was dedicated to the study of GRB. The spacecraft carries multiple instruments: the burst alert telescope (BAT), the X-ray telescope (XRT), and an UV/optical telescope (UVOT). Similar to *XMM-Newton*, *Swift* can operate these instruments simultaneously. It is designed to automatically detect bursts and quickly point the instruments at the approximate position (hence the name) to observe the rapid fading X-ray and optical/UV afterglow of GRBs. *Swift* detects roughly ~ 90 GRB per year³. Hence, the majority of the observing cycle is used for non-GRB observations. The mission provides several programs including a guest investor program (GI) as well as a target-of-opportunity program (ToO). In the latter, a limited amount of time is spent to observe transient events proposed by the community. The communication of the Science Team with the spacecraft yields a faster reaction time than other missions and allows for *Swift* observations within a few hours. The XRT uses CCD detectors and provides imaging and spectroscopy in the energy range from 0.5 keV to 10 keV. The effective area of the XRT is much lower than of the EPIC cameras. However, the fast pointing capabilities which allow for very short observations in comparison to larger missions (with smaller overhead exposure used for pointing) have made *Swift* crucial for detecting transient events and performing monitoring campaigns.

The XRT currently offers three operating modes: imaging, photon-counting, and windowed-timing mode, where spectroscopy is only possible in photon-counting (PC) and windowed timing (WT) mode. In PC mode, offers full spectral and spatial information of the camera image. Pile-up becomes severe for bright sources with count rates exceeding 0.5 counts per second. The timing mode sacrifices positional information as the 2D image is collapsed onto a 1D strip to achieve a higher time resolution through rapid read-outs. This allows to perform spectroscopy on bright sources which exceed the PC limit.

For the data reduction of the UVOT data see Sect. 9.2.5. The data reduction of XRT data is done using scripts written by L. Barragan, J. Wilms and extended by F. Krauss. The extraction pipeline is described in detail in the *Swift* users guide⁴ and summarized in Krauß et al. (2013). for the extraction of a source spectrum the newest calibration files are applied to the raw data. Event files are created filtering for certain event patterns,

³*Swift* GRB stats: https://swift.gsfc.nasa.gov/archive/grb_table/stats/

⁴*Swift* UVOT User Guide: https://swift.gsfc.nasa.gov/analysis/UVOT_swguide_v2_2.pdf

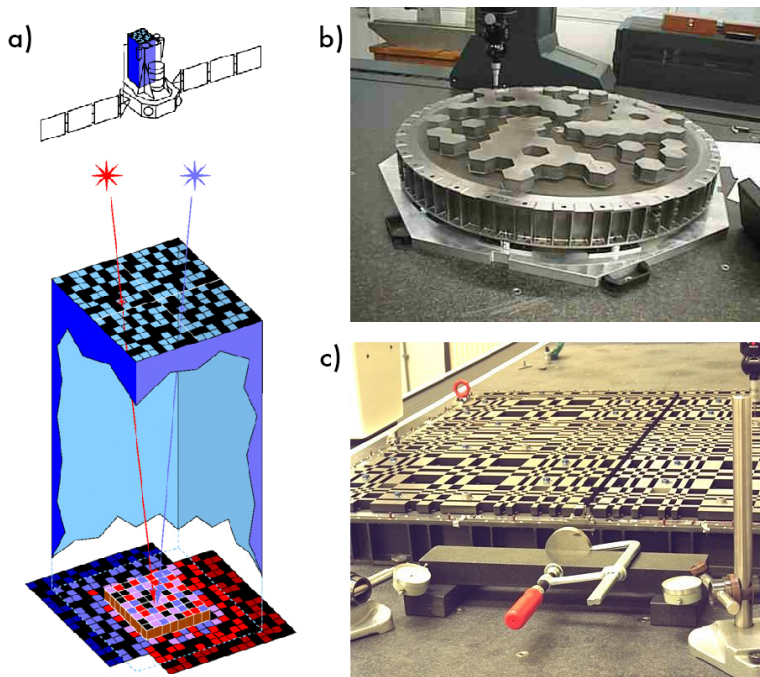


Figure 4.4: *Left panel (a):* Principle of the coded mask methods. A mask of opaque material (e.g., lead) with a pattern of openings is placed in the aperture of the instrument. Gamma-ray photons that pass through the hole project a unique shadow on the detector plane. *Right panels* show examples of the different masks used for the spectrometer (b) and imager (c) on board the *INTEGRAL* satellite. Image credits: ISDC/M. Türler, SPI/IBIS Team.

called *grades*. Source and background count spectra are extracted from a circle and annulus around the source coordinates. The radii of the source region is chosen in order to cover the entire PSF with half energy radius of $20''$. source counts from these regions are then stored in an event file. The ancillary response files is generated using the routine `xrtarf` for the source position and extraction region. The arf including the effective area of the PC and WT mode are display in Fig. 4.1.

The Burst Alert Telescope onboard the *Neil-Gehrels Swift* spacecraft operates in the range 15 keV and 150 keV and makes use of the coded-mask technique. Its aim is to provide time critical GRB triggers and source position with 4 arcmin accuracy. The instrument runs in two modes, the burst mode and survey mode (default). Within several seconds of detecting a burst, the BAT switches to burst mode and calculates an initial position and can automatically induce a spacecraft slew to the position of the burst. While searching for bursts, BAT performs an all-sky survey of the hard X-ray sky with a large FOV ($\Omega \sim 1.4$ sr) and collects data in five minute time bins. The data from the BAT can also produce a sensitive hard X-ray all-sky survey over the course of *Swift*'s two year mission. Source catalogs are regularly published by the *Swift* BAT science team.

4.1.5. The *INTEGRAL* mission

The *International Gamma Ray Astrophysics Laboratory (INTEGRAL)* was launched 2002 and carries four instruments that are co-aligned and observe the same region of the sky simultaneously. A spectrometer and an imager are sensitive to MeV photons whereas an X-ray monitor and an optical camera which help to identify the gamma-ray

sources. The spectrometer, Imager and X-ray monitor are all coded-mask telescopes.

The spectrometer on *INTEGRAL* (SPI) performs spectral analysis of gamma-ray point sources and extended regions between 18 keV and 8 MeV. The detector is made up of 19 single high-purity germanium semiconductor detectors (each detector serves as a large pixel) and gives a spectral resolution of 2 keV at 1.33 MeV. To reduce cosmic ray background the detector is shielded by an anti-coincidence system (crystals) that act as a veto system. The Imager on board the *INTEGRAL* satellite (IBIS) covers the energy range from 15 keV to 10 MeV and provides diagnostic capabilities of fine imaging, source identification and spectroscopy. Its coded mask (see Fig.4.4) is optimized for high angular resolution. The Joint European X-Ray Monitor (JEM-X) system provides angular resolution of a few arcminutes between 3 keV and 35 keV and plays a crucial role in the localization and identification of the gamma-ray sources. In contrast to the IBIS and SPI, its detector consists of an imaging micro strip gas counter made up of two identical high pressure gas chambers.

Data reduction and image reconstruction for the data used in this thesis follows the description in Beuchert, 2017.

4.2. γ -ray data

The γ -ray flux of astronomically sources ranges from $\sim 10^{-1}$ photons/m²/s in the lower energy range of ~ 100 MeV up to $\sim 10^{-7}$ photons/m²/s in the GeV band (see review by Funk 2015). The difference in photon flux goes along with different collecting areas that are needed to detect a significant number of photons from a source. Areas of the order of 1 m² are sufficient in the range of a few MeV up to a few tens of GeV and space-based instruments can be used to directly observe γ -ray sources. Current missions are the Italian γ -ray satellite *AGILE* (Tavani et al. 2008) and NASA's *Fermi Gamma-Ray Space Telescope* (Atwood et al. 2009). These instruments make use of pair creation within the detector medium to observe γ -rays.

However, large collecting areas in the range of 10^4 m² are necessary to achieve the same significance at energies above 100 GeV. Very-high energy γ -rays are thus observed indirectly with Cherenkov telescopes from ground by detecting secondary products that are caused by the interaction of γ -ray photons with the atmosphere of Earth. The two main methods for that are *imaging air Cherenkov telescopes* (IACTs) and *water Cherenkov detectors* (WCDs). Examples of current IACT facilities are H.E.S.S.⁵, MAGIC⁶, VERITAS⁷, and the *First G-APD Cherenkov Telescope* (FACT⁸). This thesis makes use of data acquired by the *Fermi* satellite and FACT due to their excellent abilities to serve as monitoring observatories.

⁵H.E.S.S.: <https://www.mpi-hd.mpg.de/hfm/HESS/>

⁶MAGIC: <https://magic.mpp.mpg.de/>

⁷VERITAS: <https://veritas.sao.arizona.edu/>

⁸FACT: <https://www.isdc.unige.ch/fact/>

4.2.1. The *Fermi* Telescope

The *Fermi Gamma-Ray Space Telescope* was launched in 2008 with the objective to study the γ -ray sky with good angular resolution and high sensitivity. The primary observing mode of *Fermi* is the *scanning mode* in which the spacecraft yields a uniform exposure over the entire sky within two orbits of 3 hours each. The daily scanning of the γ -ray sky has made *Fermi* a crucial facility for studies of high-energy sources. Pointed observations can be proposed for particular targets of opportunity.

Fermi carries two instruments, the Large Area Telescope (LAT) and the γ -ray burst Monitor (GBM). The later was designed to detect and study γ -ray burst and complements the *Swift* mission in the γ -ray regime. However, *Fermi's* primary instrument is the LAT. It operates in the range from below ~ 20 MeV up to ~ 300 GeV. Because photons at these high energies cannot be focused via reflection or refraction, they are detected through interaction with high- Z material and their conversion into electron and positron pairs. The instrument consist of a precision tracker module that tracks of the pairs as well as a calorimeter to determine the energy of the incident photon. Signals from cosmic rays are vetoed by an anti-coincidence shield whereas γ -ray photons can pass the shield and produce pairs in the tracker. The shield module also allows for an automatic filtering of signals from cosmic rays, mostly protons, and about 90% of detected signals are discarded on-flight.

Fermi-LAT data is public and provided by the mission's Science team who also provide the software and calibration files for data reduction. The extraction of *Fermi*-LAT data is described in detail in the LAT User Documentation⁹, Müller (2014), and a short summary is given by Krauss (2016). The first step in data reduction are analogous to reduction of CCD data. Detected pair conversion events within a given time range and region of interest (ROI) are selected from an event file. Here, the choice of region is tricky as the region needs to be large enough to include neighbouring sources for background rejection but must not be too large because the computation time scales with the size of the ROI. The resulting event cube lists time and energy of the detected photons. It is then filtered for good-time intervals and an exposure map as well as a live-time cube are computed. Now, in contrast to X-ray data processing, the computation of light curves and spectra from a *Fermi*-LAT data set includes the assumption of an input model. In order to associate photons with a source a model has to be fitted to the data set by applying a maximum likelihood method. The fitting includes a background model which is computed from the known *Fermi*-LAT sources taken from the second or third *Fermi* source catalog (2FGL, Nolan et al. 2012, or 3FGL, Acero et al. 2015, respectively). Also contributions from diffuse extragalactic and Galactic emission as well as extended sources need to be taken into account. A model for diffuse emission is provided by the *Fermi*-LAT science center¹⁰. The combined source models are then compared to the data. The maximum likelihood fitting method adjusts the model parameters in order to describe the data set accurately and calculates the probability that the observed data set

⁹*Fermi* Analysis Threads: <https://fermi.gsfc.nasa.gov/ssc/data/analysis/scitools/>

¹⁰*Fermi* models: <https://fermi.gsfc.nasa.gov/ssc/data/access/lat/BackgroundModels.html>

was obtained by the input model. The output may include source fluxes, light curves, and source spectra which have been corrected for instrumental effects. Significance of a source detection is described via the test statistic (TS)

$$TS = -2 \ln \frac{L_{\max,0}}{L_{\max}}, \quad (4.2.1)$$

where $L_{\max,0}$ and L_{\max} are the maximum likelihood of the null hypothesis, i.e. the background model without the source, and the model including the source, respectively. The quantity \sqrt{TS} corresponds roughly to σ significance. The *Fermi*-LAT data used in this thesis were reduced using scripts written by M. Kreter. In order to be analyzed together with X-ray data the energy flux densities had to be converted into photon flux densities. This was done using scripts written by F. Krauss.

4.2.2. The small IACT: FACT

In the last decade IACTs became the most powerful instrument for pointed observations of very high energy γ -rays. A review on the status of instrumentation of current and future Cherenkov telescopes is given in Funk (2015). The following description follows Weekes (2003).

A γ -ray photon will be absorbed by the atmosphere through pair production (see Sect.2.4.5). The first interaction takes place in ~ 20 km altitude. For energies above 10 GeV the photon splits into a pair of one electron e^- and one positron e^+ . The particles further interact with the atmosphere causing bremsstrahlung (see Sect.2.4.2) which can again produce more e^-e^+ -pairs. This yields a shower of secondary particles until the average energy is lower than a threshold energy at which the losses through ionization and bremsstrahlung are balanced and the maximum number of pairs are produced. Hence, the depth of the showers depends on the energy of the γ -ray photon. And the density of the emitted photons is proportional to the energy of the primary photon, to first order. For incident photons of 1 TeV this is roughly 10 km (Funk 2015). These high-energy particles interact with molecules in the air which produce Cherenkov light in the UV to optical range in a narrow cone.

IACTs focus the Cherenkov light in the telescope mirrors and map it onto a fast camera in the focal plane. The total amount of light is proportional to the maximum length of the shower and thus the energy of the primary γ -ray photon. The lifetime of Cherenkov pulses is in the range of nanoseconds. Hence, fast sampling cameras are required for the detection. The short exposures also help to suppress background light from natural (e.g., moon) and artificial sources (e.g., city light). Further limiting factors of measurements are turbulence in the atmosphere, such as changes in temperature, pressure, humidity, and the presence of clouds (Bretz et al. 2013b).

Air showers can also be created by high-energy cosmic rays. These showers feature a number of electromagnetic sub-showers from π^0 decay and contain muons from the decay of charged pions. The background from these showers is a factor of a ~ 1000 larger. The properties of showers from γ -rays, hadrons, and muons are reflected in the camera and



Figure 4.5: The FACT telescope at 2,200 m altitude on La Palma. The 9.5 m^2 mirror area focuses the Cherenkov light of air shower particles in the camera with G-APD photo sensors. Image from Anderhub et al. (2013a).

differ in terms of shape, signal strength, and arrival times. Monte Carlo simulations can be used to discriminate between the signals.

The *First G-APD Cherenkov Telescope* (FACT, Bretz et al. 2013a; Anderhub et al. 2013a; Bretz et al. 2014) is an IACT that is sensitive to γ -ray energies from several hundreds of GeV up to $\sim 10 \text{ TeV}$. It is located on the Canary Island La Palma at an altitude of 2,200 m and started taking data in 2011. The mirror size is only 9.5 m^2 and offers a FoV of 4.5° which is rather small compared to the large telescope (H.E.S.S, MAGIC, or VERITAS) where the mirrors have areas of more than 100 m^2 per telescope. The unique feature of FACT are the photo-sensors of the camera. As the name implies, FACT is the first IACT that uses Geiger-mode avalanche photo-diodes (G-APDs) instead of photo-multiplier tubes (PMTs) as photo-sensors. G-APDs have a higher photon detection efficiency and offer a more stable gain than PMTs. The advantage is that observations are not restricted to dark nights but can be performed even during nights with strong moon light contamination (Bretz et al. 2013a).

Besides testing the new sensors for the use in Cherenkov astronomy, FACT monitors TeV emission of a sample of bright TeV emitters (mainly HBL sources). The aim is to serve as long-term monitoring facility for bright TeV blazars, including the detection and monitoring of bright γ -ray flares in the TeV band and to correlate them with signals from lower-energy (from radio to X-rays) and neutrino detectors. The camera design and small sample size yield a high duty cycle and several hours of data per night for each source in the sample. Quicklook light curves are provided online by the FACT science team¹¹. The data processing for light curves used in this work was done by the FACT collaboration. For details on the telescope design see Bretz et al. (2014).

¹¹FACT quicklook analysis :<https://fact-project.org/monitoring/>

5. Spectroscopy and Timing Analysis Methods

In order to study the processes and environments responsible for high-energy emission in astronomical objects one makes use of the spectral and timing characteristics. In this chapter I will explain the general methods used in this thesis to study the spectral and temporal evolution of high-energy emission. The analysis is done with the *Interactive Spectral Interpretation System*¹ ISIS Version 1.6.2-32 (Houck & Denicola 2000). Originally, the software was developed for X-ray spectral fitting based on the NASA tool XSPEC². But it offers a number of features and *isisscripts*³ which allow to extend the analysis to the broadband spectrum. In the following I will use the example of X-ray analysis to motivate the spectral fitting approach and how a spectrum is interpreted in ISIS. But note that once loaded correctly into ISIS the methods to analyze a spectrum or light curve are independent of the energy range chosen.

5.1. Spectral fitting

Essentially, X-ray detectors count individual photons within a given time interval. Single events are thus also called *counts*. The data products from X-ray telescopes described in Sect. 4.1.3 are a time series of counts within a given time bin (a light curve) and a histogram of the number of counts per energy bin (count spectrum). The count spectrum shows signatures of the energy dependent optics and detector effects. The source flux $F(E)$ incident at the telescope (in photons $\text{cm}^{-2} \text{s}^{-1} \text{keV}^{-1}$) and the observed count rate $c(i)$ (counts s^{-1}) per pulse height bin/ channel i are related through an integral relation

$$c(i) = \int_0^{\infty} R(i, E)A(E)F(E)dE + B(i), \quad (5.1.1)$$

where $B(i)$ are background counts and the detector responses are specified by the redistribution matrix function (RMF) $R(i, E)$ and the ancillary response file (ARF) $A(E)$ in units of cm^{-2} (see e.g., Davis 2001a,b; Gorenstein et al. 1968). The unitless RMF defines how the energy channels of the detector (in units of pulse invariant, PI, or pulse height analysis, PHA) is mapped to a corresponding energy. In a perfect detector, the RMF is a diagonal matrix. However, there are deficiencies for example due to fluorescent photons

¹ISIS Homepage: <http://space.mit.edu/cxc/isis/>

²Xspec Homepage: <https://heasarc.gsfc.nasa.gov/xanadu/xspec/>

³This research has made use of a collection of ISIS functions (ISISscripts) provided by ECAP/Remeis observatory and MIT (<http://www.sternwarte.uni-erlangen.de/isis/>).

from detector material. The ARF describes the product of the effective area of the telescope mirrors and the quantum efficiency of the detector. Thus, it includes all reducing effects, for example, shadows from filters in front of the detector, downgrading effects, or transmission efficiency from the focusing mirrors but also depends on observational-dependent quantities such as the point-spread function (PSF) or filtering of the observed data (see e.g., Davis 2001b). In general, the observed count rate is time dependent even if the source flux is constant over the period of observation due to time-dependent effects from the instrument (e.g., pointing motion, detector electronics, thermal expansion effects, bad pixel). This means that detector response files are time-dependent and need to be adjusted through calibration (provided by the telescope service teams). The detected counts $c(i)$ also includes background counts $B(i)$ from systematic noise of the detector and unresolved sources in the sky. An short overview of different background components is given in Kreikenbohm (2013) and by the ESA Science team⁴.

Equation Eq. 5.1.1 is discretized in order to be analyzed numerically. When the count rate of the background is known (for example, from a sourceless region during the observation) the source counts S_{ph} for a given exposure time ΔT can be estimated,

$$S_{ph} = \Delta T \sum_{n=0}^{c(i)} R(i, n) A(E_n) F(E_n) \Delta E_n - B(i), \quad (5.1.2)$$

where $F(E_n)$ is the source flux in band $[E_n, E_{n+1}]$ and ΔE_n is the width of this energy band. Hence, a spectral data set includes the source spectrum, a background spectrum and the detector response files.

The primary objective for spectroscopy is to understand the physics of the emission by studying the energy distribution of the source flux $F(E)$. Because the inversion of Eq. 5.1.2 to yield $F(E)$ is not unique a common alternative method to obtain the source flux is through spectral modeling. In this approach a model $F(E, \vec{x})$ for the spectral shape is assumed which calculates the expected number of counts $M(i, \vec{x})$ per channel. Here, \vec{x} is a vector of model parameters, e.g., the normalization, spectral index, or absorbing column density. The spectral model is folded through the detector response and then compared to the data with the help of a statistical measure. This approach allows to investigated unexpected features in the spectrum and whether they are caused by calibration or related to the source. Spectral parameters \vec{x} of the model are then adjusted to obtain the best fit. The goodness of a fit is evaluated by a test statistic based on the probability (typically computed via a maximum likelihood) that the assumed model represents the data. For a Gaussian distribution of photons within an energy bin the maximum likelihood corresponds to the minimum value of χ^2 (Gorenstein et al. 1968). The application of this test statistic required at least 20 counts per energy bin. For high count rates, this can be achieved through rebinning. If this is not fulfilled it is necessary to use Cash statistics, which assumes Poisson statistics (Cash 1979).

After a good model has been found the count spectrum can be unfolded and the energy

⁴EPIC background components:

<https://www.cosmos.esa.int/web/xmm-newton/epic-background-components>

flux can be determined from the model. One should note that a spectral fit is not unique because different models can yield similar goodness-of-fits. Even though, different models with comparable goodness-of-fit yield similar results for the observed energy flux whereas the intrinsic flux can vary greatly. In order to break spectral degeneracies additional information (such as physical arguments regarding spectral parameters or constraints from timing analysis) have to be taken into account.

Spectral fitting is also applied in order to study the broad emission of AGN in Chpts. 8 and 9. In general, this is done using the energy flux spectrum in the νf_ν -representation. However, the low energy resolution, and thus large energy bins especially in the high-energy bands, limit the reconstruction of the spectral shape and flux of a source in an unambiguous way by "unfolding" the source flux and detector response (e.g., Broos et al. 2010; Getman et al. 2010; Krauss 2016). Using a spectral model to obtain the unfolded flux densities induces a large bias (Nowak et al. 2005). In order to avoid this problem in this thesis, I follow the approach by Krauss (2016) and treat all data sets in their detector space. This is possible with ISIS which allows to use both data sets with assigned response files (e.g., *XMM-Newton* EPIC, *Swift* XRT, UVOT) together with data available in flux density only (radio data, catalog fluxes) by assigning a diagonal matrix to the latter. A description how this approach is implemented in ISIS is given in Krauss (2016). ISIS scripts written by F. Krauss are used to convert flux densities of different wavelength into counts spectra that can be used for broadband fitting.

5.2. Timing Analysis

Light curves provide insights in the temporal intensity evolution of a source. An overall challenge in the analysis is the proper handling of *noise* in the data which can dilute low-amplitude fluctuations. For example, noise can be caused by stochastic processes of the source. A common approach to examine variability is to compute the Fourier transform of a light curve. The squared amplitude of the transform represents the amount of variability fluctuation as a function of temporal frequency (timescale⁻¹) visualized by the power density diagram (PSD). The shape of the PSD can be used to derived properties of the noise process (see Fig. 5.1 and Vaughan et al. 2003a). For most AGN, variability can be well represented by *red noise*, i.e. a power law shape with an index larger than 1 over a broad range of temporal frequencies (e.g., Green et al. 1993; Markowitz et al. 2003; Vaughan et al. 2003b). Vaughan et al. (2003a) show that in this case, the PSD generated from a random light curve itself is affected by statistical fluctuations and is only one realization of the stochastic process. In many cases, the data are not adequate enough to average over a large number of individual PSDs and variability is characterized by statistical moments (e.g., sample mean, variance, etc.). Though for stochastic processes there is also a large amount of randomness in these quantities (e.g., Vaughan et al. 2003a). Nevertheless, these moments can be useful to compare fluctuations of light curves from different energy bands obtained for the same time period.

Besides variance due to source intrinsic fluctuations, additional Poisson noise is introduced to the data by measurement uncertainties. Hence, to estimate the variance S^2 of

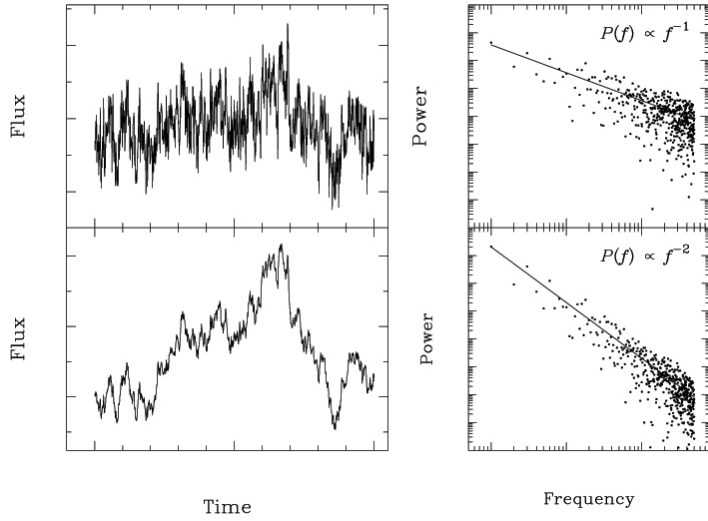


Figure 5.1: Simulated time series (*left*) and corresponding periodograms (*right*) by Vaughan et al. (2003a). *Upper panels* show an example of a flickering noise dominated light curve. The PSD is flat with larger power in short-term variability (high frequencies). *Lower panels* show a random walk time series (red noise term). These time series have steeper PSD with larger power in long-term variability (small frequencies). In general, the periodogram exhibits larger scatter for short-term variability.

source intrinsic fluctuations one computes the *excess variance* σ_{XS}^2 (Nandra et al. 1997; Edelson et al. 2002a) after subtracting the contribution of the expected measurement uncertainties $\sigma_{\text{XS}}^2 = S^2 - \overline{\sigma_{\text{err}}^2}$, with $\overline{\sigma_{\text{err}}^2} = N^{-1} \sum_{i=1}^N \sigma_{\text{err},i}^2$, for N measurements. The *fractional variability amplitude* F_{var} represents the variability amplitude in percentage terms and is given by the root mean square of the excess variance normalized by the light curve’s mean \bar{x}^2

$$F_{\text{var}} = \sqrt{\frac{S^2 - \overline{\sigma_{\text{err}}^2}}{\bar{x}^2}}, \quad (5.2.1)$$

and its uncertainty

$$\text{err}(F_{\text{var}}) = \sqrt{\left(\sqrt{\frac{1}{2N} \frac{\overline{\sigma_{\text{err}}^2}}{\bar{x}^2} F_{\text{var}}} \right)^2 + \left(\sqrt{\frac{\overline{\sigma_{\text{err}}^2}}{N} \frac{1}{\bar{x}}} \right)^2} \quad (5.2.2)$$

A typical problem when studying the variability of the broad band spectrum is the question whether a varying signal at a given energy band is causally connected to variations in another band, i.e. the goal is to determine whether the fluctuations of two signals are cross-correlated and whether this correlation occurs with a certain time delay or lag. For example, studying the time lags between fluctuations of the primary thermal or X-ray continuum from the accretion disks in AGN or XRB and the response from X-ray reflection or fluorescent emission lines are powerful diagnostics to map the accretion disks (e.g., Uttley et al. 2014; Lyubarskii 1997; Ingram & van der Klis 2013; Mastroserio et al. 2018)

A way to analyze two signals and their correlation is by computing the *cross-correlation function*. The concept is to find an input function $a(t)$ that varies in time and drives the output function $b(t)$ that varies in a related way. The relation is described by the

correlation or response function $\Phi(\tau)$. In the simplest way, this is a linear relation and can be described as a convolution (e.g., Edelson & Krolik 1988),

$$b(t) = \int_{-\infty}^{+\infty} d\tau \Phi(\tau) a(t - \tau). \quad (5.2.3)$$

A major problem in many multiwavelength campaigns is that sampling times of various observatories are very different. Observations with different telescopes are rarely simultaneous, particularly during long monitoring periods. In order to prevent interpolation between data points Edelson & Krolik (1988) have developed a *discrete correlation function* (DCF) for unevenly sampled data. The algorithm computes the auto- and cross-correlation function for those time lags (between data points) that are present in the data sets. This way, no data points have to be "invented" through interpolation. For two time series $\{a_t; t \in 1 \dots N_a\}$ and $\{b_t; t \in 1 \dots N_b\}$ with N_a and N_b elements (e.g., flux measurements) with means \bar{a} and \bar{b} , and standard deviations σ_a and σ_b , respectively, the unbinned DCF between each pair (a_i, b_j) is defined. Each pair is associated with a specific time lag $\Delta t_{ij} = t_j - t_i$ between the action and response. By binning the result in time where $\tau - \Delta\tau/2 \leq \Delta t_{ij} \leq \tau + \Delta\tau/2$ and averaging over M pairs yields

$$DCF_{ij} = \frac{1}{M} \frac{(a_i - \bar{a})(b_j - \bar{b})}{\sqrt{(\sigma_a^2 - e_a^2)(\sigma_b^2 - e_b^2)}}, \quad (5.2.4)$$

where e_a^2 and e_b^2 are the measurement errors associated with the data set. The correlation function following this algorithm of Edelson & Krolik (1988) is implemented in the *isisscripts*. In order to determine the significance of the DCF I used a bootstrap method:

1. For a given set of two light curves, with observation dates t_a, t_b , signals a_i, b_i , and measurement errors e_a and e_b , we calculate the DCF (DCF_{true}).
2. To account for the flux measurement uncertainties, the uncertainty of each point of DCF_{true} is determined by varying the flux values a_i and b_j within the confidence limits $[a_i - e_a, a_i + e_a]$ and $[b_j - e_b, b_j + e_b]$ for each measurement i and j , assuming a normal distribution. Afterwards the DCF is recalculated. The procedure is repeated for more than 5000 times which yields a probability distribution for each value of DCF_{true} from which the 1σ uncertainty of each DCF_{true} data point is derived.
3. For the significance of DCF_{true} at a given time lag, we determined the DCF for the null-hypothesis (DCF_{Null}), in which the two light curves are not correlated. For this, we shuffle the observation times t_a for one of the two light curves yielding a randomized light curve t_a^* . Each flux measurement uncertainty is taken into account by performing step 2 on this new set of light curves (t_a^*, t_b) and the DCF_{Null} is calculated. As in step 2, this procedure is repeated for more than 5000 times, which yields a probability distribution of DCF_{Null} values for completely uncorrelated light curves, from which we determined the 2σ and 3σ levels the DCF_{Null} . A value of DCF_{true} is considered significant, if it lies outside the 3σ region of DCF_{Null} .

6. The concept of machine learning

When conventional computer programs are faced with a problem or task, they strictly follow human-defined commands and provide a pre-defined result. On the contrary, machine learning (ML) algorithms use real-world examples to learn recipes and predict the outcome or solution of new problems. Originally, machine learning was part of the artificial intelligence research. However, since the 1990s it separated itself from this field and became one of its own. Its focus is on statistic-based research, providing probabilistic reasoning, and pattern recognition. The aim of imitating the human brain remains and is already implied by its name: machine *learning*. The ability to 'learn' is related to beings with cognitive skills. In this context it refers to the process of generalizing features of well-known data and constructing a model based on the pre-defined method that can be applied to new data. *Data mining* describes the exploration of a data set through machine learning and turning raw observational data into useful information. Astronomy experiences an enormous flood of data due to the ever improving observing technologies and data storage capabilities. Hence, it is not surprising that it has been among the first fields of research to use data mining to extract information from databases. In fact, data mining has been described as the fourth paradigm of knowledge discovery. The first three being the well-known pair of theory and observation as well as computer simulations. As such, it should be viewed and used as a part of a broader scientific process rather than the answer to everything.

When we look back in history of data analysis in astronomy, first and very basic applications of machine learning were already used in 1996 for light-curve parameterization of Cepheid Variables (Stetson 1996). The concept of decision trees, which will be explained later in this section, became very popular and was used in many studies. Since 2010s, the use of ML algorithms in automated analyses increased exponentially. The main applications are classification, regression, or clustering problems.

The basic concept of ML algorithms are fairly straightforward and easy to understand. In this chapter, I will give a concise overview of the different flavors of machine learning and provide a more detailed, though qualitative, explanation of the Random Forest algorithm, which is used in this thesis. For a more detailed introduction to machine learning, the reader is referred to eligible literature which suits them best. There are tons of (online) lectures, text books (e.g., Hastie et al. 2001; Bishop 2006) and research papers (e.g., Ball & Brunner 2010), as this field has become very popular in data science during the last 20 years. Unless stated otherwise, this chapter is based on Hastie et al. (2001) and Howard (2016).

Data mining means to learn qualitative features of a data set, find the underlying structures, extract important variables, detect outliers and anomalies, and test underlying assumptions. The specific way in which raw data sets are pre-processed and how scientific

information is extracted from the raw data strongly depends on the question one wishes to answer. In the following, I will differentiate between ML methods and algorithms, which are described in Sect 6.1. The method describes the way a data set is treated during the ML process. Does it serve as data set with known properties to learn from and predict output for an unknown data set, or do I want to explore the data set itself without any prior assumptions? In general, ML methods to do that are divided into *supervised* (predictive) and *unsupervised* (descriptive) learning. The detailed description of the learning process is laid down in the ML algorithms, which can be used in both methods. The algorithms are often grouped by similarity in terms of their function, such as *decision trees* or *cluster algorithms*.

Independent from the method or algorithm that were chosen, a key component of any ML problem is the set of attributes (or features) that describe the objects within the data set which one wishes to explore or learn from. In astronomical problems such attributes are often derived from a set of observations. The choice of attributes is vital: the attributes that are used to train the algorithm span up a multi-dimensional parameter space in which each training object is represented. Using all or too many attributes can worsen the generalization performance as this may result in a high-dimensional parameter space in which the objects are spread far out. This results in low-density regions, which make it difficult for the algorithm to generalize from. Furthermore, not all algorithms can cope with missing, noisy, irrelevant, or redundant attributes. It is therefore desirable to reduce the dimensionality of the attributes by selecting relevant subsets, e.g., through *forward selection* or *backward elimination*. In the former one starts with one attribute to train the algorithm and then adds more one by one iteratively. The opposite is done in the later method by taking into account all attributes first which will then be reduced after each learning process.

6.1. Supervised and Unsupervised Learning methods

The most widely used and well-known method in astronomy is supervised learning. This method relies on a *training* data set of objects for which the response (e.g. the classification of an observed source) is known with high confidence. The algorithm is trained with this data set, which means that it maps its attributes onto a finite number of outputs. This way the algorithm constructs a prediction model that connects attributes and output. Obviously, the performance of this method depends on the parameter space of the training set, which needs to cover that of the testing set. Otherwise it is not representative. The construction of the prediction model is based on minimizing a so-called cost function, which depends on the specific algorithm in use. After the algorithm learned the relation between attributes and output, the model can be applied to objects or events of unknown output (*testing* set) and make predictions.

Supervised learning algorithms such as the *artificial neural networks (ANN)* or *decision tree*-based algorithms are among the most commonly used algorithms in astronomy. But lately, with the development of CPU power, computatively expensive algorithms such as the *support vector machine* or *k-nearest neighbour* algorithm became popular, too.

Table 6.1.: Basic description of popular algorithms in supervised machine learning

Name	Description
Artificial Neural Networks (ANN)	Consists of a series of interconnected nodes (hidden nodes) with weighted connections. Each node maps object properties to the target output and has a specific activation function (e.g. threshold). See Fig. 6.1a).
Decision Trees (DT)	Starting from a root node with all objects of the parent population each node is split into sub-nodes dividing the population (e.g., through parameter thresholds). The process is repeated iteratively resulting in a tree of (child) nodes until the final layer of leaf nodes, defined by user-specific criteria, (e.g., minimum population of objects in a node or the maximum number of nodes). See Fig. 6.1b).
Support Vector Machine (SVM)	The algorithm does not create a model but rather a decision boundary, i.e. a multi-dimensional layer in the parameter space, which is defined in terms of <i>support vectors</i> . It aims at finding the hyper plane that best separates two classes of data. Input data are viewed as a set of vectors and data points closest to the classification boundary are the <i>support vectors</i> . See Fig. 6.1c).
k-nearest neighbour (KNN)	The position of each object in the input attribute space are stored in a memory. Then for each test object, the same attributes are compared to the entire training set and the output is determined using the properties of the k nearest neighbours, which are weighted by the distance in the attribute space. See Fig. 6.1d).

Table 6.1 gives a brief description of these algorithms. For detailed explanation the reader is referred to the literature cited above.

Opposed to supervised learning, unsupervised methods do not require a training set nor incorporate prior information about the data. Instead information on the data set can for example be extracted by performing independent component analyses or by identifying clusters in the parameter space by using clustering algorithms or probabilistic density functions.

Both methods can be combined to the much more complex *semi-supervised* learning

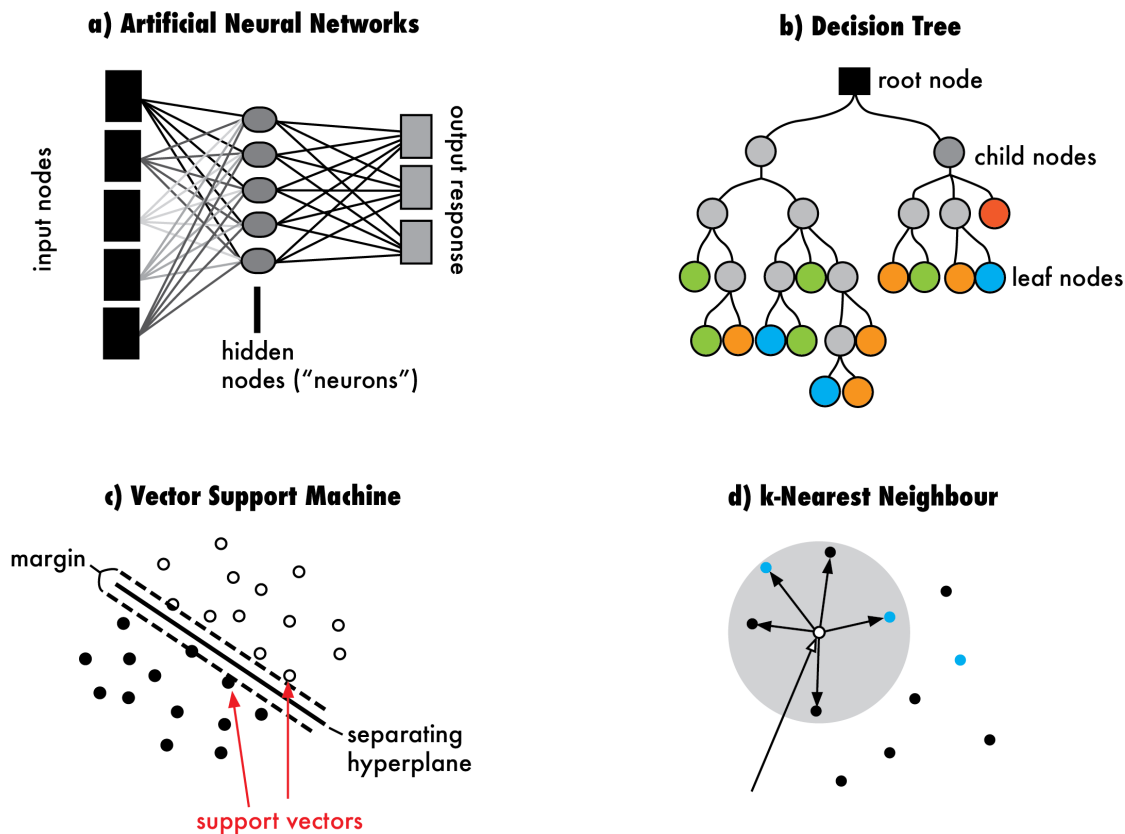


Figure 6.1.: Schematic visualization of popular supervised machine learning algorithms. See Table 6.1 for further information about the algorithm.

by using known priors while simultaneously allowing objective data interpretation. The combination of both methods can balance out their downsides. For example, supervised learning does not find new options of outputs, such as source classes, that are not in the training set. This is possible in unsupervised learning, which on the other hand ignores all known information. The choice of algorithm depends on the set of attributes of the data as well as on the application for which it will be employed. In this thesis, the random forest algorithm will be used in a supervised learning problem and is explained in more detail in the following section.

6.2. To see no forest for the trees - the supervised Random Forest algorithm

The random forest (RF) algorithm is an ensemble of classification or regression decision trees (CART, Breiman et al. 1984, see Table 6.1) and was developed by Breiman (2001) with the aim to improve the accuracy in such problems. The idea stems from two different methods to introduce randomness into the training process: ensemble learning

or "bagging" (Breiman 1996) and random split selection (Dietterich 2000; Amit & Geman 1997): Bagging consists of methods to generate many decision trees based on random sub-samples of the training set and aggregate their results through weighted votes of their outputs. In random split selection, the attribute used to split the training sample at each node is selected at random from those that result in best splits. Fig. 6.2 shows the scheme of the training process of a single tree in the forest:

A random sub-sample is chosen from the original training set, such that the original distribution is maintained (*bootstrap* method). A decision tree is trained on this bootstrap sample. At each node the algorithm determines the best-split attributes with the widely used G_{ini} Index (see Sect. 6.2.1, Eq. 6.2.1) and selects randomly out of a given number of best-split attributes. The learned structure of the decision tree defines a single prediction model, called classifier, which is tested on *out-of-bag* (OOB) training events. These are events of the original training set that were not chosen for the bootstrap sample. The outputs are stored in memory. This generation and testing of single classifiers is repeated until a large number of classifiers is generated and every training source has been part of the bootstrap or OOB sample multiple times. The OOB method allows for a direct estimate of the generalization error by computing the error rate of the OOB classifications (see 6.2.1, Eq. 6.2.4). To classify new input data, Every classifier then enters a vote for the class of an object and the results of the complete forest corresponds to the class with the majority of votes.

The inclusion of random subsets and attribute selection at each node has proven to be very stable against noise or the presence of outliers in the training data. It is also more suitable to work on high-dimensional parameter spaces than other ML algorithms (e.g., Caruana & Niculescu-Mizil 2006).

6.2.1. Performance measures of the RF classifier

The supervised random forest algorithm provides a number of parameters and measures to assess the classification power of the forest. The ones used in this thesis are discussed below.

The G_{ini} Index as sample impurity test

An important ingredient of random forest is the random selection of best-split attributes at each node. The common parameter to identify those attributes is the G_{ini} index. For a given attribute this index measures the impurity of the resulting split samples. A low value of G_{ini} (i.e., a greater decrease in G_{ini}) means that a particular predictor attribute plays a greater role in separating the data.

In general, assuming that for a given attribute A , a data set of size N with m classes is split into k sub-samples of sizes $N_1, \dots, N_{k-1}, N_k, k \in \mathbb{N}$. The impurity of the i th sub-sample is expressed by

$$G_{ini,i}(A) = 1 - \sum_{j=1}^m (p_j)^2, \quad (6.2.1)$$

6. The concept of machine learning

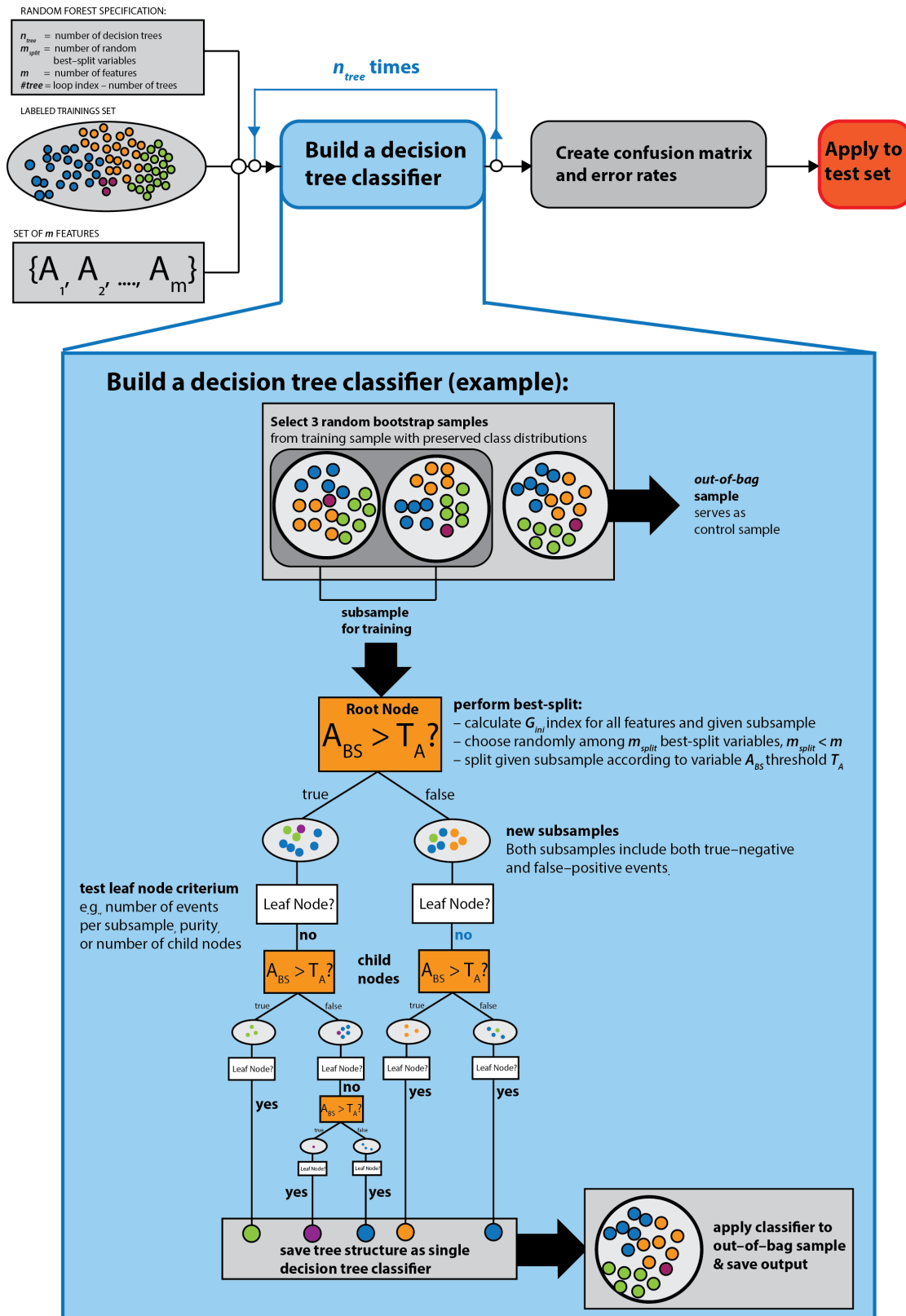


Figure 6.2.: Schematic view of the training process of the supervised random forest algorithm.

Table 6.2.: Data set for example classification of X-ray spectra in absorbed AGN.

ID	Attributes		Class
	Γ	EW(Fe K α)	
1	2.5	1200	1
2	1.5	0	0
3	1.8	300	0
4	1.8	1380	1
5	1.6	500	0

Note: Example data set of size $N=5$, with $m=2$ classes 0 (mildly absorbed), and 1 (heavily absorbed) with the X-ray photon index and equivalent width as attributes.

where p_j is the relative frequency of class $j \in \{1, \dots, m\}$ in node n . Then the G_{ini} for the complete split is defined by the weighted sum over all sub-samples

$$G_{ini}(A) = \sum_{i=1}^k \frac{N_i}{N} G_{ini,i}(A), \quad (6.2.2)$$

Tables 6.2 shows an example in which the X-ray spectral features may be used to identify heavily absorbed AGN. The training set contains five sources with two classes 0 and 1 as labels for mildly and heavily absorbed AGN, respectively. The attributes given to train a decision tree classifier are the X-ray photon index Γ and the equivalent width of the neutral iron K α fluorescence line. The G_{ini} index for each possible split of the complete sample is given in Table 6.3. Based on these values, the best splits per attribute are $\Gamma \leq 1.6$ and $EW \leq 500$, respectively.

Out-of-Bag error rates and confusion matrix

The performance of supervised ML algorithms is usually evaluated by the confusion matrix. Since each decision tree of the random forest is applied to a sub-set of the training sample, one can compare the actual and average predicted class for each object. For m classes, C_0, \dots, C_{m-1} with $m \in \mathbb{N}$, this gives a $m \times m$ matrix C_{mm} . The columns represent the predicted classes, while the rows represent the actual class:

		Predicted class				
		C_0	C_1	...	C_{m-2}	C_{m-1}
True class	C_0	$c_{0,0}$	$c_{1,0}$...	$c_{m-2,0}$	$c_{m-1,0}$
	C_1	$c_{0,1}$	$c_{1,1}$...	$c_{m-2,1}$	$c_{m-1,1}$
	...	$c_{0,1}$	$c_{1,1}$...	$c_{m-2,1}$	$c_{m-1,1}$
	C_{m-2}	$c_{0,m-2}$	$c_{1,m-2}$...	$c_{m-2,m-2}$	$c_{m-1,m-2}$
	C_{m-1}	$c_{0,m-1}$	$c_{1,m-1}$...	$c_{m-2,m-1}$	$c_{m-1,m-1}$

Table 6.3.: G_{ini} indices splitting the example data set

Split	class 0	class 1	sub-sample size	G_{ini}
$\Gamma \leq 1.6$	1	0	1	0.40
$\Gamma > 1.6$	2	2	4	
$\Gamma \leq 1.8$	3	1	4	0.30
$\Gamma > 1.8$	0	1	1	
$EW \leq 300$	2	0	2	0.26
$EW > 300$	1	2	3	
$EW \leq 500$	3	0	3	0.00
$EW > 500$	0	2	2	
$EW \leq 1200$	3	1	4	0.30
$EW > 1200$	0	1	1	
$EW \leq 1380$	3	2	5	0.48
$EW > 1380$	0	0	0	

Note: The G_{ini} index was calculated with Eq. 6.2.2 for each possible split of the complete example data set of size $N=5$.

Therefore, diagonal elements $c_{ii}, i \in \{0, \dots, m-1\}$ are the numbers of objects which have been classified correctly, while all other elements $c_{ij}, i \neq j, i, j \in \{0, \dots, m-1\}$ give the number of objects of class C_i that were *confused* for another one C_j . The predictive accuracy of a model is then calculated by the fraction of correct classifications

$$acc(c_{\{ij\}}) = \frac{\sum_{j=0}^{m-1} c_{jj}}{\sum_{i,j=0}^{m-1} c_{ij}}, \quad (6.2.3)$$

Another common measure is the error rate

$$err(c_{\{ij\}}) = 1 - acc(c_{\{ij\}}). \quad (6.2.4)$$

Consequently, the accuracy $acc(c_{\{i,j=k\}})$ and error rate $err(c_{\{i,j=k\}})$ for specific class C_k is

$$acc(c_{\{i,j=k\}}) = \frac{c_{kk}}{\sum_{i=0}^{m-1} c_{ik}}. \quad (6.2.5)$$

Choosing the best attributes ranking

After the training process, the random forest algorithm provides a ranking of the attributes based on the mean values of the G_{ini} index and the accuracy of all decision trees. On one hand it provides the mean decrease of the G_{ini} index for adding a given attribute and on the other hand the mean decrease in accuracy for removing a given at-

tribute. Both parameter can be used to identify the most important attributes in the set. Attribute which score high in both parameters rankings provide the highest predicting power.

6.3. Handling of imbalanced training sets

An imbalanced training set can cause a systematic bias in the classification with ML algorithms. A data set is imbalanced if the classification categories are not equally represented. In this case, one can distinguish between a majority and minority class. The problem occurs during the training phase: the algorithm learns that if an unknown object has attributes similar to both classes, the majority class is more likely than a rare event of the minority one. Then the resulting model is biased towards the majority class to improve its accuracy and reduce its misclassification error. For example, consider a binary case of extreme imbalance, where 98% of events belong to the majority class and 2% to the minority class. If the algorithm learns to classify all events as member of the majority class the accuracy of the training will be high as only 2% (the rare events of the minority class) would be misclassified. However, the population of the testing set may be different and the true rate of misclassification differs. The problem is crucial in scenarios in which anomalies or rare outputs are important. In these cases the training set needs to be balanced out.

A way of balancing the training sample is through data pre-processing by re-sampling the number of sources within each class. This involves random under-sampling of the majority class or random oversampling of objects in the minority class. In random under-sampling, random events of the majority class are removed from the training set. Even though this method is fast it can remove important information of the attributes and the chosen sample may not represent the true population within this class. On the contrary, random oversampling randomly picks events of the minority class that are replicated to increase the number of occurrences in the sample. Though no information is lost by this methods, it increases the likelihood of over-fitting the data, which means that the decision tree characterizes too much detail and noise in the training data, because single data points gain more weight through replication.

A more sophisticated way is provided by re-sampling methods based on unsupervised ML algorithms. In cluster-based methods, the *k-means cluster* algorithm (see Sect. 6.4 and Fig. 6.3) is applied to each the class of the training data in order to identify sub-structure within the class population. Each cluster is then independently over- or under-sampled such that the final sample represents the original class population. This methods overcomes the drawbacks of random re-sampling although there is still the possibility of over-fitting the training data due to replication.

A common approach to re-sample while avoiding over-fitting of the training data is using synthetic data generation. The goal of such approaches is to provide the classifier with more complete regions within the attribute space by creating objects that are synthesized from existing data objects. Such approaches include `DataBoost-IM` (Guo & Viktor 2004), `ADASYN` (He et al. 2008), and `SMOTE` (see section below), to name a few.

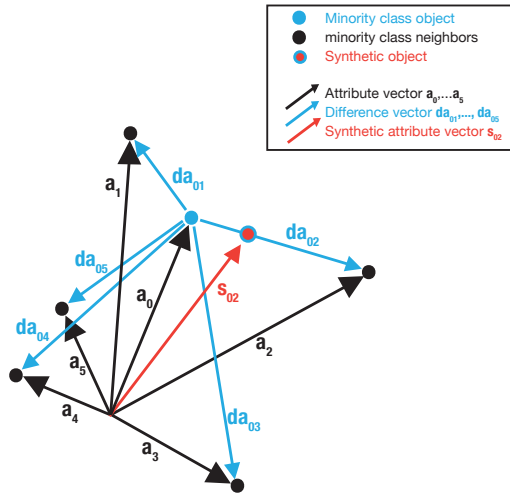


Figure 6.3: Generation of synthesized attribute vector in the multidimensional attribute space with the *k*-nearest neighbour method: for a given object of the minority class (blue point), five nearest neighbours (black points) are determined. The a synthetic object (red point) is generated by scaling one of the difference vectors. See text for further description.

Many of these approaches are based on similar sampling algorithms.

6.4. Synthetic Minority Over-sampling Technique (SMOTE)

The standard SMOTE technique combines bootstrapping and the *k*-nearest neighbour approach and was developed by Chawla et al. (2002) for the binary class problem. It was inspired by earlier work of Ha & Bunke (1997). The algorithm operates as follows:

Each object of the data set is represented by an attributes vectors, where the elements are the objects attributes values. For each object of the minority class, the algorithm determines the *k* nearest neighbours (typically $k = 5$). New synthetic attribute vectors that represent fake objects of the minority class are then generated along the line segments joining these neighbours (see Fig. 6.3 for an illustration).

The synthetic attribute vector is generated by first calculating the difference vector $\vec{d}a_i = \vec{a}_{NN} - \vec{a}_i$ between one (of the two) attribute vectors under consideration \vec{a}_i and a random vector of the nearest neighbours \vec{a}_{NN} . Multiplying the difference with a random number $r \in [0, 1]$ yields the synthesized attribute vector $\vec{a}'_i = \vec{a}_i + r \cdot \vec{d}a_i$. This means that for every attribute, this vector adds an additional point along the line segment between two specific minority class members. This approach forces decision trees to choose larger and less specific regions for the minority class, instead of focusing on isolated regions emphasized by replicated minority class data.

Depending on the amount of over-sampling that is required to balance out the minority class, a specific number of neighbours from the *k*-nearest neighbours are randomly chosen via the bootstrapping method to construct the synthesized attribute vectors. For example, if the over-sampling is 200% and $k = 5$, two out of five neighbours of each minority class object are used to generate new synthetic objects.

The SMOTE technique also provides the possibility to under-sample the majority class by randomly removing some of events from the majority class population. This procedure

is repeated until the minority class makes up a certain percentage of the majority class.

7. Taking source classification to the EXTraS level

Since over a decade current high sensitive X-ray observatories, such as *XMM-Newton* or *Chandra* are continuously taking data of the X-ray sky which provide deep insights into the spectral and time domain of astrophysical sources. There is an ever-growing mountain of archival data that is largely unexploited. With the advent of new X-ray missions, such as the *eROSITA*¹ all-sky survey or the *Athena* X-ray observatory², X-ray astronomy enters an era of new large surveys that will produce even larger and incredible amounts of data. For example, the *eROSITA* all-sky survey is expected to detect more than 4 millions of X-ray sources. Astronomers are faced with the challenge of new data at rates that are pushing beyond the limits of our ability to process in real time. Identification and classification of variable and transient sources will be a major task in the future and new source types³ are likely to be discovered.

Intelligent methods for a quick and accurate identification of astronomical sources are needed and machine-learning algorithms have been proven to be very effective in this respect. Traditional ways to classify unidentified sources involve cross-matching source positions with catalogues of other wavelengths and expert knowledge to manually draw up classification rules. Such rules are based on scientific assumptions and work well for small pieces of information that have to be processed. However, this method becomes highly complicated with increasing amount of data and information that have to be considered. In machine learning, each set of information (called feature) is represented by a real number or label. Machine learned classification models perform extremely well at finding subtle patterns in data sets with large number of features. Several authors have used machine-learning methods in astronomical applications such as photometric redshift determination (Carliles et al. 2010), variable star classification (Richards et al. 2011; Dubath et al. 2011), and light curve parameterization (Stetson 1996). Recently, Lo et al. (2014) and Farrell et al. (2015) have shown that Random Forest machine learning is well suited to classify variable X-ray sources using timing information extracted from their light curves.

This chapter describes the automated classification pipeline that me and my collaborators, Mirjam Örtel and Jörn Wilms, have developed and performed within the framework of the international EU-project *Exploring the X-ray transient and variable Sky*⁴ (EXTraS) based on the work by Lo and Farrell. The project aimed at exploring the time domain

¹Launch is expected for 2018, see <http://www.mpe.mpg.de/450415/eROSITA> for updates.

²expected launch 2028, see <http://www.the-athena-x-ray-observatory.eu/> for updates

³Note: in the following 'source type' and 'source class' is used synonymously.

⁴Project homepage: <http://www.extras-fp7.eu/>

information of the *XMM-Newton* archival data. We note, that this study does not intent to investigate the methodology for the application of automated classification in astronomy, since evidence for its use has been reported by earlier studies (see references above). But the objective of this analysis was a first multiwavelength characterization of the new transient sources that were detected during the EXTraS project.

The chapter is organized as follows: Section 7.1 introduces the EXTraS project as it is the framework of this study. In Sect. 7.2 I repeat the basic idea of Random Forest machine-learning classification, which is explained in more detail in Sect. 6. An overview of the 3XMM-DR6 catalogue and training sample that was used to define the classification model is given in 7.3. Sect. 7.4 describes the extraction of various classification features. The training process and construction of the prediction model are presented in Sect. 7.5 and 7.6, while a its applications to unidentified 3XMM and EXTraS transient sources are presented in Sect. 7.7 and 7.8. Concluding remarks and future work are given in sections 7.9.

Disclaimer

The study of this chapter has been performed in close cooperation with another PhD student Mirjam Örtel at Remeis Observatory. While the data processing for the computation of the features was split the machine-learning process was performed together to equal shares. One can expect strong similarities of the chapters in both PhD theses. Mirjam Örtel performed the major task of crossmatching all catalogs (described briefly in Sect. 7.4), as well as the data preparation of the 3XMM catalog and input data from other work packages. Based on her work, I performed the computation of the spectral and multiwavelength features (Sect. 7.4). Timing features were provided by other members of the EXTraS project. A detailed description of their computation can be found in the online documentation⁵.

7.1. The EXTraS project

EXTraS was an international project⁶ funded by the EU from 2014 to 2016. Its aim was to perform a systematic investigation of the unexplored temporal information that is buried in the serendipitous data collected by the European Photon Imaging Camera (EPIC) onboard the ESA satellite mission *XMM-Newton*. The objective was successfully achieved and all results were made public through the EXtraS webpage to be used freely by the astronomical community beginning of 2017.

This investigation included a search for fast transients that are missed by standard image analysis, and a search and characterization of variability in hundreds of thousands of sources spanning more than nine orders of magnitude in time scale and six orders of magnitude in flux.

⁵<http://www.extras-fp7.eu/index.php/it/archive-it#docs>

⁶EXTraS Collaborators: INAF/IASF Milan, INAF/OA Rome, IUSS Pavia, IMATI Milan, University of Leicester, MPE Garching; and ECAP, FAU Erlangen.

The project was organized in seven work packages (WP) that focussed on different parts of the analysis and publication. WP 2, 3 and 5 concentrated on the temporal analysis of archival *XMM-Newton* data which yielded large databases with synthetic parameters for long and aperiodic or periodic short-term variability. WP 4 was dedicated to the search for transient sources that were only brighter than the detection threshold for a very short amount of time. All time-domain results were eventually coupled with X-ray spectral and multiwavelength information, assembled by WP 7, which is described in this Chapter. This information is used to yield a multiwavelength characterization and first order X-ray classification of the new sources. Remaining WPs included a dedicated public outreach program for schools, as well as the development of the EXTraS database.

7.2. Source classification with Random Forests

The properties extracted from a data set (called 'features' hereafter) give a characterization of the observed astronomical source. The aim of classification is to turn this information into a probabilistic statement about the source type or science class of that source.

We use the supervised Random Forest (RF) algorithm for our classification (see Sect. 6.2). Supervised learning algorithms use a sample of training sources of known science class, that is characterized by a set of features, to find relations between the science class probabilities and the given set of features ('prediction model'). This model is then used to automatically predict class probabilities and the most likely class of new and unknown sources. The random forest algorithm creates an ensemble of randomized decision trees and predict the output science class via majority vote of the ensemble.

Various implementations of the RF algorithm exist. Here, we use the `randomForest` library as implemented in R, the open-source statistical analysis package by Liaw & Wiener (2002). The package has been successfully used in previous studies of automated classification of astronomical sources (e.g., Lo et al. 2014; Farrell et al. 2015). To assess the accuracy of the classification model, we use the Out-of-Bag (OBB) classification error estimate (see Sect. 6.2.1) that is implemented in the `randomForest` package and is computed within the training process.

7.3. The 3XMM-DR6 catalog

In order to define source types, a training sample based on well understood sources is required. Within the framework of the EXTraS project, we had access to a subset of the sixth data release of the Third *XMM-Newton* serendipitous source catalog (Rosen et al. 2016), 3XMM-DR6 hereafter, which served as basis for our sample definition.

Figure 7.1 shows the sky distribution of *XMM-Newton* observations during pointed (green fields) and slew (blue lines) observations. During a pointed observation of the *XMM-Newton* Observatory, a significant number of X-ray sources are observed in addition to the proposed target. On behalf of ESA, the *XMM-Newton* survey science center

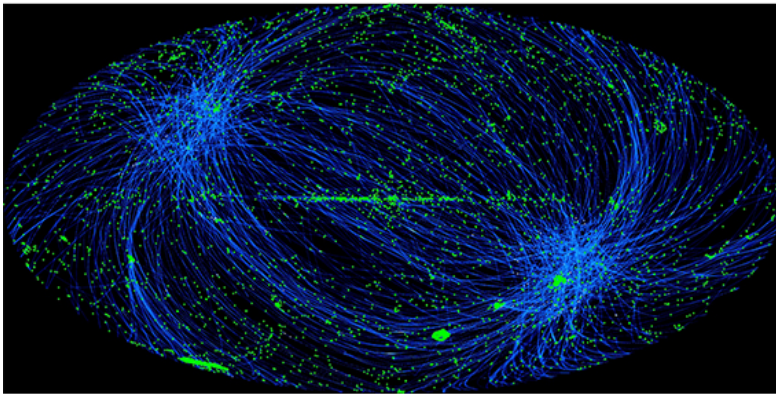


Figure 7.1: Sky distribution of *XMM-Newton* observations during pointed (green fields) and slew (blue lines) observations in Galactic coordinates. Image credit: A. Read, private communication.

(SSC) performs standard pipeline analyses of the *XMM-Newton* data and regularly releases their results in a serendipitous X-ray source catalogue since 2003. The 3XMM-DR6 is the eighth publicly released *XMM-Newton* X-ray source catalogue and contains source detections from 9160 publicly available EPIC observations made between 2000 Feb 3 and 2015 Jun 4. The non-overlapping area of the catalogue’s fields covers $\sim 982 \text{ deg}^2$ ($\sim 2\%$) of the sky.

In each *XMM-Newton* observation a source may be detected by one or all of three EPIC cameras, which in turn have multiple exposures within a given observation. In the following, the term ‘detection’ refers to the data set of a single source detected in a single *XMM-Newton* epoch in at least one of the EPIC cameras. Hence, a single detection of a source can comprise up to three spectra and light curves, one for each camera. A number of fields were observed more than once, providing additional detections of the same source at different epochs. The full 3XMM-DR6 catalogue contains more than 600,000 X-ray source detections with more than 468,440 unique X-ray sources. Almost 20% of the unique sources have multiple detection in the catalogue. For 149,968 detections, EPIC spectra and time series were automatically extracted during the standard processing of the SSC. Approximately ~ 5200 of those are variable within the timespan of their specific observation. The catalogue covers a flux span of several magnitudes with a median flux $\sim 2.4 \times 10^{-14} \text{ erg/cm}^2/\text{s}$ in the total energy band 0.2–12 keV.

The pre-release that we used during the analysis includes a smaller subset of 137,212 unique detections from the 3XMM-DR6. Spectral data from the EPIC PN/MOS cameras as well as ancillary and response matrices were re-extracted using an improved source detection algorithm by the EXTraS working package 2. In comparison to the standard processing of the 3XMM-DR6 pipeline, the algorithm performs a better estimate of the variable X-ray background, which improves the data quality of faint sources. In the following, the terms ‘3XMM’ or ‘3XMM catalogue’ refer to the pre-released version that was available to us within EXTraS.

A unique detection identifier (**detID**) is defined based on the unique combinations of observation identifier and source number of each detection. Note that there may be multiple detection which result in different **detIDs** that belong to the same source. Hence, an additional unique source identifier (**srcID**) is defined based on the 3XMM-

DR6 source name. This allows us to identify all detections in the sample that belong to the same source.

Training sample definition

Our training sample is based on the sample of Lo et al. (2014) and Farrell et al. (2015). These papers constitute the first serious attempts at autotclassification of X-ray sources with machine-learning methods, concentrating on variable X-ray sources.

The choice of the training sample was crucial for the success of the later classification. The training sample must be representative of the properties of the sources in order to ensure a faithful classification of the unknown sources. In Farrell et al. (2015), the authors assemble 873 unique sources in the training sample and distinguished between six source types: active galactic nuclei (AGN), X-ray binaries (XRB), stars, cataclysmic variables (CV), γ -ray bursts (GRB), and ultra-luminous X-ray sources (ULX). We extended the training sample in the following ways: because of the large dispersion of the spectral shapes and variability of AGN, we subdivided AGN into Seyfert 1 galaxies (S1), Seyfert 2 galaxies (S2), and BL lac objects (BL) based on the 13th edition of the AGN catalogue by Véron-Cetty & Véron (2010). X-ray binaries were subdivided into High Mass X-ray Binaries (HMXRB) and Low Mass X-ray binaries (LMXRB) using the catalogues of Galactic X-ray binaries by Liu et al. (2006) and Liu et al. (2007) and the properties of X-ray binaries in the Small Magellanic Clouds (Haberl & Sturm 2016), and cataclysmic variables were added from cross-matching the Ritter and Kolb catalogues. Finally, we did not include GRBs in the sample, due to the low number of known sources with good *XMM-Newton* data quality. Our final training sets consisted of 2911 unique sources. Compared to the initial sample of Lo et al. (2014), the fraction of source types in our sample was more balanced in such a way, that the fraction of AGN, XRB, ULX and CVs is higher. The number of sources and detections in the individual categories in the training sample are given in Table 7.1.

Figure 7.2, left panel, shows the distribution of the 3XMM sources within the training sample in Galactic coordinates. This sample was used to train the RF forest algorithm. The remaining detections and sources in the 3XMM catalog serve as test sample and to assess the resulting RF prediction model. Consequently, the test sample includes 124 402 detections of 89 697 unique sources. The skymap distribution of the test sample is shown in the right panel of Fig. 7.2.

Balancing of the Training Sample

The distribution of sources types in the training set was heavily unbalanced (see Sect.6.3). Seyfert galaxies were the most abundant source types, followed by stars. The number of sources of the most abundant class, i.e. Seyfert 1 galaxies, outnumbers those of the rarest class, ULX, by a factor of almost 100. Such imbalance can significantly degrade the performance of the algorithm because it will bias the model: as a certain parameter combination is more likely to belong to a source from the majority class than from minority classes, the algorithm tends to classify an unknown object as the majority

Table 7.1.: Break down of the training sample.

Source type	Number of sources		Number of detections	
BL	60	(2%)	104	(2%)
CV	201	(7%)	396	(5.5%)
HMXRB	33	(1%)	150	(2.5%)
LMXRB	66	(2.5%)	206	(3%)
STAR	563	(19%)	1613	(21%)
Seyfert 1 (S1)	1486	(51%)	3773	(51%)
Seyfert 2 (S2)	485	(17%)	1026	(13%)
ULX	17	(0.5%)	115	(2%)
Total	2911	(100%)	7383	(100%)

Note: Parenthesis show the fraction of the total number of sources/ detection in the training sample.

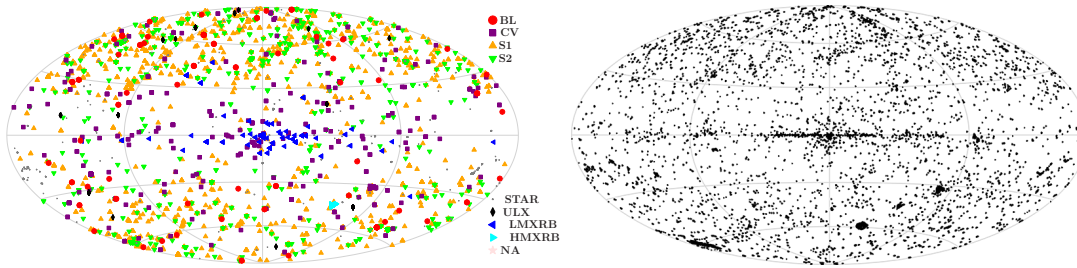


Figure 7.2.: Distribution of the sources of the unbalanced 3XMM training (*left*) and testing (*right*) sample in Galactic coordinates.

class. This also affects the accuracy for classifying different source types, leading to a high accuracy for the abundant source types and a lower one for the rarest. As rare classes can be of particular interest, it is necessary to compensate for this issue. To balance the number of sources per source class, we used the **SMOTE** algorithm (see Sect. 4.1.3), which is implemented in the **DMwR** package (Torgo, 2010). **SMOTE** creates synthetic data samples of the minority class with features selected using the k -nearest-neighbour method (Sect.4.1.3) from within the parameter space of the real sources belonging to that class. The algorithm is designed for a binary problem, in which there are two classes with one having clearly more members than the other one. In our case, we are faced with a 8-class problem. The majority class is clearly S1 (51%, of the sources/detection in the sample), while there are several classes with significantly less members, which means that there is not a clear minority class. Hence, the strategy we follow, is to apply **SMOTE** to all source classes separately, except S1, by constructing seven artificial 2-class problems. That means, for a given source class (e.g., ULX), the class is regarded as minority class and all sources that do not belong to this class form the artificial majority class (i.e., 'non-ULX'). Then **SMOTE** is applied to this 2-class problem and chose the oversampling factor

Table 7.2.: Break down of the balanced training sample.

Source type	Oversampling	Number of detections
BL	3300	3536
CV	800	3564
HMXRB	1600	3750
LMXRB	2400	3502
STAR	150	3226
Seyfert 1 (S1)	-	3773
Seyfert 2 (S2)	300	4104
ULX	3300	3910
Total	-	20 365

Note: Balanced training sample using the SMOTE algorithm with $k = 5$ nearest neighbours. The algorithm was applied to all classes except the majority class (S1) separately. See text Sect.6.4 for more information.

in such a way, that the balanced minority class has approximately the same number of detections as the S1 class. Table 7.2 lists the oversampling factors and new numbers of detections per source class.

7.4. Classification features

This section describes the features that were gathered for each X-ray source in our training and testing samples and used for the RF classification. The characterizing of a source is based on spectroscopic information obtained from the X-ray data, multiwavelength spectral energy distribution (SED) and information about the X-ray and multiwavelength variability. As can be seen from Fig. 7.2, some source types, such as XRB, are more likely to cluster around the Galactic plane, while others (e.g., Seyfert galaxies) are distributed isotropically in Galactic coordinates. Hence, we also included the Galactic longitude l and latitude b of the sources as features in all classification runs. The final list of features included in the training process is given in Table 7.6.

Spectral Features

The spectral features characterize the 0.2–12 keV spectrum of an X-ray source. The 3XMM-DR6 already provides a number of parameters such as hardness ratios in several energy bands listed in Table 7.3. They provide a first phenomenological classification of the spectrum.

For a more detailed description of the X-ray emission, we automatically modeled the *XMM-Newton*/EPIC PN & MOS spectra of each 3XMM detection using up to six spectral models. Figure 7.3 shows the distribution of background-subtracted spectral data counts in the source spectra. Because the Galactic plane extends to latitudes of $\pm 20^\circ$ the

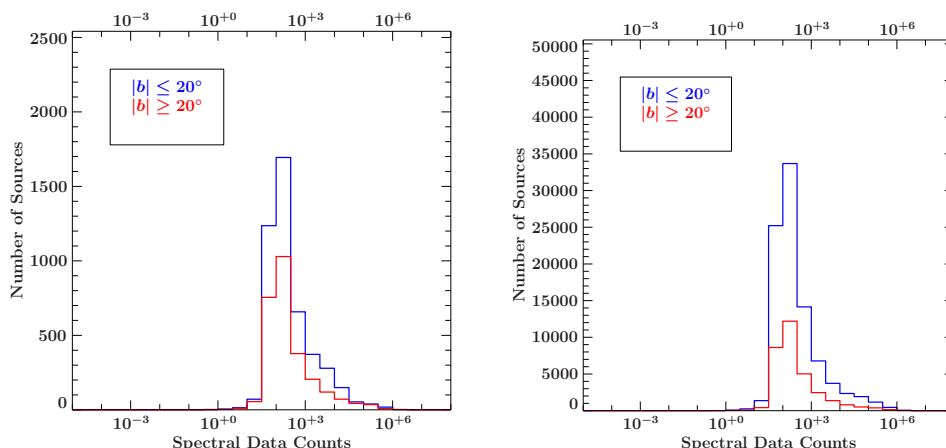


Figure 7.3.: Distribution of background-subtracted spectral data counts in the 3XMM catalogue for the final training (*left*) and test sample (*right*) and divided with respect to their Galactic latitude.

Table 7.3.: Energy bands of the 3XMM-DR6 hardness ratio

Hardness Ratio	lower band [keV]	upper band [keV]
HR1	0.2–0.5	0.5–1.0
HR2	0.5–1.0	1.0–2.0
HR3	1.0–2.0	2.0–4.5
HR4	2.0–4.5	4.5–12.0

Note: Hardness ratios are provided by the 3XMM-DR6 catalog and are defined as the ratio of the lower and upper band. For more detailed information on hardness ratios see 3XMM-DR User Guide or Rosen et al. (2016).

distributions are divided into sources with Galactic latitudes within and outside of this region. In 10% of the total catalogue, there are less than 70 counts in the total spectrum. In all other cases, the quality of the data is sufficient for spectral analysis with simple models.

Six phenomenological models are fitted to each detection of the 3XMM data (see Table 7.4). While the hardness ratios were computed from the whole energy band, the conversion from counts to photons is affected by calibration. In order to account for calibration issues in the lowest and highest energy bins we restrict the fitted energy band to (0.5–10) keV.

The choice of models is based on the work by XMMFITCAT (Corral et al. 2015). They resemble the most common spectral shapes observed in X-ray astronomy. The models are further divided into "simple" and "complex" models, where the latter are a combination of the simple ones and an additional intrinsically absorbed power law. Simple models are applied to spectral data of each detection and involve a powerlaw (`pegpwr1w`), a blackbody (`bbody`) or an ionized plasma (`apec`), where each one is modified by photo-

Table 7.4.: Spectral models used for automated fitting.

Model name	Abbreviation	Free Parameter	Constraints
Simple models:			
(a) absorbed power law	PL	$N_{\text{H}}, N_{\text{pl}}, \Gamma_{\text{pl}}$	-
(b) absorbed blackbody	BB	$N_{\text{H}}, T_{\text{bb}}$	applied to 0.5–2 keV only
(c) absorbed plasma	AP	$N_{\text{H}}, T_{\text{ap}}$	-
Complex models:			
(a) + power law	PLPL	$N_{\text{H}1}, N_{\text{H}2}, \Gamma_{\text{pl}1}, \Gamma_{\text{pl}2}$	spectral counts ≥ 500 cts
(b) + power law	BBPL	$N_{\text{H}1}, N_{\text{H}2}, N_{\text{pl}}, \Gamma_{\text{pl}}, T_{\text{bb}}$	spectral counts ≥ 500 cts
(c) + power law	APPL	$N_{\text{H}1}, N_{\text{H}2}, N_{\text{pl}}, \Gamma_{\text{pl}}, T_{\text{ap}}$	spectral counts ≥ 500 cts

Note: Parameters are: N_{H} – absorbing hydrogen column density, N_{pl} – power-law normalization, T_{bb} – blackbody temperature, T_{ap} – Apec temperature.

electric absorption in the ISM (`tbnew`⁷). Complex models are applied only if the total number of counts (all instruments added together) is larger than 500 counts in the total energy band. In this case, best-fit parameter values of the simple models serve as initial values for the complex ones. More details on the spectral models used as well as initial parameters and count rate constraints are described in Appendix Sects. A.2.

The spectral fitting is done with ISIS Version 1.6.2-32 (Houck & Denicola 2000). An automated pipeline was set up, composed of ISIS scripts, which take advantage of the `ISISscripts`⁸ provided by the Dr. Reemis Observatory. The pipeline handles the preparation of the data sets, spectral fitting, error calculation and merging of fit results of all 3XMM-DR6 detections. A detailed description of the pipeline is given in Appendix A.1. If available, the spectra of all EPIC camera of a detection are fitted simultaneously. Because of the different effective areas of the PN, MOS1 and MOS2 detectors the normalization can vary up to 20% between the respective spectra. To account for this difference in normalization a constant is included in the fit model. Unless stated otherwise, 90% confidence levels are calculated for each free parameter of interest.

In Fig. 7.4, we show example best-fits for each of the six spectral model combinations. Overall, the six model combinations perform reasonably well to describe the basic shape of the spectra.

Figures A.2 and A.3 show example hardness diagrams and combinations of best fit parameters for the training sample, separated into sources with low and high Galactic latitude, respectively. It is obvious that based on spectral properties alone, some source classes will be difficult to separate. For example, while stars and AGN occupy very distinct regions in the Γ - N_{H} plot, X-ray binaries and CVs show similar spectral shapes as AGN. Further information from timing and multiwavelength features will be necessary to separate between these source types.

⁷<http://pulsar.sternwarte.uni-erlangen.de/wilms/research/tbabs/index.html>

⁸<http://www.sternwarte.uni-erlangen.de/ISIS/>

7. Taking source classification to the EXTrAS level

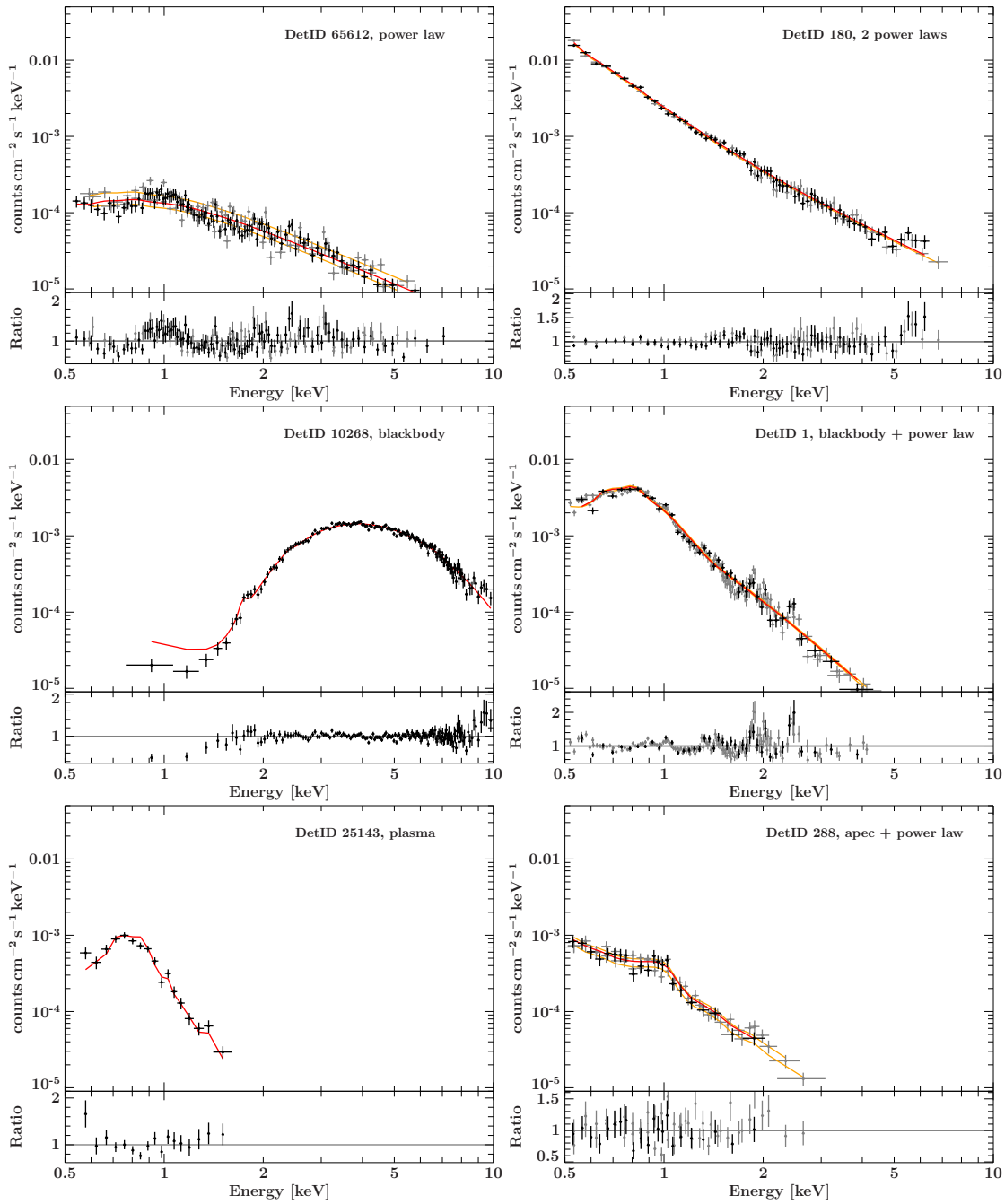


Figure 7.4.: Unfolded example EPIC PN (black) and MOS 1 & 2 (gray) spectra for best-fits for each model. Solid lines are the best-fit model to the PN (red line) and MOS (yellow line) spectra.

Multiwavelength features

In order to extract multiwavelength information, we looked for counter parts by performing a positional cross-match of the training and test sample from the 3XMM-DR6 source positions. The cross-matching was performed using the XMATCH tool developed by the ARCHES collaboration⁹. We cross-matched all detections of the 3XMM against 53 catalogs in different wavelengths. The significance of a counter part match is expressed via χ^2 . A detailed description of the cross-matching and a complete list of the matched catalogs can be found in the EXTraS archive online documentation. We compiled a mastercatalog, which contains information of all cross-matches for all our 3XMM sources. The catalog is publicly available through the EXTraS database¹⁰.

Summarizing, 4300 X-ray detections have radio counterparts, 57000 detections have IR counterparts, 54000 detections have optical counterparts, and 39500 detections have counterparts in the γ -rays. Note, since the 3XMM contains multiple detections of individual sources, the number of unique counter parts matches is smaller.

With the information of the catalogue matches, the multiwavelength indices α were computed for a given frequency band with respect to the X-ray band. These indices were used to characterize the broad band spectrum of a source of interest. Note, since the sources are variable, simultaneous multiwavelength data would be necessary to reflect the true shape of the broadband spectrum. Hence, the multiwavelength indices calculated in this study differ from the true index. Nevertheless, the information whether or not a source is detected in certain wavelength band is valuable for the class identification¹¹.

For the computation of the indices, we assume a power law as underlying broadband spectral model, so the flux density dF_1 (in Jansky) at a given frequency ν_1 (in Hz) is given by

$$dF_1 = N * \nu_1^{-\alpha}, \quad (7.4.1)$$

where N is the normalization of the power law in units of $\text{erg}/\text{cm}^2/\text{s}/\text{hz}$. The index α that describes the power law which connects the source emission at two different frequencies ν_1 and ν_2 is then given by

$$\alpha_{12} = -1 * \log \left(\frac{dF_1}{dF_2} \right) / \log \left(\frac{\nu_1}{\nu_2} \right), \quad (7.4.2)$$

where we consider the X-ray flux at 1 keV from the automated fitting method as reference flux density dF_2 .

For a given source, we use the information of the catalogue cross-matches to get the flux densities at different wavelength. Magnitudes and fluxes in $\text{erg}/\text{cm}^2/\text{s}$ are converted into flux densities in units of Jansky. If a number of possible counterparts are found for a single catalogue, we use the one with the lowest χ^2 , hence highest probability for positional coincidence. In case a source has possible counterparts in several catalogs of

⁹ARCHES: <http://www.arches-fp7.eu/>

¹⁰<http://www.extras-fp7.eu/index.php/archive>

¹¹For example, a detection in both the γ -ray and radio band can help to distinguish Seyferts from BL objects or XRB from AGN.

Table 7.5.: Specification of the multiwavelength indices.

MWL Index	Band 1	Catalogues
α_{r1x}	1.4 GHz	NVSS
α_{r5x}	~ 5 GHz	PMN, CRATES, AT20G
α_{r8x}	$\sim 8, 4$ GHz	CRATES, CGRABS, AT20G
α_{ir1x}	25 μ m	MSX6C, IRAS PSC, WISE
α_{ir2x}	12 μ m	MSX6C, IRAS PSC, WISE
α_{ir6x}	4.5 μ m	MSX6C, WISE, SDWFS, SAGE, GLIMPSE
α_{ir8x}	3.6 μ m	WISE, SDWFS, GLIMPSE
α_{ox}	~ 500 nm	SEYFERT1_ZHOU, SDSS-DR9, UKIDSS9_LAS, 2MASS-6X, USNOB-1, GSC-2.3, NOMAD
α_{uvx}	365 nm	UVEX, SDSS-DR9, GSC-2.3
α_{hx}	20 keV, 14 keV	INTEGRAL IBIS catalogue, BAT AGN catalogue
α_{gx}	100 GeV	FERMI 3FGL, EGRET
$\alpha_{planckx}$	353 GHz, 217 GHz, 545 GHz	PLANCK

Note: Indices are calculated between flux densities at frequency ν_1 with respect to the one at 1 keV from the automated fitting.

similar frequency, the given index is calculated for all catalogs and averaged to decrease the bias of variability. The different indices and frequencies as well as the catalogues considered for a given index are listed in Table 7.5.

Timing Features

As the objective of the EXTraS project was a timing analysis of the 3XMM archival data, several working groups performed intensive tests and statistical studies to extract synthetic parameters that characterize the light curves of the 3XMM X-ray sources.

WP2 members, D. Salvetti, M. Marelli, and A. Belfiore, analyzed of the aperiodic and periodic short-term variability of 3XMM detections. A complete documentation of their analysis and results can be found in the EXTraS archive¹². In order to test and characterize aperiodic short-term variability of each source, they fitted to each light curve with a series of analytical models of the source rate evolution. Full band light curves are tested against a constant and linear model and if possible against more advanced models: a quadratic function, an exponential decay, and local features like flares and eclipses, on top of a constant. Each fit yielded a parameter for the goodness-of-the-fit and fit parameters.

Furthermore, statistical features were derived including the weighted average of the count rate, the relative excess variance, doubling and halving time of the X-ray count rate, and the fraction of time that the source exhibited a count rate above or below the 1σ , 3σ , or 5σ level of the average.

In addition to this kind of variability, information on the periodic behaviour of a source can help to identify XRB or CV sources. WP3 (G.L. Israel and G. Rodriguez) studied

¹²<http://www.extras-fp7.eu/index.php/it/archive-it#docs>

the pulsations within a single observation for each 3XMM detections by using Fourier analysis of the light curves to create spectrograms. They provide peak information for every spectrogram of the 3XMM sources, such as the significance of a periodic signal, its Fourier frequency, and signal power. Figure A.5 shows example combinations of parameters derived for periodic and aperiodic variability.

7.5. Randomized detection positions

In early classification runs, we found that, unexpectedly, the Galactic longitude has a large influence on the classification, while the latitude is less important (see parameter `threexmm_l1i` in Fig. 7.5, left panel). While we would expect the Galactic latitude to be an important discriminator for distinguishing Galactic and extragalactic sources, the effect of the longitude should in principle be smaller, although it has some importance in separating the bulge and the disk population of Galactic sources. That this parameter is so important could be due to the fact that the initial spectral classification forest is based on multiple detections of single sources and the large number of extragalactic XRBs from the SMC in the sample. As this means that the same coordinate pair enters the classification multiple times, the importance of the coordinates could be exaggerated in the classification. This bias can be observed in the form of sharp peaks in the distribution of coordinates in the training sample.

To eliminate this bias, we determined the probability distribution of source positions for each class in the training sample using polynomial fits (of 6th order). We then draw random coordinates from the probability distributions derived for each class and assign these random coordinates to the detection in each source class. Figure 7.6 shows the histogram of the source positions (black line) and the best-fit of a polynomial (red solid line). For comparison, we also show the distribution of reassigned coordinates overlaid in blue. The randomization gets rid of the peaks in the distribution, that are caused by multiple visits of *XMM-Newton* in a certain region of the sky. Figure 7.7 shows the comparison of the true and redistributed coordinates for each detection within a class. Here the effect of multiple pointings is more prominent as the number of detections increases with each visit.

With these changes we reran the classification. The overall error rate is not significantly affected by the use of randomized detection positions (change of $\sim 1\%$) but as expected, the importance of the Galactic longitude is lower (compare Fig. 7.5, right panel). The training set with randomized positions is hence used in any following classification run.

7.6. Training an algorithm

We constructed various prediction models for the 3XMM. The supervised method allowed us to assess the performance using the OBB misclassification error for different groups of features and iteratively construct a minimum set of the most important classification features. To construct each training model, the RF classifier was setup with default of 500 decision trees per run. We find, that the OBB error rate is rather insensitive to the

7. Taking source classification to the EXTrAS level

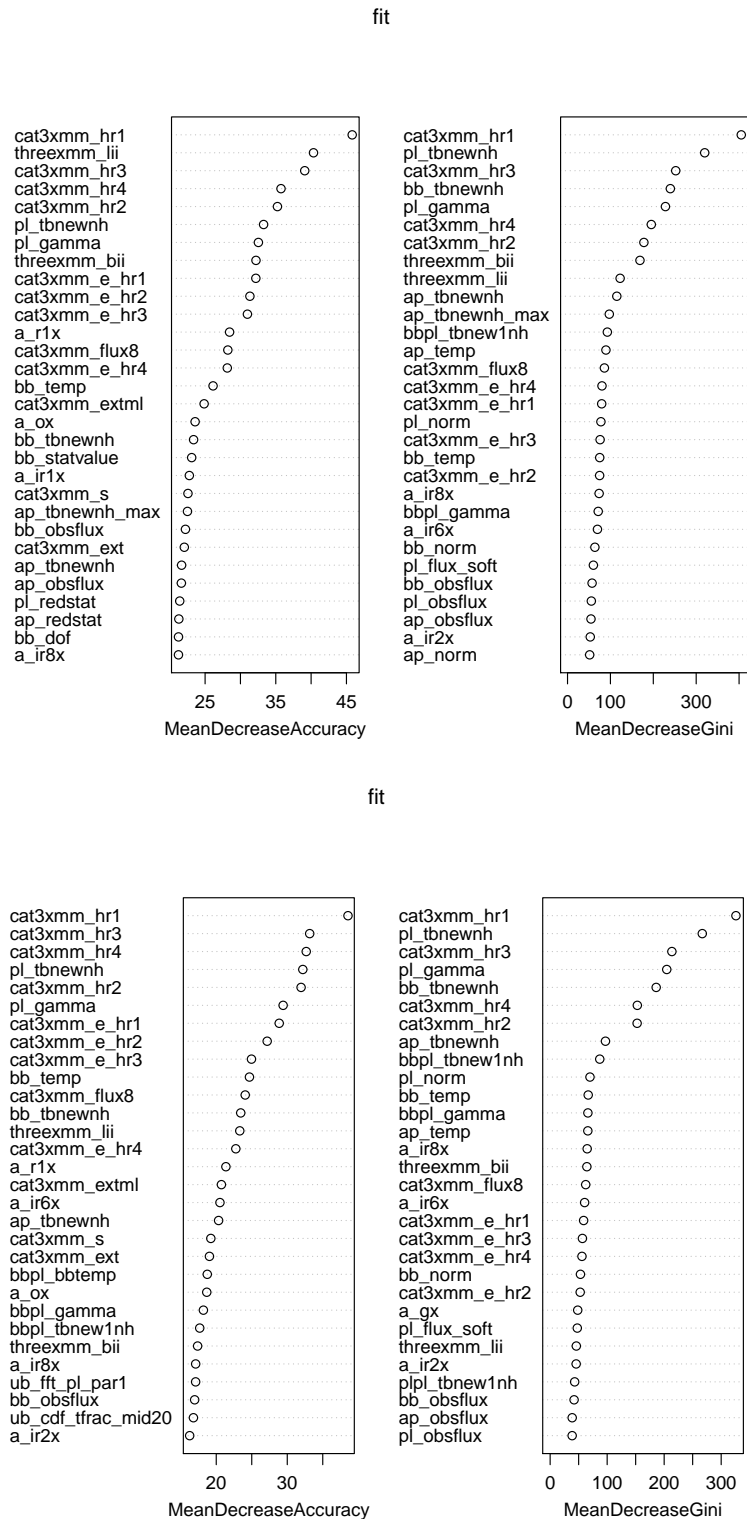


Figure 7.5.: Importance of different source properties on the source classification using hardness ratios, spectral, and multiwavelength information with true Galactic coordinates of each detection (*left*) and with randomized positions (*right*).

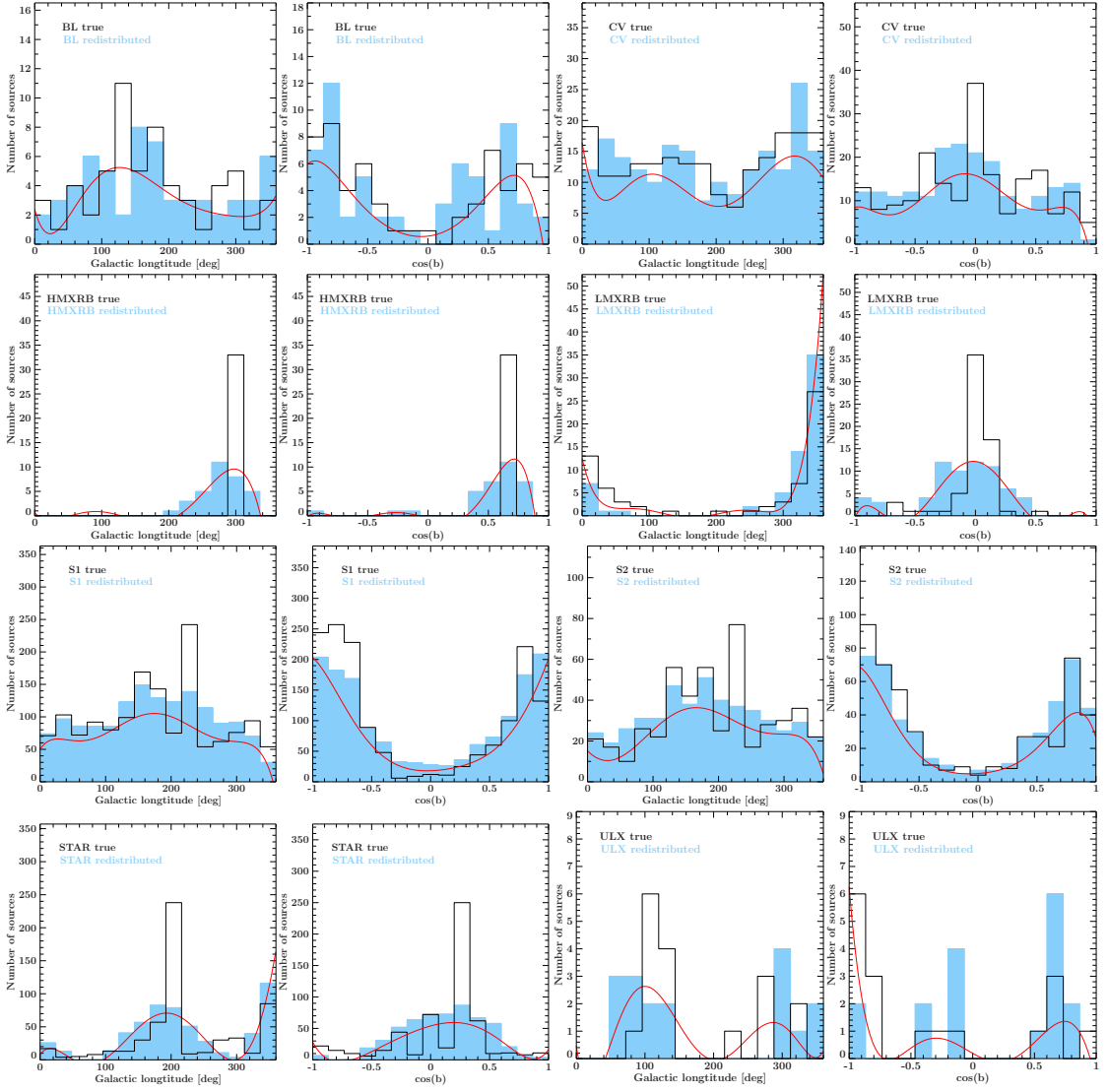


Figure 7.6.: Histogram of Galactic source positions for the sources in the training sample. The true distributions are shown as black solid line, while the blue histogram depicts the redistributed positions of each source (see text for explanation).

number of best-split features that are randomly chosen at each node to choose the best split of a branch. When we tested any number of features between 2 and 15, the error rate changes less than 1%. Hence, we follow Lo et al. (2014) who find that approximately 9 features yield the best performance.

In order to find the minimal number of features that are necessary to classify unknown sources, we started with a basic set of features (hardness ratios, source coordinates and extension) and iteratively added new groups of source attributes (spectral fit results, multiwavelength indices, and timing features). For each new group, we first included all

7. Taking source classification to the EXtraS level

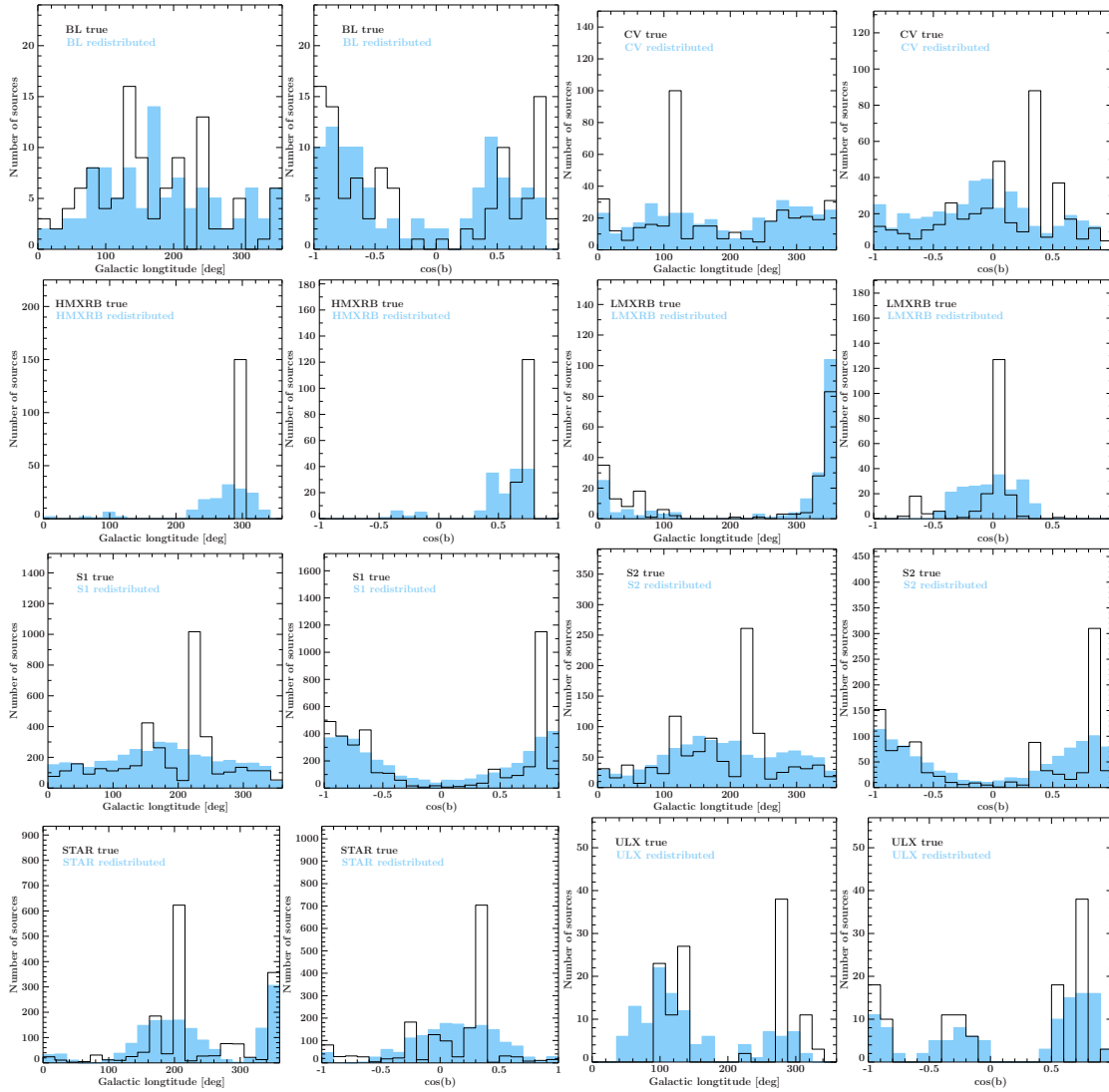


Figure 7.7.: Histogram of Galactic source positions for each detection in the training sample. The true distributions are shown as black solid line, while the blue histogram depicts the redistributed positions of each detection drawn from the distribution of unique sources.

available features and sequentially removed those of lowest relevance for the classification, by taking into account the changes in the OBB error rate (see Sect. 4.1.3) and the parameter importance provided in every classification run. Afterwards the classifier is trained again with the new set of features. The final set of features is shown in Table 7.6.

During the training, we took each individual detection of a given source as representative of the properties of this source class at a given instance in time, that is, the training already allows for the long-term spectral variability of the sources. However, we combined the separate classifications from each detection for each unique source eventually

to provide an overall classification probability.

When training the algorithm using Galactic coordinates and hardness ratios, the OBB error rate estimation for the prediction model is only 8.3%. Figure 7.8, left panel, shows the parameter importance in terms of decrease in classification accuracy when removing a specific features. The right panel shows the same with respect to the decrease of the G_{ini} index as measure for the purity of a sample at a decision tree final node (see Sect. 6.2.1). In terms of accuracy, the left panel shows that hardness ratio HR1 is the most important discriminator. The source extension flag and Galactic coordinates are less important. However, it is also important to understand in what way the classes are mixed and which classes can be well identified. This is expressed through the confusion matrix, as given by **R**, and is summarized in Table 7.7. The matrix shows the classification error made by applying the classification onto the individual observations in the training sample. A perfect classifier would place all of the data on the diagonal of the confusion matrix. Any deviations from the diagonal inform us of the types of errors that the classifier makes. Using only hardness ratios, source extension, and Galactic coordinates, there is a high degree of confusion between the source types. As Seyfert galaxies exhibit the largest variations in their X-ray spectrum, most source types are confused as S1 or S2 types. In addition, Seyfert 2 galaxies have a tendency to be classified as Seyferts 1, probably also due to the large scatter in their spectral parameters and due to the fact that the two object classes exhibit a continuum of source behaviors in the X-rays.

Adding spectral fit results, the X-ray flux (denoted by the pl_norm) becomes the most important features. Further characterization occurs by Galactic coordinates and hardness ratios, while the reduced χ^2 values seem to play only minor roles (see Fig. 7.8, right panel). Since the spectral parameters as well as the hardness ratios both describe the spectral shape of the sources, one can expect a high degree of correlation between them. However, the classifications becomes significantly worse when removing the hardness ratio features. We dropped the parameters for the goodness-of-fit, which had no effect on the error rate. The OBB error rate for the set of basic and all spectral features is 3.97%.

Afterwards all multiwavelength features were added to the list (see Fig. 7.9, left panel). The OBB error rate drops to 2.56%. The most important indices are $\alpha_{r,x}$ and $\alpha_{g,x}$ which help to distinguish between AGN and non-AGN, such as BL lacs objects and stars, which do not show strong radio or γ -ray emission. Not unexpectedly there is still a confusion between BL Lacs and Seyfert 1 galaxies due to their similar power-law spectral shapes, and also between CVs and Seyferts.

However, due to the different timescales of X-ray emission processes in these sources, information about their aperiodic and periodic short term variability may help to distinguish between them. As expected, the addition of aperiodic features decreases the predicted error fraction but additional information on periodicity yield an increase. This is likely due to the large uncertainties of the periodicity features. The number of the features is reduced until the error fraction does not worsen anymore. In the end, we include the probability of a periodic signal, the signal power and Fourier frequency in the group of timing features. Eventually, the training results in a predicted error fraction of

Table 7.6.: Final list of classification features.

Set	Feature name	Explanation
Basic	threexmm_lii	Galactic longitude l
	threexmm_bii	Galactic latitude b
Spectral	cat3xmm_hr1	Hardness Ratio HR1
	cat3xmm_hr2	Hardness Ratio HR2
	cat3xmm_hr3	Hardness Ratio HR3
	cat3xmm_hr4	Hardness Ratio HR4
	pl_norm	X-ray flux between (0.5–10) keV [10^{-12} erg/cm ² /s]
	pl_tbnwh	Hydrogen column density $N_{\text{H,PL}}$ [10^{22} cm ⁻²]
	pl_gamma	Photon index Γ_{PL}
	bb_temp	Blackbody temperature kT_{BB} [keV]
	bb_norm	Blackbody normalization N_{BB} [10^{39} erg/s]
	ap_temp	Ionized gas temperature kT_{AP} [keV]
	bbpl_bbtemp	Blackbody temperature kT_{BBPL} [keV]
bbpl_gamma	Photon index Γ_{BBPL}	
Multiwavelength	a_ir1x	MWL index $\alpha_{\text{IR1,X}}$
	a_r1x	MWL index $\alpha_{\text{R1,X}}$
	a_ox	MWL index $\alpha_{\text{O,X}}$
	a_gx	MWL index $\alpha_{\text{G,X}}$
Timing	bb_lc_fvar	Fractional variability F_{var}
	bb_lc_ave	Weighted average count rate
	bb_lc_amplit	Weighted variability amplitude
	bb_lc_co_par1	Mean count rate from a constant model
	bb_lc_dou_time	Doubling time
	bb_lc_hal_time	Halving time
	Probability	Pulse signal probability
	power	Pulse signal power
	ffr	Fourier frequency of a pulse signal

Note: The complete list of extracted features is shown in appendix Table A.5. The final list was constructed by removing those features with lowest importance for the classification and refit the prediction model to assess its effect. The basic set of features is included in all classification runs.

about 2.41%. The final list of features can be found in Table 7.6. Surprisingly, the overall influence of the timing parameters is very small (see Fig. 7.9, left panel). The hardness ratios and multiwavelength indices between radio, γ -rays and X-rays continue to have the largest influence on the classification, which is then further optimized by considering the X-ray flux, N_{H} , and the photon index, Γ . The strongest effect of the timing features is contributed by the count rate doubling time and Fourier frequency.

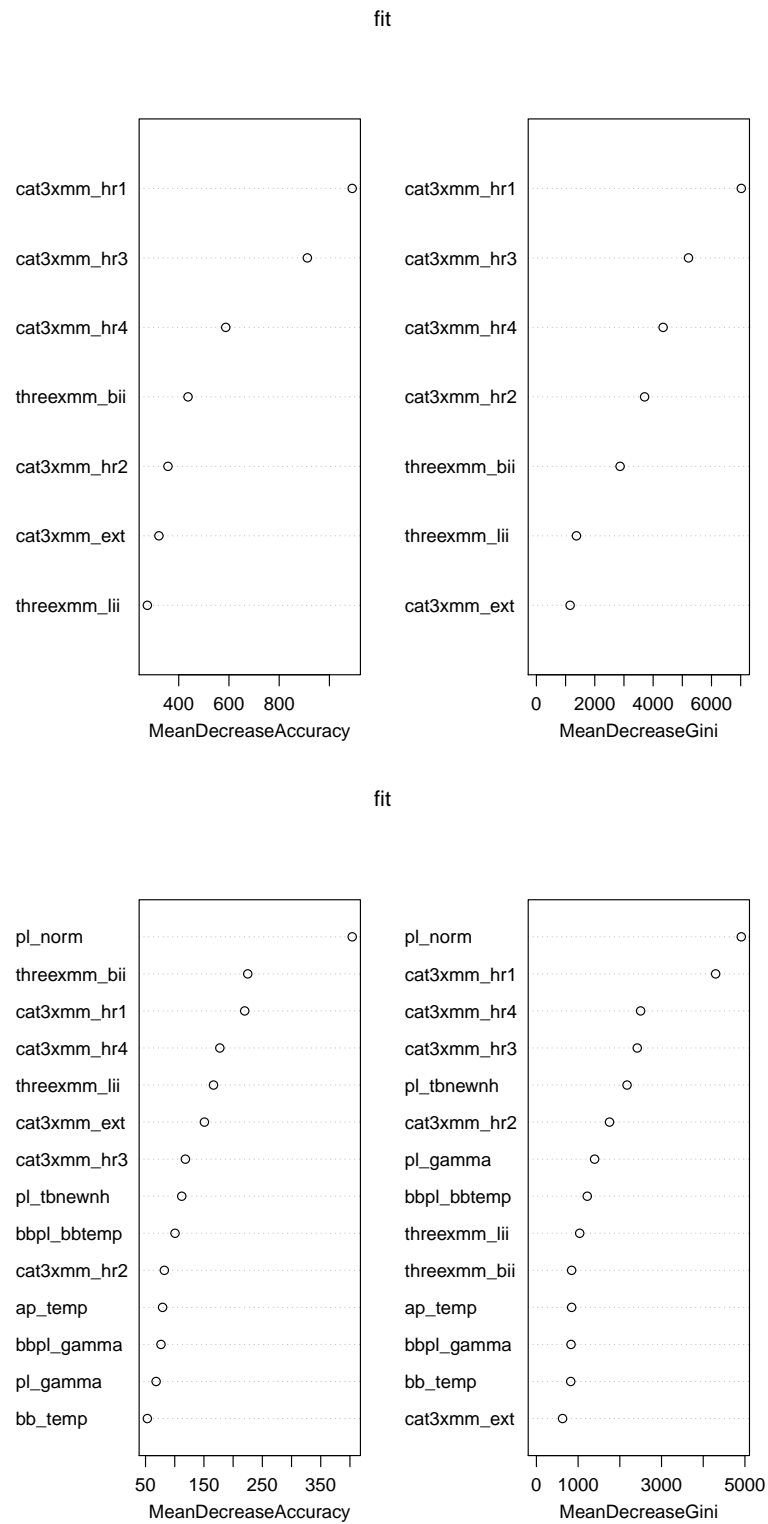


Figure 7.8.: Importance of classification features. *Left:* Training with hardness ratios only. *Right:* Training with spectral feature. All runs include source extension and Galactic coordinates.

7. Taking source classification to the EXTrAS level

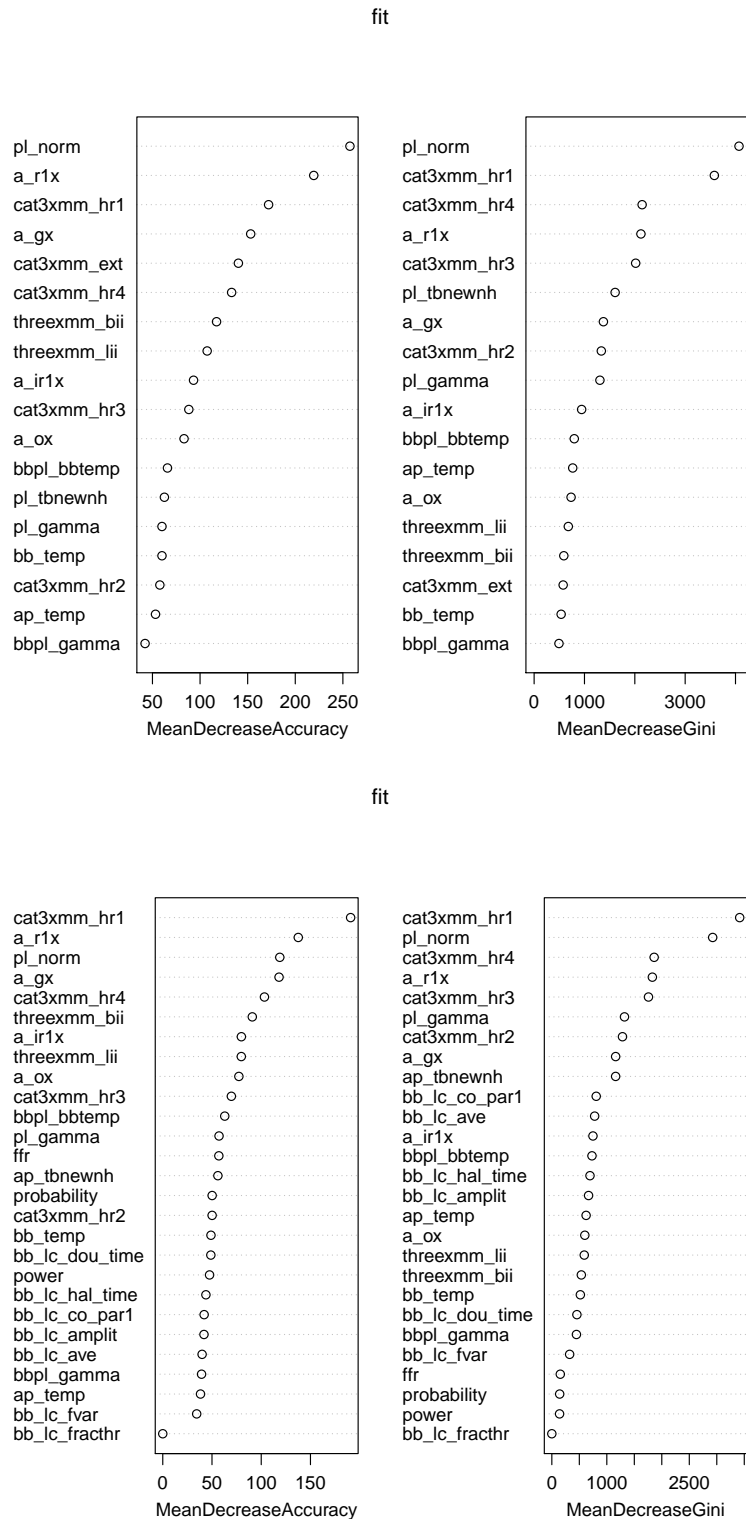


Figure 7.9.: Importance of classification features. *Left:* Training with spectral and multiwavelength features. *Right:* Training with spectral, multiwavelength, and timing features. All runs include source extension and Galactic coordinates.

Table 7.7.: Confusion matrix for different training runs.

A: Hardness ratios only									(OBB error rate 8.3%)
	BL	CV	HMXRB	LMXRB	S1	S2	STAR	ULX	Class. Error
BL	3380	34	0	2	62	17	9	32	0.04
CV	80	3055	23	52	110	189	26	29	0.14
HMXRB	0	4	3729	1	0	15	1	0	≤ 0.01
LMXRB	1	25	8	3375	3	9	34	47	0.04
S1	115	126	3	12	3204	264	18	31	0.15
S2	28	204	34	52	297	3384	55	50	0.18
STAR	15	8	2	57	15	52	3009	68	0.08
ULX	19	8	0	33	7	17	34	3792	0.03
B: All spectral features									(OBB error rate 3.97%)
	BL	CV	HMXRB	LMXRB	S1	S2	STAR	ULX	Class. Error
BL	3495	11	0	0	16	7	6	1	0.01
CV	32	3334	13	11	45	85	31	13	0.06
HMXRB	0	0	3748	0	0	1	1	0	≤ 0.01
LMXRB	3	7	0	3465	2	5	13	7	0.01
S1	34	53	3	8	3424	210	24	17	0.09
S2	8	74	9	7	242	3702	40	22	0.10
STAR	8	11	1	7	6	32	3143	18	0.03
ULX	4	3	0	0	3	7	6	3887	0.006
C: Spectral and multiwavelength features									(OBB error rate 2.56%)
	BL	CV	HMXRB	LMXRB	S1	S2	STAR	ULX	Class. Error
BL	3521	0	0	0	10	5	0	0	≤ 0.01
CV	8	3449	10	8	48	14	22	5	0.03
HMXRB	0	0	3748	0	0	1	1	0	≤ 0.01
LMXRB	1	6	0	3473	2	2	14	4	≤ 0.01
S1	11	41	2	7	3538	152	20	2	0.06
S2	6	34	7	4	212	3804	19	18	0.07
STAR	5	10	0	2	7	11	3178	13	0.02
ULX	1	0	0	0	1	0	7	3901	≤ 0.01
D: Spectral, multiwavelength and timing features									(OBB error rate 2.41%)
	BL	CV	HMXRB	LMXRB	S1	S2	STAR	ULX	Class. Error
BL	3517	0	0	0	14	5	0	0	≤ 0.01
CV	4	3460	8	5	39	19	27	2	0.03
HMXRB	0	0	3749	0	0	1	0	0	≤ 0.01
LMXRB	1	8	0	3471	1	2	14	5	≤ 0.01
S1	13	23	1	12	3541	160	21	2	0.06
S2	8	15	3	2	229	3827	10	10	0.07
STAR	2	8	0	1	8	9	3190	8	0.01
ULX	0	0	0	0	3	0	4	3903	≤ 0.01

Note: Confusion matrix obtained from our training set with 500-tree RF classification and (if possible) 9 random variable at each node. All runs include the source extension flag and Galactic coordinates and differ in the use of different spectral, multiwavelength and timing features. Rows indicate the *reference* 3XMM source types, while column represent the classifiers *predicted* type.

Table 7.8.: Class prediction for the test sample using the spectral model.

Source type	Number of sources		Number of detections	
BL	377	(0.4%)	559	(0.5%)
CV	4982	(5.6%)	6838	(5.5%)
HMXRB	830	(0.9%)	1095	(0.9%)
LMXRB	1669	(1.9%)	3004	(2.4%)
STAR	27 765	(31.0%)	40767	(32.8%)
S1	33 250	(37.1%)	44887	(36.1%)
S2	18 073	(20.1%)	23709	(19.1%)
ULX	774	(0.8%)	1402	(1.1%)
not classified	1 977	(2.2%)	2141	(1.7%)
Total	89 697		124 402	

7.7. Classification of the 3XMM-DR6 test sample

Two RF prediction models (also called 'classifiers') were tested by running it on the 3XMM test sample: one with basic, spectral, and multiwavelength features (model C, hereafter referred to as 'spectral model') and one with additional timing features (model D, called 'timing model' hereafter). For sources where there are more than one detection, we classified each detection separately and combined results by averaging the output class membership probabilities and assign the class with highest average probability.

In comparison, the 'spectral model' performs best with respect to the number of classified sources. The distribution of classified source types with a prediction probability of $\geq 60\%$ in various hardness diagrams and other feature correlation plots is shown in Appendix Sect. A.4. Overall the algorithm performs well in separating different parameter regions. Out of 124 402 detections in the test sample 98.3% were classified. The class composition of the test sample is summarized in Table 7.8. The distribution of probabilities are shown in Fig. 7.10 as blue histogram. For the majority of sources, they were higher than 50%. Overall, most test sources are classified as Seyfert galaxies or stars, similar to the distribution of the training sample. The remaining 1.7% of detections (2.2% of unique sources) could not be classified. We tested whether this number changes by choosing different numbers of random features that are used at each node and by increasing the number of decision trees per classification run. However, these changes have no effect on the number of unclassified sources. That means, there is no branch for those cases in any of the decision trees that fits their parameters. Interestingly, using a classifier build with hardness ratios only results in the same fraction of unclassified sources. Hence, we are missing representative parameter combinations in the training sample.

Keeping this issue in mind, we applied the 'timing model' which includes additional features to describe the temporal source properties. The composition of the object classes is summarized in Table 7.9. The distribution of class probabilities is shown in Fig. 7.10,

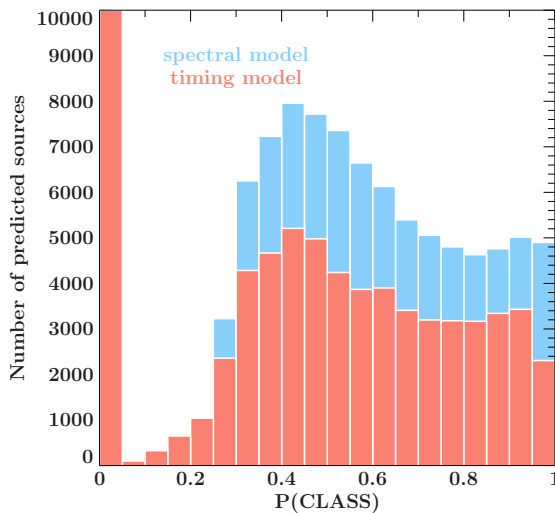


Figure 7.10: Distribution of highest class probabilities from the spectral (blue) and timing (red) classification model. The classification results between spectral and timing model differs in a fraction of $\sim 40\%$ of sources. See Fig. 7.11 for an overview.

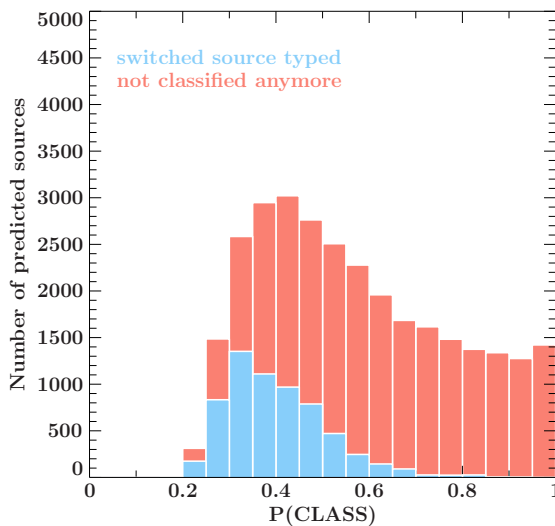


Figure 7.11: Distribution of highest class probabilities from sources classified with the spectral model that differ from the timing model such as they either switched source type (7%, blue) or were not classified (33.5%, red). Most sources that switched source type had class probabilities only marginally higher than the second best class.

in red. Even though the misclassification rate of this model is slightly better than of the spectral model, the classification strength is worse: only $\sim 58\%$ of detections were classified and 52 532 detections (32 033 objects) remain unassigned. Comparing the results of the spectral and timing model source by source, we find that the predicted classes differed in 40.5% of the sources. Figure 7.11 shows the class prediction derived from the spectral model for those sources that either resulted in a different source type (blue) or were unclassified (red) after applying the timing model. In a quarter of these sources the predicted source types changed. We note that for those sources the significance is low and predicted probabilities lay below 50% while the respective second best prediction had probabilities of $\sim 30\%$. The remaining 3/4 of the sources turned out to be classified in the spectral model but unclassified in the timing model. Among those, there were a few sources with high prediction probabilities (up to 90%). Hence, we believe that

Table 7.9.: Class prediction for the test sample using the timing model.

Source type	Number of sources		Number of detections	
BL	77	(0.1%)	96	(0.1%)
CV	1327	(1.4%)	1702	(1.4%)
HMXRB	559	(0.5%)	675	(0.5%)
LMXRB	599	(0.7%)	912	(0.7%)
STAR	16 979	(17.8%)	22 087	(17.8%)
S1	26 561	(26.0%)	32 351	(26.0%)
S2	11 363	(11.0%)	13 684	(11.0%)
ULX	199	(0.3%)	363	(0.3%)
not classified	32 033	(42.2%)	52 532	(42.2%)
Total	89 697		124 402	

Table 7.10.: Difference matrix for classification with and without timing features.

	BL	CV	HMXRB	LMXRB	S1	S2	STAR	ULX	NA	Class fraction [%]
BL	-	2	0	0	24	49	15	0	220	82
CV	1	-	29	14	361	351	533	11	2516	77
HMXRB	0	10	-	0	17	5	111	0	214	44
LMXRB	0	9	0	-	154	39	116	8	784	67
S1	2	34	33	12	-	343	524	41	10777	42
S2	6	40	3	10	128	-	520	9	9052	29
STAR	4	47	29	3	239	2255	-	1	5962	30
ULX	0	19	0	1	57	36	11	-	521	83
NA	0	0	0	0	0	0	0	0	-	0

Note: Difference between classifying with spectral and multiwavelength features and those including additional timing features. Rows indicate the source types of spectral classification, while column represent the types using additional timing classifiers.

the large number of unclassified sources was caused by unreliable timing features. For example, very low signal to noise ratios could have resulted in parameter combinations that contradicted those of the training set. The differences between the models for each class is summarized in Table 7.10. It is not surprising, that there was no improvement or difference for those sources that were already unclassified in the spectral model. Instead this fact shows that the timing features used in this classification are weak classifiers. Figure A.8 shows example distribution of the timing parameters for the complete test sample.

Figures 7.12 and 7.13 show the distribution of the classified 3XMM sources in Galactic coordinates for both classification models. We note that for many locations in the map there is an overlap between Seyfert 1, Seyfert 2, and stars. These places correspond to individual XMM pointings containing multiple sources of different classes. These sources cannot be separated due to the low resolution of the figure with respect to the size of the field of view of XMM. The distribution is close to what one would expect

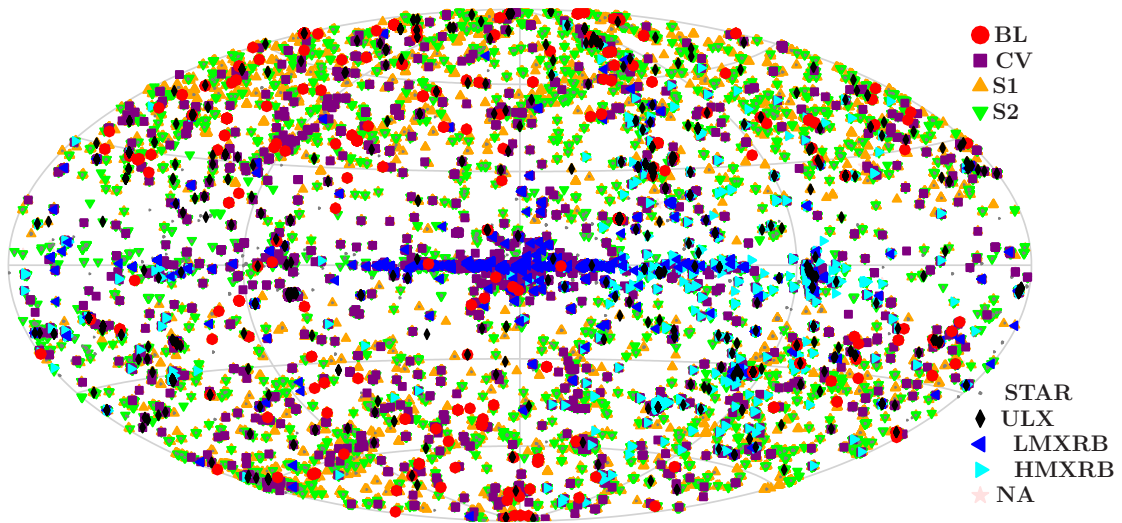


Figure 7.12.: Distribution of the predicted source types of 3XMM sources for spectral model in Galactic coordinates.

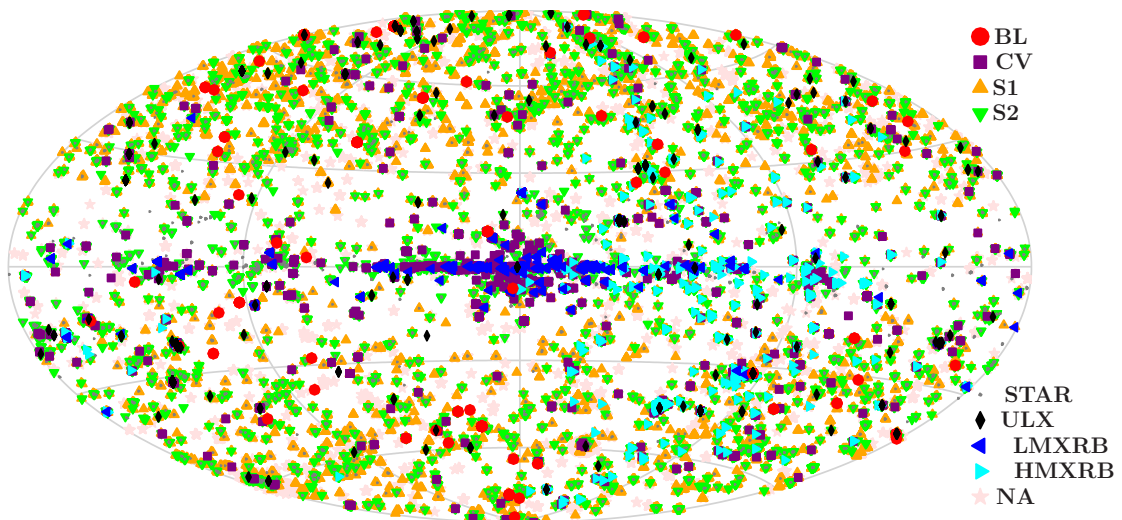


Figure 7.13.: Distribution of the predicted source types of 3XMM sources for timing model in Galactic coordinates.

from the known distributions of the input sources. Albeit, the distribution shows the combined effect of the coordinate randomization and balancing of the training sample: the broadened distribution of randomized position for HMXRB detections in the SMC was enhanced by the creation of synthesized detections which caused the classification algorithm to regard a wider range of coordinates for HMXRB.

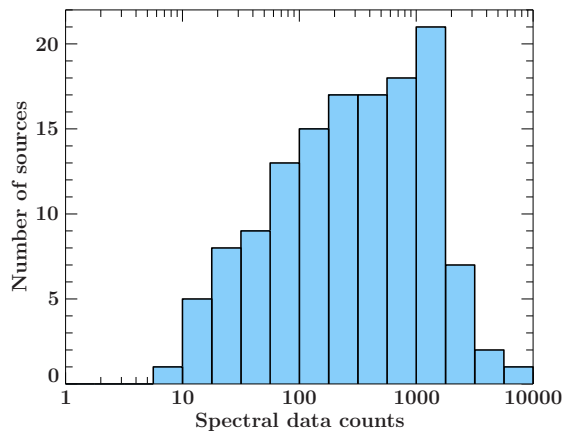


Figure 7.14: Background subtracted spectral data counts for EXTraS transient sources in the (0.2–12). keV energy band.

7.8. Classification of EXTraS transient sources

The EXTraS Transient catalog

The EXTraS transient catalog contains X-ray sources that were missed by the standard SSC source detection pipeline because they can only be significantly detected in a short time interval rather than the full observations. The search for these sources is described in detail in the EXTraS archive online documentation. Over 7700 archival *XMM-Newton* observations were automatically analyzed. Each observation was split into smaller time intervals of less than 5 ks taking into account the highly variable EPIC background. Source detection was performed on time intervals with significant count rate excess and detected sources were compared with a source list from the 3XMM-DR5. A list of transient source candidates was created from those sources which were detected in at least one time interval but which had no counterpart in the reference source list from the 3XMM-DR5. Each transient candidate was visually screened eventually. The public EXTraS transient catalog includes those 136 new X-ray sources that did not show any anomalies during the screening and which where a significant count rates excess with a duration shorter than 5 ks. A complete list of the EXTraS transients can be found in Table A.6. The distribution of background subtracted data counts summed over all three EPIC cameras in the (0.2–12.) keV energy band is shown in Fig. 7.14.

Predicted transient source classes

For the classification of the 136 transients we used the same training sample as before (see Sect. 7.3). The spectral data was provided by the work package WP4. Hardness ratios were derived equivalently to the standard method for the 3XMM using Eq. 4.1.3. We use spectral and multiwavelength features which were derived in the same way as described in Sect. 7.4. From the timing analysis of the transient sources (performed by WP3), the fractional variability amplitude as well as the count rate average were available. For 57 transient sources no reliable timing features could be extracted.

We then trained the algorithm as described in Sect. 7.6 with spectral and multiwave-

Table 7.11.: Distribution of transients per class and classification model.

Model	BL	CV	HMXRB	LMXRB	S1	S2	STAR	ULX	not classified
Spectral	0	6	2	0	30	87	10	0	1
Timing	0	33	0	0	12	20	13	0	58

length features and including only the above named timing features. As in classification of the 3XMM test sample, the spectral (model C, with spectral and multiwavelength features) and timing model (model D, with spectral, multiwavelength, and additional timing features) were applied to the transient catalogue.

The prediction error for the two models are 2.63% for the spectral and 2.46% for the timing model. Using the spectral model 135 out of 136 transients were classified. For the timing model the fraction decreases to 78 of the 136 sources. The class distribution is listed in Table 7.11. The unclassified source consists of those 57 transients without reliable timing features and the one which already showed peculiar spectral properties. Table A.7 lists the possible source types for those 58 transients as predicted by the spectral model.

Table 7.12 lists all class probabilities (derived from the timing model) for all sources for both models agree on the same source type. We note, however, that the significance of classification per source is only 25-60%. In many cases, the highest probability is only marginally higher than for other source types (e.g., TID 6). A list of transients which changed source type from one model to the other is given in Table 7.13. Except for TID 65, all transients switched from an extragalactic source type to a Galactic one (mostly from Seyferts to CV or STAR). The Galactic origin is supported by the spatial distribution of the transients (see Figs. 7.15). This may not necessarily be the case for those 58 transients that could not be classified, as they are not concentrated in the Galactic plane.

Table 7.12.: List of predicted class probabilities from the timing model, for EXTraS transients equally classified in the spectral and timing model.

TID ¹	BL	CV	LMXRB	HMXRB	STAR	S1	S2	ULX	pred. class
4	0.00	0.26	0.06	0.01	0.05	0.35	0.15	0.12	S1
6	0.01	0.27	0.03	0.01	0.18	0.17	0.30	0.03	S2
10	0.01	0.23	0.01	0.02	0.17	0.19	0.31	0.06	S2
14	0.00	0.18	0.01	0.02	0.12	0.19	0.41	0.07	S2
16	0.01	0.13	0.07	0.04	0.38	0.09	0.15	0.12	STAR
17	0.05	0.17	0.01	0.01	0.56	0.08	0.07	0.04	STAR
18	0.01	0.24	0.01	0.01	0.18	0.25	0.24	0.07	S1
28	0.03	0.08	0.00	0.00	0.04	0.29	0.54	0.00	S2
30	0.01	0.29	0.03	0.00	0.07	0.33	0.19	0.08	S1
32	0.00	0.07	0.06	0.01	0.38	0.17	0.29	0.02	STAR

¹ unique transient identifier, see Table A.6. For continuation of the table see next page

Table 7.12.: continued

TID ¹	BL	CV	LMXRB	HMXRB	STAR	S1	S2	ULX	pred. class
38	0.02	0.19	0.03	0.00	0.14	0.43	0.10	0.09	S1
43	0.00	0.58	0.01	0.05	0.12	0.09	0.14	0.00	CV
49	0.00	0.28	0.03	0.04	0.10	0.16	0.34	0.05	S2
50	0.00	0.15	0.02	0.03	0.19	0.22	0.29	0.09	S2
57	0.01	0.14	0.18	0.00	0.50	0.06	0.09	0.02	STAR
59	0.00	0.14	0.01	0.05	0.23	0.22	0.28	0.06	S2
62	0.01	0.34	0.01	0.03	0.05	0.19	0.36	0.02	S2
74	0.01	0.23	0.06	0.04	0.20	0.14	0.30	0.02	S2
75	0.00	0.30	0.05	0.01	0.11	0.34	0.17	0.03	S1
76	0.02	0.22	0.05	0.02	0.27	0.12	0.28	0.02	S2
78	0.01	0.25	0.02	0.10	0.17	0.14	0.29	0.03	S2
79	0.01	0.12	0.01	0.05	0.21	0.14	0.40	0.06	S2
81	0.00	0.43	0.01	0.06	0.08	0.15	0.24	0.01	CV
83	0.00	0.12	0.09	0.01	0.25	0.14	0.32	0.07	S2
89	0.01	0.26	0.01	0.10	0.15	0.13	0.31	0.03	S2
90	0.00	0.25	0.05	0.00	0.13	0.30	0.17	0.09	S1
92	0.01	0.20	0.06	0.05	0.16	0.17	0.35	0.00	S2
98	0.01	0.21	0.04	0.02	0.27	0.14	0.28	0.03	S2
100	0.01	0.31	0.01	0.04	0.10	0.14	0.32	0.06	S2
101	0.01	0.28	0.01	0.01	0.13	0.19	0.29	0.07	S2
121	0.03	0.33	0.01	0.04	0.15	0.16	0.23	0.06	CV
123	0.01	0.27	0.02	0.06	0.09	0.22	0.31	0.02	S2
125	0.01	0.22	0.01	0.00	0.04	0.52	0.17	0.02	S1
128	0.03	0.37	0.00	0.09	0.11	0.14	0.22	0.02	CV
129	0.02	0.19	0.00	0.00	0.03	0.57	0.17	0.01	S1
132	0.02	0.27	0.02	0.02	0.17	0.31	0.16	0.03	S1
133	0.04	0.15	0.00	0.04	0.46	0.11	0.16	0.04	STAR
134	0.02	0.27	0.01	0.01	0.03	0.49	0.16	0.02	S1
135	0.03	0.38	0.01	0.00	0.04	0.38	0.13	0.03	S1

Notes: ¹ unique transient identifier, see Table A.6.

7.9. Summary and future work

In this chapter, I presented a first automated classification of the EXTraS transient source catalog. From a pre-release of the 3XMM-DR6, which contains more than 130 000 detections of X-ray sources, we constructed a training sample. The selection of sources with known source classification was based on the work by Lo et al. (2014) and Farrell et al. (2015). We extended the sample by adding sources from public source catalogs, in order to differentiate further between BL lac objects and Seyfert galaxies as well as

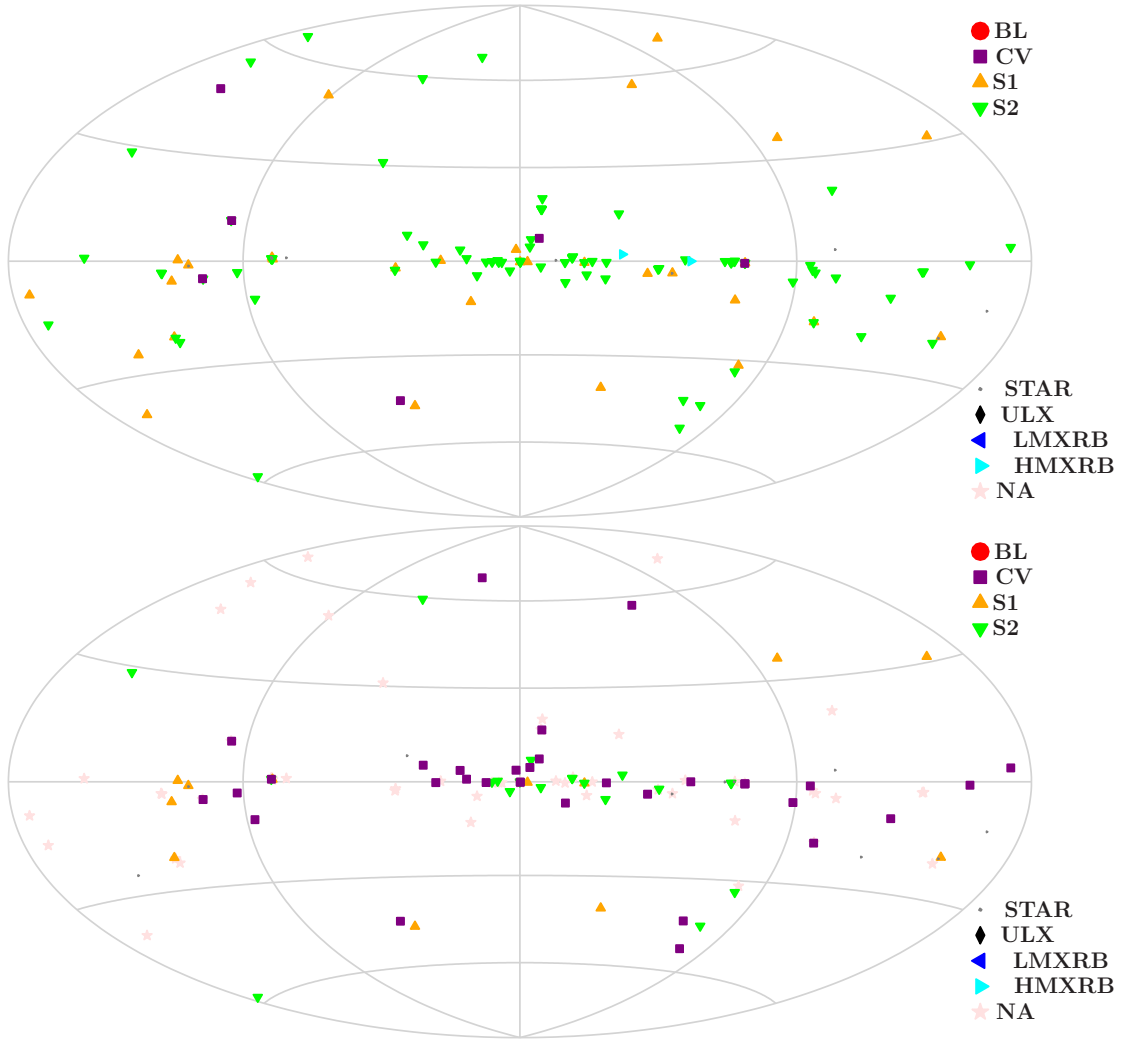


Figure 7.15.: Distribution of the classified transient sources in Galactic coordinates for the spectral (*top*) and timing (*bottom*) model.

between low-mass and high-mass XRBs. The final training sample was more balanced out with respect to the number of sources per source class and contained more than three times as many sources as the sample by Farrell et al. (2015). The 8 source classes regarded in our investigation reflect the most important ones for X-ray sources.

In order to obtain classification features, we performed a comprehensive spectral and timing analysis on the *XMM-Newton* EPIC data of each 3XMM detection. Positional cross-matches were used to find multiwavelength counterparts from which we calculated multiwavelength indices. Using a RF classifier, we obtained the lowest misclassification rate using a combination of spectral, multiwavelength and timing features. The classification of a test sample composed of 3XMM sources not in the training sample showed that

Table 7.13.: Difference matrix for classification with spectral and timing model.

	BL	CV	HMXRB	LMXRB	S1	S2	STAR	ULX	NA
BL	-	0	0	0	0	0	0	0	0
CV	0	-	0	0	0	0	0	0	2
HMXRB	0	1	-	0	0	1	0	0	0
LMXRB	0	0	0	-	0	0	0	0	0
S1	0	3	0	0	-	0	2	0	14
S2	0	16	0	0	1	-	5	0	35
STAR	0	0	0	0	0	0	-	0	6
ULX	0	0	0	0	0	0	-	-	0

Note: Difference between classifying with the spectral and timing model. Rows indicate the source types of spectral model, while column represent the predicted types using the timing model.

the algorithm was able to identify distinct regions in the multidimensional parameter space and predicted source classes with high probability. The spational distribution from the test sample was consistent with the expectations based on the distribution of the training sources and other studies of the earlier releases of the *XMM-Newton* serendipitous source catalog.

Although, the classification works well, there are a few issues, that we plan to improve in an ongoing investigation. The application of the prediction model to datasets of unknown response showed that the timing features used in this study are only weak classifiers. From the 3XMM test sample there are $\sim 40\%$ sources which could not be classified when the timing features are included. In comparison, for models without timing features 98% of the test sample is classified. This issue implies that we are missing training examples in order to cover all possible (timing) parameter combinations. In addition, contradicting features combinations may come from low signal-to-noise (spectral or timing) data (e.g., faint sources or transients). In the current classification model, we have not used the information of parameter uncertainties. The implementation of those is planned in a future step, which may improve the classification of sources and reduce the number of unassigned sources. For example, one could introduce a weighting of parameter features based on their relative uncertainty. We will invest how the classification changes by only taking into account high-snr data and implement parameter uncertainties. In particular, this is important for the search of outliers, i.e. sources which show anomalies and do not fully fit to any of the source types. Outliers of common source types are of special interest in order to find rare source types which harbour the possibility of new scientific discoveries.

The training process showed that source confusion mainly occurs between CVs, Seyfert galaxies, and STARS. A similar issue has been observed in other studies that used decision trees or RF classifiers (e.g., Richards et al. 2011; Farrell et al. 2015). Since timing features do not play a major role in the classification, the confusion of these sources may, on one hand, indicate a large similarity in the spectral and multiwavelength features among them. On the other hand, these source types make up the highest contribution of sources

in the training sample (from 7% for CVs up to 51% for S1), while the other half of classes contribute only 6% in total. Hence, even though we oversampled the minority classes in order to balance out the training sample, the algorithm preferred former majority classes for unidentified sources. This issue shows that the composition of the training sample needs to be improved, which can be done by oversampling the minority classes while carefully undersampling the majority classes at the same time and, subsequently, reducing the fraction of synthetic data sets. The balancing of multi-dimensional class problems is still under investigation. There are a few first algorithms for this task (e.g., SCUT, Agrawal et al. 2015). An alternative is to improve the composition of the original training sample by adding more observations of BL, XRB, and ULX sources and increase the parameter space of these source types.

In a final step, we applied the prediction model to the EXTraS transient source catalog and yield the first tentative source classification for these objects. Even though the overall significance of the classification was rather low, there were a few cases for which the class probability was higher than 50%. In total, $\sim 60\%$ of the catalog could be classified based on their spectral and temporal properties. We provide low-significance predictions for the remaining 40%, which for which only spectral properties were available. Transient TID 66 could not be classified in neither of the prediction models and is of particular interest. Follow-up investigation in this source are necessary to investigate the nature of this source. The spational distribution of the transient sources indicated a Galactic origin. This origin was supported by the predicted classification from the RF: almost 60% of the transients were classified as cataclysmic variable or star. Hence, our characterization can be used to make estimations and predictions on the source properties. A comparison with follow-up observations of these sources can yield further insight in their nature.

8. Unveiling the nature of PKS 2004–447

This chapter focusses on the analysis of the peculiar active galaxy PKS 2004–447. This X-ray source is part of the EXTraS training sample (EXTraS source ID 36 527) and was classified as Seyfert 1 galaxy by Farrell et al. (2015) based on its X-ray spectrum. Although, overall its classification is unclear and has long been under debate in the literature. PKS 2004–447 is also among a handful of intriguing γ -ray emitting radio-loud Narrow-Line Seyfert 1 galaxy (γ -NLS1, see Sect. 3.1.2) that has been detected by *Fermi*-LAT (Abdo et al. 2009c). The association with γ -NLS1 further supports the peculiarity of its nature: the discovery of γ -ray emission in radio-loud NLS1 confirms the existence of highly relativistic particles within a jet in these sources and challenges the well-accepted paradigm of AGN jet production (e.g., Chiaberge & Marconi 2011). As γ -NLS1 share properties of both radio-loud and quiet AGN they provide intriguing new insight in the population of γ -ray emitting AGN.

In order to study this peculiar object and gain more information on the properties of γ -NLS1, collaborators and I have set up a multiwavelength monitoring campaign, which I will describe in Sect. 8.2. The X-ray data analysis resulting from this program is the topic of Sect. 8.3. It is heavily based on Kreikenbohm et al. (2016, hereafter Kr16), where this research has first been published. The following Sects. 8.4 and 8.5 pay a closer look at the multiwavelength picture of PKS 2004–447 and puts the results in context with different source types of radio-loud AGN. Finally, Sect. 8.6 of this chapter gives a summary and outlook on further investigations on this matter.

8.1. Oh PKS 2004–447, what are thou?

The active galaxy PKS 2004–447 is located on the Southern Hemisphere at a redshift $z = 0.24$ (Drinkwater et al. 1997), which corresponds to a distance of ~ 1.2 Gpc. Among the sample of γ -NLS1, the source stands out for being the radio-loudest source so far and furthermore because its classification as NLS1 is still discussed in the literature. Oshlack et al. (2001, hereafter Osh01) first characterized the source as very radio-loud NLS1 based on its optical spectrum. The strong forbidden line emission depicted by the line flux ratio $[\text{O III}]/\text{H}\beta = 1.6$ and the narrow width of the broad Balmer lines of $\text{FWHM}(\text{H}\beta) = 1447 \text{ km s}^{-1}$ are consistent with the formal definition of NLS1. But the weak Fe II emission, $\text{FWHM}(\text{Fe II}) \leq 10 \text{ \AA}$, is unusual for this type of AGN (e.g., Boroson & Green 1992). Since then, PKS 2004–447 has been targeted by a number of different observation campaigns and sample studies which picked up on this matter (e.g., Sulentic et al. 2003; Zhou et al. 2003; Gallo et al. 2006; Komossa et al. 2006; Yuan et al. 2008; Abdo et al. 2009a). For example, Sulentic et al. (2003) suggest a type 2 AGN classification

after analysing Fe II emission in a sample of radio-loud AGN. In contrast, Zhou et al. (2003) and Komossa et al. (2006) proposed PKS 2004–447 might be a narrow-line radio galaxy. Overall the issue remains unresolved and PKS 2004–447 is usually regarded as nontypical NLS1.

In radio, the source has been listed in the Parkes Half-Jansky Flat-Spectrum catalog (PKSCAT90, Wright & Otrupcek 1990) as flat-spectrum source with a radio flux of 0.81 Jansky at 2.7 GHz and a spectral index of $\alpha_r = 0.36$ in the (2.7–5) GHz band (Drinkwater et al. 1997). In contrast, using the Australian Telescope Compact Array (ATCA), Osh01 find evidence for a steep spectral index of $\alpha_r = 0.67$ between $\sim (2\text{--}10)$ GHz as well as long-term radio flux variability on timescales of years. The ATCA image is unresolved at these frequencies, restricting its angular size to ≤ 3.6 mas or ~ 85 pc for the given redshift z . These properties are associated with Compact Steep Spectrum (CSS) or GHz-peaked sources (GPS), which are most likely objects with young jet-activity (Berton et al. 2015; O’Dea 1998). G06 support these properties using both ATCA observations as well as single-dish monitoring with the Ceduna radio monitoring campaign. They find a spectral index of $\alpha_r = 0.52$ between $\sim (2\text{--}17)$ GHz, which is constant over the course of six months, as well as evidence for moderate longterm radio flux variability. Furthermore, they report on possible short-term variability, when the 6.65 GHz flux rose for $\sim 35\%$ over 19 days, although the authors favour an extrinsic cause, e.g. interstellar scintillation, over a change of intrinsic properties.

In the sample of γ -NLS1 as well as radio-loud NLS1, PKS 2004–447 is peculiar in terms of its very high radio loudness R (Kellermann et al. 1989). The $R = f_{4.9\text{GHz}}/f_B$ describes the ratio of the radio to optical flux. Depending of the optical magnitude, Osh01 find a range of $1700 \leq R \leq 6320$, whereas G06 observed $R = 3800$ using simultaneous measurements both bands. Recently, using the 1.4 GHz flux, Foschini (2011) reports a radio loudness $R = 6358$.

Based on the empirical relation between BLR size and optical luminosity (Kaspi et al. 2000), Osh01 estimate the black hole mass from $H\beta$ line dynamics to be $\sim 10^{6.7} M_\odot$ (using high-resolution data from the Siding Spring 2.3 m Telescope). This puts PKS 2004–447 at the upper M_{BH} range of NLS1, but still at the lower end of radio-loud AGN masses (e.g., Laor 2000). However, the described method may underestimate the black hole mass due to scaling effects of the BLR geometry and orientation (e.g., Calderone et al. 2013). By analysing the polarized $H\alpha$ line Baldi et al. (2016) find $\text{FWHM}(H\alpha) \sim 9000 \text{ km s}^{-1}$, corresponding to a black hole mass of $\sim 10^{8.7} M_\odot$, which is in line with masses from radio-loud AGN (e.g., Chiaberge & Marconi 2011).

In the soft X-ray band, the source exhibits longterm variability on timescales of years (e.g., G06; Paliya et al. 2013). Analysing high signal-to-noise *XMM-Newton* data, G06 also find evidence of short-term variability on the timescale of a few ks. The (0.3–10) keV spectrum is consistent with a single power law with a relatively hard photon index of $\Gamma \sim 1.5$. However, G06 also find hints of a soft excess below 1 keV, in which case the power law takes on a slightly harder photon index of ~ 1.4 . Based on SED fitting, the authors associate the tentative soft excess emission with weak self-synchrotron Compton emission from a jet whereas the dominant power-law contribution might come from Comptonized

disk emission. Such soft excesses are commonly seen in radio-quiet NLS1. It has been observed for CSS sources but it is rather rare in blazar-like objects, for the X-ray spectrum is dominated by jet emission.

PKS 2004–447 was among the first four γ -NLS1 that were detected in the MeV–GeV energy range by *Fermi*-LAT within the first year of operation (Abdo et al. 2009c). Since then it has been listed in every *Fermi*-LAT source catalog (Abdo et al. 2010a; Nolan et al. 2012; Acero et al. 2015). The latest *Fermi*-LAT 4-year point source catalog (3FGL) lists the 3FGL J2007.8-4429 as counterpart for PKS 2004–447, with a (0.1–100) GeV photon flux of 5.6×10^{-10} photons $\text{cm}^{-2} \text{s}^{-1}$ and a simple power-law photon index of $\Gamma \sim 2.5$. Paliya et al. (2014) find evidence of moderate flux variability in the (0.1–300) GeV band as well as hints of spectral softening when the γ -ray fluxes increased between two detections with a binning of 30 days over the course of ~ 14 months.

Summarizing, PKS 2004–447 exhibits flux variability on timescales of years across the whole electromagnetic spectrum and possible short-term variability is seen from radio up to X-ray measurements. The literature reports on contradicting properties for the radio spectrum as well as the black hole mass of PKS 2004–447 and the composition of the X-ray spectrum is still unclear. While the optical spectrum and X-ray characteristics are consistent with NLS1 galaxies, the strong radio power and presence of γ -ray emission suggest a rather blazar-like nature. The existence of a relativistic jet still needs to be confirmed with high-resolution radio images. As part of an elusive sample of a new population of γ -ray emitting AGN, PKS 2004–447 requires further investigation of its spectral characteristics in order to provide more information on its nature and the properties of γ -NLS1.

8.2. The multiwavelength campaign

We have set up a multiwavelength monitoring campaign from optical to γ -rays over several months and performed additional high-angular resolution very long-baseline interferometry (VLBI) observations within the TANAMI program. These images allow for an unprecedented view of the jet structure in this source at milliarcsecond resolution. The objective of this campaign is multi-fold: pin-down the radio jet structure with VLBI images, carefully analyse the radio and X-ray emission properties with respect to its composition and spectral variability, and compute a number of quasi-simultaneous SEDs to test for changes on timescales of months.

VLBI radio observations at 8.4 GHz have been performed since October 2010 as part of the TANAMI VLBI program, after PKS 2004–447 was detected by *Fermi*-LAT. Its low declination makes it an ideal target for the Southern Hemisphere program. TANAMI tracks the radio spectrum and the structural evolution of the parsec-scale radio-jet emission before, during and after the optical/UV/X-ray campaign. In addition, the source has been observed several times at frequencies between 1.4–17.9 GHz by ATCA. Results are discussed in Schulz et al. (2016) and briefly summarized in Sect. 8.4.

We use the space observatories *XMM-Newton* and *Swift*, which are most sensitive in the soft X-rays and provide additional optical/UV coverage. Since G06 indicated mild

variability of the radio flux on a timescale of half year period and both short and longterm variability of the X-ray emission, we obtained two long *XMM-Newton* observations separated by ~ 5 months in 2012. We fill up the gap of these high-sensitivity pointings with *Swift* snapshots of ~ 1 –5 ks exposure each. The *Swift* observations were continued in May 2013, when the next *XMM-Newton* observation of PKS 2004–447 was scheduled, until the end of 2014. These data provide additional information on the longterm behaviour. The monitoring is complemented by simultaneous γ -ray observations of the *Fermi*-LAT satellite. Together, these observations by TANAMI, ATCA, *XMM-Newton*, *Swift*, and *Fermi*-LAT produce a 5-months dynamic SED from the radio to γ -ray energy range.

8.3. The X-ray view

In this section I describe the analysis of the X-ray spectrum of PKS 2004–447. It was first published in and is partly taken verbatim from Kreikenbohm et al. (2016, hereafter Kr16). However, this section also provides the analysis of new *Swift* data from 2016 and an improved analysis of the hardness ratios.

Methods and routines for X-ray imaging data reduction are described in Sect. 4.1.2. Methods for spectral and timing analysis are described in Sect. 5. Unless stated otherwise, uncertainties correspond to 90% confidence limits for one parameter of interest ($\Delta\chi^2 = 2.7$). In the following, the "standard" cosmological model ($H_0 = 73 \text{ km s}^{-1} \text{ Mpc}^{-1}$, $\Omega_M = 0.3$, and $\Lambda = 0.7$) is assumed.

Observations

The *XMM-Newton* visibility window of PKS 2004–447 in AO12 lasted from May until end of October 2012. The two *XMM-Newton* pointings took place at the beginning and end of this window and were separated by five months. Four *Swift* observations took place in between. We have continued observations with *Swift* in 2013 and 2014. To study the longterm behavior of PKS 2004–447, archival data from *XMM-Newton* and *Swift* prior to May 2012 have been included in the analysis as well as data from 2016 that were taken after the end of our campaign. Detailed information on all observations is provided in Table 8.1.

We observed PKS 2004–447 with *XMM-Newton* in 2012 for 37.9 ks on 2012 May 1 and for 39.9 ks on 2012 October 18, hereafter referred to as X-2012-05-01 and X-2012-10-18. We searched the *XMM-Newton* Science Archive¹ for archival data and found a pointing performed on 2004 April 11 (for 41.9 ks, X-2004-04-11 hereafter) which was already used in Chapter 7 for the analysis within the EXTraS project. It has first been discussed by G06 and is reanalysed in this investigation.

All observations were performed with the European Photon Imaging Camera (EPIC) using PN and MOS CCD arrays and the Reflecting Grating Spectrometer (RGS), as well as the Optical Monitor (OM). The EPIC operated in full-frame mode with the medium filter in 2004 and the thin filter in both observations in 2012. All data were reduced

¹*XMM-Newton* Science Archive: nssa.esac.esa.int/

Table 8.1.: Details of all *XMM-Newton* and *Swift* observations of PKS 2004–447.

Inst-ObsDate	ObsId	Duration	Net exposure	Spectrum counts
(1)	(2)	[ks]	[ks]	[counts]
(1)	(2)	(3)	(4)	(5)
X-2012-10-18	0694530201	39.8	34.5	10788
X-2012-05-01	0694530101	37.9	36.5	6125
X-2004-04-11	0200360201	41.9	38.4	15831
S-2016-05-07	000324920[18,19] ^a	8.0	7.9	252
S-2014-03-14	000324920[16,17] ^b	17.2	17.1	248
S-2013-11-19	000324920[14,15] ^c	17.7	16.7	523
S-2013-10-13	000324920[09-13] ^d	16.5	16.5	302
S-2013-09-27	00032492007	8.3	8.3	234
S-2013-07-07	0003249200[5,6] ^e	23.1	23.0	444
S-2012-09-30	00032492004	6.0	6.0	63
S-2012-09-12	00032492003	5.4	5.4	63
S-2012-07-22	00032492002 ^f	2.3	-	-
S-2012-07-03	00032492001	4.9	4.9	67
S-2012-03-14	00091031007	7.3	7.3	60
S-2011-11-15	00091031006	7.1	7.1	73
S-2011-09-17	00091031005	7.5	7.34	167
S-2011-07-29	00091031004 ^f	1.6	-	-
S-2011-07-25	00091031003 ^f	0.6	-	-
S-2011-07-14	00091031002	5.0	4.9	56
S-2011-05-15	00091031001	6.8	6.8	61

Note: (1) Instrument and observation date. We use the format Inst-yyyy-mm-dd: X - *XMM-Newton* EPIC, S - *Swift* XRT. (2) Observation identifier. (3) Observation duration. (4) Net exposure time after screening for flaring particle background. (5) Background-subtracted total number of counts in the (0.2–10) keV band. **Merged observations:** ^a00032492018 (2015-05-07, 3.0 ks) and 00032492019 (2016-05-11, 5.0 ks). ^b00032492016 (2014-03-14, 7.6 ks) and 00032492017 (2014-03-16, 9.7 ks). ^c00032492014 (2013-11-19, 5.5 ks) and 00032492015 (2013-11-20, 12.2 ks). ^d00032492009 (2013-10-13, 4.7 ks), 00032492010 (2013-10-20, 4.11 ks), 00032492011 (2013-10-27, 2.35 ks), 00032492012 (2013-10-29, 1.51 ks), and 00032492013 (2013-11-03, 3.88 ks). ^e00032492005 (2013-07-07, 11.4 ks) and 00032492006 (2013-07-14, 11.6 ks). ^fBecause of the relatively short exposure time, this observation was not included in the analysis.

following standard methods. Details on EPIC data sets are listed in Table 8.1. The RGS data had insufficient counts for a dedicated spectral analysis and is be discussed in this work.

Additionally, we monitored PKS 2004–447 with the *Swift* X-ray telescope (XRT) from the beginning of 2012 through the beginning of 2014. We used archival data from 2011, which were discussed by Paliya et al. (2013) and two new observations from 2016. Details of each observation are listed in Table 8.1. Three observations had relatively short expo-

sures (2.3 ks, 1.6 ks, and 0.6 ks). Owing to the low SNR in the respective X-ray spectra, they are not considered in our analysis. For all other observations, we used data from the XRT, which operated in photon-counting mode (PC). The data were reduced following standard methods. To increase the SNR of the spectra, *Swift* observations that were observed within a few days of each other were merged after checking that the spectra did not show significant flux or spectral variability between the averaged epochs.

The high-SNR X-ray spectrum with *XMM-Newton*/EPIC

Visual inspection of the *XMM-Newton* data reveals a flat and smooth spectrum for each observation (see Fig. 8.1.) The source is detected from 0.5 keV to 10 keV with sufficient spectral data counts to allow spectral modelling. We first adopted a phenomenological power-law model (`pegpwlw`) which is affected by Galactic HI absorption $N_{\text{H,Gal}} = 2.9 \times 10^{20} \text{ cm}^{-2}$, based on the Galactic Hydrogen LAB survey (Kalberla et al. 2005). The high-resolution ISM absorption model `tbnew` (Wilms et al. 2000) is used to account for neutral absorption. Cross-sections and abundances were taken from Verner et al. (1996) and Wilms et al. (2000), respectively.

Owing to the large number of spectral data counts we group the data to a SNR of 5 per energy bin. This ensures a Gaussian distribution of photons within each energy bin and allows for the use of χ^2 -statistics. For each observation, we simultaneously fit the available PN and MOS data in the (0.5–10) keV energy range. In order to take in to account the difference in effective area, we include a constant for each detector. With respect to PN, count rates of MOS1 and MOS 2 are $\sim 8\%$ lower, which is consistent with results of calibration runs (Read et al. 2014).

The absorbed power-law model yields a good fit to each spectrum. Best-fit results for the photon index Γ lie between 1.48 and 1.62. We find no evidence of intrinsic absorption. The upper limit of the column density is $N_{\text{H}} \leq 1.8 N_{\text{H,Gal}}$. This parameter is therefore fixed to $N_{\text{H,Gal}}$ to reduce the number of free parameters, which enables to better constrain the photon index. In the following, unless stated otherwise, all spectral models mentioned in this section include the Galactic absorption component with fixed column density. The *XMM-Newton* spectra are shown in Fig. 8.1, along with their best-fit models (solid line). We determine the unabsorbed energy flux in different energy bands, i.e., total band (0.5–10) keV, soft band (0.5–2) keV, and hard band (2–10) keV. For each spectrum, we perform three independent fits by taking only data within each respective band into account and compute the respective flux from this fit. The sub-bands are defined based on typical flux ranges used in the literature to facilitate comparison. The best-fit parameters and absorption-corrected fluxes of the fit are listed in Table 8.2.

In Seyfert galaxies a presence of an Fe $K\alpha$ fluorescent line is an indicator and valuable diagnostic tool of X-ray reprocessing from the material around the X-ray source (e.g., Fukazawa et al. 2011). In order to search for spectral iron line emission features, we add a narrow Gaussian line for neutral Fe $K\alpha$ emission at 6.4 keV ($\sigma_{6.4 \text{ keV}} = 1$). This component is not significant ($\Delta\chi^2 = -0.1$ for one additional free parameter). We measure an upper limit for the equivalent width of this line and find $EW_{6.4 \text{ keV}} \leq 60 \text{ eV}$ in all three observations. This value is consistent with results of G06.

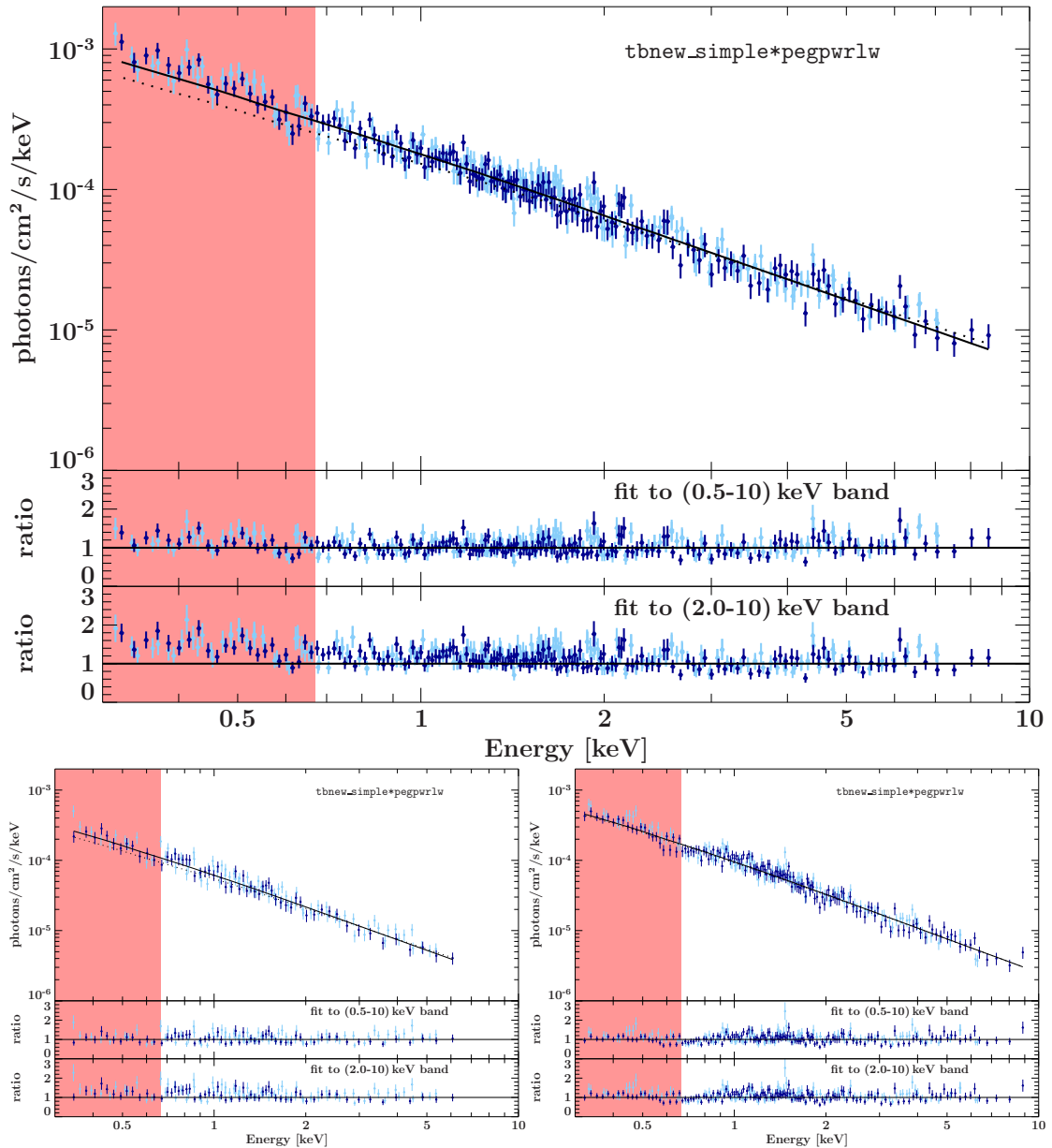


Figure 8.1.: *XMM-Newton* spectrum and best-fit results of X-2004-04-11X-2012-05-01 (*left*) and X-2012-10-18 (*right*). *Upper panel*: EPIC pn (blue) and MOS (lightblue) data, as well as corresponding best fits for an absorbed power law evaluated over (0.5–10) keV (black solid line) and (2–10) keV (black dashed-dotted line). *Mid panel*: Data-to-model ratio for the best fit over the whole (0.5–10) keV energy range. *Lower panel*: Respective residuals for fitting the (2–10) keV energy range alone, extrapolated to lower energies. The red shaded region marks the region of a tentative soft excess in X-2004-04-11.

In G06 the authors report indications of a weak soft excess below ~ 1 keV. They find that a broken power law with a spectral break at ~ 0.6 keV. Consequently, we search for the existence of such a soft excess in our data and model the spectra only above 2 keV and extrapolating the best fit down to 0.5 keV. No significant excess emission is observed in the case of X-2012-05-01 or X-2012-10-18, but the residuals suggests a possible soft excess in the data of X-2004-04-11 (see Fig. 8.1). If the additional component matches a power-law shape (e.g., synchrotron emission or thermal comptonization of a denser region) the superposition with the hard power law would match a broken power law. The spectra of all three *XMM-Newton* observations are therefore modeled with a broken power law. Fit results for the broken power law are summarized in Table 8.3. We note that results for the soft photon index Γ_1 are not well constrained because of the narrow energy range from 0.5 keV to the break energy. For X-2004-04-11, the model provides a slightly better fit than the simple power law. The best-fit parameters are consistent with results by G06, except for the soft photon index Γ_1 , which cannot be constrained well. For X-2012-05-01 it is not possible to constrain either of the photon indices when we leave the break energy free to vary. Hence, we fix it to 0.6 keV as reported in G06, which helps to constraint both Γ_1 and Γ_2 . The fit of X-2012-10-18 yields good constraints, however the break energy is significantly higher than in G06. Within its uncertainties, the hard photon index Γ_2 is roughly consistent with Γ of the single (0.5–10) keV power law in all three observations. Although, Γ_1 suggests a flattening rather than a steepening towards lower energies. This trend is rather uncommon for soft excess emission.

We test the significance of the broken power-law model and apply the F-test, where the null-hypothesis model assumes a simple power-law spectrum. A broken power-law model is considered to be significantly different from the null-hypothesis if the probability that the later is correct is less than 1% (expressed by the F-test probability p). The p -values for each data set are listed in Table 8.3. For X-2012-05-01 and X-2012-10-18, both models are statistically indistinguishable and the simple power law is sufficient to represent the data. Whereas for X-2004-04-11, the broken power law gives a slightly better fit than the simple power law. The p -value suggests that the data is inconsistent with the null hypothesis at 1% significance level. Thus, the presence of a weak soft excess is tentative. It is, however, striking that no excess is detected in the observation in 2012. Since background levels are consistent with each other in all three observations, a contribution of systematic background variations to the soft X-rays, which could mimic or cancel out a soft excess, can be excluded.

Since the origin of the soft excess is still unclear for unobscured AGN and is often modeled phenomenologically with a blackbody for a first characterization. There is a range of physical descriptions of this component (e.g. Comptonized continuum emission, bremsstrahlung, ionized reflection). In case of blazars, these components are not expected to pay a significant contribution because the beamed jet emission would outshine any of these features. Instead, soft excess emission is usually associated with synchrotron emission of the most energetic leptons in the jet. Recently, Kammoun et al. (2017) found evidence for bulk comptonization in blazars (e.g., Begelman et al. 1987; Sikora et al. 1994; Celotti et al. 2007) which provides an alternative explanation for excess

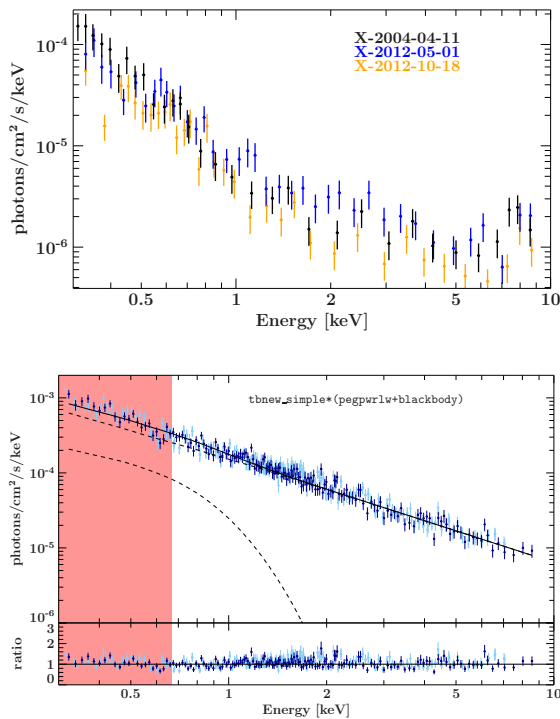


Figure 8.2: Comparison of the EPIC pn background spectra of all three *XMM-Newton* observations. No significant variation is observed that could mimic or contribute to a soft excess.

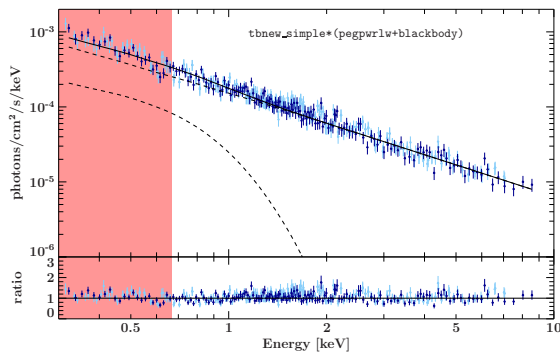


Figure 8.3: *XMM-Newton* spectrum of X-2004-04-11 with blackbody component. *Upper panel:* EPIC pn (blue) and MOS (lightblue) data, total model for an absorbed power law plus blackbody (black solid line) model components (black dashed line). *Mid panel* Data-to-model ratio for the best fit.

emission in these objects. Non-relativistic leptons travelling with a bulk Lorentz factor Γ_{Bulk} interact with photons from the accretion disk, photons scattered by free electrons external to the jet, and those reprocessed in the BLR. The comptonized spectrum from BLR photons resembles a black body that is expected to contribute to the soft X-ray range (Kammoun et al. 2017).

Accordingly, we estimate the contribution of such a component by assuming a superposition of a blackbody and a simple power law. The power law fit is performed in the (2–10) keV band and parameters are subsequently fixed to the best-fit parameters in this band (see Table 8.4). After fixing these parameters, we fit the remaining soft X-ray emission with a blackbody. This model yields a good fit of $\chi^2/\text{d.o.f.} = 396.4/398$. The contribution of the blackbody to the (0.5–2) keV flux is $(0.06 \pm 0.01) \times 10^{-12} \text{ erg cm}^{-2} \text{ s}^{-1}$, which makes up 10-20% of the power-law flux in the soft band. We apply the same fit to the data of 2012 (see Table 8.4) where no soft excess has been observed. The fits are acceptable and yield a contribution of the blackbody to the soft band between 5% and 20% of the power-law flux in the same band. We note that for these fits, the power law is slightly steeper, which may in principle hide the presence of a faint extra component.

Another way to test whether X-2004-04-11 carries an extra component with respect to 2012 is to compute the difference spectrum: by subtracting the background-subtracted EPIC PN spectra of X-2012-10-18 and X-2012-05-01 from the one of X-2004-04-11, respectively, we create two difference spectra (see Fig. 8.5). These spectra are rebinned in the same way as the original data. Consequently, no spectral bins are regarded above 7 keV, because the number of spectral data counts of the X-2012-05-01 spectrum de-

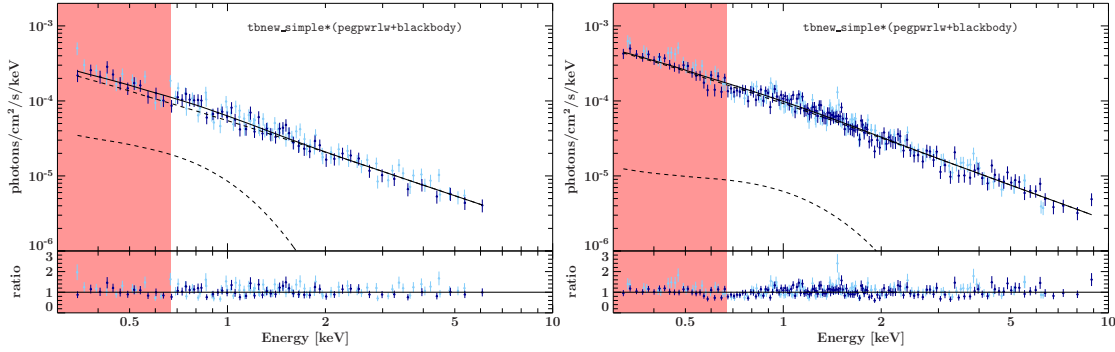


Figure 8.4.: *XMM-Newton* spectrum of X-2012-05-01 (top) and X-2012-10-18 (bottom) with blackbody component. *Upper panel* EPIC pn (blue) and MOS (lightblue) data, total model for an absorbed power law plus blackbody (black solid line) model components (black dashed line). *Mid panel* Data-to-model ratio for the best fit.

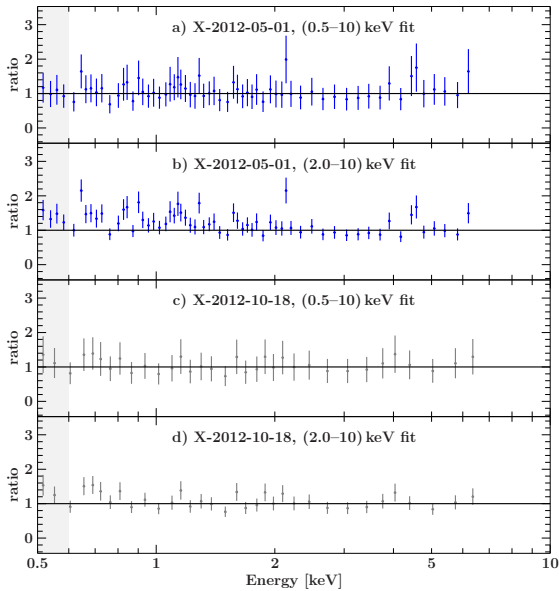


Figure 8.5: *XMM-Newton* ratio of the *XMM-Newton* EPIC PN difference spectra to a power-law model. Difference spectra were created by subtracting the background-subtracted spectra of X-2012-05-01 (blue) and X-2012-10-18 (black) from the one of X-2004-04-11. Simple power-law fits were performed on the energy ranges (0.5–7) keV and (2.0–7) keV, where the fit to the later band was then extrapolated to lower energies.

creases rapidly in this range. We fit the difference spectra with a model of Galactically absorbed power law to each of the (0.5–7) keV and (2–7) keV bands (see Table 8.5). Since the spectra of 2012 appear to show a steeper spectrum, we expect a slightly flatter Γ in the (2–7) keV range because less counts are subtracted in the hard energy band. Even though, it should be roughly consistent with those found in spectral analysis.

In the total range, the best-fit parameters of both difference spectra are consistent with those of X-2012-10-18 and X-2012-05-01 within 90% uncertainties. The best-fit values of the photon indices are slightly flatter. This is expected if the spectrum of X-2004-04-11 is harder than in 2012. Fitting only the hard band and extrapolating the fit into the soft band, a soft excess is not observed in the difference spectra, as illustrated in Fig. 8.5.

Table 8.2.: Best-fit results of the absorbed power-law model for *XMM-Newton* and *Swift* spectra.

Inst-ObsDate (1)	Γ (2)	$F_{0.5-10\text{keV}}$ (3)	$F_{0.5-2\text{keV}}$ (4)	$F_{2-10\text{keV}}$ (5)	stat/dof (statistic) (6)
X-2012-10-18	$1.60^{+0.03}_{-0.03}$	0.70 ± 0.02	0.22 ± 0.00	0.48 ± 0.02	300.0/258 (χ^2)
X-2012-05-01	$1.56^{+0.05}_{-0.05}$	0.47 ± 0.02	0.14 ± 0.00	0.33 ± 0.02	137.4/131 (χ^2)
X-2004-04-11	$1.51^{+0.02}_{-0.02}$	1.45 ± 0.03	0.42 ± 0.01	1.03 ± 0.03	388.1/398 (χ^2)
S-2016-05-07 ^h	$1.28^{+0.18}_{-0.18}$	1.59 ± 0.27	0.36 ± 0.05	1.23 ± 0.27	148.2/163 (<i>C</i>)
S-2014-03-14 ^l	$1.51^{+0.17}_{-0.17}$	0.86 ± 0.13	0.25 ± 0.03	0.61 ± 0.13	191.1/188 (<i>C</i>)
S-2013-11-19 ^h	$1.64^{+0.12}_{-0.12}$	1.52 ± 0.15	0.51 ± 0.05	1.01 ± 0.15	245.4/264 (<i>C</i>)
S-2013-10-13 ^m	$1.54^{+0.16}_{-0.16}$	0.96 ± 0.13	0.29 ± 0.04	0.67 ± 0.13	176.2/198 (<i>C</i>)
S-2013-09-27 ^h	$1.48^{+0.18}_{-0.18}$	1.50 ± 0.24	0.42 ± 0.06	1.08 ± 0.24	137.2/161 (<i>C</i>)
S-2013-07-07 ^m	$1.44^{+0.13}_{-0.13}$	1.12 ± 0.13	0.30 ± 0.03	0.82 ± 0.13	245.0/251 (<i>C</i>)
S-2012-09-30 ^l	$1.59^{+0.37}_{-0.36}$	0.52 ± 0.16	0.16 ± 0.04	0.35 ± 0.16	51.0/52 (<i>C</i>)
S-2012-09-12 ^l	$1.92^{+0.37}_{-0.36}$	0.51 ± 0.14	0.22 ± 0.06	0.29 ± 0.14	66.9/55 (<i>C</i>)
S-2012-07-03 ^l	$1.59^{+0.37}_{-0.37}$	0.68 ± 0.22	0.22 ± 0.06	0.47 ± 0.22	38.8/57 (<i>C</i>)
S-2012-03-14 ^l	$1.55^{+0.39}_{-0.38}$	0.42 ± 0.14	0.13 ± 0.04	0.29 ± 0.14	35.8/49 (<i>C</i>)
S-2011-11-15 ^l	$2.01^{+0.37}_{-0.36}$	0.39 ± 0.10	0.18 ± 0.04	0.21 ± 0.10	50.7/59 (<i>C</i>)
S-2011-09-17 ^m	$1.47^{+0.21}_{-0.21}$	1.16 ± 0.22	0.32 ± 0.05	0.84 ± 0.22	123.5/128 (<i>C</i>)
S-2011-07-14 ^l	$1.73^{+0.38}_{-0.37}$	0.58 ± 0.18	0.21 ± 0.06	0.37 ± 0.18	51.9/50 (<i>C</i>)
S-2011-05-15 ^l	$1.61^{+0.40}_{-0.39}$	0.45 ± 0.15	0.15 ± 0.04	0.30 ± 0.15	45.4/54 (<i>C</i>)
S-high	$1.50^{+0.09}_{-0.09}$	1.42 ± 0.15	0.40 ± 0.03	1.03 ± 0.15	367.9/379 (χ^2)
S-medium	$1.47^{+0.06}_{-0.15}$	0.94 ± 0.10	0.26 ± 0.02	0.68 ± 0.10	394.2/398 (χ^2)
S-low	$1.67^{+0.20}_{-0.10}$	0.48 ± 0.07	0.17 ± 0.02	0.32 ± 0.08	186.8/248 (χ^2)

Note: Best-fit parameters for the absorbed power law. The absorption column density is fixed to its Galactic value, $2.9 \times 10^{20} \text{ cm}^{-2}$, based on the survey by Kalberla et al. (2005). (1) Instrument and observation dates as in Table 8.1. (2) Power-law photon index. (3,4,5) Absorption-corrected fluxes in units of $10^{-12} \text{ erg cm}^{-2} \text{ s}^{-1}$ for the (0.5 – 10) keV, (0.5 – 2) keV, (2 – 10) keV energy ranges. (6) Statistic value per degrees of freedom (dof) for the best fit to the full band. The *Swift* data are not rebinned. Since the degrees of freedom are then given by the energy grid of the XRT it is constant for all *Swift* observations. ^{l,m,h}Observations included in the merged *Swift* data set of low (l), medium (m), or high (h) fluxes (see Sects.?? & ?? for details).

Analysis of the *Swift*/XRT monitoring data

Owing to the lower effective area of the *Swift* XRT with respect to *XMM-Newton* and shorter exposure times, the XRT spectra have significantly lower SNR, and in most observations the source is not detected above 6 keV. Therefore, we only adopt a simple power-law model, which already gives a good description of the *XMM-Newton* data. The model is fitted to the available data in the (0.5–10) keV range using the unbinned likelihood statistic **Cstat** (Cash 1979). For this purpose, we rebin the data to 1 count per bin (e.g., Krumpke et al. 2008). Best-fit parameters are listed in Table 8.2.

Table 8.3.: Results of the absorbed broken power-law model for *XMM-Newton* spectra.

Inst-Obsdate	Γ_1	Γ_2	E_B	$\chi^2/\text{d.o.f.}$	p -value
(1)	(2)	(3)	(4)	(5)	(6)
X-2012-10-18	$1.38^{+0.16}_{-0.17}$	$1.65^{+0.01}_{-0.01}$	$1.02^{+0.32}_{-0.16}$	288.6/256	0.033
X-2012-05-01	$2.40^{+1.60}_{-2.10}$	$1.56^{+0.06}_{-0.06}$	0.61 (fixed)	134.5/130	0.381
X-2004-04-11	≥ 3.05	$1.50^{+0.03}_{-0.03}$	$0.56^{+0.05}_{-0.05}$	372.1/396	0.0002

Note: Best-fit parameters for the absorbed broken power law. The absorption is fixed to its Galactic value, $3.17 \times 10^{20} \text{ cm}^{-2}$ (Kalberla et al. 2005). (1) Instrument and observation date. (2) Soft photon index below E_B . (3) Hard photon index above E_B . (4) Break energy in units of keV. (5) Fit statistics of the broken power-law model. (6) F-test p value, i.e. likelihood that the null-hypothesis model is correct (see Sect. ?? for details).

Table 8.4.: Results of the black body and power-law model for *XMM-Newton* spectra.

Inst-Obsdate	$\Gamma_{2-10 \text{ keV}}$	kT	F_{BB}	F_{PL}	$\chi^2/\text{d.o.f.}$
(1)	(2)	(3)	(4)	(5)	(6)
X-2012-10-18	1.57 ± 0.10	$0.31^{+0.10}_{-0.12}$	0.012 ± 0.005	0.216 ± 0.005	291.9/258
X-2012-05-01	1.43 ± 0.19	$0.23^{+0.06}_{-0.07}$	0.023 ± 0.005	0.128 ± 0.004	134.3/131
X-2004-04-11	1.39 ± 0.08	$0.25^{+0.06}_{-0.07}$	0.059 ± 0.009	0.383 ± 0.006	396.4/398

Note: Best-fit parameters for the absorbed simple power law and black body. The absorption is fixed to its Galactic value, $2.9 \times 10^{20} \text{ cm}^{-2}$ (Kalberla et al. 2005). (1) Instrument and observation date. (2) Photon index, fitted in the (2–10) keV band and fixed for broad band analysis. (3) Black body temperature in keV. (4,5) Absorption-corrected (0.5–2) keV flux in units of $10^{-12} \text{ erg cm}^{-2} \text{ s}^{-1}$ of the black body and the power law, respectively. (6) Fit statistics χ^2 per degrees of freedom.

The low number of spectral data counts mean that the fit parameters are affected by high uncertainties, especially during times of low flux. A way to improve statistics of the

Table 8.5.: Power-law fit of the *XMM-Newton* EPIC PN difference spectra.

Subtracted spectrum	$\Gamma_{2-10 \text{ keV}}$	$\Gamma_{0.5-10 \text{ keV}}$	$\chi^2/\text{d.o.f.}$
X-2012-10-18	1.30 ± 0.26	1.46 ± 0.09	215/193
X-2012-05-01	1.17 ± 0.18	1.43 ± 0.06	86.9/72

Note: Best-fit parameters for the simple power-law fit in the (0.5–10) keV and (2.0–10) keV energy band to the difference spectra. A difference spectrum is computed by subtracting the respective spectrum from X-2004-04-11.

spectral fit is by merging spectra of similar flux and increase the SNR. We define three flux states taking into account the results of the single observations and merge spectra with fluxes within these intervals (in units of 10^{-12} erg cm $^{-2}$ s $^{-1}$): $0.4 < F_{0.5-10\text{keV}} \leq 0.8$ (low), $0.8 < F_{0.5-10\text{keV}} \leq 1.4$ (medium), and $1.4 < F_{0.5-10\text{keV}}$ (high). This procedure gives a total exposure of 57 ks (with 837 counts) in the low-flux state, 47 ks (with 996 counts) in the medium-flux state, and 25 ks (with 795 counts) in the high-flux state. The quality of the merged spectra now enables the use of χ^2 -statistics and the spectra are analyzed analogously to the *XMM-Newton* spectra. For each of the three spectra, we find a good fit with a power-law model with no significant evidence of any other feature such as a soft excess. Best-fit parameters for these fits are listed in Table 8.2, labeled as S-low, S-medium, and S-high. There is no evidence of flux-dependent spectral variations.

Short-term X-ray variability

In the literature, both short and longterm variability has been reported for PKS 2004–447 (see Sect. 8.1). In this section, I thus analyse the variability of the X-ray emission based on the results discussed above.

G06 find evidence for short-term flux variability in the EPIC pn lightcurve of the X-2004-04-11 observation. Analysing the 300 s-binned pn lightcurve, they find a $\sim 30\%$ increase of the (0.2–10) keV count rate during the final 4 ks of the exposure. Fig 8.6 shows the EPIC pn lightcurves for the data presented in this work. For comparison, the lightcurves are binned in the same way. Owing to the number of counts, one can assume a Gaussian distribution of counts within each time bin (displayed uncertainties for each data point correspond to 1σ). The lightcurves show count rates of the source and background region for energies between (0.2–12) keV (light blue and gray, respectively). The flaring-corrected count rates are overlaid in blue and black, respectively. The mean count rates are calculated from the the flaring-corrected source lightcurve and are depicted by the blue horizontal solid lines. Dashed lines represent its 3σ levels. To test G06 claim, we excluded the final 4 ks in the calculation of the mean of X-2004-04-11. The results for this observation are shown in the top panel. One can see an increase in count rates towards the end of the observation, which G06 interpreted as short-term variability. The increased count rate is still consistent with a constant count rate at a 3σ level ($\chi^2/\text{dof} = 573.04/400$). Fig 8.6 also shows the lightcurves for the other two *XMM-Newton* observations. We do not find any evidence for variations on these timescales.

Longterm X-ray variability

The monitoring program allows us to analyze the longterm spectral variability. In the following, reported fluxes and luminosities refer to their absorption-corrected values. If not stated otherwise, source count rates refer to their background-subtracted values.

Figure 8.7 shows the evolution of the total flux of the source over time. PKS 2004–447 shows moderate X-ray flux variability on timescales of weeks to years. The scheduling of the monitoring observations does not allow to detect variability on timescales shorter than two weeks. For the *XMM-Newton* observations the highest flux is measured in 2004,

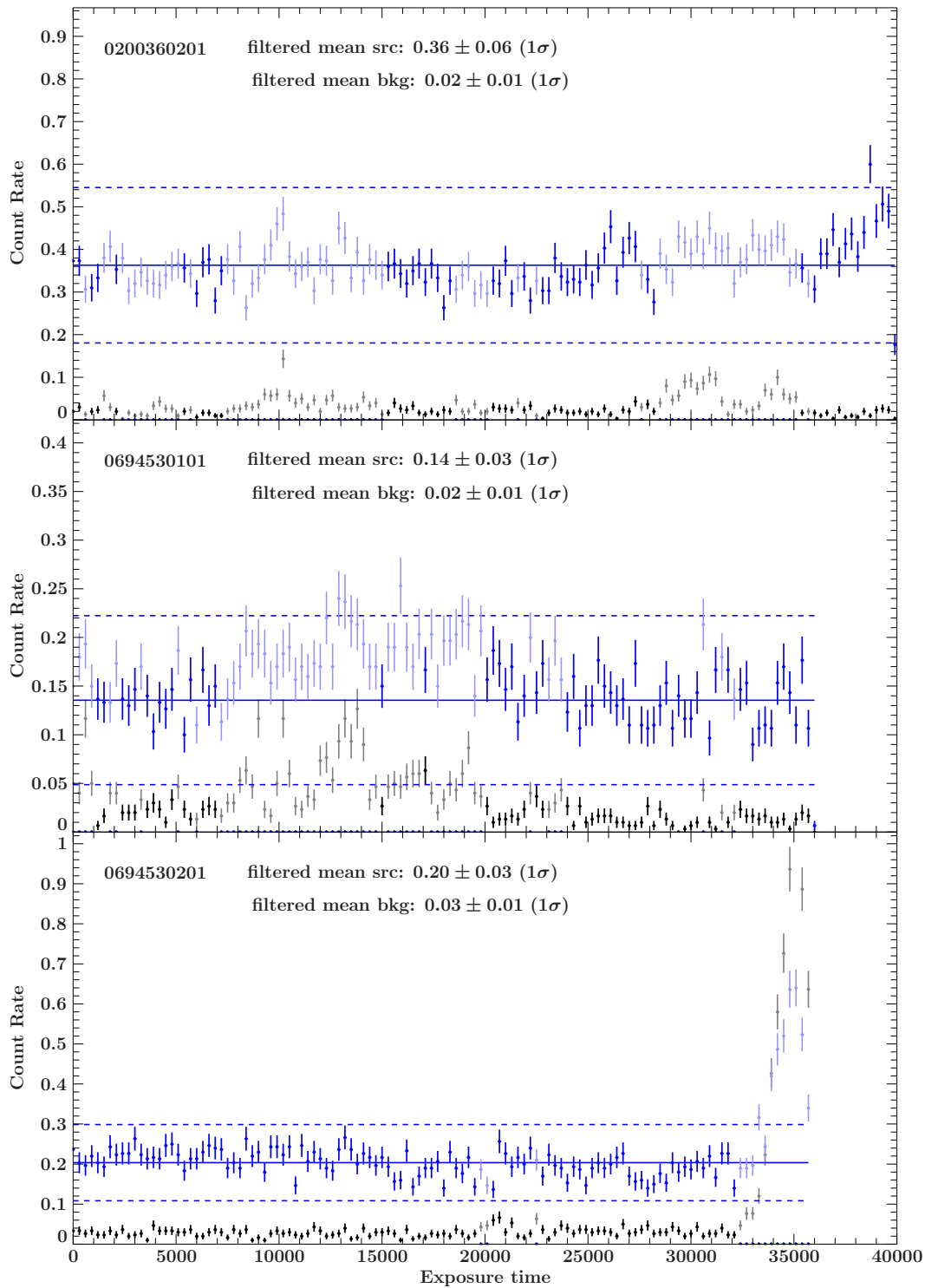


Figure 8.6.: *XMM-Newton* EPIC PN light curves for the source and background region and energies between (0.2–12) keV. Light blue and gray points depict count rates without filtering for flaring particle background. Flaring-corrected count rates are shown in blue (source region) and black (background region). Horizontal blue lines show the mean count rate of the source region (solid line) with 3σ uncertainties (dashed lines).

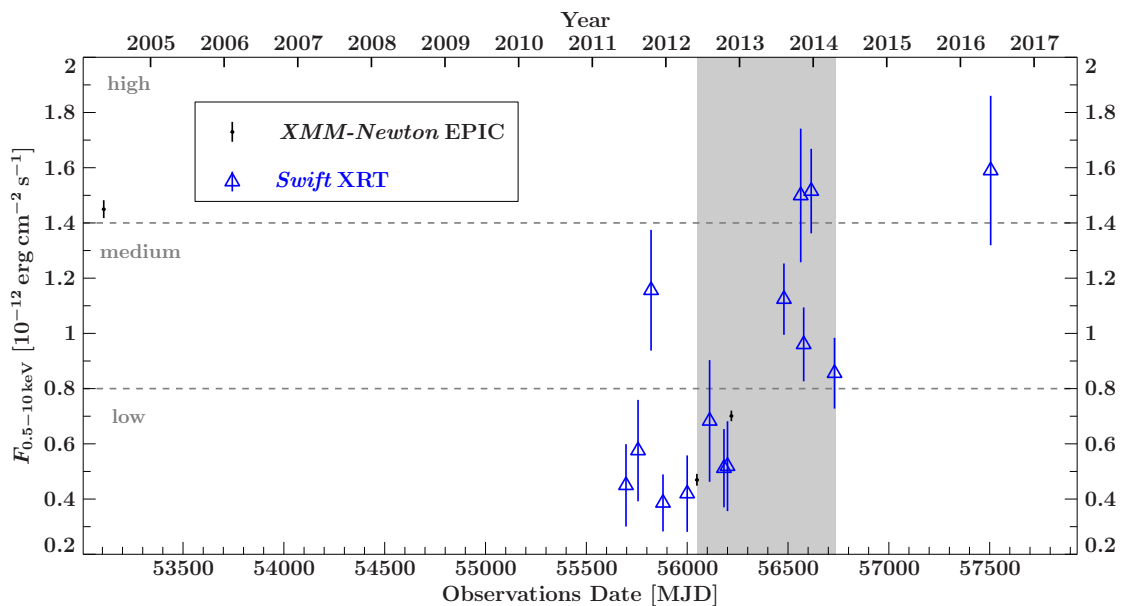


Figure 8.7.: Long-term variation of the total absorption-corrected 0.5–10 keV flux. The gray-shaded background denotes the multiwavelength monitoring period. *XMM-Newton* data are shown as black points, *Swift* data are plotted as open blue triangles. Horizontal dashed-lines denote thresholds for the low, medium and high flux ranges.

whereas the total flux is about 50% lower in those from 2012. A similar value is regained in *Swift* observations in September 2013.

We calculate the fractional variability amplitude F_{var} following the definition by Vaughan et al. 2003a, (see Eq.5.2.1). For the full (0.5–10) keV, soft (0.5–2) keV, and hard (2–10) keV energy bands the fractional variabilities are:

$$\text{full band (0.5 – 10) keV : } F_{\text{var}} = 0.47 \pm 0.13,$$

$$\text{soft band (0.5 – 2) keV : } F_{\text{var}} = 0.40 \pm 0.12,$$

$$\text{hard band (2 – 10) keV : } F_{\text{var}} = 0.50 \pm 0.18,$$

respectively. The values support the presence of mild variability. Variability in the subbands are consistent with the fractional variability of the total range within uncertainties. Hence, both the soft and hard ranges show the same variability characteristics.

For a model-independent analysis of spectral variability, we determine the number of background-subtracted source counts in the following soft and hard bands:

S1: (0.2–0.6) keV,

S2: (0.2–2.0) keV,

H1: (2.0–7.0) keV,

H2: (2.0–10) keV.

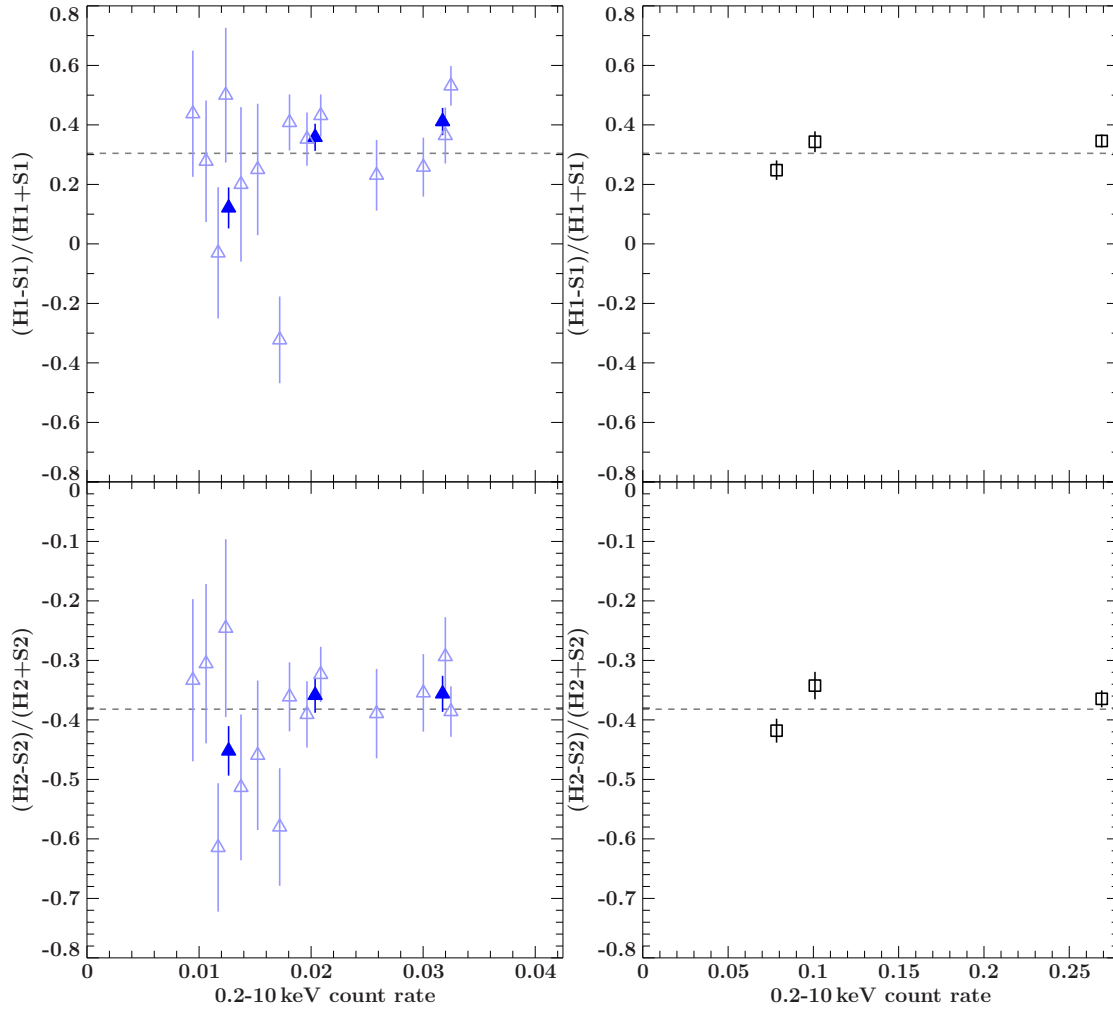


Figure 8.8.: Hardness-intensity diagram (HID): Hardness ratios $(S1-H1)/(S1+H1)$ (*top*) and $(S2-H2)/(S2+H2)$ (*bottom*) as a function of background-subtracted source count rates in the full energy band. Error bars correspond to 1-sigma uncertainties. *Left:* Results from *Swift* observations. Individual observations are shown as lightblue open symbols, while filled blue symbols denote results from merged data sets. *Right:* HID of the *XMM-Newton* data.

Since source counts are not affected by calibration issues at low energies, we extended the soft S1 and S2 bands to 0.2 keV. S2 and H2 are the common soft and hard bands used above. The addition of S1 allows to test the effect of a possible extra component below 0.6 keV in a model-independent way. H1 is defined in order to take into account the lower sensitivity of *Swift* at energies above 7 keV. 1σ uncertainties, σ_N , of the number of counts, N , in a given band were approximated following Gehrels (1986)

$$\sigma_N \approx \sqrt{N + 0.75} + 1. \quad (8.3.1)$$

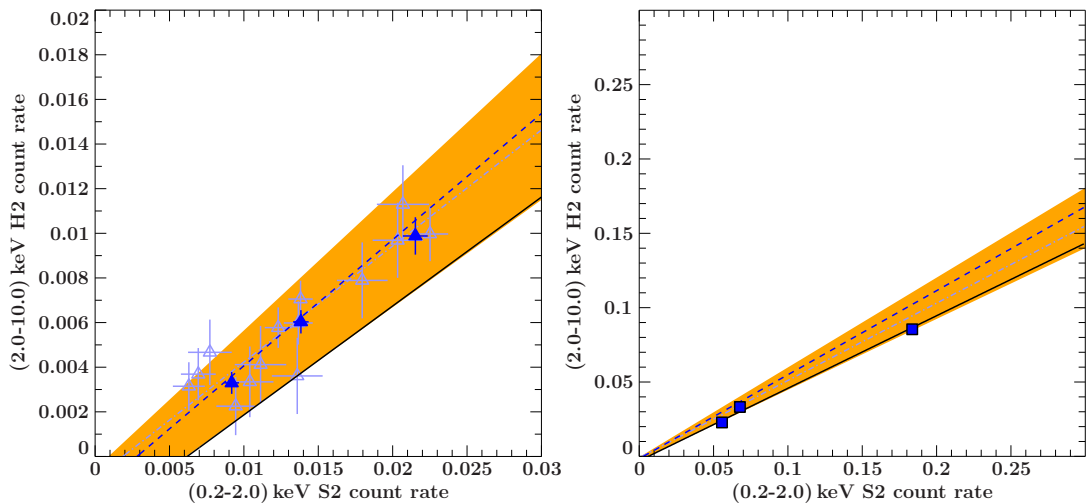


Figure 8.9.: Hard- versus soft-band diagram (HSD): Comparison of the count rates in the soft (0.2–2) keV and hard (2–10) keV band. Error bars correspond to 1-sigma uncertainties. *Left:* Results from *Swift* observations. Individual observations are shown as lightblue open symbols, while filled blue symbols denote results from merged data sets. *Right:* HSD of the *XMM-Newton* data. Both panels show the best-fit linear regressions for low-SNR *Swift* (dashed-dotted), merged high-SNR *Swift* (dashed), and *XMM-Newton* (solid) data. The combined 1σ uncertainties of all three fits are shown as orange-shaded region.

The number of detected counts strongly depends on the energy-dependent effective area of a given instrument. Thus, for similar fluxes we expect different count rates and number of counts for *Swift* XRT and *XMM-Newton* EPIC PN. There are no simultaneous observations of both *Swift* and *XMM-Newton*, which could serve to calculate the conversion factor between these instruments. Thus, counts of both detectors are analyzed separately for each telescope.

Hardness ratios HR are derived using the fractional difference $HR = (H - S)/(H + S)$, for the soft (S) and hard (H) band and are plotted as a function of the total source count rate (hardness intensity diagram, HID) for the different instruments (see Fig. 8.8). For the ratio $H1-S1/H1+S1$, the ratio is positive, since S1 covers a smaller range of the spectrum. In both hardness ratios the effects of the reduced sensitivity of *Swift* in the hard band is visible in a wider spread of values towards low count rates. The effect increases using only the narrow energy bands S1 and H1 of the spectrum. Averaging does not counter the bias, for missing photons in the hard band cannot be reconstructed. The average hardness ratio of $(H2 - S2)/(H2 + S2) = -0.39$ is computed from all available high-SNR data. For both instruments, the data are consistent with a constant HR.

Spectral analysis of the *XMM-Newton* data yielded hints of a second spectral component visible below 2 keV. We also tested the presence of a non- or a less-variable component by comparing the variation in the count rates in the soft and hard bands (see Fig. 8.9, for the hard versus soft band diagram, HSD). A linear dependency between these bands would suggest that the flux variation of the different spectral bands are cor-

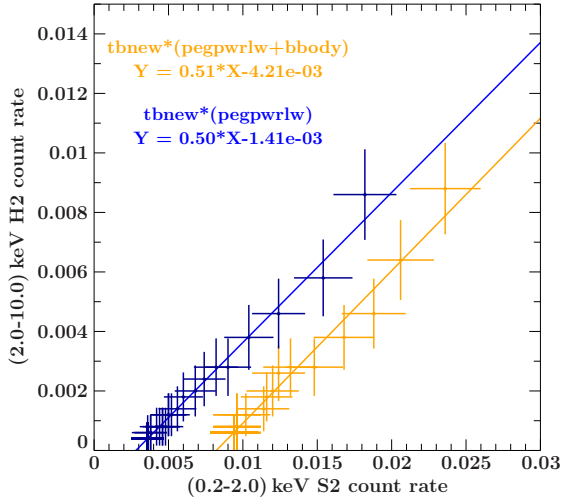


Figure 8.10: HSD derived from simulated *Swift* spectra with 5 ks exposure and power-law fluxes between $(10^{-17}\text{--}10^{-12}) \text{ erg cm}^{-2} \text{ s}^{-1}$. Solid lines denote linear regressions. See text for more detailed explanation.

related, for example, if the spectrum is dominated by variation of a single component. The presence of a less varying or independent component would induce a deviation from a linear relation.

There is a wide spread at lower *Swift* count rates. However, the data are overall consistent with a linear relation between the soft and hard bands. We performed a linear regression to (a) only *XMM-Newton* data, (b) the whole *Swift* data set, and (c) only merged high-SNR *Swift* data (see Table 8.6). We found a relation that deviates from a line through the origin at a 1σ level. Taking into account the uncertainties of all three regressions the linear fit shows a positive offset of $(0.89 - 6.1) \times 10^{-3} \text{ cts s}^{-1}$ in the soft band. This corresponds to an integrated (0.5–2) keV flux of $(0.016 - 0.11) \times 10^{-12} \text{ erg cm}^{-2} \text{ s}^{-1}$, for both a blackbody with a temperature of 0.25 keV (see Table 8.4) or a power-law component with $\Gamma \sim 1.6$. However, such an offset can also occur, when the source count rate for a given exposure time is too low such that no counts are detected in the hard band. The sensitivity limit for *Swift*/XRT is $2 \times 10^{-14} \text{ erg cm}^{-2} \text{ s}^{-1}$ for a 10 ks exposure. In order to check whether the offset can be associated with a weak extra component or the sensitivity limit of *Swift*/XRT, we simulated *Swift*/XRT spectra using (i) a model that consists of an absorbed power law and the blackbody found for X-2004-04-10 (Table 8.4), and (ii) just a Galactically absorbed power law. For the simulated spectra, we assumed an exposure time of 5 ks and power-law fluxes between $(10^{-17}\text{--}10^{-12}) \text{ erg cm}^{-2} \text{ s}^{-1}$ (while the black body flux was assumed to be constant). Figure 8.10 shows the expected HSD for both simulations. As one can see from the comparison, the blackbody component fitted to X-2004-04-11 is not strong enough to cause any deviations from a linear fit within the sensitivity limit of XRT. In both cases, we would expect an offset from the origin, although it would be larger in case of an extra component than the observed value. We conclude that the offset we found in the data is fully consistent with an offset caused by the sensitivity limit of *Swift*/XRT.

Table 8.6.: Results from the linear regression to the HSD.

Data set	Slope a	Offset b [counts s ⁻¹]	χ^2 (dof)
a) <i>XMM-Newton</i>	0.488 ± 0.019	-0.0030 ± 0.0015	6.9 (3)
b) <i>Swift</i>	0.520 ± 0.035	-0.0010 ± 0.0005	22.6 (14)
c) <i>Swift</i> merged	0.565 ± 0.037	-0.0016 ± 0.0005	1.2 (3)

Note: Best-fit parameters for the linear regression $C_{\text{soft}} = aC_{\text{hard}} + b$, where C_{soft} and C_{hard} are the spectral counts in the soft and hard bands, respectively. Uncertainties correspond to 1-sigma uncertainties.

Discussion of the X-ray emission

The X-ray emission of PKS 2004–447 in the (0.5–10 keV) energy range is described best by a simple, Galactically-absorbed power law. A tentative soft excess is observed in the *XMM-Newton* spectrum of 2004. However, this excess is not detected in our new observations from 2012. The difference spectrum is described well by a simple power law, but the SNR is not sufficient to draw any conclusion on an excess below 2 keV (see Fig. 8.5 and Table 8.5). The power-law spectrum and photon index are reminiscent of the non-thermal X-ray emission of type-1 AGN. In addition, the spectrum exhibits flux variability across the entire band. Comparing best-fit models of each observation, we find evidence of weak spectral variability, while there is no evidence of any absorption beyond the Galactic one. This suggests that the power-law component itself varies, owing to the stochastic nature of the emission process or caused by changes in the emission region (e.g., Vaughan et al. 2003a). Although we do see evidence of weak spectral variability from spectral fitting, the variations between the source brightness and spectral shape are not correlated (Fig. 8.8). The linear behavior of the count rates in the HSD (Fig. 8.9) can be explained by a single dominating (power-law) component that exhibits changes in its normalization. These variations cause a homogeneous flux variation across the full (0.5–10) keV band. For the interpretation of the X-ray spectrum we consider the following three possible scenarios:

- (I) a non-jet-dominated X-ray spectrum (characteristic of Seyfert galaxies), for which the unbroken power-law spectrum is associated with thermal inverse-Compton scattering of optical and UV photons from the accretion disk in the disk corona. A soft excess in these sources may be caused by relativistically blurred reflection from the accretion disk (Crummy et al. 2006) or thermal Comptonization of disk emission by a population of electrons with low temperature and high optical depth (see, e.g., Haardt & Maraschi 1993b). We note that the photon index of PKS 2004–447 is significantly harder than those observed in radio-quiet NLS1s (see, e.g., Vaughan et al. 1999; Zhou & Zhang 2010; Grupe et al. 2010).
- (II) a Seyfert-like X-ray spectrum that is contaminated by a significant contribution from synchrotron emission of a relativistic jet. In this scenario which was also

proposed by G06, jet-synchrotron emission contributes to the soft X-ray spectrum in 2004, while the dominating power law can be associated with the Seyfert-like component. The detection in γ -rays, however, suggests that the jet dominates at higher energies. Thus, we do not favor any scenario where the jet emission only contributes in the form of a soft excess.

- (III) a jet-dominated X-ray spectrum, characteristic of blazars, in which the spectrum is associated with X-ray emission from the jet alone. Emission from the accretion disk is negligible. Within the framework of leptonic models, blazar X-ray spectra may be comprised of both synchrotron emission and inverse-Compton emission from relativistic particles in the jet plasma (see, e.g., Maraschi et al. 1992a; Dermer & Schlickeiser 1993; Bloom & Marscher 1996; Ghisellini et al. 1998, 2010b; Böttcher et al. 2013). The jet-like non-thermal origin for the dominating X-ray emission is supported by the flat photon index with respect to radio-quiet NLS1s. This is consistent with values typically found in blazars, particularly FSRQs (see, e.g., Fan et al. 2012; Rivers et al. 2013; Dai & Zhang 2003; Sambruna et al. 2004). In this scenario, the hard power law can be interpreted as inverse-Compton emission from the jet and synchrotron emission would account for the tentative soft excess in the data of 2004. Alternatively, as recently reported by Kammoun et al. (2017), bulk Comptonization of accretion disk photons that were reprocessed in the BLR can account for such an excess in blazars.

Although, the flat photon index favours the third scenario, profound evidence comes from an multiwavelength investigation.

Soft excess or no soft excess?

A faint soft excess is detected only tentatively in the *XMM-Newton* observation X-2004-04-11, consistent with findings by G06. This component could not be verified by our new *XMM-Newton* observations in 2012. Fitting a power law to the *XMM-Newton* data only in the (2–10) keV range (see dashed lines in Fig. 8.1) leads to an excess emission of $F_{\text{SX}} \sim 6 \times 10^{-14} \text{ erg s}^{-1} \text{ cm}^{-2}$ in the (0.5–2) keV band (see Sect. 8.3). If described by a black body, the soft excess yields a flux contribution of 5% to 20% of the power-law flux and a black body temperature between 0.25 keV and 0.3 keV.

It remains questionable whether the soft excess existed in the data of X-2004-04-11. A variable soft component may explain the lack of excess emission in the data of 2012. We note that in radio-quiet Seyferts that include a few NLS1s, there have been cases where the soft excess varies independently from and more slowly than the hard power law (Turner et al. 2001; Edelson et al. 2002b; Mehdipour et al. 2011; Arévalo & Markowitz 2014), and even seems to disappear from one X-ray observation to the next on timescales of years (Markowitz & Reeves 2009; Rivers et al. 2012). Such a component would cause deviations from a linear dependency in the HSD, which is not observed at a 1σ -level. Although, we find evidence of an offset from the origin that might result from a less varying component of $(1.6 \leq F_{\text{offset}}^{0.5-2 \text{ keV}} \leq 11) \times 10^{-14} \text{ erg s}^{-1} \text{ cm}^{-2}$ (consistent F_{SX}).

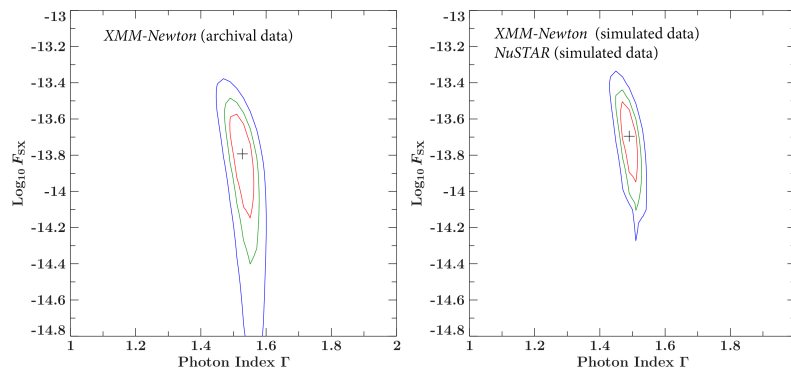


Figure 8.11.: 68%- (red), 90%- (green), and 99%- (blue) confidence contours of the soft excess flux and the photon index of the power law continuum for the *XMM-Newton* observation in 2004. *Left panel:* Using only *XMM-Newton*/EPIC pn spectrum, the excess emission cannot be detected significantly within the sensitivity flux limit of $2 \times 10^{-15} \text{ erg s}^{-1} \text{ cm}^2$ ($\log F_{\text{SX}} = -14.7$) for the derived net exposure time of 35 ks in 2004 (*XMM-Newton* User Handbook). *Right panel:* A fit to the combined simulated *XMM-Newton* and *NuSTAR* spectra for 50 ks yields a significant detection of the soft excess component.

However, simulations suggest that the offset is most likely caused by the sensitivity limit of *Swift*/XRT in the hard band. On the contrary, the variable nature of the soft excess can be explained in the context of bulk comptonization of cold lepton from the jet. Since the strength of this component strongly depends on the acceleration, i.e. the bulk Lorentz factor Γ_{bulk} and Doppler factor δ of the leptons, the component varies if the acceleration of leptons is not continuous and one expects correlated flux variability of the power law and black body.

Hence, since the soft excess was not detected during a low flux period of the source, it might only be detectable in a high-flux state. To address this problem, we have set up target-of-opportunity observations with *XMM-Newton* (AO16) and *NuSTAR* (Cycle 2) to observe the source simultaneously in a high-flux state. We use weekly *Swift* observations to monitor the flux state during the combined visibility windows of *XMM-Newton* and *NuSTAR*. The resulting high-sensitivity observations and broader energy range will put stronger constraints on the hard power-law component and test for excess emission in the soft band (see contours in Fig. 8.11). Information of the hard X-ray spectrum can also be used to look for hard X-ray signatures of the soft component (e.g., Haardt & Maraschi 1993b; Crummy et al. 2006).

8.4. The multiwavelength view of PKS 2004–447

In the previous section, a detailed analysis of the X-ray emission has been presented. However, from this energy range alone it was challenging to pin down the composition of the X-ray spectrum, as the source exhibits properties of both radio-loud and radio-quiet type 1 AGN. In order to get a comprehensive view on the source, it is necessary to

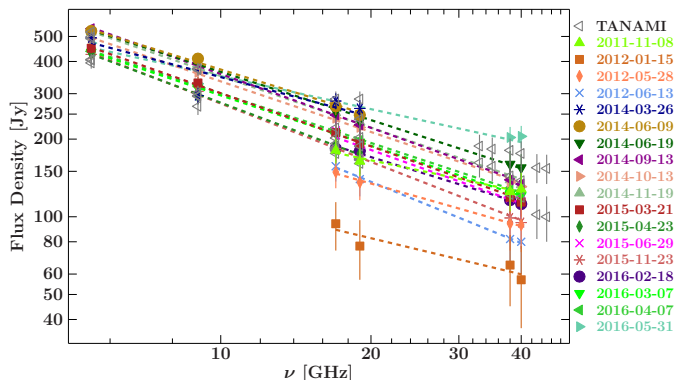


Figure 8.12: Spectrum of ATCA monitoring between 5.5 GHz and 40 GHz from 2011 Nov 08 to 2016 May 31. Dashed lines represent power-law fits to simultaneous observations.

consider its broadband properties. In this section, I describe the construction of a series of simultaneous SEDs to analyze the temporal evolution of the broad band spectrum.

Collecting Multiwavelength data

Our *XMM-Newton* and *Swift* monitoring provided simultaneous observations from optical/UV to X-rays that were supplemented by our ATCA radio monitoring observations as part of the TANAMI program, as well as continuous monitoring at γ -ray frequencies with *Fermi*-LAT. The following subsections briefly describe the data sets that were used to construct the spectra.

ATCA radio data

We analyse several simultaneous multi-frequency single-dish observations obtained by ATCA at 5.5 GHz, 9.0 GHz, 33.0 GHz, 35.0 GHz, 43.0 GHz, and 45.0 GHz from 2010 Feb 13 until 2016 May 27. The analysis and results for data until 2014 Mar 26 has been published in Schulz et al. (2016, hereafter S16) and shall only be briefly summarized here. For the analysis presented in this work, we also include ATCA observations of the calibrator program C1730 between 2014 and 2016. For this period, flux densities at frequencies 5.5 GHz, 9 GHz, 38 GHz, and 40 GHz are obtained from the public calibrator database of the Australian Telescope National Facility (ATNF).

The data show moderate variability in flux density up to a factor of two and a persistent steep radio spectrum between 1.7 GHz and 40 GHz. The ATCA radio spectrum from 2010 until 2014 has been published by S16. The complementary radio spectrum until mid 2016 is shown in Fig. 8.12. Over the years the spectral index α varied moderately between ~ -0.4 and ~ -0.9 with a weighted mean of $\alpha_{\text{wm}} = -0.64 \pm 0.10$. These values are consistent with results from earlier studies by Oshlack et al. (2001) and Gallo et al. (2006). Although, the simultaneous spectrum between 1.38 GHz and 2.4 GHz from 2004 presents a significantly flatter spectral index $\alpha_{1.38-2.4} = -0.21 \pm 0.08$. This flattening suggests that a turnover in the radio spectrum occurs below 2 GHz.

¹See ATNF public archive <http://www.narrabri.atnf.csiro.au/calibrators/>

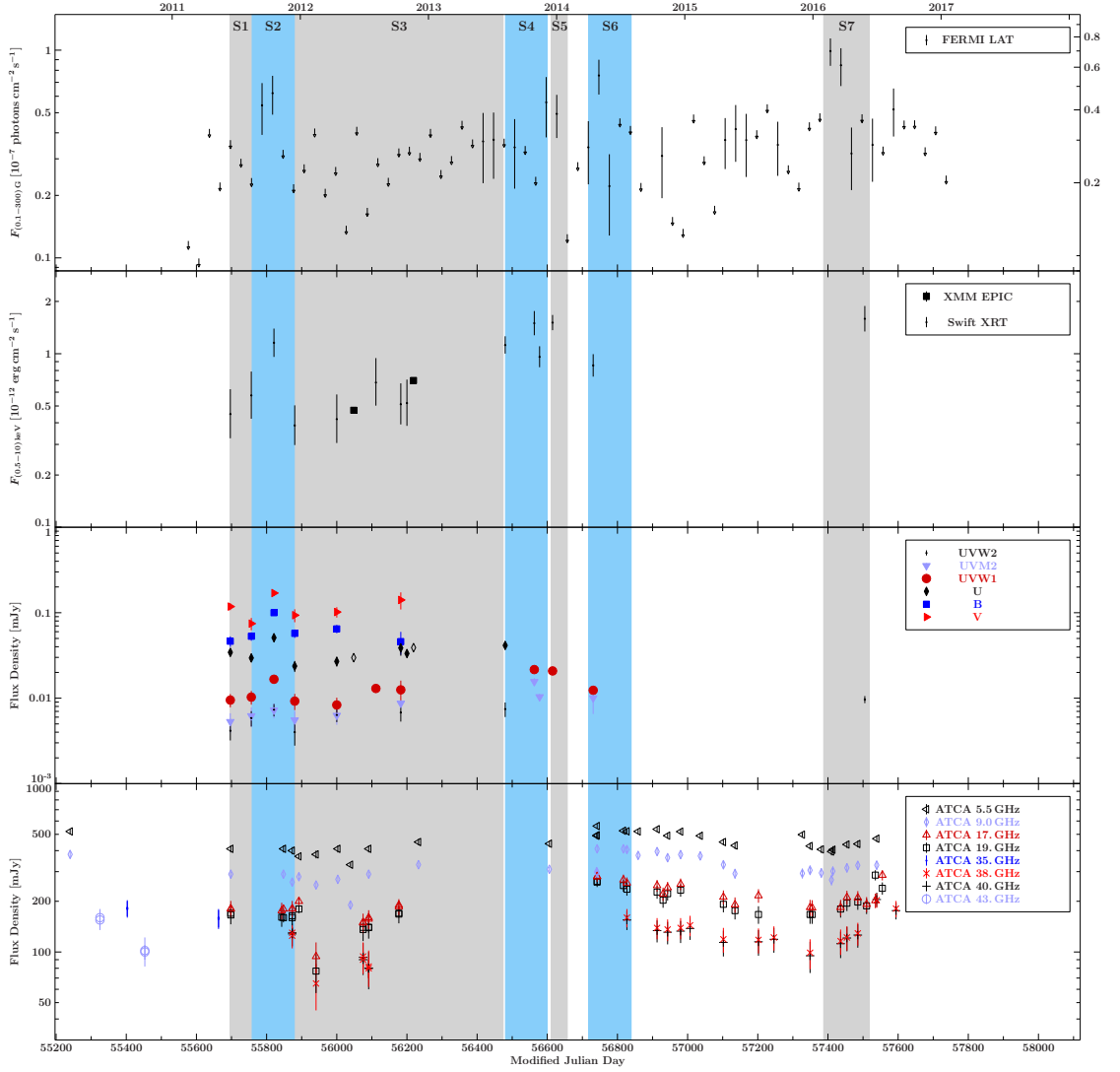


Figure 8.13.: Multiwavelength light curves from γ -rays (*top*) to radio (*bottom*) from 2010 until 2017. Instruments are *Fermi*-LAT, *Swift*/XRT and *XMM-Newton*/EPIC, *XMM-Newton*/OM & *Swift*/UVOT (UV filters), *XMM-Newton*/OM & *Swift*/UVOT (optical filters). Shaded regions were used for quasi-simultaneous SEDs (see text for more information). *Fermi*-LAT light curve is binned to 30 days with a significance threshold of $TS = 9$. Upper limits are shown as downward arrows. Radio, optical/UV, and X-ray data points correspond to single observations. Note that the y-axes are in logarithmic scale.

The radio light curve of our ATCA TANAMI monitoring and additional ATCA calibrator observations are shown in the bottom panel of Fig. 8.13.

***XMM-Newton*/OM and *Swift*/UVOT optical and UV data**

We use measurements in the optical and UV energy bands, that were obtained simultaneously to the X-ray observations using *XMM-Newton*/OM and *Swift*/UVOT. Observations with the optical and UV filters are available for all our monitoring observations between 2011 and 2013. For observations later than 2014, only UV filters were available. The standard data reduction pipelines of these instruments provided energy fluxes for each possible filter U,B,V,UW1,UW2, and UWM1. The observed flux densities for each filter and instrument are shown in Fig. 8.13. For spectral analysis of these fluxes, we included the XSPEC model `redden` to account for extinction by a diffuse interstellar medium (with $R_v = 3.1$, Cardelli et al. 1989), and Galactic hydrogen column density in the fit model.

***Swift*/BAT**

Non-simultaneous *Swift*/BAT data is used for reference in the hard X-ray range. We extracted the BAT-spectrum from the 104-month survey maps and fit it using a power law in the range of 20-100 keV. The resulting flux in this energy range is compatible with zero within its 3σ uncertainty. Therefore, we consider the measurement as an upper limit, with a value equal to the previously derived uncertainty.

***Fermi*-LAT data**

For the analysis of the *Fermi*/LAT γ -ray data, we used the *Fermi* Science Tools (version v10r0p5) together with the reprocessed Pass 8 data and the P8R2_SOURCE_V6 instrument response functions. For a given time period, we performed the standard analysis in a region of interest of 10° around PKS 2004–447 in an energy range of 100 MeV to 300 GeV. We construct a model that contains all 3FGL sources within the ROI and fits them with a free normalization constant. The model also includes a Galactic diffuse and isotropic diffuse emission component.

We used a free spectral index during the spectra calculation, while it was fixed for the light curve analysis. A 30 day binning was necessary to achieve the *Fermi*/LAT γ -ray light curve between 2011 until 2017, applying a Bayesian-blocks analysis. The significance is determined by the maximum likelihood approach which is expressed by the test statistic TS , which is the ratio of the likelihood values with and without an extra source component. To account for upper limits we use a threshold of $TS = 25$ for the spectra and $TS = 9$ for the light curve. The upper limit calculation is based on the method of Feldman & Cousins (1998).

The temporal behavior of the broadband emission

Figure 8.13 shows the multiwavelength lightcurve of PKS 2004–447. The source is variable on different timescales across the whole electromagnetic spectrum. Table 8.7 lists the fractional variability from the radio to X-ray bands. It is obvious that F_{var} increases with frequency from $\sim 14\%$ in the radio band up to $\sim 50\%$ in the X-ray band. Due to

Table 8.7.: Fractional variability amplitude for different frequency bands

Band	5.5 GHz	17 GHz	38 GHz	B	UVW1	(0.5-10) keV
F_{var}^a	0.12 ± 0.03	0.16 ± 0.03	0.22 ± 0.11	0.31 ± 0.10	0.34 ± 0.10	0.48 ± 0.13

the few detections in γ -rays no variability measure was calculated for this range. Above 0.1 GeV the source is detected at fluxes ranging from $(0.2\text{--}10) \times 10^{-7}$ photons $\text{cm}^{-2} \text{s}^{-1}$. Upper limits in the range of $(0.09\text{--}0.5) \times 10^{-7}$ photons $\text{cm}^{-2} \text{s}^{-1}$ imply flux variability with similar amplitude as in the X-ray band.

From Fig. 8.13, it appears that variability in the optical, X-ray, and γ -ray are correlated, although the scarceness of the data does not allow for a profound study of cross-correlation. Thanks to the simultaneous observations of the instruments onboard the X-ray satellites, we observe the same flux variations in the optical/UV and X-ray bands. This behaviour is most prominent in 2011. Both the X-ray and optical flux increased by $\sim 35\%$ within the two months between 2011 Jul 14 to 2011 Sep 17, and have decreased to its former flux state until 2011 Nov 15. The brightest observed state in the X-ray and optical/UV band coincides in time with the only *Fermi*-LAT detection between 2011 and mid-2013. This coincidence of an X-ray medium to high flux and a *Fermi*-LAT detection reoccurs in the end of 2013 and the beginning of 2014. However, the X-ray sampling does not provide enough information to state about the X-ray flux before these detections in γ -rays or beginning of 2016. Thus, the simultaneous detection in 2011 might be just a coincidence.

Opposed to the high energies, the radio flux is only weakly variable. During 2011 it appears to be at a constant flux level (e.g., ~ 300 mJy at 9 GHz). However, we lack observations between 2011 May 17 and 2011 Oct 14, when the source became brighter at higher energies and we cannot rule out variability in radio between May and October 2011. Beginning of 2016 there is a period of high X-ray and γ -ray flux (shaded region) which is followed by a radio flux increase at frequencies higher than 19 GHz. A denser sampling of simultaneous observations could clarify if there is an underlying correlation for such an incident.

In order to investigate the spectral evolution of the broadband emission, we constructed a series of seven SEDs from radio to γ -rays based on the X-ray and γ -ray flux states. The time ranges, for which the SEDs were built are marked as (alternating) blue and gray shaded regions in the multiwavelength light curve. The SEDs are shown in Fig. 8.14. The optical and X-ray data were corrected for absorption and extinction in the ISM and are shown as gray data points. However, as the source is only affected by Galactic absorption, the effect is barely noticeable. Furthermore, the multiwavelength data that was studied by G06 in 2004 are also shown in red symbols for comparison in every panel. The same holds for the *Swift*/BAT upper limit in blue.

There are a number of physical leptonic and hadronic models (see Sect. 3.2.4) for blazar emission. Because of the large number of free parameters and assumptions on the emission site (such as the size of the emission region or shape of the electron energy distribution within the jet), these models require an extraordinary spectral data coverage

8. Unveiling the nature of PKS 2004–447

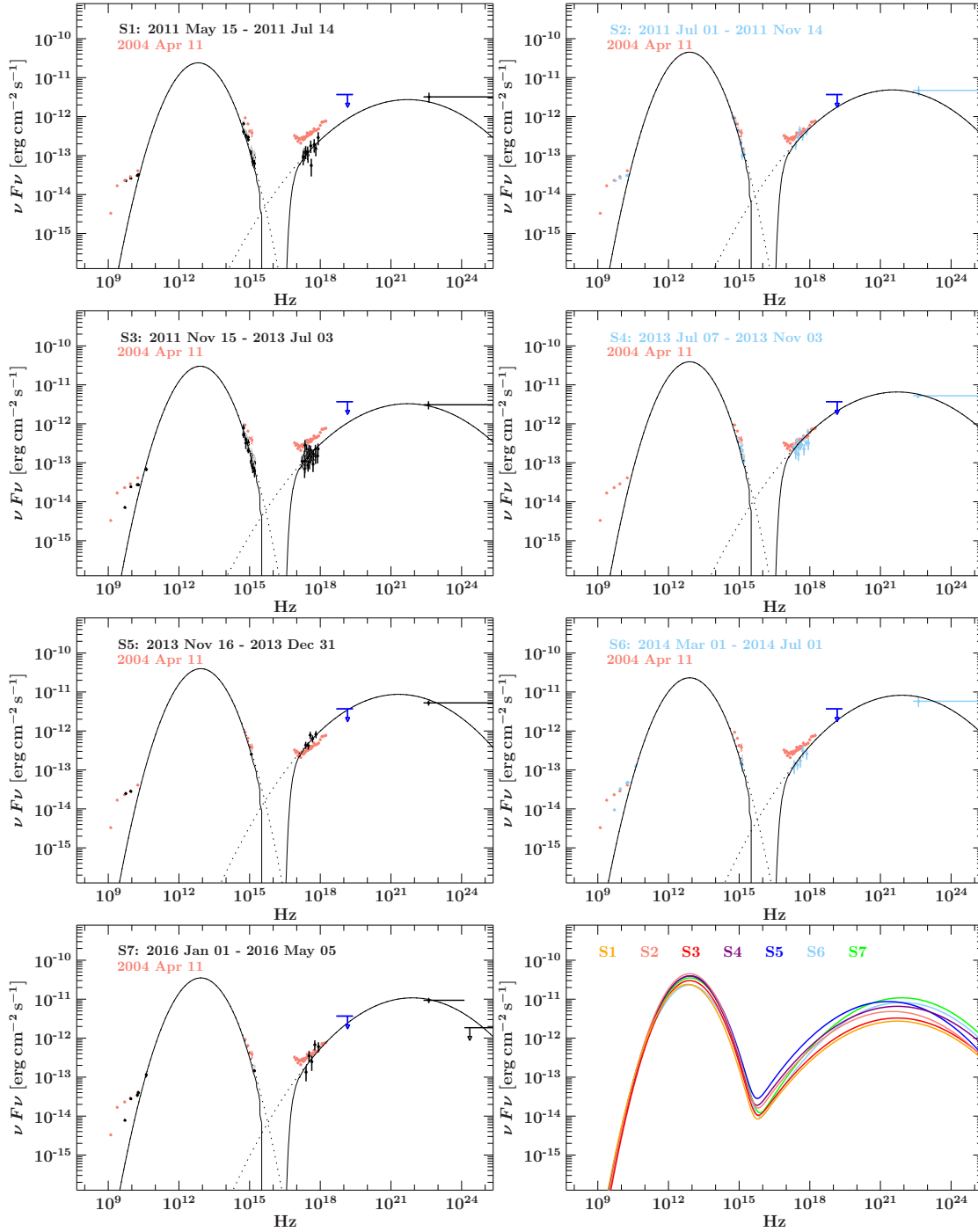


Figure 8.14.: Quasi-simultaneous observed SED of PKS 2004–447 for different observing periods (see Text). Black symbols denote observed data. Gray symbols are absorption-corrected data. We also show the broadband data used by G06 in red symbols and the *Swift*/BAT upper limit (blue arrow). The SEDs are described by hand with a combination of two logarithmic parabolas affected by absorption extinction by the ISM. See table 8.8 for model parameters. The panel at the bottom right compares the used models to described the SED in each state.

to yield good constraints on fit parameters. In reality, spectral fits to stationary SEDs are often degenerate. Given these limitations, we assume a phenomenological log parabola model to describe the SEDs. Our model includes two log parabolas as well as two multiplicative models for absorption and extinction in the ISM. The final model string in `isis` reads `tbnew_simple*redden*(logpar(1)+logpar(2))`.

This model does not provide any physical interpretation. Nevertheless, Massaro et al. (2004a) have shown, that such a model is suitable to describe the leptonic synchrotron and self-synchrotron Compton (SSC) radiation of blazars. Despite its simplicity, the log-parabolic model can be used to estimate the position of the emission peak, as well as, the peak flux density for the low and high-energy emission humps (e.g., Krauß et al. 2016; Massaro et al. 2004a,b, 2006). Furthermore, Krauß et al. (2016) have shown that the peak properties derived from the log parabola model for blazars are consistent with the well-established blazar sequence.

The observed radio emission most likely originates in an emission region much larger than the one of the high-energy radiation. This is supported by the low variability amplitude in the radio band, presumably due to longer light traveling timescales through the emitting region. Thus, the data points at radio frequencies are be treated as an upper limit. This approach allows us to describe the optical/UV spectrum with a single log parabola. The second log parabola is used to describe the X-ray to γ -ray emission. The overall model has six free parameters, the normalizations K_i of the log parabolic curves, as well as their photon index α_i and the spectral curvature β_i at $E_{\text{pivot},i}$. The model performance is best for pivot energies close to the lower end of the fitted energy range (Massaro et al. 2004a). Hence, we fix $E_{\text{pivot},1} = 0.0078 \text{ eV}$ (corresponding to $\sim 1.8 \times 10^{12} \text{ Hz}$) and $E_{\text{pivot},2} = 10 \text{ keV}$ for the low and high-energy hump, respectively.

Even with this simple model, it is not possible to obtain a good fit by minimizing the test statistic automatically. This is due to the fact that the large statistical weight of the data lies at a very narrow band of the spectrum (between 10^{15} Hz and 10^{18} Hz), while only upper limits or few data points exist at the lowest and highest frequency ranges. Nevertheless, we describe the data by setting the parameters by hand and changing as few parameters as possible until we find a reasonable description of all SEDs. The objective is to find a parameterization in order to compare the broad band emission among different states. Table 8.8 gives the parameters for the different SED sets, peak energies and peak fluxes, derived from the log parabola (Massaro et al. e.g., 2004a). From the log parabolas one can derive the corresponding power-law photon index at 1 keV in the X-ray band (e.g., Massaro et al. 2004a),

$$\Gamma(1 \text{ keV}) = \alpha + 2\beta \log \left(\frac{1 \text{ keV}}{E_{\text{pivot}}} \right). \quad (8.4.1)$$

The derived values are $\Gamma_1 = 6.3$ for the contribution of the low-energy parabolic component and $\Gamma_2 = 1.35$ for the high-energy component. The latter is slightly harder than our results for the 0.5 keV to 10 keV range of Sect. 8.3. Although Γ_2 is consistent with the photon index between 2 keV to 10 keV in *XMM-Newton* data of 2004. However, the flux contribution of the low-energy log-parabola in the (0.5-2) keV range is only

Table 8.8.: SED model parameters* of PKS 2004–447

SED	$\log_{10}(K_1^a)$	α_1	β_1	$\log_{10}(K_2^a)$	α_2	β_2	$\nu F_{\nu,1}^b$	$\nu F_{\nu,2}^b$	ν_1^c	ν_2^c
s1	8.25	1.50	0.46	−5.60	1.50	0.075	23.96	2.72	6.57×10^{12}	5.20×10^{21}
s2	8.47	1.40	0.48	−5.30	1.50	0.080	44.97	4.83	7.93×10^{12}	3.21×10^{21}
s3	8.30	1.40	0.48	−5.52	1.50	0.075	29.98	3.27	7.93×10^{12}	5.20×10^{21}
s4	8.41	1.40	0.48	−5.22	1.50	0.075	38.97	6.54	7.93×10^{12}	5.20×10^{21}
s5	8.41	1.40	0.46	−5.00	1.50	0.085	39.71	8.69	8.46×10^{12}	2.17×10^{21}
s6	8.20	1.45	0.44	−4.34	1.40	0.085	23.13	8.24	7.93×10^{12}	8.18×10^{21}
s7	8.36	1.40	0.46	−4.22	1.40	0.085	35.13	10.80	8.46×10^{12}	8.18×10^{21}

Note:

* The parameters were adapted by hand and do not represent an actual fit using a likelihood minimization algorithm. The purpose of this parametrization is to compare the relative spectral shape with among different source states.

^a Normalization in units of $\text{photons cm}^{-2} \text{s}^{-1} \text{keV}^{-1}$

^b peak flux of the log parabola in units of $10^{-12} \text{ erg cm}^{-2} \text{s}^{-1}$

^c peak frequency of the log parabolic model in units of Hz

$\sim 6 \times 10^{-15} \text{ erg cm}^{-2} \text{s}^{-1}$. Thus, it cannot account for the tentative soft excess observed in X-2004-04-11 (see Sect. 8.3).

Discussion

In previous studies, G06 have modeled the SED of PKS 2004–447 from the radio band to hard X-ray band using a simple one-zone synchrotron self-Compton (SSC) model. They find that the X-ray spectrum required an additional non-thermal emission component of $(1.2 \pm 0.4) \times 10^{-14} \text{ erg s}^{-1} \text{cm}^{-2} \text{keV}^{-1}$ at 2 keV to explain the data. They argue that the X-ray spectrum is dominated by thermal Comptonization in addition to a weak SSC component that gives rise to the tentative soft excess. Paliya et al. (2013) also modeled the averaged SED over several month in 2011 using *Swift* and *Fermi-LAT* data. They fitted a jet-emission model that consisted of an SSC and an external Compton component in the high-energy range. A thermal Comptonization component was not needed to fit the X-rays. They concluded that the SED of PKS 2004–447 resembles the distribution of flat-spectrum radio quasars (FSRQ). For these sources, hard X-ray emission above 2 keV is interpreted as inverse-Compton emission (either SSC or external Compton radiation), which suggests a non-thermal jet origin for the X-ray spectrum of PKS 2004–447.

From our analysis with a phenomenological log parabola model, it is obvious that the X-ray emission belongs to the high-energy hump of the SED. In contrast, the optical/UV emission lies at the declining part of the low-energy emission hump with a corresponding peak frequency of $\nu_1 \sim 10^{12} \text{ Hz}$. This low-energy emission may be associated with either synchrotron jet emission or thermal emission of the host galaxy or accretion disk.

Further evidence for a dominating synchrotron contribution to the optical band, comes from modeling different emission states. The series of SEDs can be described with two

log parabolas which mainly vary in their peak flux. This result suggests that at the optical emission varies in the same way as the X-ray band and is dominated by jet emission originating from the same particle population as the X-rays. This can also be observed in the multiwavelength lightcurve, which shows tentative evidence for simultaneous variations in the optical to γ -rays. For blazars such correlation between the optical and X-ray band implies synchrotron and self-synchrotron Compton radiation of relativistic particles within the radio jet. In this case, the optical radiation resides at the declining part of the synchrotron spectrum (with a peak frequency in the range of low-frequency peaked BL Lac objects) and the X-rays trace the spectral rise of the inverse Compton upscattered component. For the purpose of discussion, we assume based on the arguments above, that the optical/UV emission can be associated with synchrotron emission from the relativistic radio jet, while the X-ray band is dominated by SSC emission.

This conclusion is consistent with findings of a stationary SED in previous studies (Abdo et al. 2009c; Paliya et al. 2013). However, it contradicts the interpretation of G06. The different interpretations stem from a different treatment of the radio data in the study of the source SED in G06. The authors included ATCA data as well as the optical/UV data in their synchrotron fit model. This yielded a broader and weaker synchrotron hump than in our description. Subsequently, the resulting inverse Compton emission from this component was not strong enough to fully account for the X-ray data. We note, that this approach also underestimates the γ -ray emission assuming the γ -ray flux in 2004 was similar to the one in 2011 (compare set S2), when the radio to X-ray spectrum matched that in 2004.

As already reported by S16, there is evidence for radio spectral variability, but especially at 9 GHz to 19 GHz the flux density is consistent with the data from 2004, while emission of the optical/UV to X-ray band vary significantly compared to their values in 2004 and similar to the γ -ray band. Since the single-dish observations cannot resolve the jet, we conclude that the radio emission does not come from the same region as the compact high-energy emission but originates from a larger emission region and includes the whole radio source. The low amplitude of the radio fractional variability with respect to X-rays supports this explanation. A larger emission region also explains the lack of correlated variations between the radio and X-ray band due to restrictions of the light traveling times.

8.5. The nature of PKS 2004–447

In the following sections we thus discuss the results of this work in the context of CSS/GPS and in comparison with the other well-studied γ -NLS1.

A young jet source? Comparison with CSS sources

CSS and gigahertz-peaked spectrum (GPS) galaxies are bright radio sources, which are considered to be young radio galaxies based on their peaked radio spectra and compact jet structure (e.g., O’Dea 1998; Stanghellini 2003; Fanti et al. 2011; Randall et al. 2011, and

references therein). The same scenario has been discussed for γ -NLS1 due to their low black hole masses and high accretion rates (e.g., Foschini et al. 2015; Berton et al. 2015). However, these conclusions are based on black hole mass measurements of γ -NLS1 which might be underestimated (Baldi et al. 2016; Calderone et al. 2013).

As part of the TANAMI VLBI program, PKS 2004–447 is regularly observed at 8.4 GHz. The first milliarcsecond resolution image from 2010 has been analyzed and discussed in S16. The image shows an extended one-sided jet with a dominant compact VLBI core and a high brightness temperature, $T_b = (5.7 \pm 1.4) \times 10^{10}$ K. As the source is not resolved in archival VLBI data at 1.5 GHz from the VLBA and VLA, we derive an upper limit of the projected large-scale size ~ 11 kpc. The compactness of the source, along with its steep radio spectrum is consistent with the classification of Compact Steep Spectrum (CSS) radio sources. Given its classification as γ -NLS1, the CSS morphology of PKS 2004–447 plays an important role for the link between γ -NLS1 and CSS sources.

Beside PKS 2004–447, there are two significant detections of a compact GPS/CSS sources by *Fermi*-LAT (PKS 1718–649 and PMN 1603–4904, Migliori et al. 2016; Müller et al. 2016a, respectively). In X-ray, these objects show evidence for the presence of Seyfert-like components, such as a Fe $\kappa\alpha$ line (Müller et al. 2015) or complex variable absorption (e.g., Beuchert et al. 2018, accepted for publication in A&A). We note, that these sources are most likely young radio galaxies, seen at a larger angle between the line of sight and the jet axis. The dominance of jet emission in PKS 2004–447 may result from a smaller viewing angle between the line-of-sight and jet axis.

The X-ray properties of a sample of GPS/CSS quasars have been studied by Siemiginowska et al. (2008, S08 hereafter), Kunert-Bajraszewska et al. (2014), and Siemiginowska et al. (2016). In most cases, the linear size of GPS/CSS sources in radio is smaller than the spatial resolution of current X-ray instruments. This means that X-ray emission from the entire complex radio structure (i.e., core, jet, and hot spots) is contained within the extraction region of the X-ray point source. Their X-ray spectra can typically be modeled well by a featureless power law. The power-law indices range from 1.5 and 2.2, with the majority between 1.7 and 2. Their photon index is typically close to those of radio-quiet quasars, but there are cases where the power law is flat, similar to radio-loud sources. S08 report that for these cases, the X-ray emission can be associated with emission from the radio structure. The X-ray absorption-corrected luminosities of GPS/CSS sources are in the range of $(10^{44} - 10^{46})$ erg s $^{-1}$. The X-ray photon index and unabsorbed luminosity of PKS 2004–447 thus agree with properties of low-powered CSS sources, where the radio jet contributes to the X-ray spectrum.

For some GPS/CSS sources, S08 find more complex spectra with evidence of intrinsic absorption of $\sim 10^{-21}$ cm $^{-2}$ and/or a soft excess. The (0.5-2) keV flux contribution of the latter is on the order of 10^{-14} erg cm $^{-2}$ s $^{-1}$. The origin of this emission is not yet well understood. Different theoretical predictions include thermal emission through jet-gas interactions with the interstellar medium. The flux of the tentative soft excess of PKS 2004–447 in the soft band is consistent with findings by S08. In the context of CSS sources, this may indicate interaction between the young radio jet and the surrounding medium, but further studies are necessary.

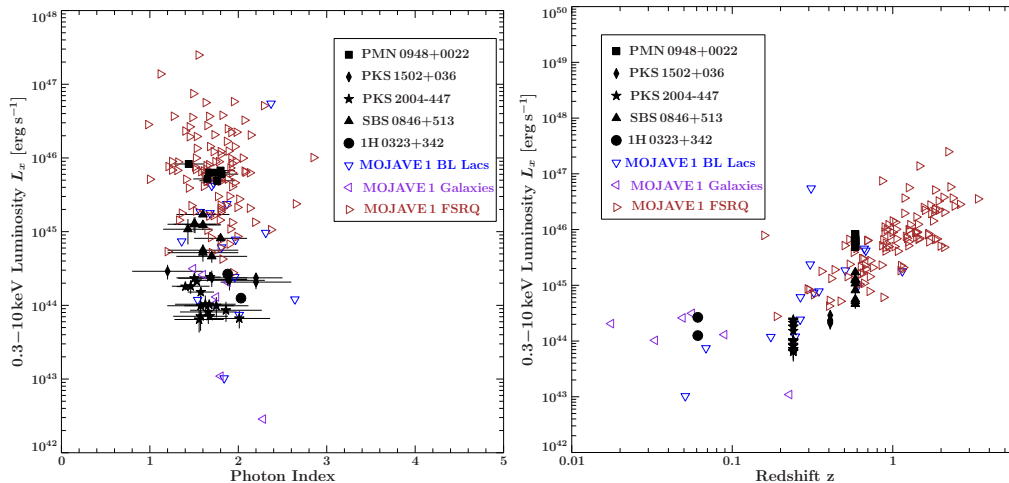


Figure 8.15.: *Left panel:* X-ray luminosity L_X in the (0.3–10) keV band as a function of photon index for γ -NLS1 galaxies in this paper (black filled symbols) and the MOJAVE 1 sample (open symbols). *Right panel:* Comparison of (0.3–10) keV X-ray luminosity L_X as a function of redshift z for the MOJAVE 1 sample (open symbols) and γ -NLS1 sources (black filled symbols) discussed in this paper.

One of a kind? Comparison with other γ -NLS1s and blazars

Foschini et al. (2015) have studied the multiwavelength properties of 43 radio-loud NLS1 galaxies, including the seven γ -NLS1 known so far. PKS 2004–447 is the second closest γ -NLS1. It is also the radio-loudest and only southern-hemisphere source in the small sample. But most strikingly, it is the only CSS source in the sample so far. One should note, that Karamanavis et al. (2017) reported another steep spectrum NLS1, RX J2314.9 + 2243 within the F-GAMMA project. However, there is only a tentative detection at γ -rays, yet.

Besides PKS 2004–447, the sources that have been studied in the most detail so far are PMN J0948+0022, PKS 1502+036, 1H 0323+342, and SBS 0846+513 (Abdo et al. 2009c,a; D’Ammando et al. 2012, 2014b; Yao et al. 2015). Information on their X-ray properties is taken from the literature (Zhou et al. 2007; Yuan et al. 2008; Abdo et al. 2009c; D’Ammando et al. 2012, 2014b, 2013a; Paliya et al. 2013; Rivers et al. 2013; Bhattacharyya et al. 2014; Yao et al. 2015). Table 8.9 provides results of the simplest best-fit model for each source.

In the radio band, we observe that the 15 GHz luminosities span two orders of magnitude, and both flux and spectral variability are observed in all sources, though the persistent step radio spectrum in PKS 2004–447 is unique in this sample (S16). For comparison, we include results for PKS 2004–447 from Sect. 8.3 averaged over all observations.

All five γ -NLS1 objects show moderate X-ray flux variability. Only the closest, γ -NLS1

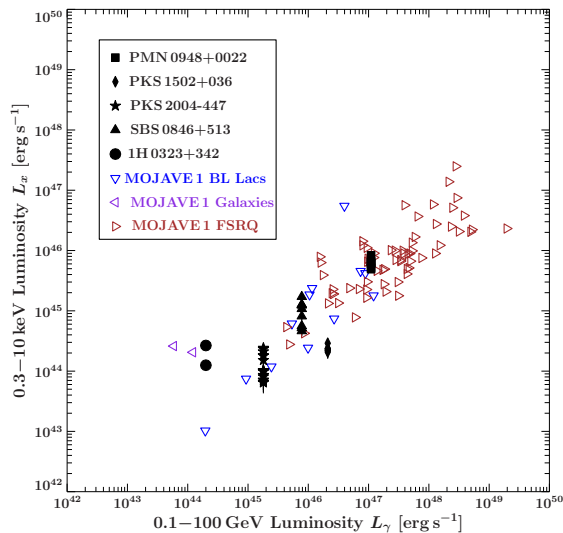


Figure 8.16: Comparison of (0.3–10) keV X-ray luminosity L_X as a function (0.1–100) GeV luminosity L_γ of the MOJAVE 1 sample (open symbols) and γ -NLS1 sources (black filled symbols) discussed in this paper.

(1H 0323+342), shows flaring activity on timescales of days (Paliya et al. 2014; Yao et al. 2015). No evidence was found of absorption beyond the Galactic value in any of these objects. It is therefore reasonable to conclude that variations in flux imply changes in the luminosity and/or spectral shape, rather than changes in the obscuration of the primary radiation. Spectral variability is observed in two cases (PKS 2004–447, 1H 0323+342) and suspected in two more (PKS 1502+036, PMN J0948+0022).

Results from X-ray analyses reported in the literature mentioned above were used to calculate the X-ray luminosities using the K correction by, for example, Ghisellini et al. (2009). In Figure 8.15, we show the X-ray luminosities of γ -NLS1s as a function of the photon index. The luminosities span a range of almost two orders of magnitude from 10^{44} erg s $^{-1}$ to 10^{46} erg s $^{-1}$, while the photon indices ranges from 1.2 up to 2.2. However the majority of Γ cluster between 1.5 and 1.8.

We compare this to the X-ray properties of blazars forming a statistically complete sample of radio-selected extragalactic jets (MOJAVE 1, Lister & Homan 2005) that were detected by *Fermi*-LAT (see Figs. 8.15 and 8.16). The X-ray data on the MOJAVE 1 sources were obtained from single *Swift* observations (Chang 2010). X-ray luminosities of the γ -detected MOJAVE 1 sources span a wider range from 10^{42} erg s $^{-1}$ to a few 10^{47} erg s $^{-1}$. In Figs. 8.15 and 8.16, we show the X-ray luminosity of both samples as a function of the redshift and γ -ray luminosity taken from the 2FGL catalog (Nolan et al. 2012). For each γ -NLS1 source, we used the weighted mean of the X-ray luminosities from different observations. The blazar distribution shows the known sequence from high-luminosity FSRQs detected at high redshifts to lower luminosity BL Lac objects observed at lower redshifts (see, e.g., Fossati et al. 1998). The X-ray and γ -ray luminosities of γ -NLS1 lie in the same range as blazars. More intriguingly, their luminosities fall into a region that is occupied by BL Lac objects and low-luminosity FSRQs. This result is consistent with the findings of Paliya et al. (2013), who analyzed non-simultaneous SEDs of two γ -NLS1s, namely PKS 2004–447 and PKS 1502+036. In comparison to the

Table 8.9.: Overview of X-ray spectral properties of γ -ray emitting and radio-loud NLS1 galaxies.

Source	Redshift	Model	$\Gamma_{\text{soft}}^{\text{a}}$	$\Gamma_{\text{hard}}^{\text{b}}$	E_{B}^{c}	F_{X}^{d}	Variability ^e	Ref
1H0323+342	0.061	PL	-	2.02 ± 0.06	-	14.0 ± 0.1	F/S	(1)
PKS 1502+036	0.409	PL	-	1.7 ± 0.2	-	0.3 ± 0.7	F/(S)	(2)
PKS 2004–447	0.240	PL	-	1.58 ± 0.11	-	0.7 ± 0.4	F/S	(*)
PMN J0948+0022	0.585	BPL	$2.14^{+0.03}_{-0.02}$	$1.48^{+0.04}_{-0.03}$	$1.72^{+0.09}_{-0.11}$	$4.59^{+0.03}_{-0.05}$	F/(S)	(3)
SBS 0846+513	0.584	PL	-	1.47 ± 0.25	-	0.8 ± 0.4	F	(4)

Note: Overview of spectral parameters of known γ -ray and radio-loud NLS1 galaxies for the simplest best-fit models in the literature. ^aPhoton Index, in the case of PMN J0948+0022 γ_1 represents the photon index before the break energy. ^bPhoton Index after the break energy of the broken power law. ^cBreak energy in units of keV of the broken power law. ^dX-ray flux in units of $10^{-12} \text{ erg s}^{-1} \text{ cm}^{-2}$ in the range of (0.3–10) keV in case of PMN J0948+0022, PKS 1502+036, and SBS 0846+513, and (0.2–10) keV for 1H0323+342. ^eVariability of the X-ray spectrum. Flux variability is denoted as F, spectral variability as S. Indications of variability that has not been confirmed are shown in parenthesis. **References:** (1) Abdo et al. (2009c); (2) Paliya et al. (2013); (3) D’Ammando et al. (2014b); (4) D’Ammando et al. (2012); (*) this work.

SED of a typical BL Lac and FSRQ source, they found that their broadband spectra can be regarded as intermediate between both blazar types, although they bear a closer resemblance to the SED of FSRQs. Similar results have been obtained by Foschini et al. (2015).

In comparison to other γ -NLS1 and blazars, X-ray and γ -ray properties of PKS 2004–447 are compatible. As for the SED, the source is similar to low-powered blazars. With respect to γ -NLS1, it is interesting to note, that the jet emission plays a more dominant role in the optical spectrum of PKS 2004–447 than in the other five γ -NLS1 Abdo et al. (2009a). The most striking difference is seen in the radio morphology of PKS 2004–447. So far, it is the only CSS source among NLS1, that have been significantly detected at γ -rays. The tentative detection of RX J2314.9+2243 might be just a matter of sensitivity.

8.6. Summary and future work

In this chapter, I presented the first longterm multiwavelength variability study of the peculiar active galaxy PKS 2004–447. The detailed X-ray spectroscopy revealed a persistent hard non-thermal spectrum, which only moderately varied in spectral shape and brightness. Using multiwavelength information, this emission could be associated with the high-energy emission from the relativistic radio jet. Analysing the SED at different source flux states allowed us to relate the optical emission to the low-energy synchrotron emission of the jet.

With respect to earlier studies of this source, we confirm that a non-thermal jet emission dominates the whole SED at the given spectral resolution, which is reminiscent of low-powered blazars. Surprisingly, the detailed spectral analysis of the high-SNR *XMM-Newton* data from 2004 shows tentative evidence for excess emission in the X-ray band

below 1 keV, which was not detectable at a lower flux state in 2012. The existence of this excess emission in PKS 2004–447 is still an open question. Contrary to G06, we can exclude a significant contribution of the synchrotron radiation from the relativistic radio jet based the description of the SEDs.

In order to test and analyse this component, we have obtained simultaneous *XMM-Newton* and *NuSTAR* observations of the source, complemented by *Swift* monitoring snapshots in May 2016. Since the tentative soft excess component was only observe in 2004 in a high-flux state, the objective of these snapshots is monitor the source flux. A flux state similar to 2004 would trigger the high-SNR *XMM-Newton* and *NuSTAR* observations. The combination of these instruments will provide a high-SNR spectrum from 0.5 keV up to 50 keV and allow us to better constrain the hard X-ray spectrum. This knowledge is necessary to pin down the excess emission in the soft spectrum. In addition, since different models for the soft excess predict different hard X-ray signatures, we can use the *NuSTAR* observation to analyze those. The results will be discussed in a future paper.

Among γ -NLS1, PKS 2004–447 remains peculiar due to its radio spectrum and because its formal classification as NLS1 has been doubted due to its weak optical Fe II emission. Earlier studies of the source optical spectrum did not take into account the contribution of jet emission. Therefore, Fe II emission may be underestimated. We performed multiple spectroscopy observations of the optical spectrum of PKS 2004–447 with FORS2 aboard the VLT in the (4400–5400)Å wavelength range. This range contains the important line emission of the Fe II complex, H β and [O III]. The high-SNR and spectral resolution provided by the FORS2 allows for a careful analysis of the iron emission as well as the broad and narrow component of H β . From the broad H β line, we will determine FWHM(H β) with respect to the continuum. We performed multiple observations to further test for longterm and intranight variability. The data will be discussed in a future publication.

In our analysis of VLBI images at 8.4 GHz and 1.5 GHz confirmed the compact steep spectrum classification (see S16). In this work, we find that also the X-ray properties are in agreement with this classification. The classification as γ -NLS1 and CSS source makes PKS 2004–447 an interesting object to study the link between these two types of objects and test the scenario of young radio galaxies.

9. Time-resolved high-energy emission in Mrk 421

The previous sections demonstrated how source classification benefits from the combination of spectral and timing analysis. In this section, I present two years of multi-wavelength monitoring observations of the blazar Mrk 421 to explore its non-thermal jet emission in the spectral and time domain to draw conclusions on the emission region and particle population.

As described in Sect.3.2.4, Blazars are a subclass of active galactic nuclei with relativistic jets closely aligned to our line of sight. They emit highly variable radiation across the whole electromagnetic spectrum from radio to very high energies. A distinct feature of blazars is their extreme variability on time scales from minutes to years (e.g., Wagner & Witzel 1995b; Aleksić et al. 2014a,b; Tavecchio et al. 2010; Hayashida et al. 2015). While spectral modeling of their stationary spectral energy distribution is degenerated, further constraints of jet emission processes can be drawn from studying the variability pattern of their non-thermal high-energy emission (e.g., Weidinger & Spanier 2015).

In order to break down spectral model degeneracies and to draw conclusions on the emission region and mechanisms, collaborators and I have set up a multiwavelength monitoring program of blazars. For this program, I have successfully obtained the necessary observing time of several X-ray satellites (e.g., *XMM-Newton*, *Swift*, and *INTEGRAL*) and coordinated the data analysis and target-of-opportunity observations for these satellites for all sources in the sample. The aim of this program is to gather unprecedented time-resolved SED of blazars during a TeV outburst. In this chapter I present the first long-term multiwavelength (MWL) study of data acquired for the blazar Mrk 421 within this program between 2015 and 2017. I exploit the timing domain and perform a time-resolved study of the source's high-energy spectrum.

An overview of the Blazar MWL Program as well as its targets and observational details is given in Sect. 9.1. The following sections focus on the study of the long-term multiwavelength monitoring data of Mrk 421. Sect. 9.2 describes the observations and data processing of the various used instruments. I perform a basic variability analysis and study the inter-band cross-correlation of the X-ray and broadband emission in Sects. 9.3 and 9.4, respectively. The derived time-resolved SEDs are presented in Sect. 9.5. In Sect. 9.6 I discuss the results of this analysis and summarize the conclusions in Sect. 9.7. Since this study is an ongoing projects.

9.1. The Blazar Monitoring Program

Our multiwavelength program makes use of a combination of simultaneous observations in the X-ray and TeV energy bands that are triggered on our dense monitoring in these bands. The combination of the blazar TeV monitoring program conducted by the *First G-APD Cherenkov Telescope* (FACT) (Anderhub et al. 2011, 2013b) with quasi-simultaneous observations with *XMM-Newton*, *INTEGRAL*, *Swift*, and *Fermi*, offers the possibility to collect a superior data set.

The largest fraction¹ of identified blazars detected at TeV energies are *high synchrotron-peaked BL Lac* (HSP or HBL) objects (see Sect. 3.1.2 for information on blazars or Fig. 3.3). Accordingly, our targets are bright HBLs within the FACT sample. The low-energy synchrotron emission in these sources peaks above 10^{15} Hz (Fossati et al. 1998). Thus, using an observed energy range from optical to very high energies covers both the low and high-energy humps of their SED. The low-energy hump of the synchrotron radiation is observed by combining optical and X-ray measurements of *Swift* or *XMM-Newton*, while high-resolution observations of *INTEGRAL* IBIS/ISGRI above 10 keV covers the declining part of the synchrotron hump as well as the transition to the high-energy hump. Fermi/LAT and FACT data supplement the rise and decline of the high-energy emission in the γ -ray and TeV band.

The objective of our program are continuous observations of both the synchrotron and high energy component of a strong blazar flare. The biggest limitation of existing multiwavelength-campaign data sets are observational data gaps, missing pre or post-flare information or too short SED monitoring time ranges. For this reason, the program is set up of a combination of long-term temporal and wide-band spectral coverage which complement each other and are explained in more detail below. The sample currently comprises three sources Mrk 501, 1ES 1959+650, and Mrk 421. In this work, I will present an exemplary study of Mrk 421. This source has been the most variable among the three during the monitoring so far. Monitoring data of Mrk 501 (which was in a quiescent state) has been analysed and published in the bachelor thesis by Sin (2017) under my supervision. HBL 1ES 1959+650 exhibited a bright TeV and X-ray flare in 2016. The analysis of these multiwavelength data, for which I contributed to the reduction and spectral modelling of the *Swift* XRT data, is reported in Shukla et al. (2018).

9.1.1. Long-Term Monitoring at TeV and X-ray energies

The first component of the blazar MWL program is a continuous long-term monitoring of the TeV γ -ray emission, conducted by FACT (see Sect. 4.2.2), and a weekly optical/UV and X-ray monitoring by *Swift*. Within the visibility windows of a target FACT conducts nightly observations of at least 1 hour in the very high energy band. X-ray data are provided by weekly scheduled 1 ks *Swift*/XRT (0.3–12 keV) observations during the overlap of the visibility windows with FACT, *INTEGRAL*, and the *Swift*/BAT (15 keV–150 MeV) monitoring program (see Table 9.1). While FACT is a TeV program, dedicated to blazar

¹see TeVCat <http://tevcap.uchicago.edu/>

Table 9.1.: Combined visibility windows of FACT, *INTEGRAL* and *Swift* for all targets.

Cycle	Mrk 421	Mrk 501	1 ES 1959+650	Approved ToO Time
mc14*	2014 May 01 - May 30 2014 Nov 23 - Dec 14	2014 Jul 12 - Sep 03 2015 Feb 17 - Apr 05	2014 May 03 - Sep 26 -	500 ks ^I , 20 ks ^s , 0 ^x
mc15	2015 Apr 21 - Jun 05 -	2015 Feb 10 - Apr 21 2015 Jun 26 - Sep 15	- -	500 ks ^I , 20 ks ^s , 0 ^x
mc16	2016 Apr 21 - Jun 18 2016 Dec 01 - Dec 24	2016 Jan 27 - Apr 20 2016 Jun 26 - Oct 03	- -	500 ks ^I , 20 ks ^s , 100 ks ^x
mc17	2017 Apr 23 - Jun 20 2017 Nov 06 - Dec 14	2017 Jan 25 - Apr 17 2017 Jul 11 - Oct 05	2017 Apr 10 - Nov 20 -	500 ks ^I , 20 ks ^s , 100 ks ^x 500 ks ^I , 20 ks ^s , 100 ks ^x

Note: The combined visibility windows were defined by the overlap of the visibilities for each instrument. *INTEGRAL* windows were defined to ensure at least 400 ks of exposure. For *XMM-Newton* windows, we require at least 80 ks of visibility. FACT windows are constrained by nights of strong moon containment and limits on the zenith angle. ^I *INTEGRAL*, ^s *Swift*, ^x *XMM-Newton*, * mc: monitoring cycle

Table 9.2.: Overview of accepted proposals for the blazar monitoring program

Proposal ID	Cycle (Observing period)	PI	granted observing time
Joint <i>Swift</i>–<i>INTEGRAL</i> program:			(<i>Swift</i> / <i>INTEGRAL</i>)
1240032	AO–12 (1/2014–12/2014)	A. Kreikenbohm	46 ks (ToO +monitoring)/ 500 ks (ToO)
1340027	AO–13 (1/2015–12/2015)	A. Kreikenbohm	56 ks (ToO +monitoring)/ 500 ks (ToO)
1440026	AO–14 (1/2016–12/2016)	A. Kreikenbohm	56 ks (ToO +monitoring)/ 500 ks (ToO)
1540029	AO–15 (1/2017–12/2017)	K. Leiter	68 ks (ToO +monitoring)/ 500 ks (ToO)
<i>XMM-Newton</i> program:			
078397	AO–15 (5/2016 – 4/2017)	A. Kreikenbohm	118 ks (ToO*) for Mrk 501 & Mrk 421
080431	AO–16 (5/2017 – 4/2018)	K. Leiter	79 ks (ToO*) for 1 ES 1959+650

Note: * Accepted ToO proposals by *XMM-Newton* can be triggered within 3 subsequent observing cycles.

monitoring, we obtained *Swift* monitoring observations by applying for independent joint *Swift*–*INTEGRAL* proposals, which are summarized in Table 9.2.

The combination of these observatories allows for a quick detection of a flare in TeV energies and provides pre- and post-flare SED information of the source. In addition, the monitoring offers a great opportunity to distinguish between a strong time lag of flares in different energy bands as well as an orphan flare. The short *Swift* snapshots during the overlap of FACT and *INTEGRAL* visibility windows are used to monitor the source flux and exclude a false positive identification of an orphan flare.

9.1.2. Broadband target-of-opportunity observations

Our science goal of time-resolved SEDs during a blazar outburst requires a strong flare lasting long enough to be observed simultaneously by numerous instruments. Further restrictions arise from the overlap of visibility windows of all participating observatories. Table 9.1 lists the combined visibilities for FACT, *Fermi*-LAT/LAT, *INTEGRAL*, *Swift*, and *XMM-Newton*. On average the overlap sums up to a few weeks per source and monitoring cycle (mc).

Upon a bright TeV flare seen by FACT, a series of highly-sensitive optical/UV and X-ray observations are triggered, involving long and simultaneous observations of *XMM-Newton*, *INTEGRAL*, and *Swift*. The duration of these observations is estimated based on the duration of the flare under the assumption that it is caused by cooling of accelerated electrons. FACT provides a quick-look analysis of the data during its acquisition. Thus, allowing us to react quickly to an outburst. The trigger is an FACT event rate above a certain threshold, which is regularly optimized depending on the calibration of the camera.

Among the above mentioned X-ray satellite missions, *Swift* has the shortest reaction time and observes the source within hours after the trigger. The strategy for *Swift* is to perform short snapshots of 1 ks to 2 ks once per day for 25 days after the flare to obtain detailed post-flare information. Additionally, the first *Swift* observations serve as bridge between the trigger and the start of *XMM-Newton* and *INTEGRAL* pointings. *XMM-Newton* performs a long continuous exposure (40 ks to 80 ks) upon trigger. The data enables us to follow the X-ray spectral evolution with a time-resolution of hours. Subsequent short exposures take place daily until the end of the *INTEGRAL* observation. The latter consists of 500 ks as soon as possible after the trigger alert. Depending on the brightness of the flaring source, these observations can be split into multiple spectra during data reduction to resolve the spectral evolution of the hard X-ray emission during the outburst.

In the high-energy regimes, FACT will continue to observe the flaring source and we make use of the continuous monitoring by *Fermi*-LAT. Figure 9.1 shows a schematic view of the multiwavelength observation schedule.

9.1.3. The HBL Target Mrk 421

Markarian 421 (Mrk 421, $z=0.031$, Ulrich et al. 1975) is located in a distance of ~ 134 Mpc and is among the closest TeV blazars. The AGN is optically identified with a very bright elliptical galaxy (e.g., Ulrich et al. 1975; Kikuchi & Mikami 1987) which harbors a central supermassive black hole of $M_{\text{BH}} = 10^{8.29} M_{\odot}$ (Wang et al. 2004). Mrk 421 is also one of the most luminous sources in the high-energy sky. It was the the first extragalactic object that was observed at TeV energies (Punch et al. 1992) and has been the target of many observing programs.

Several studies of the high-energy emission revealed that the source frequently exhibits rapid flares and outbursts at TeV and X-ray energies. TeV flares on timescales of days are commonly observed. Flare duration on the timescales of 15 minutes timescale are

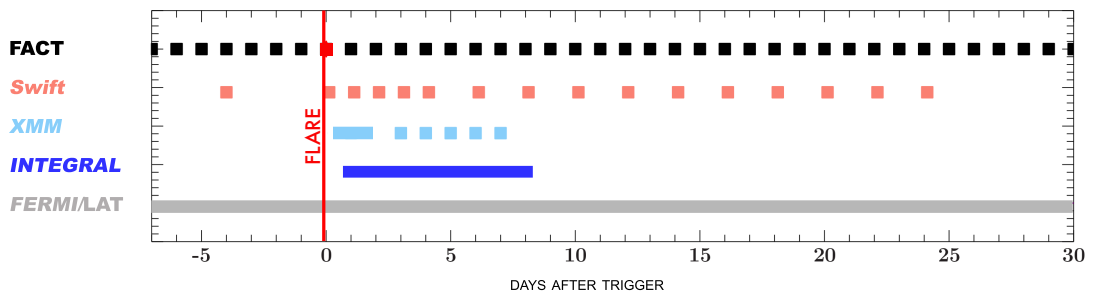


Figure 9.1.: Schematic overview of the multiwavelength ToO program. During the combined FACT and *INTEGRAL* visibility windows, a target’s state is monitored by FACT (nightly), *Fermi*-LAT (continuously), and *Swift* (weekly). As soon as the FACT event rate exceeds the trigger threshold (red vertical line) trigger alerts are sent to *Swift*, *XMM-Newton* and *INTEGRAL*. *Swift* snapshots of 1 ks to 2 ks serve as bridge between trigger and the start of high-sensitivity observations, as well as follow-up to study the source evolution over a period of 25 days. Deep high-sensitivity pointings are performed by *XMM-Newton* and *INTEGRAL*. The combined observations from optical to TeV energies cover both the low and high-energy hump of the target’s SED.

detected (Gaidos et al. 1996). Also, the X-ray flux has been observed to vary on timescales of hours to days (e.g., Kapanadze et al. 2016). These rapid flares are typical evidence² for beamed TeV emission. Gaidos et al. (1996) required high Doppler factors of $\delta \geq 9$ to explain the observed TeV and X-ray flares. Values between 10 to 15 were found in similar studies involving the observations of high-energy flares (e.g., Aharonian et al. 2005b; Aleksić et al. 2015b). Further support for high Doppler factors were found by fitting the broadband spectrum of Mrk 421 with basic leptonic synchrotron self-compton models (e.g., Bednarek & Protheroe 1997; Maraschi et al. 1999).

Being one of the closest blazars, the large-scale and parsec-scale radio structure of Mrk 421 has been imaged extensively by several authors (e.g., Piner et al. 1999; Charlot et al. 2006; Piner et al. 2010). Figure 9.2 shows a VLBI observation of the parsec-scale radio jet structure observed with the *Very Long Baseline Array* (VLBA). The contour images of the flux density show a bright, compact core with a collimated one-sided jet structure that extends up to a few parsec to the north-west. In contrast to expectations from the VHE emission, kinematic studies of the radio jet in Mrk 421 show the presence of a handful of emission components that are all either stationary or move slowly along the jet (e.g., Piner et al. 1999; Blasi et al. 2013; Lister et al. 2016). Piner et al. (1999) derived a an angle of $\theta \sim 0.4^\circ$ between the jet axis and the line-of-sight for the sub-parsec VLBI jet and an apparent jet speed of $\lesssim 0.3c$. The small viewing angle and subluminal motion are confirmed by more recent high-sensitivity VLBI studies, (e.g.,

²Simple light traveling arguments require very small emission regions to explained minutescale TeV flux variations. In the context of synchrotron and inverse Compton synchrotron emission such small region sizes yield high pair-production opacities that would hinder the escape of unbeamed TeV photons. High Doppler factors in jets seen under small viewing angles imply the existence of emission components that move superluminally within the jet which can be tested through highly sensitive VLBI radio observations.

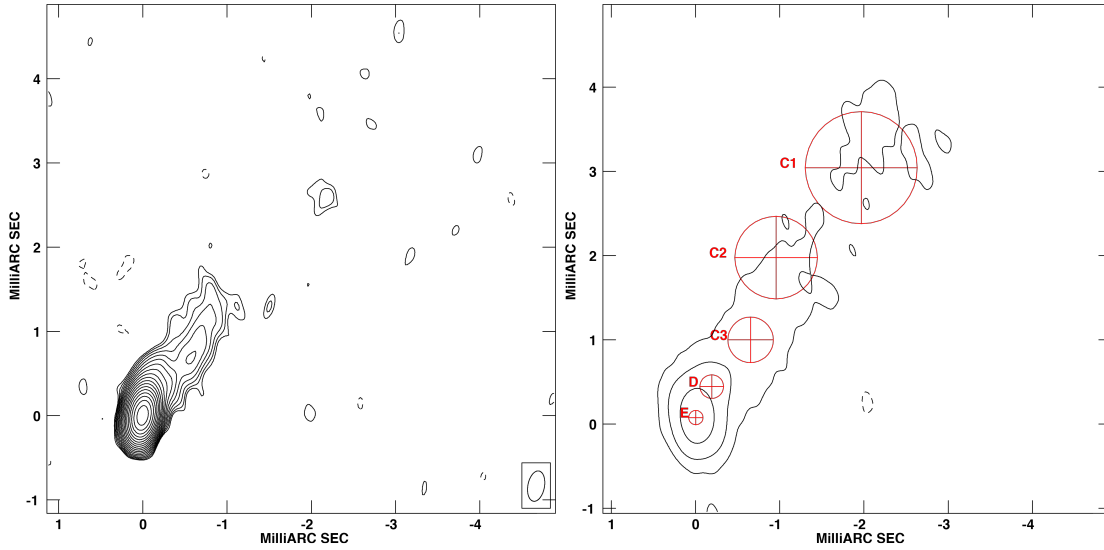


Figure 9.2.: Parsec-scale radio jet structure of Mrk 421 (Blasi et al. 2013). *Left:* VLBA image at 43 GHz from November 2011. The flux contours correspond to $(-1, 1, \sqrt{2}, 2, \dots) \times 0.55$ mJy/beam. *Right:* VLBA image from July 2011 at 43 GHz, contoured at $(-1, 1, 10, 100) \times 0.4$ mJy/beam. Overplotted are emission components (red) derived through fitting 2D Gaussian components to the data. By comparing model-fit of different observing epoch, the authors derived subluminal apparent component speeds between $0.02c$ and $0.24c$.

Piner & Edwards 2005; Charlot et al. 2006; Piner et al. 2010). For example, Blasi et al. (2013) constrained the viewing angle to be $2^\circ \leq \theta \leq 5^\circ$. Subluminal apparent speeds, such as observed in Mrk 421, is found in many TeV blazars and suggests that plasma in the radio emission region moves with low jet bulk velocities with a low Doppler factor δ . Mrk 421 is thus an example for the unresolved inconsistency of the bulk Doppler factors derived from radio and high-energy observations (see Sect. 3.2.4).

Due to its brightness and large variability, Mrk 421 has been the target of numerous multiwavelength observation in order to study the properties of TeV blazars and the origin of the high-energy emission. The broadband energy emission of Mrk 421 is dominated by non-thermal jet emission and shows two prominent humps (see Sect. 3.2). One being a polarized emission hump at lower energies from radio to X-rays which is associated with a distribution of relativistic leptons in the jet and that radiate via the synchrotron process. The other one is located at higher energies which peaks in the γ -ray band. The origin of this high-energy emission is still debated. Mrk 421 is highly variable at all frequencies on different timescales. The shortest one was measured by Gaidos et al. 1996, who detected TeV flux variability on timescales of ~ 15 minutes. Throughout the studies Mrk 421 shows different activity states: typical non-flaring activity states are referred to as *quiescent* or *low state*. Hence, flaring states are called *active* or *high state*. Aleksić et al. (2015a) studied the quiescent state over four months in 2009. They find that Mrk 421 shows significant variability in all bands, even though no bright flares were observed. The authors interpreted the broadband emission in the standard leptonic

one-zone SSC model (see Sect. 3.2.4). A strong flux correlation between emission in the X-ray and VHE γ -ray bands over the duration of the four months was found. A similar study was performed on the flaring state of Mrk 421 for 13 consecutive days in 2010 (Aleksić et al. 2015b). The strong correlation of the X-ray and VHE γ -ray flux could be confirmed during the flares. Their flux relation was relatively linear consistent with SSC, although a quadratic flux relation was also seen by Fossati et al. (2008) during a flare in 2001. The broadband emission during the 2010 flare was well described by a two-zone leptonic model including a flaring and a quiescent region. Bartoli et al. (2016) performed another extensive multiwavelength study over 4.5 years from 2008 until mid 2013. They observed several variations of the low and high energy SED humps which confirmed the flux correlation between the X-ray and VHE band over such long timescales. In addition, though statistically not correlated, they found that the GeV γ -ray and UV band show similar degrees of variability and suggested that emission in these bands may originate in co-spatial regions further downstream of the jet. Overall, the long-term, steady-state broadband spectral energy distributions of Mrk 421 is well described by both one-zone and multi-zone leptonic scenarios or hadronic models. So far, none of the known emission models could be ruled out. Detailed studies of the spectral evolution of the broadband spectrum during an outburst with information of the pre- and post flare state of the blazar are rare. A first time-series of the broadband spectrum of Mrk 421 on daily timescale has been reported by Aleksić et al. (2015b).

An investigation of the possible neutrino flux by Mrk 421 was presented by Petropoulou et al. (2016). Using time-dependent data from *RXTE*, *Whipple*, and *HEGRA*, they tested different hadronic models to estimate the expected neutrino flux on Earth. From SED modelling of Mrk 421 during a 13-day flare in 2010, they calculated the expected neutrino flux of high-energy neutrinos and found hints for a correlation between PeV neutrinos and γ -ray photons. The inferred mean neutrino event rate was ~ 0.57 events/year for energies above 100 TeV. However, they concluded that due to the short duration of the flare, a significant signal for IceCube would require the accumulation of similar flares over several years. An association of a neutrino event with Mrk 421 would be the smoking gun evidence for the presence of proton in the AGN jet.

9.2. Observations and data processing

In this section I present more than two years of the blazar monitoring data on Mrk 421. The set up of the campaign provides a dense monitoring of HBL blazars with weekly *Swift* and daily FACT observations during the defined visibility windows.

9.2.1. FACT data

Mrk 421 is continuously observed at TeV energies with FACT. In this thesis, I use preliminary light curves obtained between December, 2015, and May, 2016. For the night of the TeV flare, preliminary FACT spectra were extracted. The data reduction and extraction of light curves as well as spectra were performed and provided by the FACT team.

9.2.2. *Fermi*-LAT data

For the analysis of the *Fermi*/LAT (Atwood et al. 2009; Ackermann et al. 2012a) γ -ray data we used the *Fermi* Science Tools (v10r0p5) together with the reprocessed Pass 8 data and the P8R2_SOURCE_V6 instrument response functions. We performed the analysis in a region of interest (ROI) of 10° around Mrk421 in an energy range of 100 MeV to 300 GeV. We used a zenith angle cut of 90° and the GTMKTIME cut DATA_QUAL=1 && LAT_CONFIG=1 together with the LAT event class = 128 and the LAT event type =3. The background model used to extract the γ -ray signal includes a Galactic diffuse-emission component and an isotropic component. For the modeling of the diffuse components we used the Galactic diffuse emission model gll_iem_v06.fits and the isotropic diffuse model iso_P8R2_SOURCE_V6_v06.txt. The spectral parameters were estimated using the unbinned maximum-likelihood technique (Mattox et al. 1996) in the energy range 300 MeV to 300 GeV. All 3FGL sources within the ROI are contained in the background model and are fitted with a free normalization constant.

We used a free spectral index during the spectra calculation, while it was fixed to the value listed in the 3FGL catalog (1.77 ± 0.01) for the light curve analysis. A one and three-day as well as a one-week day binning were used to compute the *Fermi*/LAT γ -ray light curve, by applying a Bayesian-blocks analysis. To account for upper limits we adopted a threshold of $TS = 25$ for the spectra and $TS = 9$ for the light curves. The upper limit calculation is based on the method of Feldman & Cousins (1998).

For a series of time-resolved SEDs, we extracted eleven LAT spectra. For the description of the spectral shape, the spectra were individually fitted with a simple powerlaw. Due to the short time bins, the SNR of the spectra were low and no further complex model was assumed. Results of the power-law fits are summarized in Table 9.3. For the first two SED bins only an upper limit or single energy bin was retrieved. We found, that the MeV to GeV spectrum is variable in flux and consistent with constant spectral hardness.

9.2.3. *INTEGRAL* data

At hard X-rays, an *INTEGRAL* observed the target for of 200 ks from 2015 Dec 18 and 2015 Dec 20 after a trigger on Dec 17, 2015. We extracted data from the coded mask instrument *INTEGRAL*/IBIS within 20–40 keV. Above, the source spectrum drops significantly. We build a mosaic by using a set of 50 *INTEGRAL* available pointings (also called "science windows") between 2015 Dec 18 and 2015 Dec 20. Each science window is required to include Mrk 421 at a maximum distance of 14° from the pointing center of the instrument, which guarantees the use of the entire field of view of the IBIS detector from the fully coded field of view ($8.3^\circ \times 8^\circ$) to the zero-coded field of view ($29.1^\circ \times 29.4^\circ$). Mrk 421 is detected with a significance of 6.2σ and a count-rate of 0.5 counts/s. The flux density in the (20–40) keV band is $(3.1 \pm 0.6) \times 10^{-11} \text{ keV keV}^{-1} \text{ cm}^{-2} \text{ s}^{-1}$ at 30 keV. This value also considers the correction factor of 1.4, i.e., the RMS of the background significance.

Table 9.3.: Power-law fits to *Fermi*-LAT (0.1-300) GeV spectra

Spectrum	MJD start	MJD stop	Photon Index
S1	57372.5	57373.5	-
S2	57373.5	57374.5	-
S3	57374.5	57383.5	1.7 ± 0.2
S4	57383.5	57387.5	1.4 ± 0.2
S5	57387.5	57389.5	$2.2^{+2.1}_{-0.7}$
S6	57389.5	57393.5	1.6 ± 0.1
S7	57721.0	57744.5	1.7 ± 0.3
S8	57744.5	57752.5	1.8 ± 0.2
S9	57752.5	57758.5	1.7 ± 0.2
S10	57758.5	57762.5	$1.2.5^{+1.7}_{-0.6}$
S11	57762.5	57770.5	1.7 ± 0.3

9.2.4. *Swift* XRT data

We include all XRT observations performed since December 2015. They sum up to 209 exposures. All *Swift*/XRT data were processed with standard methods, using the most recent software packages (HEASOFT 6.15.1). The data were reduced, calibrated and cleaned by means of the XRTPIPELINE script using standard filtering criteria and the latest calibration databases. We selected single and double pattern events for observations in both photo counting (pc) and window timing mode (wt). Source and background light curves and spectra were extracted using circular areas with radii of 35 pixels for the source and an annular region of 35–50 pixels for the background region. For those observations taken in pc mode, three observations are affected by pile-up. In this case we adopted a annular source region of 20-35 pixels to exclude the affected inner pixels within the point spread function.

Analysis of the X-ray spectra

The source spectra were analyzed using ISIS v1.6.2 (Houck & Denicola 2000). The data were grouped to a signal-to-noise ratio $snr \geq 5$. Following Massaro et al. (2004a), we applied a log-parabolic model in the (0.5–10) keV energy range (ISIS syntax: `tbnew*logpar`),

$$F(E) = K (E/E_1)^{-(\alpha+\beta \log(E/E_1))} \text{ ph}/(\text{cm}^2\text{s keV}), \quad (9.2.1)$$

The free parameters of the model are the normalization K , the photon index α at a user-defined folding energy E_1 (fixed to 1 keV), and the spectral curvature β . This model has been found to well describe the X-ray emission of Mrk 421 in various emission states

(e.g. Massaro et al. 2004a; Tramacere et al. 2007; Sinha et al. 2015). The log parabola is modulated by Galactic HI absorption $N_{\text{H,Gal}} = 1.53 \times 10^{20} \text{ cm}^{-2}$, based on the Galactic Hydrogen LAB survey (Kalberla et al. 2005). The high-resolution ISM absorption model `tbnew`³ (Wilms et al. 2000) is used to account for neutral absorption. Cross-sections and abundances were taken from Verner et al. (1996) and Wilms et al. (2000), respectively.

From the best-fit results we computed the energy E_{peak} of the peak flux of the log-parabolic,

$$E_{\text{peak}} = E_1 10^{(2-\alpha)/2\beta} \text{ keV}. \quad (9.2.2)$$

This energy is an estimate on the position of the synchrotron peak in the SED of Mrk 421 assuming a single emission region. The model yielded good fits for all of the observations. Table B.1, in the appendix, shows the results for all observations in cycle mc15, mc16, and mc17. Fluxes in the (0.5–10) keV range were computed from the best-fit model using the convolution model `cflux`.

9.2.5. *Swift* UVOT data

We used measurements in the optical and UV energy bands, that were performed simultaneously to the X-ray observations using *Swift* Ultraviolet/Optical Telescope (UVOT; Roming et al. 2005). The instrument obtained data in ultraviolet band-passes, UVW1, UVM2, and UVW2 with central wavelengths of 260 nm, 220 nm, and 193 nm, respectively. The Level 2 products were used to extract photometry information using the standard UVOT routines `uvotimage` and `uvotpha`. Count rates were extracted from a 5 arcsec circular source region around Mrk 421. The background was taken from an annulus also positioned on the source with inner and outer radius of 40 arcsec and 60 arcsec, respectively. In this way, flux measurements were obtained for 77 observations.

In case of the remaining observations the summation of different UVOT images was not possible using standard pipeline products due to missing aspect corrections. A correction of the image coordinates (via `uvotskycorr`) was determined and applied, however, this was not successful in all cases because of stray light of a nearby bright star in the FOV. Hence, for these 77 observations photometry data was extracted manually for every image using the routine `uvotsource`. The source region was selected from an unaffected UVOT image. In case of 35 observations there were no UVOT images.

In total, it was possible to obtain UV flux information for 174 observations mainly in the UVW1 filter. All UV fluxes were corrected for Galactic extinction with $EB - V = 0.015 \text{ mag}$ (Schlegel et al. 1998) at each spectral band (Fitzpatrick 1999). The corrected flux densities for each filter are shown in Fig. 9.4.

³Wilms, J., Jutt, A. M., Schulz, N. S., Nowak, M. A. (2012), published at <http://pulsar.sternwarte.uni-erlangen.de/wilms/research/tbabs/>

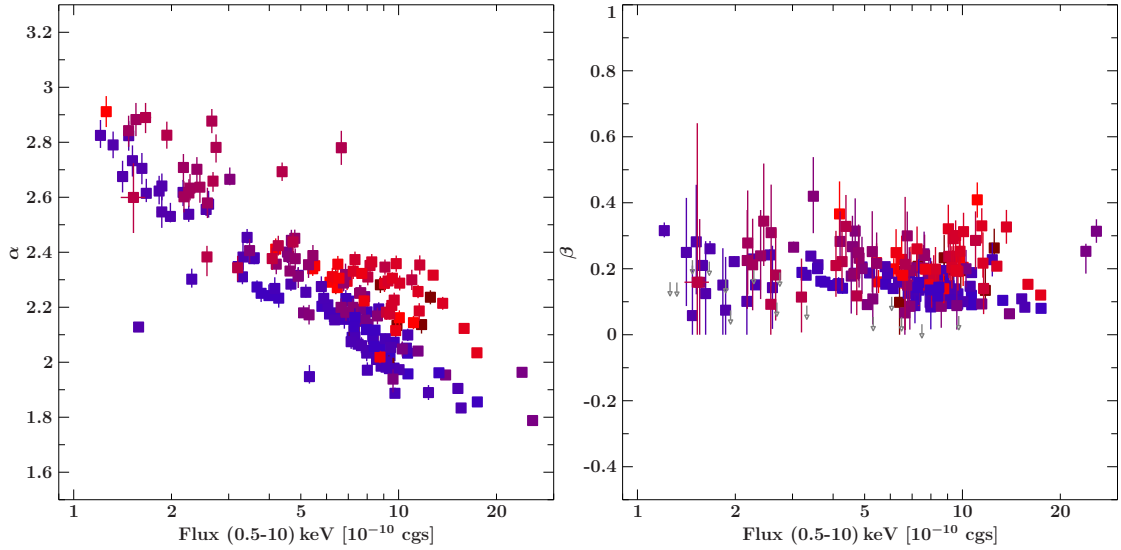


Figure 9.3.: Temporal evolution of best-fit parameters for all *Swift*/XRT observations. Color gradient depict temporal evolution (see Fig. 9.4). The color gradient encode the time information of the observation from red in 2015 to blue in 2017.

9.3. The long-term evolution of the X-ray spectrum

The absorbed log parabola model perform well describing all X-ray spectra. Figure 9.3 shows the best-fit values of the model parameters α and β evolving with the source flux in the (0.5–10) keV energy band. Parameter uncertainties correspond to their 90% confidence limits. The source exhibits a clear harder-when-brighter trend over several outbursts, while the curvature parameter lies between 0.05 and 0.5. The color gradient encode the time information of the observation from red in 2015 to blue in 2017. There is a significant difference in the evolution of the spectral hardness between the blue and the red data, implying that the spectrum was harder in outburst shown in 2017 (blue data points) compared to the outburst of 2015 (shown in red data symbols), while the curvature was consistent within the uncertainties.

9.4. Multiwavelength Variability and Correlation Studies

Figure 9.4 shows the multiwavelength light curve of Mrk 421 from December 2015 until May 2017. The color gradient represents temporal information where red data points corresponds to observations in 2015 which evolve into blue data points taken in 2017.

The source is highly variable showing variations on both long (monthly) and short (daily) timescales. Overall, the shortest timescales for flux variability is seen in the TeV and X-ray light curves, while the γ -ray and ultraviolet emission varies on much longer timescales. In addition to the long-term variations there are short outburst of much lower amplitude than in the TeV or X-ray emission.

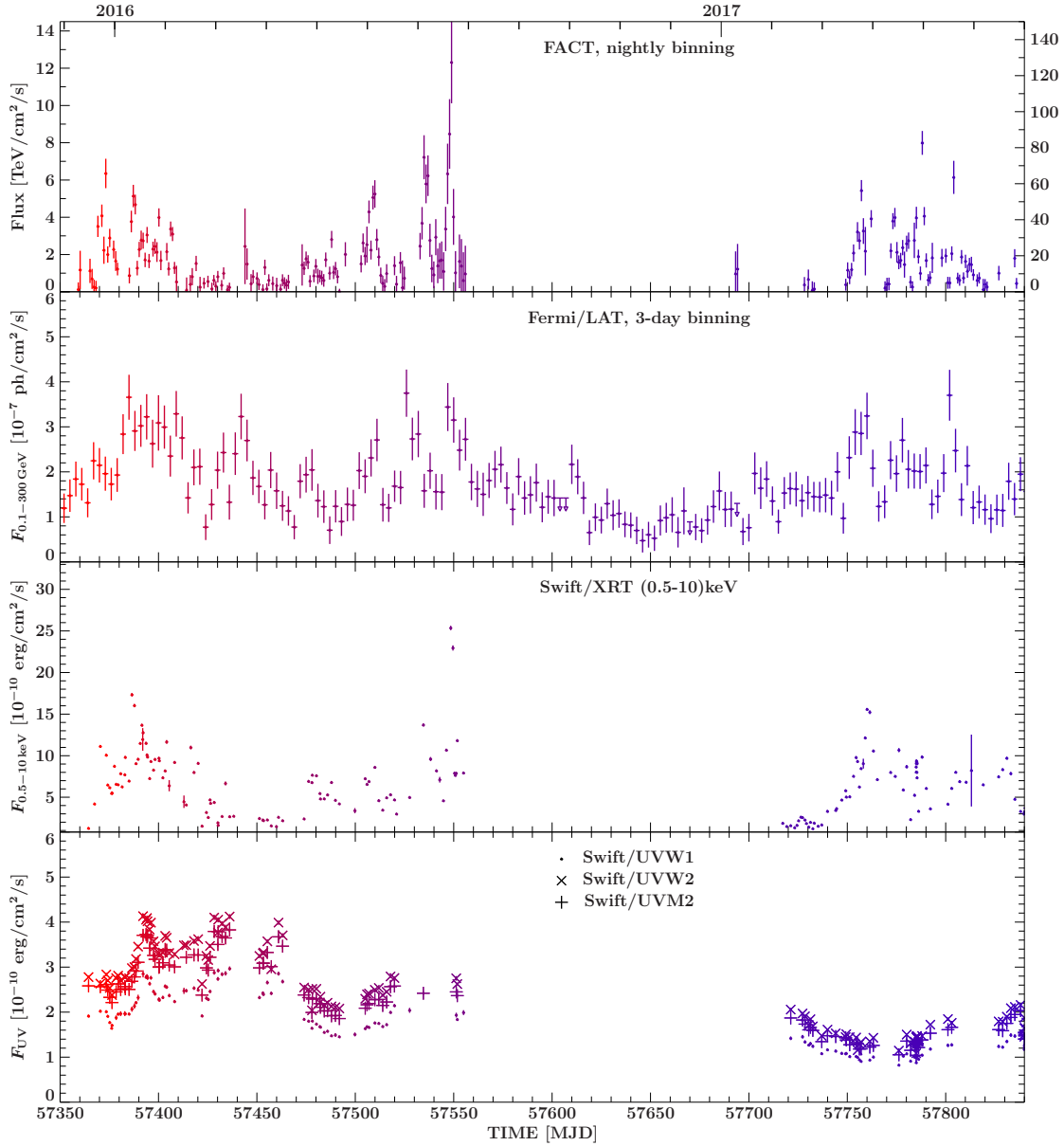


Figure 9.4.: Long-term broadband light curve of Mrk 421 from December 2015 until May 2017, involving monitoring data by FACT, *Fermi*-LAT, *Swift*/BAT, *Swift*/XRT, and *Swift*/UVOT (from top to bottom panel).

To quantify the variability, we determined the fractional variability amplitude $F_{var}(\nu)$ (see Eq. 5.2.1) for each frequency band. The uncertainty of F_{var} is calculated following Ahnen et al. (2016a)

$$\Delta F_{var} = \sqrt{F_{var}^2 + err(F_{var})} - F_{var}, \quad (9.4.1)$$

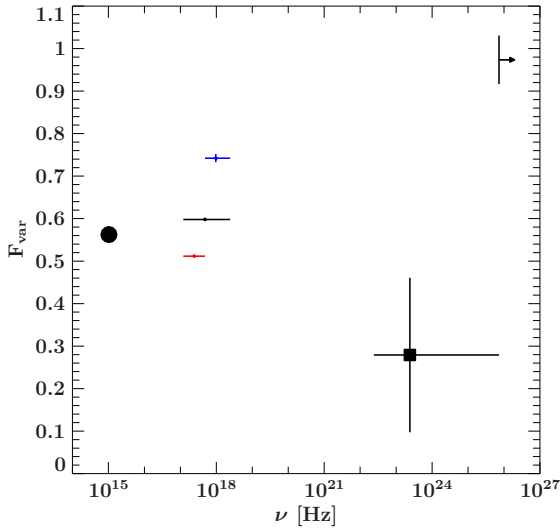


Figure 9.5: Fractional variability amplitude for different energy bands calculated for the duration of the whole monitoring with *Swift*/UVOT at 2600 Å (circle), *Swift*/XRT (points) for the (0.5-2) keV (red), (2-10) keV (blue), and (0.5-10) keV energy range (black), *Fermi*-LAT (square) for (0.1-300) GeV, and FACT (left-to-right arrow) for energies above 750 GeV.

where $err(F_{\text{var}})$ is the error of the fractional variability amplitude as defined in Vaughan et al. (2003a) (also see Eq. 5.2.2). As this quantity is sensitive to the binning of the light curve, we used the daily binned *Fermi*-LAT and FACT light curves for a better comparison. The results are depicted in Fig. 9.5.

Mrk 421 exhibits strong variability across the whole electromagnetic spectrum with the strongest variability of $\sim 95\%$ in the TeV band. The γ -ray band shows the lowest level of variability. In X-rays and in the ultraviolet band the source exhibits an equally strong variability of $\sim 60\%$ with a slightly stronger amplitude in the hard X-ray band. We note, that the sampling of these observations differs from daily observations to one per week. Thus, variability could be underestimated in these bands.

9.4.1. Inter-band cross-correlation studies

During the monitoring period, there were several outburst in the TeV range on very short (hours) time scales. These outburst were accompanied by flux increases in the X-ray and γ -rays band. The flux-flux relationship during outbursts between different energy bands give first information on correlated emission. Because of the different and/or uneven sampling rate, the one with the respective denser sampling had to be rebinned in order to compare a pair of light curves. Hence, for each observation at t_0 of the sparser sampled light curve, we looked for observations in the denser sampled one which took place within $t_0 \pm 12$ h. If there were none, we averaged all observations that took place between the observation prior and after t_0 but within a maximum of $t_0 \pm 1.5$ days. Thus, the rebinned light curve contained time bin sizes between 12h and 3 days, depending on the sampling of the sparser sample light curve.

In Fig. 9.6 we plotted the relationships between fluxes of different energy bands with respect to a sub-linear, linear, and quadratic relation. The flux densities within each band were normalized to the maximum observed flux within a visibility windows (VW, see Table 9.4) The upper panels show the fluxes of the TeV and GeV γ -ray bands with

Table 9.4.: Overview of different time interval selections.

Use	Notation	MJD start	MJD end	Description
MWL monitoring	VW1	57358	57550	Visibility window 1
	VW2	57717	57864	Visibility window 2
DCF analysis	T1	57358	57500	DCF time frame 1
	T2	57420	57550	DCF time frame 2
	T3	57717	57770	DCF time frame 3
	T4	57770	57864	DCF time frame 4
Time-resolved SEDs	S1	57372.5	57373.5	SED set 1 incl. ToO trigger
	S2	57373.5	57374.5	SED set 2 incl. <i>INTEGRAL</i> obs.
	S3	57374.5	57383.5	SED set 3
	S4	57383.5	57387.5	SED set 4
	S5	57387.5	57389.5	SED set 5
	S6	57389.5	57393.5	SED set 6
	S7	57721.0	57744.5	SED set 7
	S8	57744.5	57752.5	SED set 8
	S9	57752.5	57758.5	SED set 9
	S10	57758.5	57762.5	SED set 10
	S11	57762.5	57770.5	SED set 11

respect to the quasi-simultaneous X-ray flux and visibility windows. The lower panels show the X-ray and GeV band fluxes plotted against the UV flux.

The VHE vs. X-ray flux evolution during different outbursts is consistent with both a linear and quadratic relationship. In comparison, the correlation between the GeV γ -ray and the X-ray band follows a flatter trend. Overall, although there is some scatter for different outbursts, the X-ray to γ -ray and X-ray to TeV light curves are tightly correlated. The respective Spearman rank and Pearson correlation coefficients are listed in Table 9.5. On the contrary to the high-energy emission, there is no direct correlation of the UV flux with either the X-ray emission, the high-energy flux at γ -rays, nor emission at TeV energies.

In order to study the possible inter-band correlation of flux changes between different energy bands taking into account possible time lags, we calculated the discrete correlation function (DCF) following Edelson & Krolik (1988), see Sect.5.2, Eq.5.2.3. We use the most detailed light curves in each energy band (i.e., nightly binning for FACT and *Fermi*-

³The scatter may stem from the rebinning process or the stochastic nature of the process.

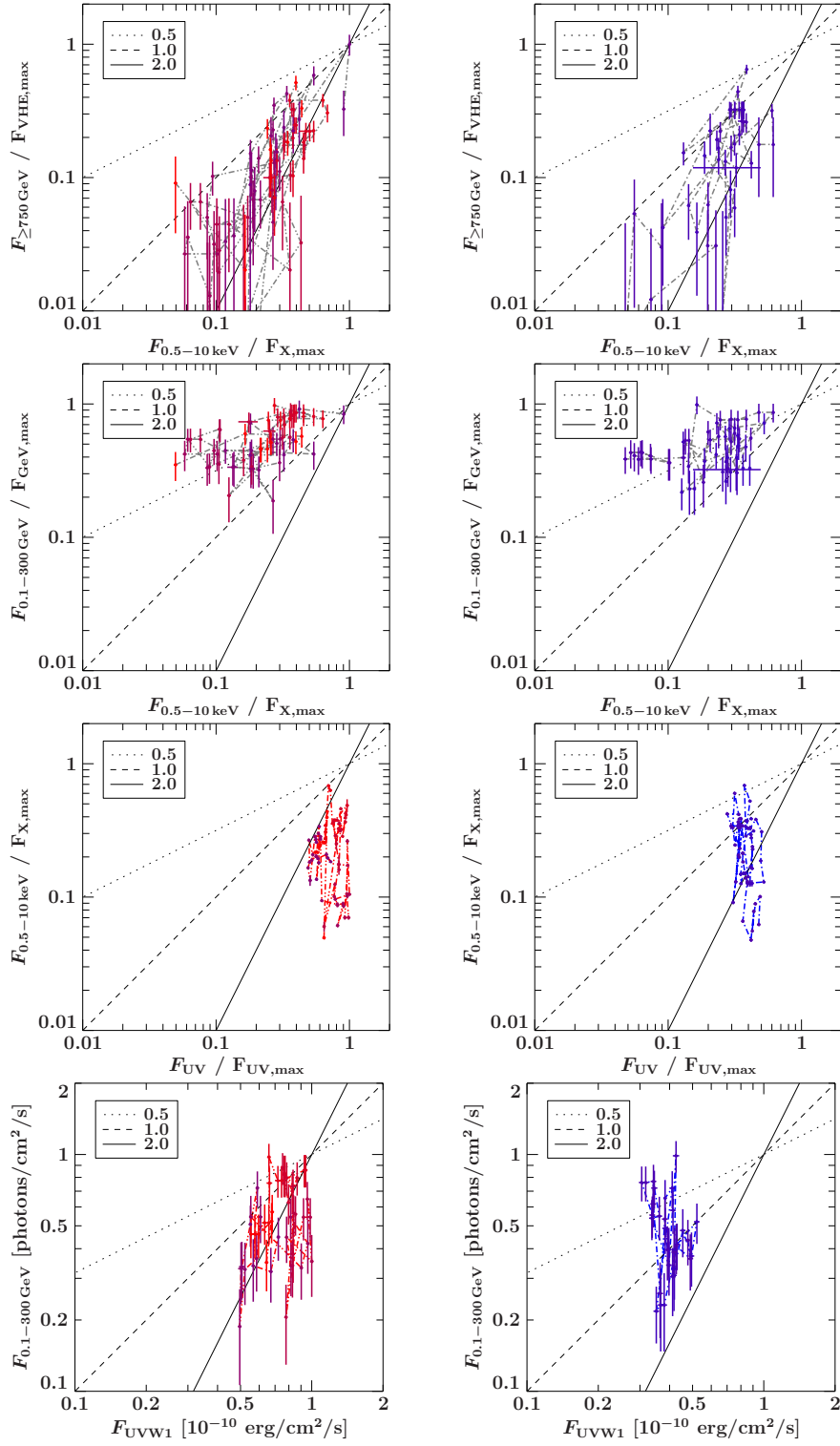


Figure 9.6.: Flux-flux correlations of UV (2600 Å), X-ray (0.5-10 keV), γ -ray (0.1-300 GeV), and TeV emission for visibility window VW1 (*left panels*) and visibility window VW2 (*right panels*). Color gradient depict temporal evolution (see Fig. 9.4).

Table 9.5.: Flux-Flux Correlation Coefficients

Flux-Flux set	ρ	p_ρ -value	r	p_r -value
X-rays – TeV	0.73	$\leq 10^{-6}$	0.72	$\leq 10^{-6}$
X-rays – γ -rays	0.55	$\leq 10^{-5}$	0.62	$\leq 10^{-6}$
UV - γ -rays	0.41	0.21	0.58	0.06
UV - X-rays	0.09	0.65	0.31	0.10

Note: Spearman rank correlation coefficient ρ and Pearson linear correlation coefficient r for all four flux-flux plots in Fig 9.6 with their corresponding p -values. A correlation is considered significant if the corresponding p -value is lower than 1%.

LAT) and probe time lags in steps of 3 days up to a maximum shift of 96 days. The step size corresponds to a median of the observation separation of the uneven sampling in the X-ray light curve. The maximum step size covers approximately half the duration of one visibility windows.

The DCF was computed separately for the two visibility windows VW1 and VW2 (see Table 9.4 for an overview of the time frames used throughout the analysis). The results are shown in Figs. 9.7. Panels (a)-(c) show the DCF between the UV emission and the X-ray, γ -ray, and TeV emission. We find no significant time lags or correlation at a 3σ level. Although there is a hint of a tentative positive correlation between the UV and γ -ray emission at 2σ (see panel b), where the UV emission lags the γ -ray emission by $dt \sim 10$ days. In the panels (d)-(f), we show the cross-correlations between the high-energy bands. All three bands are significantly correlated. The highest correlation is found between XRT and FACT without time lag within the uncertainties, $dt = 0 \pm 1.5$ days. This DCF also shows a second slightly weaker but still significant peak at $dt = 13 \pm 1.5$ days. This time lag corresponds to the separation of the two outbursts on the TeV light curve (see Fig. B.2). Hence, this lag is likely caused by the high sampling resolution of the TeV light curve. The DCFs between the XRT and LAT as well as LAT and FACT also show a positive correlation at $dt = 0 \pm 1.5$ days.

Figure 9.7 (g)-(l) show the corresponding results of the DCF for the second visibility window. Overall the data is much more noisy in this shorter period. On one hand this is caused by a sparser sampling (e.g., in the X-ray and UV band), on the other hand, the source exhibits a higher level of variability (e.g., in the TeV band), which allows to attribute an outburst in a single band to multiple ones in another band. From the DCF between the UV and *Fermi*-LAT, we find a significant anti-correlation where the γ -rays leads the UV data by $dt = 16 \pm 1.5$ days. No significant correlation is found for the UV – X-ray or UV – TeV light curves. At high energies, the correlation between X-ray and TeV emission is still very strong. The second peak in the DCF between XRT and FACT has disappeared, which supports the spurious nature in the first visibility window. The correlations between the GeV γ -ray emission and the X-ray as well as the TeV band are still marginally significant at 2σ . For all three bands, the derived time lag

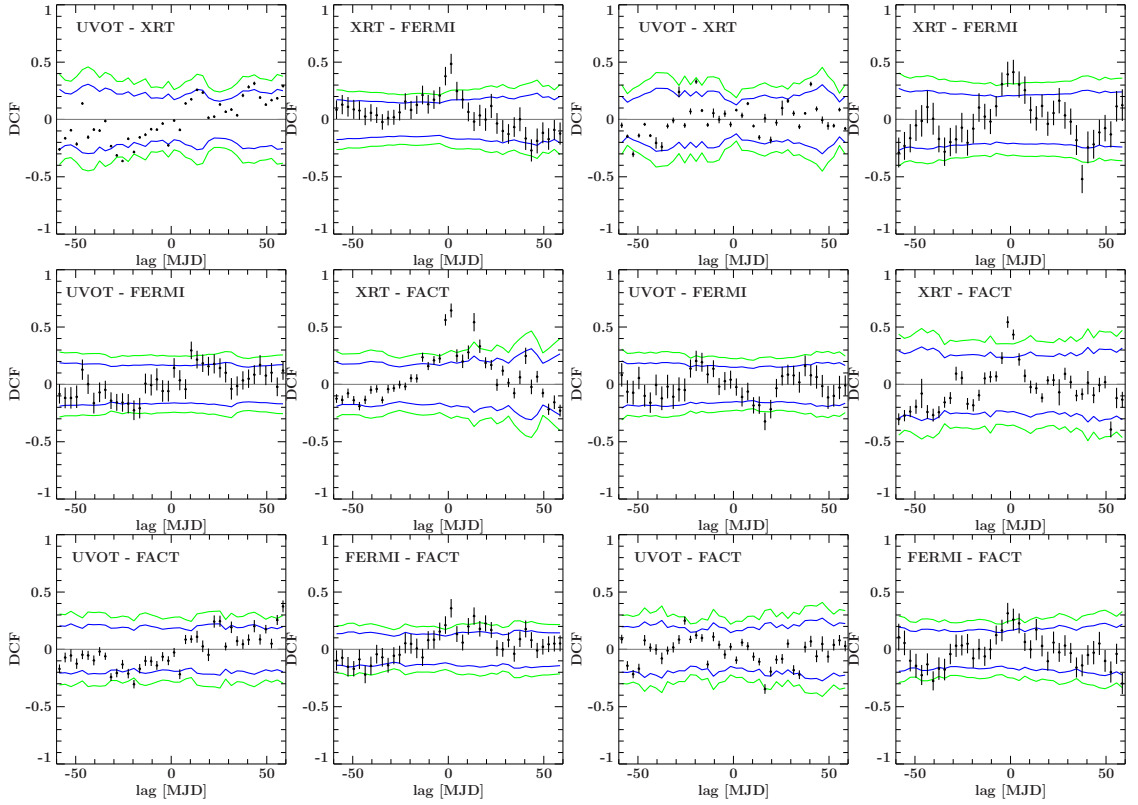


Figure 9.7.: *Panels (a-f):* Results for the discrete cross-correlation function for observations period MJD 57358-57550. *Panels (g-l):* Results for the discrete cross-correlation function for observations period MJD 57717-57864.

is $dt = 0 \pm 1.5$ days.

We further studied the DCF for shorter times scales, in order to test the possibility of an orphan flare in the outburst of 2015. Furthermore, if different emission processes dominate at different time scales it is possible that the cross-correlation between the energy bands is variable as well. Four short time periods are defined T1, T2, T3, and T4 (see Table 9.4 for details). Except for period T2 the maximum tested time lag is 30 days. In case of the longer time range of T2 it is 60 days. The results are shown in Figs. B.6 and B.7 in the Appendix. The difference between T1 and T2 is that in T2 we excluded the period of strong TeV outbursts in December 2015, while in T1 we excluded the period of numerous outbursts in June/July 2016. For T3 and T4 there were not enough data and the DCF is fully consistent with the null-hypothesis.

Overall the X-ray and TeV emission was highly correlated during the whole monitoring campaign. The X-ray emission was also moderately correlated with the γ -ray emission, which could stem from an underlying long-term variation. The γ -ray emission does not correlate with the TeV emission during the first TeV flare in 2015 but may be correlate with the second one in T1 with a time lag of $\sim 13 \pm 2.5$ days. For all other time ranges

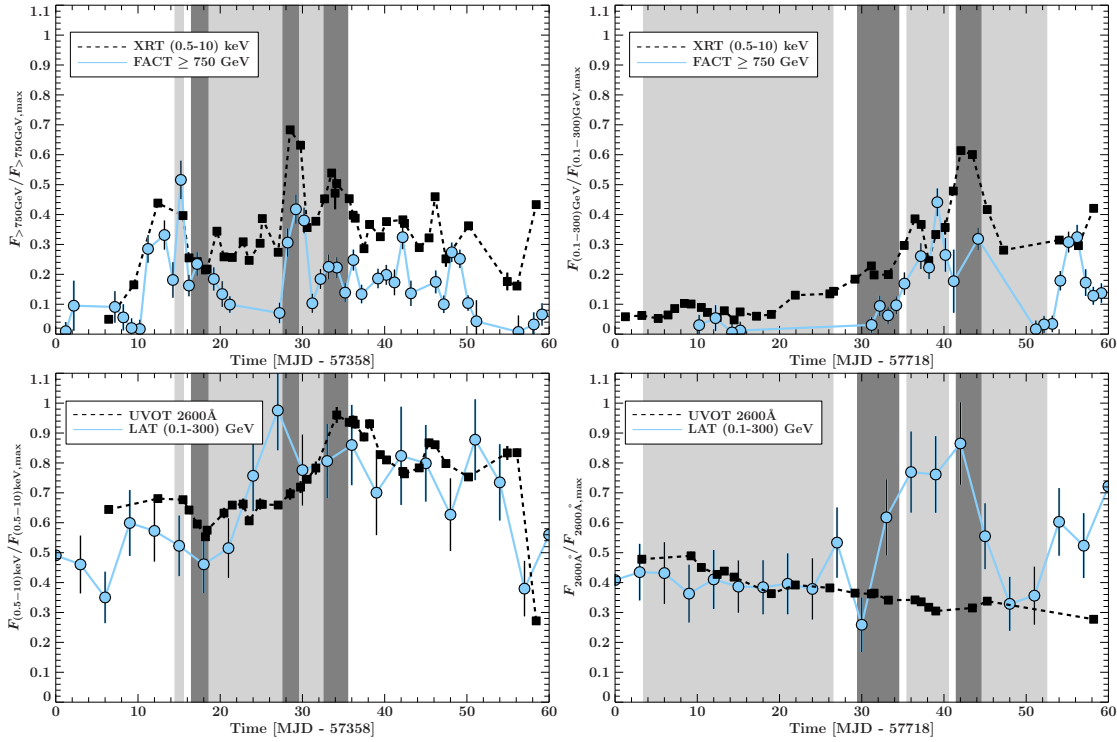


Figure 9.8.: Observed light curves normalized by the maximum flux observed in a given band during the complete monitoring period. *Left panels:* zoom in on the activity in 2015 and beginning of 2016. *Right panels:* zoom in on the activity in the beginning of 2017. Shaded regions mark time frames for which simultaneous SEDs were assembled.

the GeV emission shows a correlation with zero time lag. The UV emission is only tentatively correlated with γ -rays during the VW1 period and anti-correlates during the second visibility windows.

9.5. Time-resolved Spectral Energy Distributions of Mrk 421

From the analysis of the long-term multiwavelength light curves we selected periods in which Mrk 421 exhibited bright TeV γ -rays outbursts that are well sampled across all bands from ultraviolet to the TeV band. These periods are MJD (57358 – 57418) and MJD (57718 – 57778). Fig. 9.8 zooms in on the light curves of these periods. The light curves are normalized to their maximum observed flux during the complete monitoring period from 2015 to 2017. Upper panels compare the normalized light curves of FACT and *Swift*/XRT since the DCF found the highest degree of correlation in these bands. The lower panels show the normalized light curves of *Swift*/UVOT and *Fermi*-LAT. With respect to a typical high-peaked BL Lac SED, upper panels correspond to the declining part of the two emission humps, while lower panels correspond to the rising part. Left and right panels show the same light curves for the activity in 2015 and 2017, respectively.

During the first period (left panels), we observed two significant flux increases in TeV and X-rays that happened on short timescales of days. The first one, on 2015 Dec 17, was very bright in TeV and exceeded our trigger limit for our multiwavelength ToO program (see Sect. 9.1). Subsequently ToO triggers were sent to *Swift* and *INTEGRAL* (*XMM-Newton* was not yet part of the program in cycle mc15). The details of the observations are described above (Sect. 9.2). A second outburst is observed two weeks later. Compared to the TeV light curve, the X-ray emission does not revert to its pre-flare level but shows a additional long-term variation.

There is no flux increase in neither the γ -ray nor ultraviolet emission during the first TeV outburst. Instead, these bands show a moderate flux increase which varies on longer time-scales (weeks). If the emission in GeV is connected to the very high-energy emission at TeV this increase suggests either a soft lag of the order of ~ 11 days or a hard lag of the order a few days, which is in line with the DCF (see Fig. 9.7 e).

The second time range (*right panels*) shows a very different behavior. The high-energy emission from X-rays to TeV is low in the beginning and shows a flux increase on the timescale of ~ 10 – 20 days, although the X-ray band evolves slower than the TeV band. This increase is also observed simultaneously in the GeV band. The UV flux, on the other hand, consistently drops during the time frame, without indications of short-term variations.

The different variability behavior between the wavelength bands may hint to differences between the processes that are responsible for the outbursts. We assembled six SEDs (S1 – S6) for the first time range and five (S7 – S11) for the second one (see Table 9.4 and shaded regions in Fig. 9.8). UV and X-ray observations were stacked within the defined time range to compute averaged spectra for each SED set. Since FACT and *Fermi*-LAT spectra are model dependent, a series of spectra were extracted from the data as described in Sect. 9.2.

Figures 9.9 and 9.10 show the SED series for each time frame set with the best-fit in the UV to X-ray band. At the time of writing, FACT spectra were only available for the flaring night. Thus, no fit was performed in the γ -ray bands. The SED evolves from left to right and top to bottom. In every SED we show the simultaneous data in color (red for the first outburst in 2015 and blue for the second outburst in 2017) while all other SED sets are plotted in gray for comparison.

To examine the synchrotron emission for Mrk421 that peaks between the UV and X-ray band, each SED was fit with a log parabola in the these bands. The *Fermi*-LAT and FACT data were not taken into account for the spectral fits, since the TeV data, that is necessary to constrain the high-energy hump, is yet being processed at the time of writing. The model is set up as in Sect. 9.2.4 with an additional multiplicative component (Xpsec model: **redden**) to account for Galactic extinction of the UV data from the ISM. In order to model the exact shape of the synchrotron emission further studies using physical models need to be applied including the high-energy spectra from MeV to TeV energies. In this work, I concentrate on a phenomenological description with the log parabola model of the low-energy hump in order to investigate whether the difference between the outburst in 2015 and 2017 differ in their spectral evolution. This

Table 9.6.: Best-fit of the time-resolved UV to X-ray SEDs.

SED	α^a	β^b	$E_{p,\text{syn}}^c$ [keV]	$\nu F(\nu)_{p,\text{syn}}^d$ [10^{-10} ergs cm $^{-2}$ s $^{-1}$]	χ_{red}^2 e (dof)
s1	2.19 ± 0.02	0.12 ± 0.01	0.16 ± 0.05	4.97 ± 0.14	2.78(90)
s2	2.27 ± 0.01	0.13 ± 0.01	0.09 ± 0.01	3.89 ± 0.08	2.79(89)
s3	2.22 ± 0.01	0.11 ± 0.01	0.11 ± 0.02	3.92 ± 0.07	2.83(86)
s4	2.30 ± 0.02	0.14 ± 0.01	0.08 ± 0.03	4.52 ± 0.23	1.71(87)
s5	2.32 ± 0.02	0.16 ± 0.01	0.10 ± 0.02	6.04 ± 0.25	2.18(92)
s6	2.28 ± 0.01	0.15 ± 0.01	0.11 ± 0.02	7.64 ± 0.17	3.63(98)
s7	2.62 ± 0.01	0.22 ± 0.01	0.04 ± 0.00	2.58 ± 0.09	1.39(94)
s8	2.31 ± 0.01	0.17 ± 0.01	0.12 ± 0.02	3.09 ± 0.09	1.16(94)
s9	2.06 ± 0.01	0.10 ± 0.01	0.50 ± 0.11	3.24 ± 0.03	1.36(89)
s10	1.89 ± 0.01	0.05 ± 0.01	12.63 ± 6.70	5.43 ± 0.18	4.50(99)
s11	2.06 ± 0.01	0.09 ± 0.01	0.44 ± 0.17	3.10 ± 0.05	1.94(97)

Note: a photon index at 1 keV, b curvature parameter, c synchrotron peak energy, d respective peak flux, e fit statistic, reduced χ^2 and degrees of freedom.

phenomenological approach yields useful estimates on the peak properties (e.g., Massaro et al. 2004a; Tramacere et al. 2007; Krauß et al. 2016). Best-fit results for each SED are summarized in Table 9.6. Best-fit models are overplotted in Figs. 9.9 and 9.10. The simple phenomenological model worked well describing the X-ray data of the source. However, it genuinely overpredicted the UV flux at longest wavelengths and failed to describe the hardness of the UV spectrum. Nevertheless, the fits are sufficient to yield a good estimation of the synchrotron peak positions and associated fluxes.

The evolution of the SED shows that on one hand during the outburst in 2015 the synchrotron peak flux increased, while the peak position remained rather unchanged at 0.1 keV. On the other hand, during the outburst in 2017, the opposite behaviour is observed, i.e., the peak moves to higher energies up to ~ 12 keV. In addition, the synchrotron peak overall broadens with increasing peak flux, opposed to the outburst in S1 – S6. The peak position is shown in Fig. 9.11 in comparison to the derived peak flux as well as the observed emission in the UV, X-ray, GeV and TeV band. Fig. 9.11 a) clearly shows a peak shift in 2017 from 0.04 keV to 12 keV. The X-ray flux increased as the synchrotron peak moved into the XRT band pass and decreased in an identical relationship. The UV flux decreased naturally as the total synchrotron hump moved to higher energies until it saturated while the hump appeared to broaden. It is worth noting that during the brightest spectral state (S10) the logpar model extended into the *Fermi*-LAT band pass and matched the observed spectrum. The γ -ray evolution against

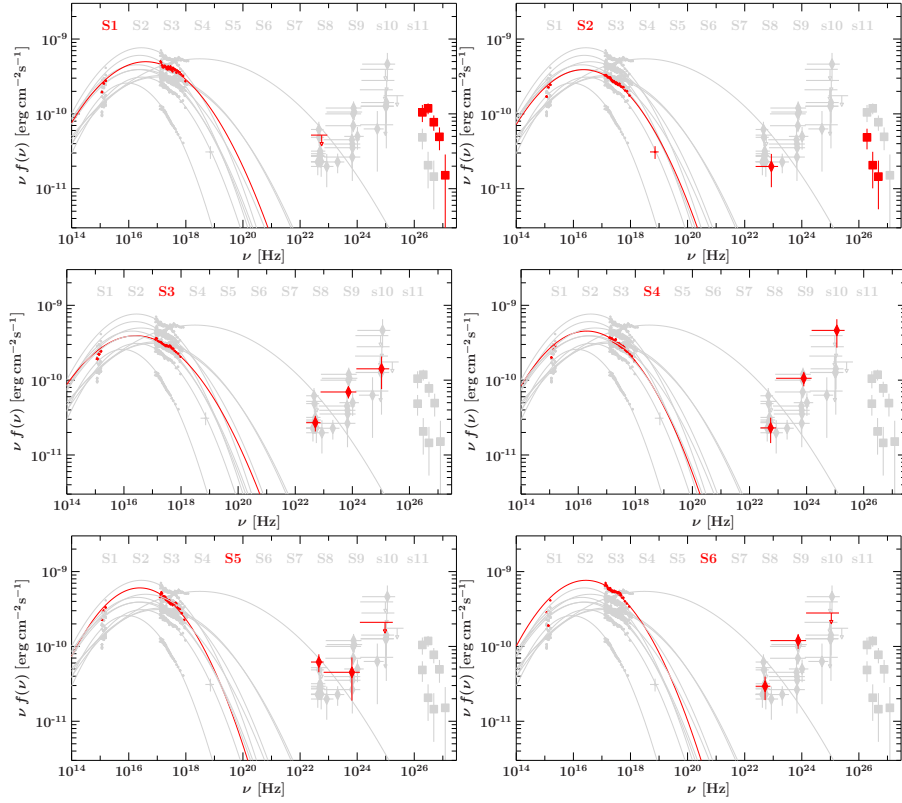


Figure 9.9.: Time-resolved SEDs from the outbursts in 2015 (S1 – S6, in red) . UV and X-ray data have been corrected for Galactic extinction and photo-absorption. Solid lines depict best-fits of a log parabolic model fitted to the UV and X-ray data.

the peak position is shown in Fig. 9.11 c). The TeV flux varied alike the synchrotron peak flux in 2015. The γ -ray flux evolution in 2017 was similar between the MeV and GeV. With respect to the synchrotron peak flux in the TeV did not return to the same flux level after the brightest state in S10 but exhibited a significantly lower level.

At the time of writing, two preliminary spectra at energies above ≥ 750 GeV were available for two SEDs S1 and S2, which showed significant variations. *Fermi*-LAT spectra of 2 to 5 spectral bins were available for the majority of SED sets, except for S1 and S2. For these sets the integration time was one day and the overall flux was low. The TeV spectrum with a simultaneous upper limit at GeV energies suggest a narrow high-energy peak. Throughout the outburst the GeV emission showed tentative spectral variability, suggesting that the high-energy peak became brighter as well.

For the series S7 – S11 in 2017 no FACT spectrum is available yet. However, given the longer time ranges, all *Fermi*-LAT spectra contain at least 2 and up to 5 significant data bins. The GeV spectrum showed significant spectral variations while the synchrotron emission increased, where highest-energy bins showed the largest variations. The *Fermi*-LAT spectrum covered the rising part of the high-energy hump in all SEDs.

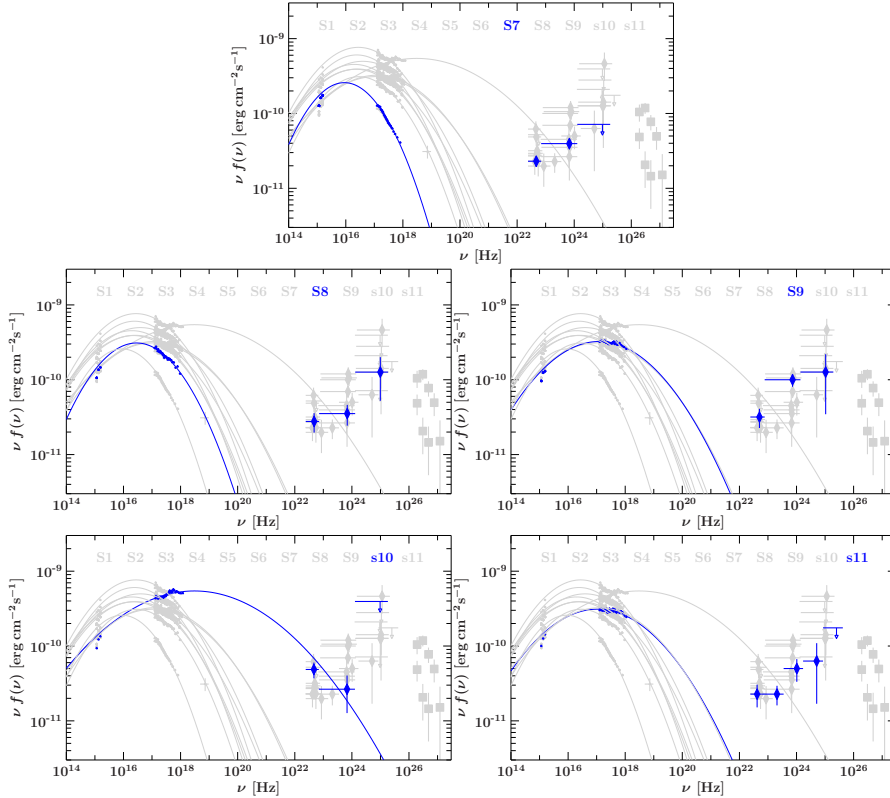


Figure 9.10.: Time-resolved SEDs from the outbursts in 2017 (S7 – S11, in blue). UV and X-ray data have been corrected for Galactic extinction and photo-absorption. Solid lines depict best-fits of a log parabolic model fitted to the UV and X-ray data.

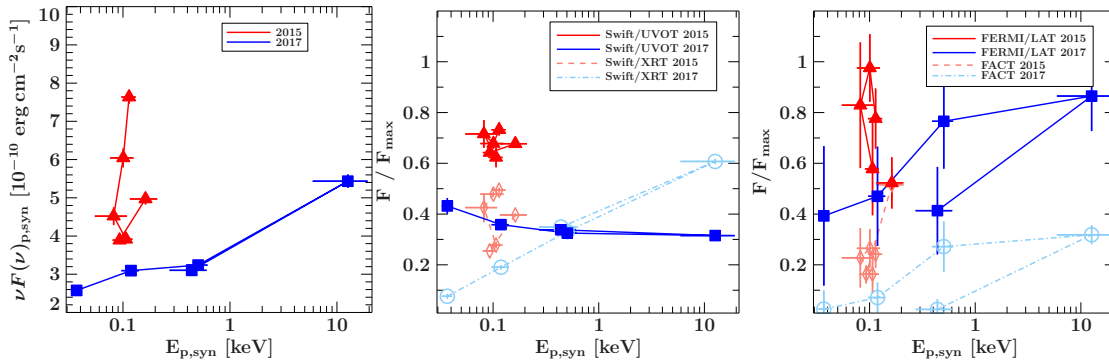


Figure 9.11.: Synchrotron peak position derived from the time-resolved SED fitting against the best-fit synchrotron peak flux (*left panel*), normalized fluxes in the TeV and GeV γ -ray band (*mid panel*), as well as normalized fluxes in the UV and X-ray band (*right band*). Results for the time SEDs S1 – S6 are shown in red/gray, while blue/black correspond to results of SED sets S7 – S9.

9.6. Discussion

During our multiwavelength monitoring period from Dec 2015 to May 2017, Mrk 421 exhibited a typical moderate activity state with variability across the whole observed energy bands from UV to very high-energy γ -rays above 750 GeV (compare e.g., Fossati et al. 2008; Aleksić et al. 2015a,b; Zhu et al. 2016; Bartoli et al. 2016; Kapanadze et al. 2016, and references therein). The largest variability of $\sim 80\%$ to $\sim 95\%$ was observed in the (2-10) keV X-ray band and at very high-energy γ -rays with an increasing variability amplitude at higher energies within these bands. During the monitoring period these bands exhibited variations on short timescales of days. In comparison, both the UV and (0.5-2) keV X-ray band exhibited a rather moderate but similar level of variability $\sim 55\%$ and 60% , respectively, while a significantly lower variability amplitude of $\sim 30\%$ was found in the 100 MeV – 300 GeV γ -ray band (see Fig 9.5). This double hump trend in the fractional variability amplitude has been observed in both low- and high activity states as well as during flare events (e.g., Aleksić et al. 2015a,b; Baloković et al. 2016; Fossati et al. 2008; Ahnen et al. 2016b; Pian et al. 2013), which implies that similar processes dominate the variability in quiescent and flaring states. The UV emission was dominated by strong variations on long timescales of weeks, while the soft X-ray (0.5-10) keV band exhibited additional variation on time scales of days. At GeV γ -rays, although this band was affected by a low SNR, there were hints of variations on timescales of a few days and weeks. The high-sampled TeV light curve on the other hand mainly exhibited variability on timescales of days. With respect to the two emission humps of the SED, the UV and MeV/GeV γ -ray band cover the increasing parts of the two humps in the SED of Mrk 421.

Our correlation analysis shows, that across the whole monitoring duration, there was a strong correlation with no time lag between (0.5-10) keV X-rays and emission at energies above 750 GeV. This correlation was dominated by the short-term flux variations on daily timescales and indicates that the regions in which the X-ray and VHE radiation were produced were causally connected or most likely co-spatial. Comparing the evolution of the simultaneous flux, we found that it is steep and consistent with a linear or quadratic relationship (see Fig 9.6, upper panels). A strong correlation with no time lag between the X-ray and VHE emission has been observed in previous multiwavelength campaigns for both low and high-activity states (e.g., Pian et al. 2014; Acciari et al. 2011c; Bartoli et al. 2016; Aleksić et al. 2015a) as well as for flaring states (Giebels et al. 2007; Fossati et al. 2008; Aleksić et al. 2015b; Acciari et al. 2009b). The study presented in this work confirms the correlation also exists during our 18 months of monitoring with moderate activity including periods of low flux as well as outbursts. A steep flux-flux relationship between the X-ray and VHE band is also consistent with previous results from the literature. Fossati et al. (2008) observed a quadratic relationship during a flaring event for both in and decreasing fluxes. Aleksić et al. (2015a) found evidence for a linear relationship during a quiescent state of Mrk 421 in 2009. The difference might be that flares are produced by different physical mechanisms than the variations during quiescent state. We showed time-resolved flux-flux variations for both low-activity as well as several short

outbursts and found that the relationship followed slightly different tracks for different outbursts (see Fig 9.6), while the overall correlation was steep.

Between GeV γ -rays and both the X-ray and VHE band we found a tentative correlation without time lag. The flux evolution between these bands is much flatter. This correlation is mainly driven by variations on a weekly timescale in the first visibility window (see Sect. B.2 in the appendix). With respect to blazar emission models (see Sect. 3.2.4), the GeV band is often a mixture of multiple emission components (of different regions or particle populations). In this context, the lower significance of correlation and flatter flux-flux evolution might stem from the fact, that the high energy emission is made up of multiple emission components that overlap at GeV γ -rays. The emission sites or processes of these components may not necessarily be co-spatial or causally related.

The multiwavelength light curves (see Fig. 9.4) indicate that the observed emission in the ultraviolet band may not have traced the same processes that were observed in the simultaneous light curves at X-ray energies and above. This hint was supported by the correlation analysis, which showed that to a great extent the simultaneous flux evolution between the UV and X-ray as well as the γ -ray band occurred independently from each other. The only hints of correlated emission was observed with respect to the GeV γ -ray band (see Fig. 9.7 b and h). On one hand, there is a tentative positive correlation with a soft lag of 10 days driven by the flux increase on weeks timescale in the first visibility window (see Fig. 9.6). A positive correlation has also been found in some previous studies of X-ray flares (e.g., Kapanadze et al. 2016; Buckley et al. 1996; Shukla et al. 2012). During a bright flare activity in February 2010, Shukla et al. (2012) found correlated emission between optical emission, X-ray and γ -ray emission between 0.2 GeV and 200 GeV. The authors concluded that in these flares UV and X-ray data originated from the same emission region in which the injection of fresh electrons that cool via SSC mechanisms caused the flux variation. Tramacere et al. (2009) analyzed the UV and X-ray SED from 2013 over a duration of 6 months using phenomenological logpar models. They concluded that the UV data in this time range is consistent with synchrotron radiation from the low-energy tail of the relativistic electrons within the same emission region. However, there are many studies, that find a weak anti-correlation between UV and γ -ray emission (e.g., Aleksić et al. 2015a) or none at all (e.g., Baloković et al. 2016), which is usually taken as an indicator of more than one emitting particle population that contribute to the spectrum. A weak anti-correlation was also observed during the second visibility window. To our best knowledge, this is the first time for Mrk 421 that both correlated and anti-correlated emission is observed during a single observational campaign. The UV light curve shows an overall long-term variation. This raises the possibility that both the correlation and anti-correlation could originate by chance from an independent variation of the UV emission region as suggested by several authors (e.g., Aleksić et al. 2015a; Sinha et al. 2015).

From the extensive monitoring data, we extracted a series of simultaneous SEDs which cover the entire rise and fall of two high-energy outbursts. The time-resolved SEDs showed two distinct evolutionary patterns for the low-energy hump during the outbursts in 2015 and 2017. Because TeV data that cover the highest-energy γ -rays were not yet

computed by the time of writing, the high-energy hump could not be constrained yet. The rising part was covered by low-SNR *Fermi*-LAT spectra, which varied moderately in flux. Although, there was tentative evidence for spectral changes during both outbursts, all spectra are consistent with a flat power-law spectrum. Hence, in the following we will focuss on the discussion of the UV to X-ray SED and only take into account variability information for the high-energy emission.

During the outburst in 2015, only the brightness of the low-energy emission hump increased without significantly changing the position or width. On the contrary, in 2017, a synchrotron peak shift from lower to higher energies was observed that was furthermore accompanied by an increase of the peak flux and an apparent broadening of the emission hump. Fitting the time-resolved UV to X-ray SED simultaneously, we observed a harder-when-brighter trend during the outburst of 2017 and which was accompanied by a decreasing spectral curvature with increasing flux (see Table 9.6). The latter implies a shift of the synchrotron peak into the X-ray spectrum with possible additional broadening of the log parabola. This yields in a very flat spectrum at the peak energy. Once the peak energy decreases and the hump becomes narrower a stronger curvature is needed to fit the UV and X-ray spectra.

Since the SEDs were only fitted with a phenomenological model, we cannot exclude that the UV spectrum arises from a different particle population than the X-ray emission. The lack of correlation between emission in the UV and X-ray band is consistent with such a scenario (e.g., Chen et al. 2011). If the synchrotron emission hump is made up of emission from regions that are independent from each other, an increase of only the high-energetic emission component could then mimic the observed effects. Such a scenario was already proposed during an outburst in April 2013 (Sinha et al. 2015). The authors showed that the observed synchrotron emission in the UV and (0.3–79) keV band came from two distinct regions. In that case, the X-ray emission originated from a region much more compact than the other one emitting at UV energies.

9.6.1. Interpretation in the context of leptonic jet scenarios

The results of the spectral timing analysis can be compared to predictions from different jet models. Because crucial VHE spectra are yet missing in the analysis of Mrk 421 result cannot provide conclusive evidence for either of the jet scenarios. However, it is worth to put them in context. The soft energy hump is thought to results from relativistic electrons in both leptonic and lepto-hadronic jet models. Hence, in this section, I compare the results of the spectral timing analysis discussed above with respect to leptonic jet scenario (see Sect. 3.2.4). A discussion with respect to the hadronic case is given in Sect. B.3 of the appendix only, because detailed spectral modelling (in particular of the VHE spectrum) is necessary to draw conclusions for hadronic or lepto-hadronic models. It should be noted, that the string correlation between X-rays and TeV γ -rays are also consistent with a pure hadronic or lepto-hadronic case, in which low-energy photons are produced by electrons that stem from high-energetic pion decay. Evidence for such hadronic processed would be the association of an neutrino event with the Mrk 421. Recently, Kadler et al. (2016) showed that blazars and γ -ray outbursts of blazars, in particular, are capable of explaining

the PeV neutrino events observed by IceCube.

The simplest scenario, the one-zone leptonic model, assumes that an electron population with electron energy distribution $n(\gamma)\gamma d\gamma$ in a single emission region with magnetic field B , region size R and Doppler factor δ is accelerated and cools via synchrotron emission. The synchrotron photons subsequently serve as target photon field for the same population of relativistic electrons, which inverse Compton (IC) upscatter these photons to higher energies in the MeV to TeV band (also called synchrotron self-Compton or SSC, Ghisellini et al. e.g., 1998).

In this scenario, TeV emission is produced from the IC scattering of the highest energetic electrons with synchrotron photons above the peak frequency. The strong correlation between X-rays and TeV γ -rays in both high and low activity states is therefore naturally explained within SSC models. Consequently, synchrotron photons at optical and UV energies that are emitted by lower energetic electrons are upscattered to MeV and GeV energies. However, IC emission from high-energy photons and low-energy electrons (or vice versa) may also contribute to the MeV/GeV range which could dilute a correlation between UV and lower-energetic γ -ray emission (e.g., Abdo et al. 2011b).

The observed double hump structure of the fractional variability amplitude suggests that within each emission hump, respectively, variability increased with energy and the strongest variability occurred at the highest energies. Because cooling timescales of electrons through synchrotron and inverse Compton radiation (in Thomson regime) scale as $t_{\text{cool}} \propto \gamma \left(\frac{d\gamma}{dt}\right)^{-1} \propto \gamma^{-1}$ (see Sect. 2.4), emission at higher energies will be more variable, hence such trend is not surprising within the SSC scenario. Subsequently, the fast cooling of the high-energetic electrons implies the existence of injection or acceleration of energetic electrons to maintain the X-ray emission.

The connection between X-ray and TeV emission is further supported by the steep flux-flux evolution presenting a linear or quadratic relation. Assuming that flux variations are caused by injection of particles in the form of a linear increase in the number of cooling electrons and correspondingly seed photons, a quadratic increase of the IC scattering rate is expected (if the IC scattering takes place in the efficient Thomson regime). A flatter relationship indicates that the scattering process is less efficient as in the case of the scattering in the Klein-Nishima regime, (e.g., Baloković et al. 2016). Our results for the first visibility window (VW1) from 2015 to 2016 show many tracks of similar steepness between linear and quadratic which can be interpreted as hints that particle injection caused the flux variations and the IC scattering happened at least partly in the KN regime.

More information on the processes that drove the outbursts may come from the time-resolved SED modelling and the evolution of the synchrotron peak shift with increasing peak flux. The strength of the synchrotron hump strongly depends on the magnetic field, region size, Doppler factor, and the normalization of the electron energy distribution in the emission region. By studying three months of X-ray emission of Mrk 421, Tramacere et al. (2007) found a positive correlation between the synchrotron peak height and position described by a power law. In the context of a homogeneous single emission zone, they related the power law index to properties of the emission region and

acceleration mechanisms and found that the correlation could be explained by stochastic acceleration of the electrons (see Sect. 2.4.7). We observed two outburst with different trends of the synchrotron peak position and height. The increase of the synchrotron peak height without any peak shift in 2015 implies, that only the normalization of the synchrotron spectrum changed during the outburst, which supports particle injection as driving process.

Certainly, the process responsible for the outburst in 2015 differed from the one causing the outburst in 2017. The synchrotron peak and energy evolution followed a very different trend. This trend is flatter than what was observed by Tramacere et al. (2007). Contrary to 2015, there is a clear peak shift to higher energies for an increasing peak flux. Pian et al. (2014) also detected a synchrotron peak shift accompanied by spectral hardening in the X-ray band during one of the brightest flares of Mrk 421 in 2013. One should note, that the authors also found possible correlated emission between UV and X-rays during the flare which was not observed in the discussed outbursts in this study. Hence, the conditions for the outburst in 2017 may still differ from Pian et al. (2014). A simultaneous peak-shift of the synchrotron and IC peak was observed for the first time by Baloković et al. (2016) during a period of low-activity. In both cases, the authors concluded that the peak shift indicated the injection/acceleration of new high-energy electrons, that cool via synchrotron and IC emission and caused a deformation of the electron energy distribution. Such a scenario could explain the peak shift and spectral hardening of the X-ray spectrum with increasing flux, if the maximum electron energy increased during the process.

In the context of a single emission region, the broadening of the synchrotron hump observed in our time-resolved SEDs from 2017, may suggest an achromatic acceleration mechanism, e.g., first order Fermi acceleration (see Sect 2.4.7), magnetic diffusion or magnetic reconnection. Such acceleration processes change the energy density through energy momentum diffusion or injection of new particles and alter the emissivity of the electrons. For example, a change in the magnetic field would shift the peak position to higher energies as the flux increases. Furthermore, it would allow to confine higher energetic electrons and hinder particle escape outside the emission region, thus broaden the synchrotron emission hump. However, these hint stems from a phenomenological modeling of the data and can only serve as an indicator. Detailed time-dependent physical modeling of the complete SED including TeV spectra are necessary to provide stronger constraints on the process and the underlying particle energy distribution.

Even though the one-zone SSC model provides reasonable explanations of the X-ray to TeV flux correlations and X-ray harder-when-brighter trend, the lack of a correlation between the UV emission and those at higher energies is challenging. In many studies such models require extreme emission region properties or unusual electron energy distributions (e.g., Baloković et al. 2016; Abdo et al. 2011b). Often these models fail to explain the exact shape of the γ -ray data (not modeled in this work). Many authors have thus investigated the possibility of multiple emission regions, which are not necessarily co-spatial or causally connected (e.g., Sinha et al. 2015; Aleksić et al. 2015a; Chen et al. 2011). Sinha et al. (e.g., 2015) found striking evidence for different emitting

regions of differing compactness from time-resolved spectral analysis during a bright flare in February 2013. Baloković et al. (2016) found that even the lowest state of activity is consistent with a scenario of multiple emission sites in which variations are caused by stochastic second-order Fermi processes. A different geometry was proposed by Chen (2017), who reports on evidence for a two-zone spine-sheath structure. Chen et al. (2011) studied the time-dependent multiwavelength variability of Mrk 421 for different scenarios assuming two electron populations. They found that uncorrelated radiation between UV and high-energy emission from X-rays to TeV is consistent with the case in which there is a steady-state foreground emission (e.g., from a former acceleration process, such as episodic particle acceleration, e.g., Sinha et al. 2015) that is not causally connected nor co-spatial with the accelerated electron population and which dominates in the optical and UV band. Radiation from a more compact emission region with accelerated particles dominates in the X-ray regime. In case the two particle populations are causally connected, e.g., if accelerated electrons are injected into a steady-state population, one can expect correlated emission between the optical/UV band and the GeV γ -rays, as in the outburst in 2015. The results of our correlation analysis is thus consistent with the first case, assuming that the tentative positive and negative correlations between UV and GeV γ -rays are by coincidence. But given the highly variable physical conditions within a jet stream, it is also possible, that we see both cases in the different outbursts, i.e. during the outburst of 2015, we observe the overall increase of the synchrotron hump after a blob of accelerated electrons was injected into a population of steady-state electrons. But during the outburst in 2017, the evolution of the UV emission region is unaffected by the acceleration of particles which cause a hardening and flux increase at higher energies, thus mimicking a peak shift. In both cases, one would expect a quadratic flux increase between X-rays and TeV γ -rays, while the evolution in the declining phase is linear or sub-linear.

9.7. Summary

In this chapter, I presented a first investigation of the broadband monitoring data of the HBL Mrk 421 that were obtained within our Blazar Monitoring MWL program. The Blazar Monitoring MWL program is dedicated to observe HBL blazars during a TeV outburst, in order to obtain time-resolved SEDs which shall be used to constrain competing jet emission models. The study, presented in this thesis, explored multiwavelength monitoring data in both the spectral and timing domain for the first two years of the program. The analysis showed that the monitoring data already harbors valuable information on the jet emission in Mrk 421 and conclusions for the selection of outbursts to trigger on in the continuation of the program.

Even though the source did not show major flaring activity during the monitoring period of Dec 2015 and May 2017, we measured significant variability from UV to VHE γ -rays. The high-energy emission from keV to TeV is strongly correlated without time-lag throughout the whole monitoring campaign, where the strong correlation between emission in the X-rays and TeV band is more significant. These are also the spectral

bands with the highest variability amplitude. A positive correlation between X-rays and TeV γ -rays has been frequently observed observations of this source. We confirm the presence of this correlation on timescales of years, which can be explained in both leptonic and hadronic jet scenarios. In the former case, the correlation is arises naturally in the SSC model. In the hadronic case, the correlation is an indicator for the presence of secondary emission from charged pion decay. Because these mechanism are accompanied by neutrino production, Mrk 421 might be a candidate source for neutrino and cosmic ray acceleration.

While the correlation between X-rays and TeV is well established there are contradicting reports from different authors and observational campaigns on correlated or anti-correlated emission, or no correlation as all, between the UV and GeV γ -ray bands. This is the first time, that both a tentative positive correlation and anti-correlation between these bands is observed within a single campaign including periods of low and high activity. However, we find evidence for an overall long-term variation of the UV flux. Hence, we argue, that the most likely explanation of the different correlation reports is that the UV emission is not causally connected to the high energy emission. Thus, the phenomenological fits to the SED and interband correlation analyses indicate that emission in the UV stems from a different emission zone than X-rays and γ -rays.

More intriguingly, we observed different spectral evolutions of the broadband spectral energy distribution for different flares which are indicative of different mechanism that are responsible for flares in this source. In the context of leptonic jet scenarios, the outburst in 2015 can be explained by simple injection of leptons without alteration of the EED. In contrast, the outburst in 2017 shows evidence for a more complex explanation, such as achromatic particle acceleration or injection of electrons which changes the EED and cause the low-energy emission hump to widen. Another explanation is that we are seeing different emission regions in the UV and X-ray band. The later is supported by the correlation studies.

The analysis emphasizes the approach of time-resolved SED modeling with physical models including the VHE spectrum. The addition of FACT monitoring data is crucial to investigate the spectral evolution at TeV energies and constrain the high-energy hump. Only then, we can put stronger constraints on the mechanism that caused the different outburst behaviour. Nevertheless, the investigation using spectral-timing analysis in the UV to GeV γ -ray bands only proved to be valuable. The Blazar Monitoring MWL program will continue to monitor Mrk 421, Mrk 501 and 1ES 1959+650. And physical SED models will be used in combination with TeV spectra to study the dynamical SEDs of HBLs. Results from this study can be used to refine the program and trigger criteria for example, the duration of the flare or a quicklook analysis of the X-ray data could be used to find interesting outbursts. On the other hand, this analysis showed, that it will not be reasonable to include the optical/UV emission in order to trigger on high-energy outbursts.

10. Summary and Conclusion

The aim of this thesis is the investigation and classification of high-energy emitting AGN and the jet phenomenon. The powerful AGN jets accelerate particles up to relativistic speeds. Whether the jet plasma is composed of leptons only or if they are capable of accelerating hadronic particles as well is an open question. These relativistic hadrons or signatures of their interaction with matter or electromagnetic radiation could be detected in the form of cosmic rays and extraterrestrial neutrinos. In the context of the variable high-energy sky, AGN with relativistic jets are therefore prime candidates for accelerating ultra-high energy cosmic rays or neutrinos. Since strong high-energy emission is a characteristic signature of accelerated particles, it is essential to understand the different emission processes that contribute to the broadband spectrum of jetted AGN. Additional knowledge of the physical parameters of these objects is necessary to understand their formation and evolution. By far, blazars are the most dominant source type in the high-energy γ -ray sky. They exhibited frequent high-energy flares and are well suited to study the relative contribution of different emission processes during flaring and quiescent states. But there is a growing number of jetted AGN at a larger angle to the jet axis that are detected in this energy band. These non-blazars are excellently suited to study differences and similarities in the low- and high-energy emission processes with respect to blazars. Nowadays, there is a large number of satellites and observatories that provide the opportunity to observe the high-energy emission of AGN in outburst or to monitor the long-term broadband emission in different energy bands simultaneously. Combining the spectral and temporal information on the multiwavelength spectrum offers a powerful tool to study the spectral evolution of jetted AGN.

In this thesis, I present three studies which all deal with the topic of classification on different levels and shed light on different aspects of these extraordinary objects. I show how one can use spectral and timing analysis to characterize unknown X-ray sources (Chpt. 7) which may harbor scientific discoveries. Furthermore, I illustrate the diverse temporal and spectral evolution of high-energy emitting AGN on the non-blazar PKS 2004–447 (Chpt. 8) and the classical blazar Mrk 421 (Chpt. 9).

In the first study (Chpt. 7), source classification in the classical sense is performed on a large data set, i.e. the 3XMM point source catalog of the *XMM-Newton* satellite by using supervised machine learning algorithms. The aim of this project is the set up of an automated classification pipeline which will facilitate the search for interesting objects for future X-ray satellite missions, such as *eROSITA*. By using archival *XMM-Newton* data, I derive spectral features for more than 130,000 unique detections and a sample of 135 transient detections of unknown source class. The information of catalog cross-matches performed by Mirjam Örtel, is used to derive multiwavelength features for each detected source. Together with timing features provided by the *EXTraS* team, we train

a supervised random forest machine learning algorithm based on a well-defined training set of the 3XMM. The classifier is tested on the remaining sources of the 3XMM and eventually applied to the sample of transient sources. We show that the automated method requires a very thorough examination of the training sample. Although the training sample is balanced by oversampling beforehand, the algorithm has problems distinguishing between Seyfert galaxies, CVs, and stars in the Galactic disk, which make up the most abundant source types in the unbalanced training set. In general, the training process showed that the combination of spectral, timing and multiwavelength features performs best in classifying a large set of objects with the lowest misclassification rate of $\sim 2.4\%$. The X-ray source flux and hardness ratios had the greatest influence on the first separation. If available, the radio flux and Fourier frequencies can provide a further distinction. Although, the influence of the timing features can only be tested to a limited extent since many sources do not have enough data to provide significant constraints on the parameters. The addition of timing features results in a slight improvement of the misclassification rate but it also leads to the situation that more sources (42%) cannot be classified at all. In case of the transients, 60% are classified. The classification of the 135 transient is therefore to be understood as an indication for the respective source type only.

For the other two projects, the methods of time-resolved spectroscopy was used to study two individual sources in more detail. Both objects belong to the class of γ -ray-emitting AGN. Among these objects NLS1 are a relatively new source type. Only a handful of sources are detected in γ -rays so far (γ -NLS1). This group of radio-loud AGN are intriguing in that they are a distinct group of AGN (besides blazars and radio galaxies) hosting powerful relativistic jets while having different properties than blazars and radio galaxies, such as high-mass accretion and small SMBH masses. Nevertheless, they share a relativistically beamed jet and a double-humped SED. The only γ -NLS1 on the Southern Hemisphere so far is PKS 2004–447 which lies at the lower end of the luminosity distribution of γ -NLS1. The source is part of the TANAMI VLBI program and is regularly monitored at radio frequencies. In Chpt. 8, I focus on the high-energy emission of PKS 2004–447, for which I have acquired monitoring observations in the X-ray and UV/optical range with *XMM-Newton* and *Swift* as part of the TANAMI program. The X-ray data show a hard featureless power-law shape ($\Gamma_X \sim 1.35$) which can be identified with the high-energy hump of the jet emission, using time-resolved spectroscopy of the broadband spectrum. The timing analysis reveals a moderate flux and spectral shape variability of the optical and X-ray emission. Archival *XMM-Newton* data from 2004 show hints for a soft emission component in excess to the hard power law which cannot be confirmed by our new observations from 2012 when the source has been in a lower flux state. Using time series analysis methods, I show that such emission is not present in the lowest detectable flux states of the sources which excludes the presence of a constant emission component that is independent of the hard power-law emission. Whether this component exists only in high flux states will be tested in newly acquired spectroscopic data from simultaneous observation with *XMM-Newton* and *NuSTAR*. The optical/UV and X-ray observations are supplemented by VLBI and

single-dish radio observations by the TANAMI program and ATCA as well as γ -ray observations of the *Fermi*-LAT instrument. By combining multi-wavelength spectra at different times, I compute a series of SEDs of PKS 2004–447 and analyze the evolution of the broad band spectrum. This allows me to identify the optical emission with the low-energy hump of the jet emission. Further evidence for correlated flux variability between both humps is indicative of a causal connection between both humps (e.g., through a synchrotron/SSC or EC scenario). The SED of this source is very similar to typical examples of FSRQ and does not present any unusual properties in comparison to known blazars. Interestingly, the VLBI data show a compact jet structure and a steep radio spectrum consistent with a compact steep spectrum source, classifying PKS 2004–447 as a young radio galaxy, in which the jet is still developing. Besides PKS 2004–447 a few young radio galaxies have been detected at γ -rays so far (e.g., PKS 1718–649 or PMN J1603–4904, see appendix ??). In addition, PKS 2004–447 plays the role of an outsider in the sample of γ -NLS1 as well because its classification as NLS1 is not yet 100% clarified. For these purposes I have obtained several new optical spectroscopy observations which will be analyzed with respect to optical classification properties of NLS1 and the influence of possible variability on these parameters.

The third investigation (Chpt. 9) presented in this thesis introduces the blazar monitoring program. By observing a blazar simultaneously with several instruments during a VHE outbursts, the program aims at providing extraordinary data sets to allow for the generation of a series of dynamical SEDs. These SEDs can be used to study temporal and spectral evolution of the broadband spectrum during the outburst to investigate particle acceleration and emission processes of blazar flares, and derive information on the composition of the jet plasma. The program makes use of the dense VHE monitoring by the FACT telescope. So far, there are three sources in our sample that we have been monitoring since 2014. I present the data and the first analysis of the active blazar Mrk 421, which has had a moderate outbreak in 2015 and triggered our program for the first time. The correlation analysis of light curves in different emission bands finds a tight correlation between the X-ray and VHE emission during the complete duration of the monitoring as well as the flare and confirms results by previous studies over shorter time periods. In addition, the data set covers a sufficiently large time span, which shows evidence for both correlated and anti-correlated emission of the optical/UV and HE emission, for the first time. A closer look at the variations of the optical/UV light curve suggests that these correlations occur by chance and the bands are probably not causally connected. This conclusion is supported by spectral evolution of the SEDs. Two different flaring behaviors are observed, which differ by the presence or lack of a peak shift of the low-energy emission hump. These results indicate that more than one emission region participated in the broadband emission of Mrk 421 during the observations. In the end, an important part of the program are a series of VHE spectra during the outbursts and the dynamic SEDs, which are necessary to distinguish between hadronic and lepton emission processes. Unfortunately, the VHE spectra are still under construction at the time of writing. The given data allows both a leptonic or hadronic interpretation.

All three projects showed that the combination of spectral and temporal studies of the

broadband emission of high-energy emitting objects (AGN in particular) are a powerful tool to classify both the source type as well as the emission processes. While large blind studies such as the automated pipeline can help to find interesting objects, dedicated observing and monitoring campaigns are required to clarify an object's nature.

A. EXTraS

A.1. Automated fitting pipeline

Figs. A.1 show basic schemes of the automated fitting pipeline for an absorbed powerlaw model model. For all models the following tasks are performed:

- To account for spectra with low numbers of spectral data counts, each spectrum is rebinned to contain at least 3 counts per bin (cpb) and Cash Statistics (CSTAT) is used as a test statistic for all fits.
- The default minimization method is POWELL with a tolerance of 20%. If the minimization fails SUPLEX (a sub-space searching SIMPLEX method) is used with 1% tolerance. To speed up the computation of parameter uncertainties POWELL is used with 1% tolerance and a maximum of 300 iterations.
- The total energy band (0.5–10) keV is divided into two sub-bands: the soft band (0.5–2) keV and hard band (2–10) keV. These bands are used during the fitting pipeline.
- The defined spectral model is fitted without Galactic absorption to an energy sub-band (soft or hard) where the respective model dominates. This allows to obtain fallback parameters in case a specific parameter cannot be constrained in the full band of (0.5–10) keV. Subsequently the model is fitted with Galactic absorption to the full energy range and flux densities are determined for all energy bands.
- For each model, 90% confidence limits are calculated for every variable parameter if the fit statistic $C/d.o.f.$ ¹ is less or equal to 10. This limit is an empirical value in order to avoid divergence during the minimization process. If ISIS cannot constrain the value of a certain parameter the parameter is fixed. The fixed values are not the same for all observations. They are computed during each fitting process (see model description Sect. A.2) and depend on the spectral model, energy band and data quality.
- Results of each model is stored in a separate FITS table that are combined to a single master table.

¹degrees of freedom = number of energy bins - number of free model parameters

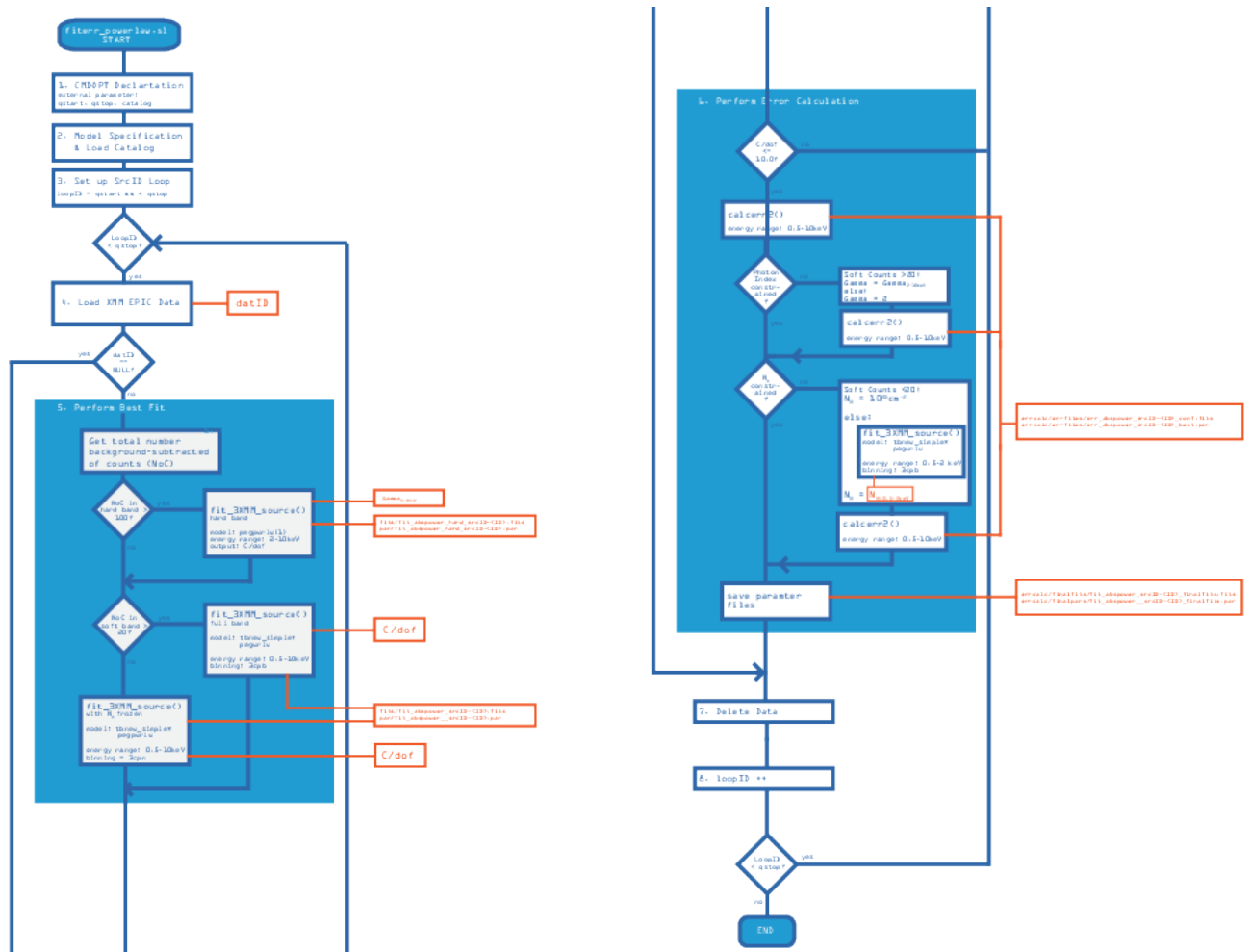


Figure A.1.: Exemplary scheme of the fit process for the absorbed power-law model.

Fluxes

Observed fluxes are computed for each model from the respective best-fit model in the range in which the spectral fit was evaluated. Thus, a direct comparison of fluxes is only possible in the soft band. Observed fluxes are computed from the Galactically absorbed model. Absorption corrected fluxes are calculated for the total band. For model including a power law, fluxes are also computed for the power law in the soft and hard band.

A.2. Spectral Model description

This section describes the application of various spectral models that were applied to *XMM-Newton* EPIC data (see Sect. 7.4). Table A.1 summarizes the fit models used throughout the analysis.

Table A.1.: Spectral models used for automated fitting.

Simple models		Complex models:	
1)	powerlaw (<code>pegpwlw</code>)	4)	power law (1) + intrinsically absorbed power law*
2)	blackbody (<code>bbody</code>)	5)	black body (2) + intrinsically absorbed power law
3)	ionised plasma (<code>apec</code>)	6)	ionised plasma (3) + intrinsically absorbed power law

Note: All models listed are additionally absorbed by global Galactic absorption N_{H} using the `isis` model string `tbnew_new*(model_name)`. * `isis` model string: `tbnew_new*(pegpwlw(2))`

Table A.2.: Initial parameter values for the absorbed power-law model.

Parameter	isis name	initial value	freeze	min	max	unit
$N_{\text{H,pl}}$	<code>tbnew_simple(1).nh</code>	$-^a$	0	0	100	10^{22} cm^{-2}
Γ_{pl}	<code>pegpwlw(1).PhoIndex</code>	2	0	-2	9	-
N_{pl}	<code>pegpwlw(1).norm</code>	1	0	0	10^{10}	$10^{-12} \text{ ergs s}^{-1} \text{ cm}^{-2}$
E_{min}	<code>pegpwlw(1).eMin</code>	0.5	1	-100	10^{10}	keV
E_{max}	<code>pegpwlw(1).eMax</code>	10	1	-100	10^{10}	keV

Note: ^a If there is a Galactic hydrogen column density $N_{\text{H,gal}}$ for the coordinates of the corresponding detection the initial value for $N_{\text{H}}=N_{\text{H,gal}}$, otherwise $N_{\text{H}} = 10^{22} \text{ cm}^{-2}$. E_{min} and E_{max} are the lower and upper limit for the energy range in over which the power-law flux density is integrated. For frozen parameter freeze = 1.

Absorbed power-law model:

An absorbed power-law component is among the most commonly used spectral shapes to describe the non-thermal spectral shape of an X-ray source, such as active galactic nuclei (AGN) or X-ray binaries (XRB). The model is applied in all energy bands. The free parameters are listed in Table A.1. Initial values for all parameters are listed in Table A.2. If the number of background-subtracted spectral data counts in the hard subband is above 100 cts, the first step of the fitting process calculates the photon index Γ_{hard} in the hard band. The unabsorbed power law is fitted to the hard energy band, where non-thermal emission is not affected by photo-electric absorption. If the number of counts in the hard spectrum is less than 100 counts $\Gamma_{\text{hard}} = 2$. In case the photon index of the best-fit model of the full energy band cannot be constrained during the error calculation, Γ_{pl} is fixed to the value of Γ_{hard} and the calculation is run again.

Afterwards the whole energy range is fitted including absorption. If the data quality is sufficient, i.e. the number of counts in the soft band is larger than 20, the absorbing column density is set to the value of the Galactic column density. Otherwise, N_{H} is set to 10^{22} cm^{-2} , following the XMMFITCAT analysis by Corral et al. (2015).

The observed flux is determined using the implemented ISIS function `energyflux` of the absorbed power-law model in the full energy range. The normalization of `pegpwlw` corresponds to the integrated power-law flux density between the specified parameters

Table A.3.: Initial parameter values for the absorbed blackbody model.

Parameter	isis name	initial value	freeze	min	max	unit
$N_{\text{H, BB}}$	tbnew_simple(1).nh	$-^a$	0	0.01	150	10^{22} cm^{-2}
T_{BB}	bbbody(1).kT	0.5	0	0.0001	20	keV
N_{BB}	bbbody(1).norm	1	0	0	10^{10}	$L_{39} D^{-2b}$

Note: ^a If there is a Galactic hydrogen column density $N_{\text{H, gal}}$ for the coordinates of the corresponding detection the initial value for $N_{\text{H}} = N_{\text{H, gal}}$, otherwise $N_{\text{H}} = 10^{22} \text{ cm}^{-2}$. ^b L_{39} is the luminosity in units of $10^{39} \text{ erg s}^{-1}$ and D^{-2b} the luminosity distance in units of 10 kpc. For frozen parameter freeze = 1.

E_{min} and E_{max} . In addition to the flux of the total energy band, soft and hard fluxes in the corresponding bands are computed by adjusting the E_{min} and E_{max} and re-evaluating the model in the given energy band.

90% single-parameter confidence limits are computed for every free model parameter if the C value per degree of freedom (C/d.o.f.) is less than a empirical value 10. In case Γ_{pl} is unconstrained within these limits (i.e. lower or upper confidence limit is pegged at parameter hard limits), Γ_{pl} is frozen to the value of Γ_{hard} or to 2 depending on the data quality of the hard band. Then the error calculation is run again. If the absorbing column density N_{H} is unconstrained, the alternative value of N_{H} is computed if the number of counts in the soft band is larger than 20 counts. In this case, the best-fit model is fitted to the soft band only, to compute $N_{\text{H, soft}}$ and N_{H} is fixed to this value. Otherwise, N_{H} is fixed to 10^{20} cm^{-2} . The error calculation is run again, after every fixing of an unconstrained parameter.

Absorbed blackbody:

This model is used to describe soft X-ray emission in sources involving AGN, XRB and supersoft novae. It is only applied to the soft energy band of the spectrum. The initial parameters are listed in Table A.3. After the best-fit has been found the observed flux density is determined for the soft energy band.

90% uncertainties are calculated if C/d.o.f. is less than 10.0. In case the blackbody temperature kT_{BB} is unconstrained it is fixed to the alternative blackbody temperature kT_{soft} . If the pn spectrum has less than 20 counts in the soft band $kT_{\text{soft}} = 0.1 \text{ keV}$. For a good-quality spectrum kT_{soft} is computed by fitting an unabsorbed blackbody in the soft energy range. If the hydrogen column density N_{H} is unconstrained it is fixed to 10^{20} cm^{-2} .

Table A.4.: Initial parameter values for the absorbed thermal model.

Parameter	isis name	initial value	freeze	min	max	unit
$N_{\text{H,ap}}$	tbnew_simple(1).nh	$-^a$	0	0.01	150	10^{22} cm^{-2}
T_{ap}	apec(1).kT	0.5	0	0.0001	20	keV
N_{ap}	apec(1).norm	1	0	0	10^{10}	
z_{ap}	apec(1).Redshift	0	1	0	10	
A_{ap}	apec(1).Abundanc	1	1	0	10^{10}	A_{solar}

Note: ^a If there is a Galactic hydrogen column density $N_{\text{H,gal}}$ for the coordinates of the corresponding detection the initial value for $N_{\text{H}}=N_{\text{H,gal}}$, otherwise $N_{\text{H}} = 10^{22} \text{ cm}^{-2}$. For frozen parameter freeze = 1.

Absorbed thermal emission:

Apec is used for modeling thermal emission of a collisionally ionized plasma. It uses data from the atomic database AtomDB v3.0.2². Opposed to the power-law model it is intended to describe the spectral shape of stars, galaxies, and galaxy clusters. The absorbed thermal model is applied to both the total and soft spectrum. For fitting the soft spectrum the pn spectrum needs to have more than 20 counts in the soft energy band. Initial values are listed in Table A.4. The alternative plasma temperature $T_{\text{ap,soft}}$ is computed by removing the absorption component and fitting the model in the soft band if the spectrum fullfills the condition described above. The alternative temperature is used to fix the best-fit plasma temperature T_{ap} in case it cannot be constrained. If the conditions to fit the soft band are not met, $T_{\text{ap,soft}}$ is set to 1 keV. The fixed value used in case the column density cannot be constrained is again 10^{20} cm^{-2} . After determining the alternative values, the absorbed thermal model is applied to the total band. Observed fluxes are determined from the best-fit model in the total range. The 90% confidence limits are calculated and parameter values are fixed to there alternative values if they cannot be constrained within their limits.

Complex models:

Complex models are an extension of the simple models. They are only applied if the total number of spectral data counts is larger than 500 cts, and the number of counts in each of the sub bands (soft and hard band) is larger than 50 cts. The basic syntax is a simple model (power law, blackbody, or apec) plus an intrinsically absorbed power law, where both components are additionally modulated by Galactic absorption. It is used to account for spectra with an additional non-thermal component. Results from the simple model fits serve as input parameters for the complex model. Handling of unconstrained parameters is equivalent to simple models. If the power law component results to be insignificant for a fit after error calculation, the fit is not taken into account and not

²<http://www.atomdb.org/>

listed in the result table.

A.3. Complete List of Classification Features

Table A.5.: List of all classification features extracted in this analysis.

Set	Feature name	Explanation
3XMM ^a	cat3xmm_ext	3XMM extended source flag
	threexmm_bii	Galactic longitude
	threexmm_lii	Galactic latitude
	cat3xmm_hr1	Hardness Ratio HR1
	cat3xmm_hr2	Hardness Ratio HR1
	cat3xmm_hr3	Hardness Ratio HR1
	cat3xmm_hr4	Hardness Ratio HR1
	cat3xmm_e_hr1	1 σ error on HR1
	cat3xmm_e_hr2	1 σ error on HR2
	cat3xmm_e_hr3	1 σ error on HR3
	cat3xmm_e_hr4	1 σ error on HR4
	Spectral ^b	nhgal
ap_norm		AP normalization
ap_obsflux		Observed flux from AP model [erg/cm ² /s]
ap_tbnewnh		Hydrogen Column density $N_{H,AP}$ [10 ²² cm ⁻²]
ap_temp		Ionized gas temperature kT_{AP} [keV]
ap_uabsflux		Apec (0.5–10) keV flux [10 ⁻¹² erg/cm ² /s]
appl_apnorm		APPL apec normalization
appl_aptemp		Ionized gas temperature kT_{APPL} [keV]
appl_gamma		Power-law photon index Γ_{APPL}
appl_norm		APPL power-law (0.5–10) keV flux [10 ⁻¹² erg/cm ² /s]
appl_obsflux		Observed flux from APPL model [erg/cm ² /s]
appl_pl_flux_tot		(0.5–10) keV power-law flux from APPL model [erg/cm ² /s]
appl_tbnew1nh		global column density $N_{H,APPL,1}$ [10 ²² cm ⁻²]
appl_tbnew2nh		power-law column density $N_{H,APPL,2}$ [10 ²² cm ⁻²]
bb_norm		BB normalization N_{BB}
bb_obsflux		Observed flux from BB model [erg/cm ² /s]
bb_tbnewnh		Hydrogen Column density $N_{H,BB}$ [10 ²² cm ⁻²]
bb_temp		Blackbody temperature kT_{BB} [keV]
bb_uabsflux		Blackbody (0.5–10) keV flux [10 ⁻¹² erg/cm ² /s]
bbpl_bbnorm		BB normalization N_{BBPL}
bbpl_bbtemp	Blackbody temperature kT_{BBPL} [keV]	

Model abbreviation: AP - apec, BB - blackbody, PL - power-law, see Table 7.4.

See next page

Table A.5.: continued

Set	Feature name	Explanation
	bbpl_gamma	Power-law photon index Γ_{BBPL}
	bbpl_norm	BBPL power-law (0.5–10) keV flux [10^{-12} erg/cm ² /s]
	bbpl_obsflux	Observed flux from BBPL model [erg/cm ² /s]
	bbpl_pl_flux_tot	(0.5–10) keV power-law flux from BBPL model [erg/cm ² /s]
	bbpl_tbnew1nh	global column density $N_{\text{H, BBPL},1}$ [10^{22} cm ⁻²]
	bbpl_tbnew2nh	intrinsic column density $N_{\text{H, BBPL},2}$ [10^{22} cm ⁻²]
	pl_flux_hard	(2-10) keV power-law flux from PL model [erg/cm ² /s]
	pl_flux_soft	(0.5-2) keV power-law flux from PL model [erg/cm ² /s]
	pl_norm	(0.5-10) keV power-law flux from PL model [10^{-12} erg/cm ² /s]
	pl_gamma	Power-law photon index Γ_{PL}
	pl_obsflux	Observed flux from PL model [erg/cm ² /s]
	pl_tbnewnh	Hydrogen Column density $N_{\text{H, PL}}$ [10^{22} cm ⁻²]
	plpl_gamma1	soft power-law index $\Gamma_{\text{PLPL},1}$
	plpl_gamma2	hard power-law index $\Gamma_{\text{PLPL},2}$
	plpl_norm1	soft power-law (0.5-10) keV flux [10^{-12} erg/cm ² /s]
	plpl_norm2	hard power-law (0.5-10) keV flux [10^{-12} erg/cm ² /s]
	plpl_obsflux	Observed flux from PLPL model [erg/cm ² /s]
	plpl_tbnew1nh	global column density $N_{\text{H, PLPL},1}$ [10^{22} cm ⁻²]
	plpl_tbnew2nh	intrinsic column density $N_{\text{H, PLPL},1}$ [10^{22} cm ⁻²]
	ap_redstat	reduced C value for AP model
	appl_redstat	reduced C value for APPL model
	bb_redstat	reduced C value for BB model
	bbpl_redstat	reduced C value for BBpl model
	pl_redstat	reduced C value for PL model
	plpl_redstat	reduced C value for PLPL model
MWL ^b	a_gx	MWL index $\alpha_{\text{G},\text{X}}$
	a_hx	MWL index $\alpha_{\text{H},\text{X}}$
	a_ir1x	MWL index $\alpha_{\text{IR1},\text{X}}$
	a_ir2x	MWL index $\alpha_{\text{IR2},\text{X}}$
	a_ir6x	MWL index $\alpha_{\text{IR6},\text{X}}$
	a_ir8x	MWL index $\alpha_{\text{IR8},\text{X}}$
	a_ox	MWL index $\alpha_{\text{IO},\text{X}}$
	a_r1x	MWL index $\alpha_{\text{R1},\text{X}}$
	a_r5x	MWL index $\alpha_{\text{R5},\text{X}}$
	a_r8x	MWL index $\alpha_{\text{R8},\text{X}}$
	a_uv	MWL index $\alpha_{\text{UV},\text{X}}$

Model abbreviation: AP - apec, BB - blackbody, PL - power-law, see Table 7.4.

See next page

Table A.5.: continued

Set	Feature name	Explanation
Timing ^c	Short-term variability	Light curve properties
	bb_cdf_tfrac	fraction of time spent more than ...
	_abo1s	... 1 σ above the average rate
	_abo3s	... 3 σ above the average rate
	_abo5s	... 5 σ above the average rate
	_bel1s	... 1 σ below the average rate
	_bel3s	... 3 σ below the average rate
	_bel5s	... 5 σ below the average rate
	bb_lc_amplit	amplitude of rate excursion ($\max(\text{rate})-\min(\text{rate})$)/2
	bb_lc_ave	weighted average rate
	bb_lc_nblocks	number of bayesian blocks
	bb_lc_fragment	fragmentariness of the light curve (number of block \leq 1 ks)
	bb_lc_fvar	weighted fractional variability amplitude
	bb_lc_hal_time	light curve halving time
	bb_lc_dou_time	light curve doubling time
	bb_lc_kurt	weighted reduced kurtosis on the distribution of the rate
Timing II ^c	Short-term variability	Best-fit parameter values
	bb_lc_co_par1	constant rate of constant fit model
	bb_lc_ec_par1	constant rate of constant+eclipse fit model
	bb_lc_ec_par2	drop in rate during eclipse
	bb_lc_ec_par3	epoch of ingress into eclipse
	bb_lc_ec_par4	epoch of egress from eclipse
	bb_lc_ex_par1	constant rate of exponential decay fit model
	bb_lc_ex_par2	normalization of the decay component
	bb_lc_ex_par3	characteristic decay time
	bb_lc_fl_par1	constant rate of flare fit model
	bb_lc_fl_par2	flare normalization
	bb_lc_fl_par3	flare epoch
	bb_lc_fl_par4	characteristic flare decay time
	bb_lc_li_par1	constant rate of linear fit model
	bb_lc_li_par2	linear coefficient
	bb_lc_qu_par1	constant rate of quadratic fit model
	bb_lc_qu_par2	linear coefficient
	bb_lc_qu_par3	quadratic coefficient
Timing III ^d	peridic variability	

Model abbreviation: AP - apec, BB - blackbody, PL - power-law, see Table 7.4.

See next page

Table A.5.: continued

Set	Feature name	Explanation
	probability	probability of a periodoc signal
	power	signal power
	ffr	Fourier frequency of the signal
	bestfreq	best-fit frequency of periodic light curve
	bestp	best-fit periode of periodic light curve

Notes: The final list of extracted features is shown in Table 7.6.

^a provided by 3XMM-DR6/EXTraS Transient catalogue

^b extracted in this study

^c provided by WP2 for short-term variability

^d provided by WP3 for periodic variability

A.4. Example Parameter Correlations for the Train, Test and Transient Sample

A.4.1. Training sample

A.4.2. Test sample

A.4.3. Transient sample

A.5. Complete list of EXTraS Transient sources

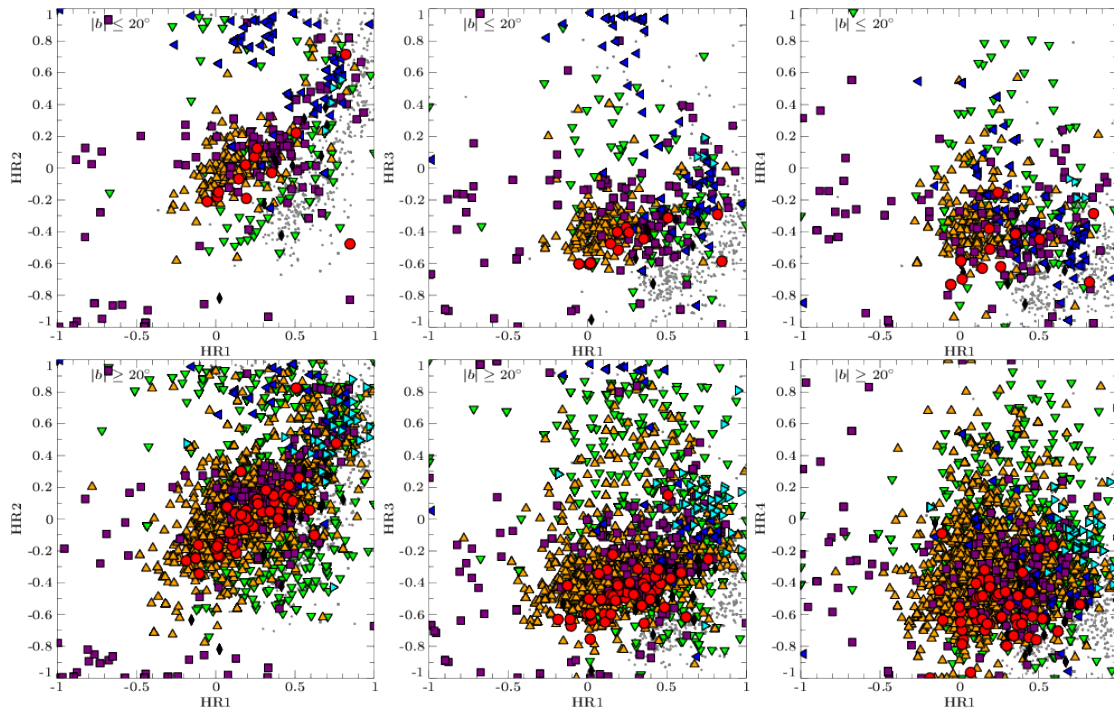


Figure A.2.: Hardness diagrams for the sources of the training sample that are close ($|b| \leq 20^\circ$, top row) or farther away ($|b| > 20^\circ$, bottom row) from the Galactic plane. The symbols for the sources are the same as in Fig. 7.2: AGN (red circle), CV (purple square), S1 (orange triangle top), S2 (green triangle down), STAR (grey dot), ULX (black diamonds), LMXRB (blue triangle left), HMXRB (cyan triangle right), NA/not classified (beige star).

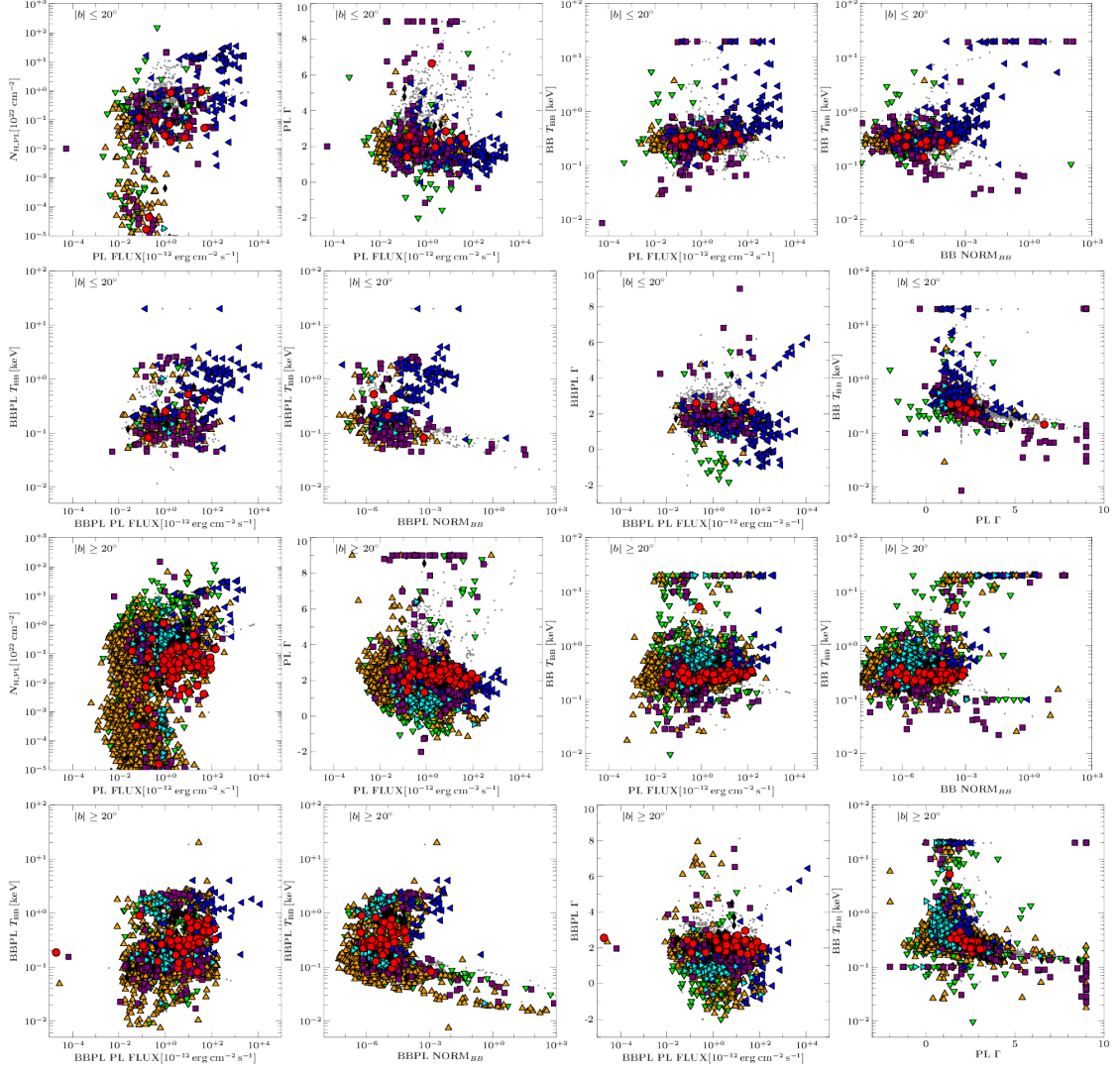


Figure A.3.: Correlation of various spectral parameters for the sources of the training sample for sources that are close ($|b| \leq 20^\circ$) or farther away ($|b| > 20^\circ$) from the Galactic plane. The symbols for the sources are the same as in Fig. 7.2. Plotted parameters are: EP8 flux provided by the 3XMM, flux (PL Flux) and photon index Γ of the simple power law (PL) in the (0.5–10) keV band, absorbing hydrogen column density N_{H} , backbody temperature k_{B} of the simple (BB) and complex (BB+PL) model, power law photon index of the complex models (PLPL and APPL).

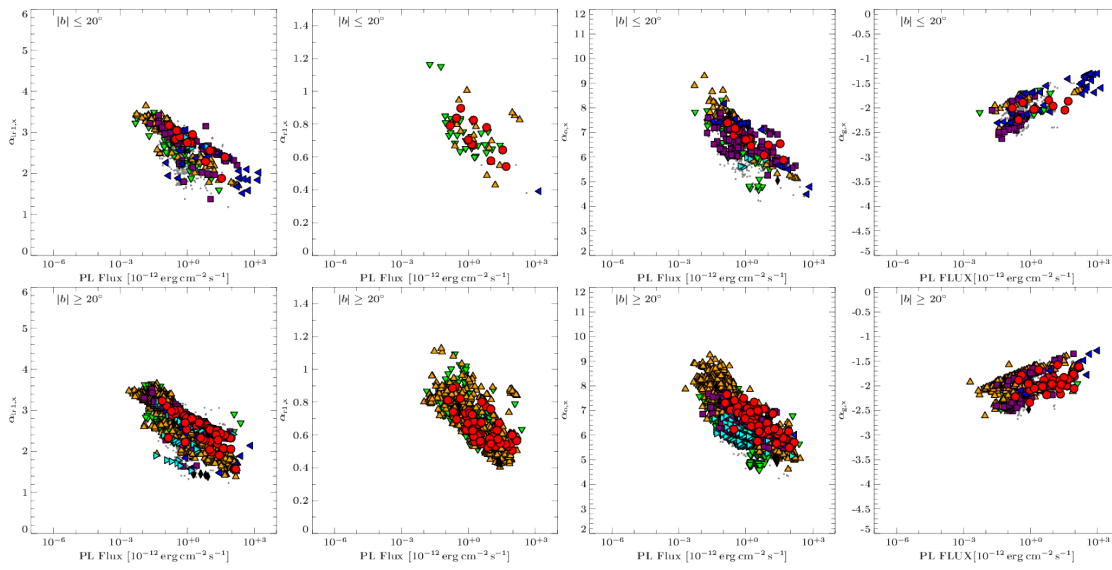


Figure A.4.: Multiwavelength indices as a function of the X-ray flux for the sources of the training sample that are close to ($|b| \leq 20^\circ$) or farther away ($|b| > 20^\circ$) from the Galactic plane. The symbols for the sources are the same as in Fig. 7.2: AGN (red circle), CV (purple square), S1 (orange triangle top), S2 (green triangle down), STAR (grey dot), ULX (black diamonds), LMXRB (blue triangle left), HMXRB (cyan triangle right), NA/not classified (beige star).

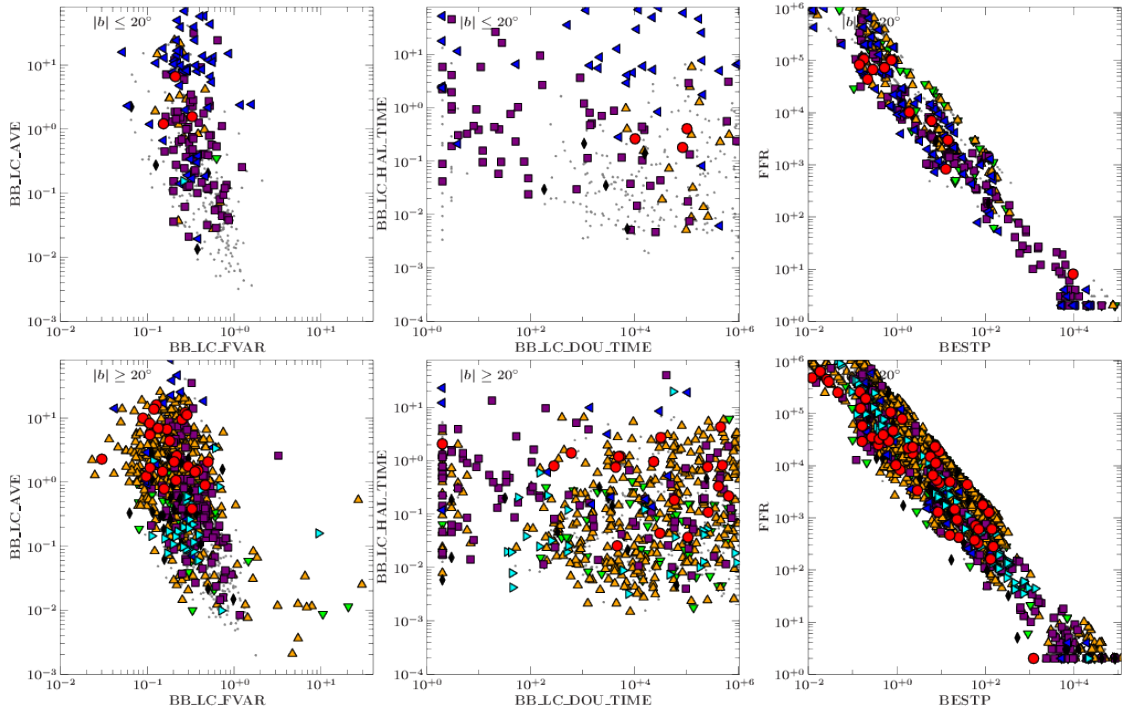


Figure A.5.: Correlation of various timing parameters for periodic and aperiodic variability (from WP2 and WP3) for the sources of the training sample for sources that are close ($|b| \leq 20^\circ$) or farther away ($|b| \geq 20^\circ$) from the Galactic plane. The symbols for the sources are the same as in Fig. 7.2.

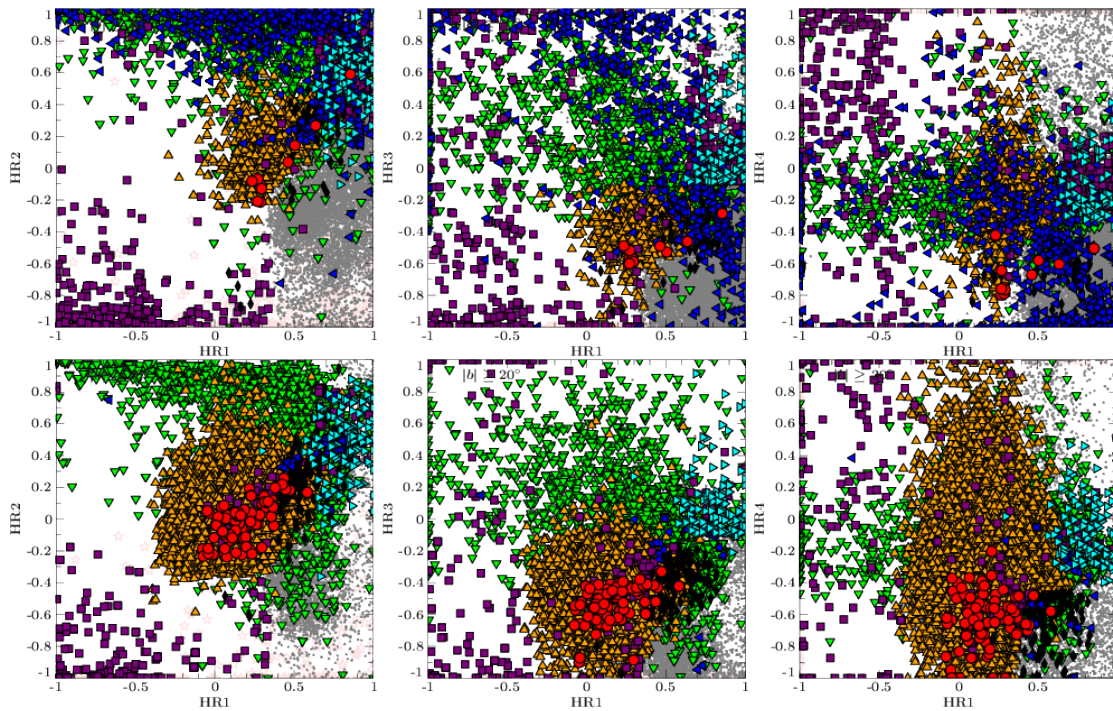


Figure A.6.: Correlation of various hardness ratios for the sources of the test sample for sources that are close ($|b| \leq 20^\circ$) or farther away ($|b| \geq 20^\circ$) from the Galactic plane. The classification run involves spectral information of the X-ray and broadband spectrum as well as parameters describing aperiodic and periodic variability. Information of longterm variability is not included. The symbols for the sources are the same as in Fig. 7.2.

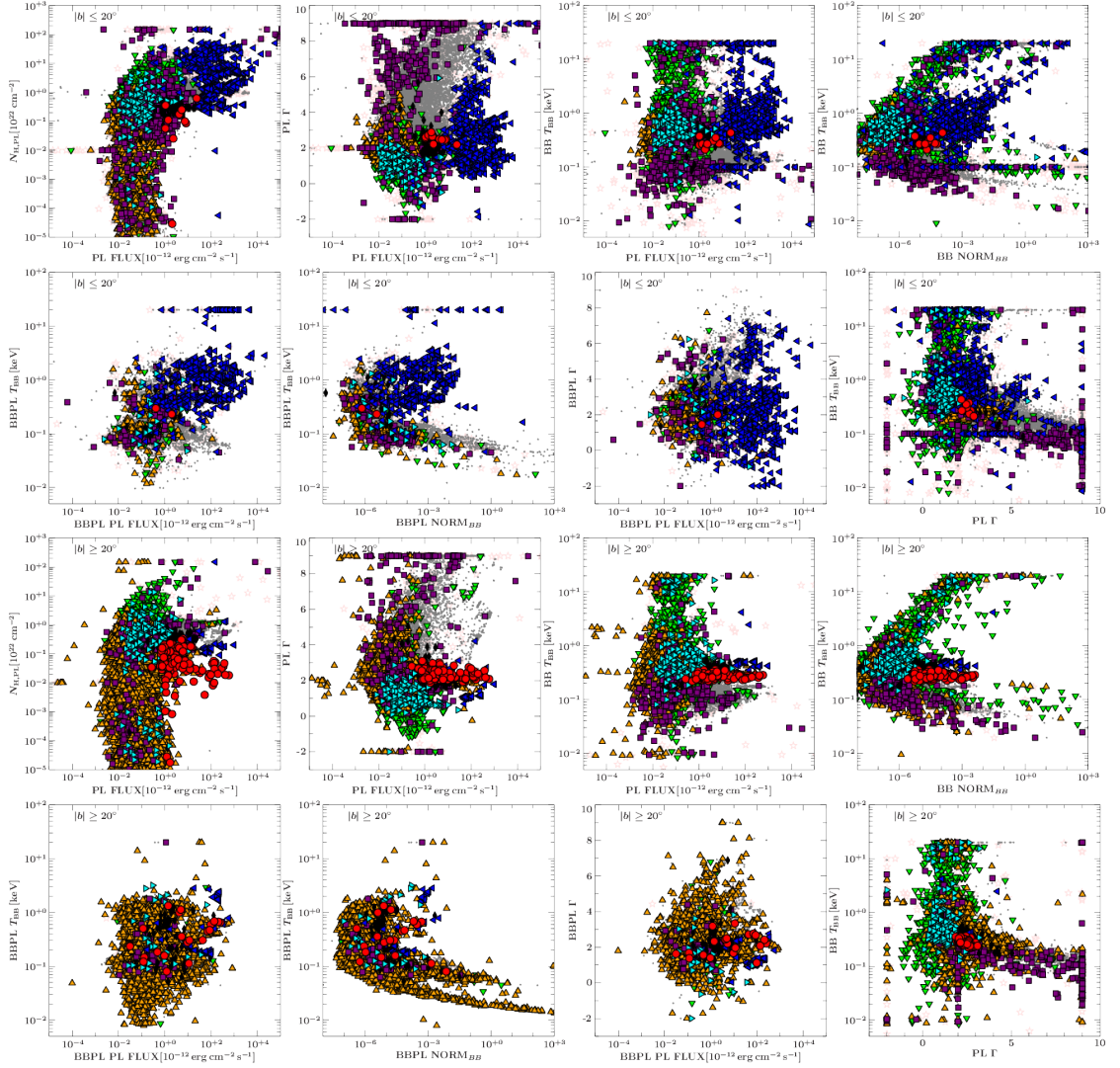


Figure A.7.: Correlation of various spectral parameters for the sources of the test sample for sources that are close ($|b| \leq 20^\circ$) or farther away ($|b| \geq 20^\circ$) from the Galactic plane. The classification run involves spectral information of the X-ray and broadband spectrum as well as parameters describing aperiodic and periodic variability. Information of longterm variability is not included. The symbols for the sources are the same as in Fig. 7.2.

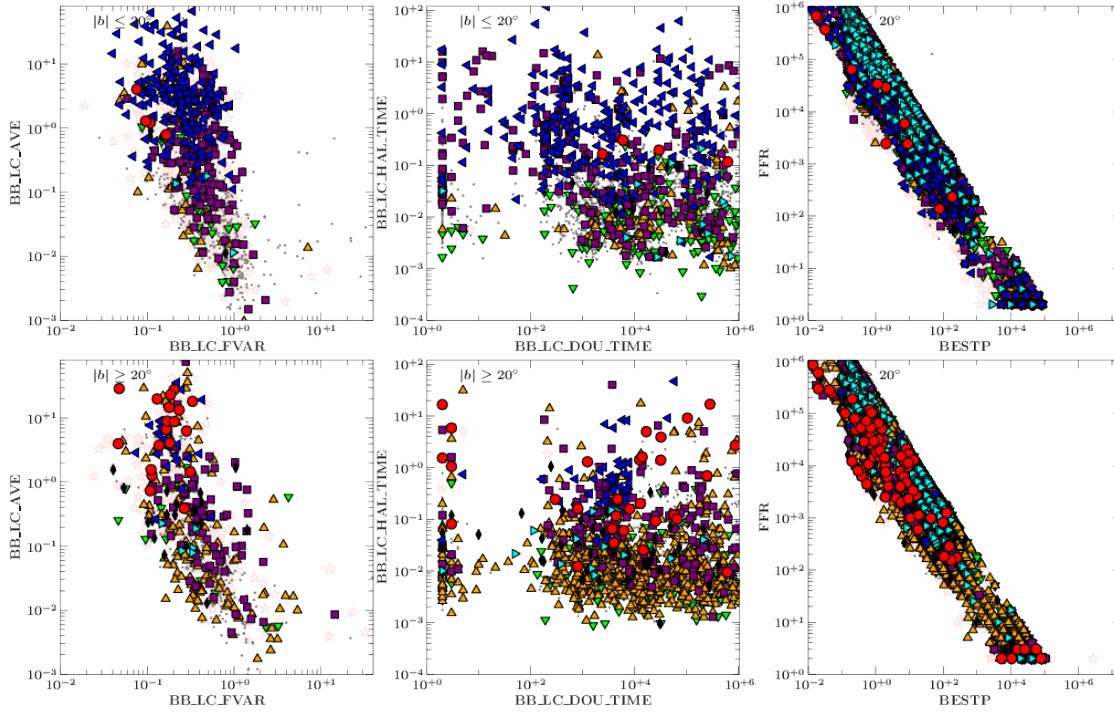


Figure A.8.: Correlation of various timing parameters (from WP2 and WP3) for the sources of the test sample for sources that are close ($|b| \leq 20^\circ$) or farther away ($|b| \geq 20^\circ$) from the Galactic plane. The classification run involves spectral information of the X-ray and broadband spectrum as well as parameters describing aperiodic and periodic variability. Information of longterm variability is not included. The symbols for the sources are the same as in Fig. 7.2.

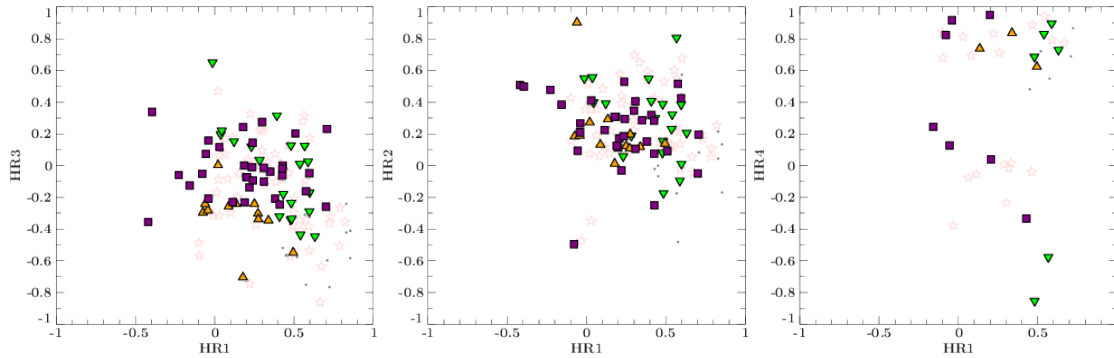


Figure A.9.: Hardness diagrams for transient sources. The symbols for the sources are the same as in Fig. 7.2.

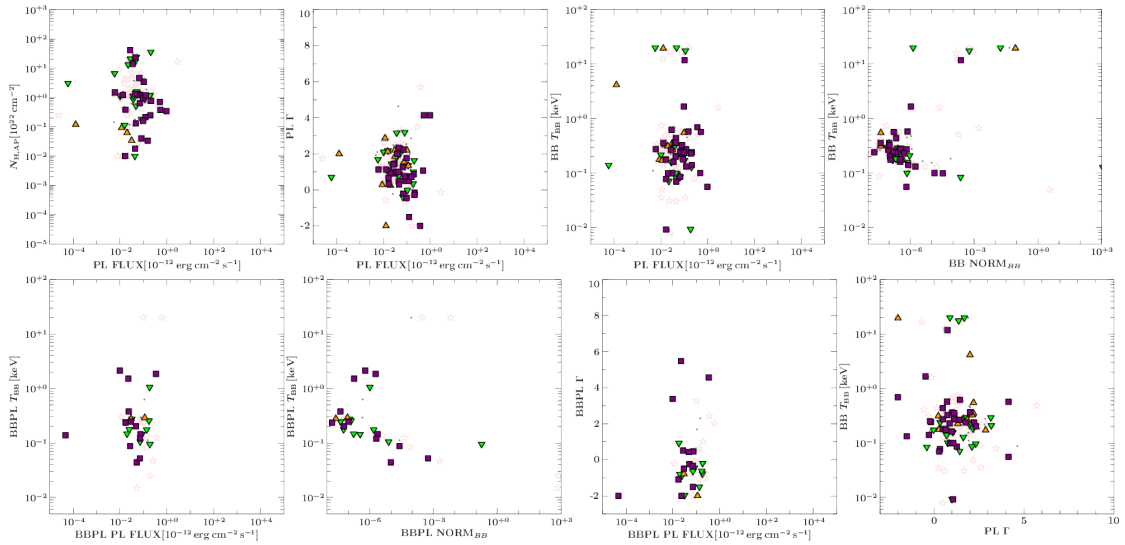


Figure A.10.: Correlation of various spectral parameters for transient sources. The symbols for the sources are the same as in Fig. 7.2.

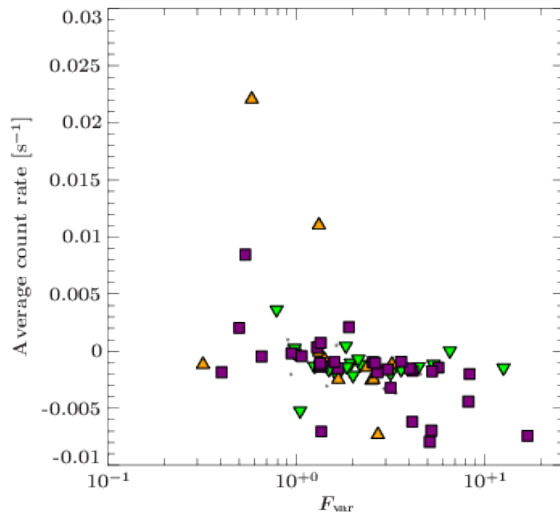


Figure A.11: Correlation of the fractional variability amplitude and average count rate for transient sources. The symbols for the sources are the same as in Fig. 7.2.

Table A.6.: Properties of EXTraS transient sources.

TID ¹	Name	ObsID	Ra ²	Dec ²	Counts	Rate [counts s ⁻¹]	Flux ³ [erg cm ⁻² s ⁻¹]
0	EXMM J001930.4+591440	0693390101	4.88	59.24	120 ± 15	0.05 ± 0.01	0.09 ± 0.03
1	EXMM J002115.2+592518	0693390101	5.31	59.42	75 ± 10	0.13 ± 0.02	0.15 ± 0.05
2	EXMM J003954.6+401810	0402560601	9.98	40.30	13 ± 4	0.04 ± 0.02	0.33 ± 0.31
3	EXMM J004322.3+413432	0690600401	10.84	41.58	54 ± 10	0.02 ± 0.00	0.03 ± 0.02
4	EXMM J004449.9+415244	0109270301	11.21	41.88	115 ± 15	0.05 ± 0.01	0.06 ± 0.03
5	EXMM J020825.7+352826	0084140101	32.11	35.47	40 ± 8	0.03 ± 0.01	0.05 ± 0.03
6	EXMM J022701.8-053144	0404964801	36.76	-5.53	23 ± 6	0.03 ± 0.01	0.09 ± 0.05
7	EXMM J023126.0-712906	0510181701	37.86	-71.48	144 ± 18	0.19 ± 0.03	0.37 ± 0.21
8	EXMM J023135.0-603743	0675010401	37.90	-60.63	55 ± 9	0.52 ± 0.09	1.05 ± 0.54
9	EXMM J025737.3+132247	0112260201	44.41	13.38	27 ± 6	0.06 ± 0.01	0.08 ± 0.06
10	EXMM J031659.2-663214	0405090101	49.25	-66.54	117 ± 12	0.22 ± 0.02	0.26 ± 0.05
11	EXMM J035849.7+541255	0112200301	59.71	54.22	30 ± 7	0.01 ± 0.00	0.17 ± 0.05
12	EXMM J042225.1+281148	0101440701	65.60	28.20	57 ± 10	0.04 ± 0.01	0.06 ± 0.04
13	EXMM J045638.4+302913	0671960101	74.16	30.49	30 ± 7	0.02 ± 0.00	0.02 ± 0.03
14	EXMM J051723.2-685921	0113000501	79.35	-68.99	28 ± 7	0.03 ± 0.01	0.07 ± 0.05
15	EXMM J053219.8-072932	0690200201	83.08	-7.49	143 ± 17	0.17 ± 0.02	0.28 ± 0.09
16	EXMM J053508.2+095532	0402050101	83.78	9.93	555 ± 38	0.16 ± 0.01	0.32 ± 0.03
17	EXMM J053521.8-055403	0112660101	83.84	-5.90	272 ± 20	0.15 ± 0.01	0.27 ± 0.03
18	EXMM J053546.1-051051	0134531701	83.94	-5.18	215 ± 20	0.17 ± 0.02	0.22 ± 0.04
19	EXMM J053928.4-691943	0113020201	84.87	-69.33	37 ± 8	0.02 ± 0.00	0.05 ± 0.03
20	EXMM J061723.5+225537	0600110101	94.35	22.93	39 ± 8	0.34 ± 0.07	0.66 ± 0.33
21	EXMM J061751.0-325214	0092360101	94.46	-32.87	66 ± 10	0.03 ± 0.00	0.04 ± 0.01
22	EXMM J063553.4+054141	0146870401	98.97	5.69	98 ± 15	0.17 ± 0.03	1.16 ± 0.51
23	EXMM J065442.8-240004	0652250601	103.68	-24.00	195 ± 17	0.17 ± 0.02	0.31 ± 0.07

see next page

Table A.6.: continued

TID ¹	Name	ObsID	Ra ²	Dec ²	Counts	Rate [counts s ⁻¹]	Flux ³ [erg cm ⁻² s ⁻¹]
24	EXMM J070206.1-111429	0654880301	105.53	-11.24	54 ± 10	0.06 ± 0.01	0.07 ± 0.05
25	EXMM J070238.9-114145	0654880401	105.66	-11.70	32 ± 8	0.02 ± 0.01	0.02 ± 0.02
26	EXMM J070810.2-492944	0653510301	107.04	-49.50	46 ± 9	0.01 ± 0.00	0.05 ± 0.02
27	EXMM J070900.0-492415	0653510501	107.25	-49.40	13 ± 5	0.06 ± 0.03	0.16 ± 0.47
28	EXMM J072837.7+674629	0302400301	112.16	67.77	41 ± 9	0.02 ± 0.00	0.02 ± 0.01
29	EXMM J080344.1-400619	0159360501	120.93	-40.11	48 ± 7	0.05 ± 0.01	0.61 ± 0.19
30	EXMM J082521.5+261559	0603500301	126.34	26.27	69 ± 11	0.05 ± 0.01	0.55 ± 0.22
31	EXMM J083215.8-452454	0672040101	128.07	-45.41	18 ± 5	0.23 ± 0.07	0.64 ± 0.58
32	EXMM J083833.5-355215	0303230301	129.64	-35.87	37 ± 8	0.02 ± 0.00	0.03 ± 0.02
33	EXMM J083916.3-454613	0603510701	129.82	-45.77	65 ± 12	0.02 ± 0.00	0.06 ± 0.02
34	EXMM J084638.5-525906	0201910101	131.66	-52.99	224 ± 21	0.06 ± 0.01	0.15 ± 0.03
35	EXMM J084839.3-453548	0159760301	132.16	-45.60	118 ± 18	0.12 ± 0.03	0.24 ± 0.06
36	EXMM J092441.0-213122	0065940501	141.17	-21.52	43 ± 9	0.35 ± 0.08	1.92 ± 0.93
37	EXMM J100422.2-701215	0099020301	151.09	-70.20	52 ± 9	0.02 ± 0.00	0.03 ± 0.02
38	EXMM J103154.4-142301	0203770101	157.98	-14.38	28 ± 7	0.07 ± 0.02	0.18 ± 0.12
39	EXMM J103528.6+631021	0403760401	158.87	63.17	158 ± 22	0.21 ± 0.03	1.97 ± 0.52
40	EXMM J104421.4-593453	0112560201	161.09	-59.58	90 ± 14	0.07 ± 0.01	0.31 ± 0.08
41	EXMM J104435.8-593120	0112580601	161.15	-59.52	66 ± 11	0.03 ± 0.01	0.10 ± 0.03
42	EXMM J104439.0-593700	0112560201	161.16	-59.62	61 ± 10	0.07 ± 0.01	0.12 ± 0.04
43	EXMM J104450.1-594208	0160160901	161.21	-59.70	40 ± 8	0.01 ± 0.00	0.41 ± 0.12
44	EXMM J104520.8-593254	0311990101	161.34	-59.55	37 ± 9	0.02 ± 0.01	0.04 ± 0.03
45	EXMM J104620.4+524822	0200480201	161.58	52.81	80 ± 11	0.15 ± 0.02	0.24 ± 0.10
46	EXMM J111116.9-602649	0051550101	167.82	-60.45	68 ± 11	0.05 ± 0.01	0.12 ± 0.06
47	EXMM J111245.2-603617	0051550101	168.19	-60.60	61 ± 9	0.10 ± 0.02	0.13 ± 0.06

see next page

Table A.6.: continued

TID ¹	Name	ObsID	Ra ²	Dec ²	Counts	Rate [counts s ⁻¹]	Flux ³ [erg cm ⁻² s ⁻¹]
48	EXMM J111653.2+440231	0651330301	169.22	44.04	38 ± 7	0.10 ± 0.02	1.63 ± 0.76
49	EXMM J111844.6-612232	0150790101	169.69	-61.38	66 ± 13	0.02 ± 0.00	0.04 ± 0.02
50	EXMM J111939.8-611834	0672790201	169.92	-61.31	95 ± 12	0.15 ± 0.02	0.92 ± 0.30
51	EXMM J113622.2-613751	0201160401	174.09	-61.63	74 ± 12	0.02 ± 0.00	0.03 ± 0.01
52	EXMM J113835.0+170650	0066950201	174.65	17.11	55 ± 10	0.03 ± 0.01	0.05 ± 0.02
53	EXMM J124840.7-055437	0153450101	192.17	-5.91	59 ± 9	0.09 ± 0.02	0.11 ± 0.04
54	EXMM J131233.2-624631	0510980101	198.14	-62.78	62 ± 10	0.05 ± 0.01	0.19 ± 0.04
55	EXMM J132724.8-620703	0036140201	201.85	-62.12	24 ± 6	0.01 ± 0.00	0.04 ± 0.03
56	EXMM J141157.0-651343	0111240101	212.99	-65.23	56 ± 9	0.07 ± 0.01	0.13 ± 0.05
57	EXMM J141328.4-651755	0111240101	213.37	-65.30	72 ± 10	0.09 ± 0.01	0.25 ± 0.06
58	EXMM J142517.6+225545	0143652301	216.32	22.93	149 ± 18	0.18 ± 0.03	0.28 ± 0.15
59	EXMM J144350.6-621945	0504810301	220.96	-62.33	95 ± 13	0.21 ± 0.03	0.38 ± 0.15
60	EXMM J144707.3-622053	0504810201	221.78	-62.35	58 ± 11	0.04 ± 0.01	0.08 ± 0.05
61	EXMM J150230.1-413335	0555630301	225.63	-41.56	58 ± 12	0.09 ± 0.02	0.13 ± 0.21
62	EXMM J151033.9+333059	0303930101	227.64	33.52	62 ± 12	0.09 ± 0.02	0.20 ± 0.07
63	EXMM J151552.5+561021	0673920301	228.97	56.17	31 ± 7	0.02 ± 0.01	0.02 ± 0.02
64	EXMM J151819.8-615757	0555690901	229.58	-61.97	382 ± 31	0.22 ± 0.02	0.34 ± 0.08
65	EXMM J154227.2-522431	0152780201	235.61	-52.41	52 ± 11	0.06 ± 0.01	0.20 ± 0.07
66	EXMM J161132.6-603430	0550451101	242.89	-60.58	39 ± 8	0.03 ± 0.01	0.03 ± 0.02
67	EXMM J161510.5-224401	0555650301	243.79	-22.73	33 ± 7	0.06 ± 0.01	0.07 ± 0.04
68	EXMM J161753.9-505650	0113050701	244.47	-50.95	40 ± 8	0.02 ± 0.00	0.27 ± 0.08
69	EXMM J162705.9-244015	0305540601	246.77	-24.67	61 ± 11	0.02 ± 0.00	0.16 ± 0.03
70	EXMM J162714.7-245135	0305540701	246.81	-24.86	254 ± 18	0.58 ± 0.04	1.20 ± 0.23
71	EXMM J162721.5-244146	0305541101	246.84	-24.70	66 ± 11	0.08 ± 0.01	0.32 ± 0.06

see next page

Table A.6.: continued

TID ¹	Name	ObsID	Ra ²	Dec ²	Counts	Rate [counts s ⁻¹]	Flux ³ [erg cm ⁻² s ⁻¹]
72	EXMM J162729.5-243917	0305540701	246.87	-24.65	151 ± 15	0.04 ± 0.00	0.36 ± 0.04
73	EXMM J163547.9-472914	0502140101	248.95	-47.49	29 ± 7	0.05 ± 0.01	0.35 ± 0.12
74	EXMM J164340.4-542138	0603220201	250.92	-54.36	46 ± 8	0.17 ± 0.03	0.23 ± 0.14
75	EXMM J164707.0-455158	0410580601	251.78	-45.87	89 ± 14	0.05 ± 0.01	0.41 ± 0.08
76	EXMM J164709.7-455034	0505290201	251.79	-45.84	113 ± 14	0.08 ± 0.01	0.72 ± 0.10
77	EXMM J165201.9-415313	0602020201	253.01	-41.89	51 ± 9	0.01 ± 0.00	0.03 ± 0.01
78	EXMM J165415.0-415314	0109490401	253.56	-41.89	64 ± 11	0.05 ± 0.01	0.19 ± 0.05
79	EXMM J165430.4-415455	0109490601	253.63	-41.92	58 ± 10	0.02 ± 0.00	0.06 ± 0.02
80	EXMM J170208.5-485246	0204730301	255.54	-48.88	75 ± 14	0.07 ± 0.02	0.24 ± 0.13
81	EXMM J170213.4-295801	0205580201	255.56	-29.97	97 ± 14	0.06 ± 0.01	0.09 ± 0.04
82	EXMM J170759.6-410042	0406580101	257.00	-41.01	31 ± 8	0.02 ± 0.01	0.14 ± 0.05
83	EXMM J171042.4-280452	0206990401	257.68	-28.08	23 ± 6	0.05 ± 0.01	0.05 ± 0.04
84	EXMM J171420.6-381830	0670330101	258.59	-38.31	219 ± 19	0.30 ± 0.03	0.48 ± 0.11
85	EXMM J171924.9+264033	0500670201	259.85	26.68	52 ± 13	0.04 ± 0.01	0.08 ± 0.07
86	EXMM J172020.7-290720	0552002601	260.09	-29.12	319 ± 24	0.15 ± 0.01	0.20 ± 0.05
87	EXMM J173432.0-255552	0202680101	263.63	-25.93	163 ± 19	0.08 ± 0.01	0.19 ± 0.05
88	EXMM J173602.1-444555	0146420101	264.01	-44.77	70 ± 11	0.03 ± 0.00	0.04 ± 0.02
89	EXMM J173613.1-353035	0606200101	264.05	-35.51	39 ± 8	0.13 ± 0.03	0.72 ± 0.52
90	EXMM J174033.7-310504	0301730101	265.14	-31.08	21 ± 5	0.08 ± 0.02	0.15 ± 0.11
91	EXMM J174535.5-285929	0674601101	266.40	-28.99	77 ± 12	0.12 ± 0.02	0.60 ± 0.12
92	EXMM J174537.2-285500	0506291201	266.41	-28.92	55 ± 10	0.02 ± 0.00	0.07 ± 0.04
93	EXMM J174544.9-290504	0202670601	266.44	-29.08	86 ± 12	0.12 ± 0.02	0.22 ± 0.08
94	EXMM J174553.3-290445	0604300801	266.47	-29.08	244 ± 20	0.25 ± 0.02	0.37 ± 0.08
95	EXMM J174617.8-291150	0505670101	266.57	-29.20	62 ± 12	0.08 ± 0.02	0.44 ± 0.16

see next page

Table A.6.: continued

TID ¹	Name	ObsID	Ra ²	Dec ²	Counts	Rate [counts s ⁻¹]	Flux ³ [erg cm ⁻² s ⁻¹]
96	EXMM J174628.4-290617	0202670701	266.62	-29.10	42 ± 8	0.15 ± 0.03	0.35 ± 0.15
97	EXMM J175954.5-240928	0503850101	269.98	-24.16	49 ± 10	0.04 ± 0.01	0.06 ± 0.04
98	EXMM J180041.1-224343	0135742601	270.17	-22.73	63 ± 11	0.09 ± 0.02	0.50 ± 0.15
99	EXMM J180152.2-231706	0145970401	270.47	-23.28	41 ± 9	0.02 ± 0.00	0.05 ± 0.02
100	EXMM J180452.2-274315	0305970101	271.22	-27.72	186 ± 15	0.15 ± 0.01	0.34 ± 0.05
101	EXMM J180542.6-211847	0405750201	271.43	-21.31	70 ± 12	0.02 ± 0.00	0.05 ± 0.01
102	EXMM J180614.4-212650	0673690101	271.56	-21.45	34 ± 8	0.02 ± 0.00	0.20 ± 0.06
103	EXMM J181008.1-194543	0301270501	272.53	-19.76	24 ± 6	0.04 ± 0.01	0.30 ± 0.10
104	EXMM J181243.3-104054	0500030101	273.18	-10.68	82 ± 11	0.05 ± 0.01	0.13 ± 0.03
105	EXMM J181836.6-134818	0605130101	274.65	-13.80	69 ± 12	0.06 ± 0.01	0.22 ± 0.06
106	EXMM J182806.2+063510	0201730301	277.03	6.59	89 ± 11	0.18 ± 0.02	0.31 ± 0.09
107	EXMM J182903.1+003008	0402820101	277.26	0.50	60 ± 10	0.07 ± 0.01	0.34 ± 0.07
108	EXMM J183205.9-191433	0404720201	278.02	-19.24	23 ± 6	0.05 ± 0.01	0.10 ± 0.06
109	EXMM J183630.3-064816	0503320601	279.13	-6.80	41 ± 9	0.02 ± 0.00	0.11 ± 0.03
110	EXMM J184100.9-053819	0604820301	280.25	-5.64	51 ± 9	0.02 ± 0.00	0.08 ± 0.02
111	EXMM J190757.0-205142	0671850301	286.99	-20.86	263 ± 23	0.19 ± 0.02	0.25 ± 0.08
112	EXMM J191119.6+045739	0694870201	287.83	4.96	25 ± 6	0.02 ± 0.00	0.03 ± 0.05
113	EXMM J191400.9+045016	0075140401	288.50	4.84	55 ± 11	0.02 ± 0.00	0.03 ± 0.02
114	EXMM J201744.3+372759	0670480401	304.43	37.47	42 ± 8	0.03 ± 0.01	0.05 ± 0.03
115	EXMM J203138.2+413027	0305560201	307.91	41.51	60 ± 10	0.02 ± 0.00	0.05 ± 0.01
116	EXMM J203222.9+414045	0305560201	308.10	41.68	36 ± 9	0.09 ± 0.03	0.34 ± 0.12
117	EXMM J203254.4+410638	0505110401	308.23	41.11	513 ± 31	1.10 ± 0.07	7.67 ± 0.73
118	EXMM J203304.8+410048	0165360101	308.27	41.01	40 ± 9	0.03 ± 0.01	0.52 ± 0.18
119	EXMM J203317.5+411303	0200450201	308.32	41.22	53 ± 10	0.03 ± 0.01	0.09 ± 0.03

see next page

Table A.6.: continued

TID ¹	Name	ObsID	Ra ²	Dec ²	Counts	Rate [counts s ⁻¹]	Flux ³ [erg cm ⁻² s ⁻¹]
120	EXMM J203323.8+411847	0200450501	308.35	41.31	61 ± 12	0.01 ± 0.00	0.05 ± 0.01
121	EXMM J203347.9+601124	0401360101	308.45	60.19	70 ± 13	0.18 ± 0.04	0.22 ± 0.14
122	EXMM J203352.8+412516	0505110301	308.47	41.42	144 ± 18	0.08 ± 0.01	0.32 ± 0.09
123	EXMM J203400.9+412801	0505110401	308.50	41.47	45 ± 9	0.05 ± 0.01	0.20 ± 0.07
124	EXMM J203412.5+602046	0691570101	308.55	60.35	48 ± 9	0.02 ± 0.00	0.03 ± 0.02
125	EXMM J212805.1-651052	0670380101	322.02	-65.18	100 ± 13	0.33 ± 0.05	0.69 ± 0.47
126	EXMM J213452.0+473048	0650591701	323.72	47.51	42 ± 8	0.06 ± 0.01	0.10 ± 0.05
127	EXMM J214407.1+382511	0602310101	326.03	38.42	96 ± 14	0.04 ± 0.01	0.52 ± 0.17
128	EXMM J215645.3-074944	0404910701	329.19	-7.83	41 ± 8	0.04 ± 0.01	0.07 ± 0.04
129	EXMM J215653.6-114708	0103860501	329.22	-11.79	23 ± 6	0.08 ± 0.02	0.13 ± 0.10
130	EXMM J224259.1+530613	0654030101	340.75	53.10	238 ± 19	0.19 ± 0.01	0.46 ± 0.06
131	EXMM J224401.5+531513	0654030101	341.01	53.25	37 ± 8	0.06 ± 0.01	0.18 ± 0.09
132	EXMM J230201.7+584917	0057540301	345.51	58.82	60 ± 11	0.06 ± 0.01	0.10 ± 0.05
133	EXMM J230219.5+583338	0057540101	345.58	58.56	52 ± 9	0.05 ± 0.01	0.13 ± 0.05
134	EXMM J232545.2+613150	0404720301	351.44	61.53	29 ± 7	0.04 ± 0.01	0.12 ± 0.06
135	EXMM J235822.8+563209	0553510301	359.59	56.54	183 ± 19	0.18 ± 0.02	0.60 ± 0.17

Notes: ¹ Transient identifier, ² equatorial coordinates (J2000), ³ total flux in the (0.3–12) keV energy band.

A.6. Auxiliary class predictions of EXTraS Transient sources

Table A.7.: List of predicted class probabilities from the spectral model, for EXTraS transients with unreliable timing properties.

TID ¹	BL	CV	LMXRB	HMXRB	STAR	S1	S2	ULX	pred. class
0	0.00	0.14	0.01	0.04	0.03	0.17	0.60	0.00	S2
1	0.00	0.14	0.01	0.03	0.00	0.20	0.61	0.00	S2
2	0.00	0.02	0.00	0.01	0.02	0.43	0.49	0.02	S2
3	0.02	0.10	0.01	0.01	0.03	0.34	0.48	0.00	S2
9	0.00	0.05	0.01	0.02	0.04	0.44	0.43	0.01	S1
11	0.06	0.24	0.04	0.05	0.14	0.18	0.28	0.01	S2
12	0.01	0.16	0.01	0.06	0.09	0.14	0.50	0.01	S2
13	0.00	0.02	0.00	0.00	0.00	0.51	0.45	0.00	S1
15	0.01	0.09	0.00	0.08	0.04	0.20	0.56	0.02	S2
19	0.00	0.04	0.00	0.03	0.21	0.37	0.34	0.01	S1
24	0.00	0.11	0.06	0.00	0.21	0.25	0.33	0.05	S2
25	0.00	0.15	0.00	0.00	0.02	0.23	0.59	0.00	S2
27	0.00	0.04	0.00	0.02	0.01	0.60	0.32	0.00	S1
29	0.01	0.04	0.00	0.05	0.07	0.34	0.46	0.03	S2
31	0.00	0.19	0.00	0.00	0.01	0.35	0.41	0.04	S2
33	0.00	0.15	0.01	0.00	0.05	0.32	0.38	0.07	S2
36	0.00	0.22	0.00	0.03	0.06	0.20	0.49	0.00	S2
37	0.00	0.01	0.00	0.01	0.01	0.62	0.34	0.00	S1
39	0.02	0.31	0.10	0.04	0.07	0.21	0.24	0.00	CV
44	0.00	0.06	0.01	0.05	0.39	0.19	0.23	0.06	STAR
45	0.03	0.19	0.03	0.01	0.05	0.32	0.38	0.00	S2
46	0.00	0.05	0.00	0.04	0.12	0.22	0.57	0.00	S2
48	0.01	0.07	0.00	0.00	0.00	0.30	0.62	0.00	S2
52	0.00	0.03	0.00	0.00	0.00	0.61	0.36	0.00	S1
55	0.00	0.08	0.04	0.32	0.01	0.19	0.36	0.00	S2
56	0.00	0.22	0.02	0.01	0.15	0.31	0.28	0.02	S1
60	0.00	0.03	0.01	0.04	0.01	0.31	0.61	0.00	S2
61	0.00	0.15	0.01	0.15	0.00	0.22	0.47	0.00	S2
63	0.00	0.02	0.00	0.00	0.00	0.53	0.44	0.00	S1
66	0.00	0.00	0.00	0.00	0.00	0.00	0.00	0.00	NA
67	0.00	0.07	0.00	0.01	0.04	0.38	0.48	0.01	S2
71	0.00	0.22	0.02	0.02	0.23	0.23	0.25	0.02	S2
72	0.00	0.15	0.01	0.08	0.02	0.28	0.46	0.00	S2
73	0.01	0.10	0.10	0.10	0.05	0.20	0.43	0.00	S2

¹ unique transient identifier, see Table A.6. For continuation of the table see next page

Table A.7.: continued

TID ¹	BL	CV	LMXRB	HMXRB	STAR	S1	S2	ULX	pred. class
77	0.00	0.10	0.04	0.03	0.05	0.27	0.51	0.00	S2
80	0.00	0.10	0.05	0.04	0.24	0.27	0.27	0.04	S2
82	0.00	0.18	0.01	0.12	0.00	0.32	0.36	0.00	S2
84	0.00	0.06	0.01	0.11	0.39	0.16	0.24	0.04	STAR
85	0.00	0.12	0.00	0.02	0.07	0.38	0.40	0.00	S2
91	0.00	0.13	0.04	0.13	0.03	0.27	0.40	0.01	S2
95	0.00	0.30	0.03	0.17	0.02	0.17	0.31	0.00	S2
96	0.00	0.15	0.07	0.07	0.17	0.25	0.23	0.05	S1
97	0.00	0.10	0.03	0.04	0.01	0.25	0.57	0.00	S2
99	0.00	0.05	0.04	0.04	0.01	0.18	0.67	0.00	S2
102	0.01	0.26	0.01	0.11	0.01	0.22	0.38	0.01	S2
108	0.00	0.09	0.01	0.03	0.01	0.31	0.55	0.00	S2
109	0.01	0.10	0.00	0.04	0.02	0.44	0.35	0.03	S1
111	0.00	0.14	0.00	0.04	0.00	0.42	0.40	0.00	S1
112	0.01	0.23	0.01	0.04	0.01	0.35	0.35	0.01	S1
113	0.06	0.21	0.01	0.05	0.21	0.20	0.22	0.04	S2
114	0.10	0.18	0.01	0.05	0.23	0.21	0.13	0.08	STAR
115	0.00	0.19	0.00	0.02	0.01	0.51	0.25	0.00	S1
116	0.01	0.15	0.06	0.03	0.27	0.19	0.20	0.09	STAR
118	0.07	0.03	0.02	0.03	0.04	0.46	0.36	0.00	S1
119	0.00	0.19	0.01	0.13	0.03	0.27	0.37	0.00	S2
120	0.00	0.13	0.10	0.01	0.48	0.12	0.12	0.04	STAR
124	0.01	0.32	0.01	0.06	0.02	0.26	0.32	0.00	S2
131	0.01	0.38	0.01	0.10	0.05	0.19	0.25	0.01	CV

Notes: ¹ unique transient identifier, see Table A.6.

Table A.8.: Differences between classified EXTraS transients between the spectral and timing model prediction.

TID ¹	Spectral Model Class	Confidence	Timing Model Class	Confidence
5	S1	0.51	STAR	0.25
7	S2	0.43	CV	0.42
8	S2	0.41	CV	0.34
20	S2	0.37	CV	0.40
21	S2	0.33	STAR	0.31
22	S2	0.52	CV	0.37

¹ unique transient identifier, see Table A.6. For continuation of the table see next page

Table A.8.: continued

TID ¹	Spectral Model Class	Confidence	Timing Model Class	Confidence
23	S2	0.47	CV	0.42
26	S2	0.50	CV	0.36
34	S2	0.39	CV	0.47
35	S2	0.47	CV	0.33
40	S2	0.38	CV	0.31
41	S1	0.28	STAR	0.32
42	S2	0.42	STAR	0.23
47	S2	0.38	STAR	0.37
51	S2	0.33	STAR	0.32
53	S1	0.53	CV	0.32
54	HMXRB	0.38	CV	0.30
58	S2	0.44	CV	0.48
64	S1	0.32	CV	0.46
65	HMXRB	0.28	S2	0.32
68	S2	0.41	CV	0.31
69	S2	0.29	STAR	0.31
70	S2	0.36	CV	0.35
86	S2	0.43	CV	0.30
87	S1	0.41	CV	0.39
88	S2	0.32	CV	0.28
93	S2	0.32	CV	0.34
94	S2	0.33	CV	0.27
117	S2	0.49	S1	0.35
G				

Notes: ¹ unique transient identifier, see Table A.6.

B. Mrk 421

B.1. Spectral fit results of all Mrk 421 *Swift* observations.

Table B.1.: Best-fit results for a log parabolic model for *Swift*/XRT observations.

ObsDate	ObsID	α	β	$F_{(0.5-10)\text{ keV}}$	C_{red} (dof)
57858	00031630004	$1.86^{+0.03}_{-0.03}$	$0.31^{+0.06}_{-0.06}$	13.30 ± 0.20	1.01 (334)
57860	00031630005	$1.82^{+0.02}_{-0.02}$	$0.16^{+0.04}_{-0.04}$	17.45 ± 0.22	1.12 (422)
57862	00031630007	$2.13^{+0.03}_{-0.03}$	$0.15^{+0.07}_{-0.07}$	7.29 ± 0.13	1.18 (271)
57863	00031630008	$2.11^{+0.03}_{-0.03}$	$0.15^{+0.06}_{-0.06}$	7.94 ± 0.14	1.13 (282)
57865	00031630009	$2.13^{+0.03}_{-0.03}$	$0.12^{+0.06}_{-0.06}$	8.43 ± 0.15	0.85 (306)
57867	00031630010	$2.04^{+0.03}_{-0.03}$	$0.15^{+0.06}_{-0.06}$	8.41 ± 0.15	0.99 (292)
57872	00031630011	$2.16^{+0.03}_{-0.03}$	$0.16^{+0.07}_{-0.07}$	7.34 ± 0.13	1.12 (265)
57378	00034228001	$2.02^{+0.02}_{-0.02}$	$0.14^{+0.04}_{-0.04}$	8.72 ± 0.12	1.12 (385)
57378	00034228002	$2.30^{+0.02}_{-0.02}$	$0.19^{+0.05}_{-0.05}$	6.55 ± 0.08	1.15 (313)
57381	00034228003	$2.20^{+0.03}_{-0.03}$	$0.22^{+0.07}_{-0.07}$	7.83 ± 0.13	1.02 (270)
57382	00034228004	$2.31^{+0.03}_{-0.03}$	$0.25^{+0.07}_{-0.07}$	6.25 ± 0.10	1.23 (249)
57383	00034228005	$2.30^{+0.03}_{-0.03}$	$0.26^{+0.07}_{-0.07}$	7.70 ± 0.12	1.03 (263)
57387	00034228006	$1.99^{+0.02}_{-0.02}$	$0.24^{+0.04}_{-0.04}$	17.32 ± 0.21	1.12 (383)
57388	00034228007	$2.11^{+0.02}_{-0.02}$	$0.19^{+0.05}_{-0.05}$	16.02 ± 0.20	1.03 (357)
57390	00034228008	$2.28^{+0.03}_{-0.03}$	$0.27^{+0.06}_{-0.06}$	9.57 ± 0.13	1.15 (281)
57391	00034228009	$2.26^{+0.02}_{-0.02}$	$0.33^{+0.05}_{-0.05}$	11.47 ± 0.14	1.22 (300)
57392	00034228010	$2.27^{+0.03}_{-0.03}$	$0.35^{+0.06}_{-0.06}$	12.77 ± 0.16	0.98 (296)
57394	00034228011	$2.18^{+0.03}_{-0.03}$	$0.24^{+0.06}_{-0.06}$	11.48 ± 0.17	0.95 (294)
57394	00034228012	$2.29^{+0.03}_{-0.03}$	$0.31^{+0.06}_{-0.06}$	10.09 ± 0.14	1.17 (284)
57394	00034228013	$2.36^{+0.03}_{-0.03}$	$0.25^{+0.07}_{-0.07}$	9.83 ± 0.16	1.00 (255)
57395	00034228014	$2.33^{+0.03}_{-0.03}$	$0.26^{+0.07}_{-0.07}$	7.25 ± 0.11	1.00 (261)
57396	00034228015	$2.30^{+0.03}_{-0.03}$	$0.20^{+0.06}_{-0.06}$	9.30 ± 0.14	0.91 (276)
57397	00034228016	$2.36^{+0.03}_{-0.03}$	$0.20^{+0.07}_{-0.07}$	8.26 ± 0.13	1.13 (261)
57398	00034228017	$2.22^{+0.03}_{-0.03}$	$0.28^{+0.06}_{-0.06}$	9.55 ± 0.14	1.07 (285)
57400	00034228018	$2.23^{+0.03}_{-0.03}$	$0.19^{+0.06}_{-0.06}$	9.69 ± 0.14	1.10 (293)
57400	00034228019	$2.19^{+0.03}_{-0.03}$	$0.27^{+0.06}_{-0.06}$	9.39 ± 0.14	1.03 (289)
57402	00034228020	$2.37^{+0.03}_{-0.03}$	$0.16^{+0.07}_{-0.07}$	7.34 ± 0.12	0.96 (254)
57403	00034228021	$2.35^{+0.03}_{-0.03}$	$0.18^{+0.06}_{-0.06}$	8.16 ± 0.12	1.20 (268)
57404	00034228022	$2.35^{+0.03}_{-0.03}$	$0.14^{+0.08}_{-0.08}$	11.65 ± 0.23	1.15 (230)

^a Fluxes given in $10^{-10}\text{ erg cm}^{-2}\text{ s}^{-1}$. For continuation of the table see next page.

Table B.1.: continued

ObsMJD	ObsID	α	β	$F_{(0.5-10)\text{ keV}}^a$	C_{red} (dof)
57405	00034228023	$2.10^{+0.21}_{-0.18}$	$0.00^{+0.57}_{-0.00}$	6.39 ± 0.67	1.34 (13)
57408	00034228025	$2.19^{+0.03}_{-0.03}$	$0.23^{+0.07}_{-0.06}$	9.18 ± 0.16	1.21 (268)
57413	00034228026	$1.87^{+0.40}_{-0.65}$	$0.00^{+1.45}_{-0.00}$	4.46 ± 0.75	3.02 (2)
57414	00034228027	$2.44^{+0.03}_{-0.03}$	$0.24^{+0.08}_{-0.12}$	4.08 ± 0.09	0.90 (196)
57416	00034228028	$2.30^{+0.04}_{-0.04}$	$0.29^{+0.09}_{-0.09}$	10.98 ± 0.22	0.98 (214)
57418	00034228029	$2.31^{+0.04}_{-0.03}$	$0.17^{+0.06}_{-0.11}$	7.98 ± 0.15	1.05 (264)
57420	00034228030	$2.35^{+0.03}_{-0.03}$	$0.24^{+0.07}_{-0.07}$	9.08 ± 0.14	1.15 (262)
57422	00034228031	$2.60^{+0.12}_{-0.13}$	$0.16^{+0.48}_{-0.16}$	1.53 ± 0.13	1.65 (35)
57424	00034228032	$2.34^{+0.06}_{-0.05}$	$0.08^{+0.16}_{-0.08}$	3.16 ± 0.10	1.13 (179)
57425	00034228033	$2.37^{+0.05}_{-0.05}$	$0.12^{+0.13}_{-0.12}$	2.56 ± 0.08	1.02 (154)
57426	00034228034	$2.43^{+0.04}_{-0.04}$	$0.15^{+0.09}_{-0.09}$	4.68 ± 0.09	1.25 (230)
57426	00034228035	$2.42^{+0.04}_{-0.04}$	$0.23^{+0.08}_{-0.10}$	4.26 ± 0.08	0.96 (212)
57428	00034228036	$2.69^{+0.04}_{-0.03}$	$0.35^{+0.08}_{-0.12}$	4.37 ± 0.07	1.11 (194)
57430	00034228037	$2.83^{+0.05}_{-0.05}$	$0.00^{+0.07}_{-0.00}$	1.93 ± 0.05	1.00 (121)
57430	00034228038	$2.90^{+0.05}_{-0.05}$	$0.00^{+0.23}_{-0.00}$	1.63 ± 0.04	0.84 (119)
57432	00034228039	$2.65^{+0.04}_{-0.03}$	$0.00^{+0.10}_{-0.00}$	2.68 ± 0.05	1.10 (167)
57434	00034228040	$2.82^{+0.05}_{-0.05}$	$0.28^{+0.15}_{-0.27}$	6.66 ± 0.23	1.02 (112)
57436	00034228041	$2.91^{+0.04}_{-0.04}$	$0.18^{+0.14}_{-0.14}$	2.66 ± 0.06	1.33 (150)
57438	00034228042	$2.78^{+0.05}_{-0.05}$	$0.03^{+0.15}_{-0.03}$	2.71 ± 0.07	0.94 (141)
57451	00034228043	$2.64^{+0.05}_{-0.06}$	$0.34^{+0.17}_{-0.14}$	2.45 ± 0.07	1.06 (139)
57453	00034228044	$2.62^{+0.05}_{-0.05}$	$0.21^{+0.14}_{-0.14}$	2.26 ± 0.06	0.98 (149)
57453	00034228045	$2.60^{+0.06}_{-0.06}$	$0.30^{+0.14}_{-0.18}$	2.18 ± 0.07	1.01 (133)
57455	00034228046	$2.65^{+0.03}_{-0.09}$	$0.00^{+0.20}_{-0.00}$	2.27 ± 0.08	1.06 (121)
57457	00034228047	$2.89^{+0.06}_{-0.07}$	$0.13^{+0.23}_{-0.13}$	1.55 ± 0.05	0.94 (113)
57460	00034228048	$2.85^{+0.05}_{-0.05}$	$0.00^{+0.23}_{-0.00}$	1.48 ± 0.05	1.15 (117)
57461	00034228049	$2.58^{+0.06}_{-0.06}$	$0.31^{+0.15}_{-0.16}$	2.58 ± 0.08	0.83 (138)
57463	00034228050	$2.71^{+0.05}_{-0.05}$	$0.23^{+0.15}_{-0.15}$	2.18 ± 0.06	1.21 (139)
57474	00034228051	$2.70^{+0.05}_{-0.05}$	$0.24^{+0.14}_{-0.13}$	2.39 ± 0.06	1.09 (150)
57476	00034228052	$2.32^{+0.04}_{-0.04}$	$0.20^{+0.07}_{-0.11}$	6.91 ± 0.14	1.02 (221)
57478	00034228053	$2.29^{+0.03}_{-0.03}$	$0.30^{+0.07}_{-0.07}$	6.76 ± 0.11	1.11 (245)
57478	00034228054	$2.25^{+0.03}_{-0.03}$	$0.24^{+0.06}_{-0.06}$	7.65 ± 0.12	1.17 (274)
57480	00034228055	$2.25^{+0.03}_{-0.03}$	$0.20^{+0.07}_{-0.07}$	7.58 ± 0.13	1.10 (259)
57482	00034228056	$2.39^{+0.04}_{-0.04}$	$0.22^{+0.09}_{-0.09}$	5.45 ± 0.11	0.99 (205)
57482	00034228057	$2.45^{+0.03}_{-0.03}$	$0.25^{+0.09}_{-0.08}$	4.79 ± 0.09	1.05 (218)
57484	00034228058	$2.38^{+0.04}_{-0.04}$	$0.23^{+0.09}_{-0.09}$	4.81 ± 0.10	0.95 (209)
57486	00034228059	$2.43^{+0.03}_{-0.04}$	$0.18^{+0.21}_{-0.07}$	5.28 ± 0.15	1.02 (167)
57488	00034228060	$2.29^{+0.03}_{-0.03}$	$0.15^{+0.08}_{-0.08}$	6.78 ± 0.13	1.03 (235)

^a Fluxes given in $10^{-10}\text{ erg cm}^{-2}\text{ s}^{-1}$. For continuation of the table see next page.

Table B.1.: continued

ObsMJD	ObsID	α	β	$F_{(0.5-10)\text{ keV}}^a$	C_{red} (dof)
57490	00034228061	$2.34^{+0.04}_{-0.04}$	$0.23^{+0.10}_{-0.09}$	4.63 ± 0.09	1.17 (207)
57492	00034228062	$2.36^{+0.04}_{-0.04}$	$0.28^{+0.09}_{-0.09}$	4.20 ± 0.08	1.09 (211)
57505	00034228064	$2.20^{+0.03}_{-0.03}$	$0.20^{+0.07}_{-0.07}$	7.23 ± 0.13	0.92 (254)
57506	00034228065	$2.20^{+0.03}_{-0.03}$	$0.06^{+0.07}_{-0.06}$	6.54 ± 0.14	1.14 (262)
57507	00034228066	$2.18^{+0.03}_{-0.03}$	$0.08^{+0.07}_{-0.07}$	6.89 ± 0.13	0.88 (262)
57510	00034228067	$2.17^{+0.03}_{-0.03}$	$0.09^{+0.07}_{-0.06}$	8.59 ± 0.16	1.15 (273)
57512	00034228068	$2.38^{+0.04}_{-0.04}$	$0.27^{+0.09}_{-0.09}$	4.59 ± 0.09	1.01 (203)
57514	00034228069	$2.40^{+0.04}_{-0.04}$	$0.42^{+0.12}_{-0.11}$	3.45 ± 0.09	1.27 (178)
57516	00034228070	$2.31^{+0.04}_{-0.04}$	$0.18^{+0.13}_{-0.06}$	4.93 ± 0.08	1.17 (223)
57518	00034228071	$2.17^{+0.04}_{-0.04}$	$0.07^{+0.13}_{-0.05}$	5.30 ± 0.11	1.03 (240)
57520	00034228072	$2.44^{+0.04}_{-0.04}$	$0.31^{+0.10}_{-0.10}$	4.68 ± 0.10	0.91 (193)
57538	00034228073	$1.93^{+0.04}_{-0.04}$	$0.09^{+0.09}_{-0.08}$	9.60 ± 0.25	1.07 (239)
57543	00034228075	$2.10^{+0.08}_{-0.09}$	$0.31^{+0.21}_{-0.18}$	7.11 ± 0.34	1.16 (102)
57545	00034228076	$2.41^{+0.04}_{-0.04}$	$0.16^{+0.10}_{-0.09}$	4.57 ± 0.10	1.05 (195)
57546	00034228077	$2.12^{+0.02}_{-0.02}$	$0.17^{+0.09}_{-0.03}$	10.66 ± 0.13	1.16 (309)
57550	00034228078	$1.87^{+0.02}_{-0.02}$	$0.23^{+0.04}_{-0.04}$	22.95 ± 0.31	1.27 (420)
57551	00034228079	$2.23^{+0.03}_{-0.03}$	$0.20^{+0.08}_{-0.07}$	7.88 ± 0.14	1.12 (246)
57552	00034228080	$2.01^{+0.02}_{-0.04}$	$0.17^{+0.06}_{-0.05}$	11.80 ± 0.14	1.09 (332)
57550	00034228082	$2.15^{+0.03}_{-0.03}$	$0.18^{+0.07}_{-0.07}$	7.88 ± 0.14	1.19 (277)
57551	00034228083	$2.19^{+0.03}_{-0.03}$	$0.25^{+0.07}_{-0.07}$	7.62 ± 0.13	0.95 (268)
57717	00034228084	$2.54^{+0.06}_{-0.06}$	$0.08^{+0.16}_{-0.08}$	1.87 ± 0.07	1.17 (135)
57719	00034228085	$2.82^{+0.06}_{-0.06}$	$0.05^{+0.16}_{-0.05}$	1.48 ± 0.04	1.01 (128)
57721	00034228086	$2.55^{+0.06}_{-0.04}$	$0.00^{+0.08}_{-0.00}$	1.58 ± 0.04	1.36 (124)
57723	00034228087	$2.79^{+0.05}_{-0.06}$	$0.00^{+0.16}_{-0.00}$	1.33 ± 0.04	1.04 (117)
57724	00034228088	$2.70^{+0.06}_{-0.06}$	$0.13^{+0.16}_{-0.13}$	1.62 ± 0.05	0.91 (132)
57725	00034228089	$2.62^{+0.05}_{-0.05}$	$0.10^{+0.12}_{-0.10}$	2.17 ± 0.05	1.06 (161)
57726	00034228090	$2.58^{+0.05}_{-0.05}$	$0.14^{+0.13}_{-0.13}$	2.60 ± 0.07	1.10 (161)
57727	00034228091	$2.58^{+0.04}_{-0.04}$	$0.18^{+0.12}_{-0.12}$	2.56 ± 0.06	0.94 (168)
57728	00034228092	$2.58^{+0.05}_{-0.05}$	$0.14^{+0.12}_{-0.14}$	2.26 ± 0.06	0.98 (150)
57729	00034228093	$2.63^{+0.05}_{-0.05}$	$0.13^{+0.13}_{-0.13}$	1.84 ± 0.05	0.87 (155)
57730	00034228094	$2.68^{+0.06}_{-0.06}$	$0.25^{+0.17}_{-0.16}$	1.41 ± 0.04	1.05 (132)
57731	00034228095	$2.62^{+0.05}_{-0.06}$	$0.02^{+0.15}_{-0.02}$	1.98 ± 0.06	0.88 (138)
57732	00034228096	$2.88^{+0.06}_{-0.07}$	$0.03^{+0.23}_{-0.03}$	1.21 ± 0.04	1.10 (106)
57733	00034228097	$2.64^{+0.05}_{-0.05}$	$0.03^{+0.14}_{-0.03}$	1.88 ± 0.05	0.96 (147)
57735	00034228098	$2.73^{+0.06}_{-0.06}$	$0.28^{+0.17}_{-0.16}$	1.52 ± 0.04	1.20 (129)
57737	00034228099	$2.62^{+0.06}_{-0.06}$	$0.31^{+0.17}_{-0.17}$	1.67 ± 0.05	0.89 (123)
57740	00034228100	$2.39^{+0.05}_{-0.05}$	$0.00^{+0.09}_{-0.00}$	3.30 ± 0.15	1.36 (102)

^a Fluxes given in $10^{-10}\text{ erg cm}^{-2}\text{ s}^{-1}$. For continuation of the table see next page.

Table B.1.: continued

ObsMJD	ObsID	α	β	$F_{(0.5-10)\text{ keV}}^a$	C_{red} (dof)
57744	00034228101	$2.48^{+0.04}_{-0.04}$	$0.16^{+0.10}_{-0.10}$	3.42 ± 0.07	0.90 (187)
57747	00034228102	$2.30^{+0.04}_{-0.04}$	$0.14^{+0.08}_{-0.08}$	4.66 ± 0.10	0.99 (223)
57749	00034228103	$2.32^{+0.04}_{-0.04}$	$0.12^{+0.09}_{-0.09}$	5.78 ± 0.13	1.09 (205)
57749	00034228104	$2.37^{+0.02}_{-0.06}$	$0.08^{+0.12}_{-0.06}$	5.02 ± 0.08	0.87 (216)
57751	00034228105	$2.26^{+0.04}_{-0.04}$	$0.23^{+0.09}_{-0.09}$	5.05 ± 0.11	1.14 (212)
57753	00034228106	$2.08^{+0.03}_{-0.03}$	$0.15^{+0.06}_{-0.06}$	7.52 ± 0.12	1.15 (309)
57754	00034228107	$1.98^{+0.03}_{-0.03}$	$0.13^{+0.06}_{-0.05}$	9.77 ± 0.15	1.17 (329)
57755	00034228108	$2.04^{+0.03}_{-0.03}$	$0.19^{+0.06}_{-0.06}$	9.30 ± 0.15	0.85 (305)
57756	00034228109	$2.20^{+0.03}_{-0.03}$	$0.10^{+0.07}_{-0.07}$	6.23 ± 0.11	1.04 (259)
57757	00034228110	$1.98^{+0.01}_{-0.01}$	$0.20^{+0.02}_{-0.02}$	8.45 ± 0.05	1.25 (555)
57758	00034228111	$2.14^{+0.10}_{-0.10}$	$-0.06^{+0.22}_{-0.21}$	9.04 ± 0.59	0.91 (70)
57759	00034228112	$1.90^{+0.03}_{-0.03}$	$0.24^{+0.05}_{-0.05}$	12.13 ± 0.17	1.03 (351)
57761	00034228114	$1.83^{+0.03}_{-0.02}$	$0.25^{+0.05}_{-0.06}$	15.22 ± 0.23	1.04 (357)
57760	00034228115	$1.74^{+0.02}_{-0.01}$	$0.26^{+0.03}_{-0.04}$	15.56 ± 0.14	1.32 (515)
57763	00034228116	$2.02^{+0.03}_{-0.03}$	$0.22^{+0.05}_{-0.05}$	10.56 ± 0.15	1.10 (335)
57765	00034228117	$2.08^{+0.03}_{-0.03}$	$0.09^{+0.05}_{-0.05}$	7.12 ± 0.11	0.90 (343)
57772	00034228118	$2.03^{+0.03}_{-0.03}$	$0.18^{+0.06}_{-0.06}$	7.98 ± 0.12	1.05 (315)
57774	00034228119	$2.06^{+0.02}_{-0.02}$	$0.00^{+0.03}_{-0.00}$	7.51 ± 0.10	1.04 (308)
57776	00034228120	$2.09^{+0.04}_{-0.04}$	$0.21^{+0.09}_{-0.09}$	10.67 ± 0.24	1.05 (219)
57778	00034228121	$2.23^{+0.04}_{-0.04}$	$0.19^{+0.08}_{-0.08}$	5.88 ± 0.12	0.97 (223)
57780	00034228122	$2.23^{+0.04}_{-0.04}$	$0.11^{+0.09}_{-0.09}$	8.67 ± 0.21	1.00 (212)
57782	00034228123	$2.30^{+0.06}_{-0.06}$	$0.15^{+0.14}_{-0.11}$	2.31 ± 0.07	0.96 (163)
57784	00034228124	$1.98^{+0.04}_{-0.03}$	$0.00^{+0.03}_{-0.00}$	5.24 ± 0.15	1.11 (180)
57785	00034228125	$2.03^{+0.02}_{-0.02}$	$0.00^{+0.06}_{-0.00}$	8.01 ± 0.14	1.07 (286)
57785	00034228126	$2.01^{+0.03}_{-0.03}$	$0.09^{+0.06}_{-0.06}$	9.07 ± 0.19	1.14 (291)
57785	00034228127	$1.99^{+0.03}_{-0.03}$	$0.07^{+0.06}_{-0.07}$	9.36 ± 0.17	1.13 (298)
57785	00034228128	$2.03^{+0.02}_{-0.02}$	$0.05^{+0.08}_{-0.05}$	9.17 ± 0.18	0.89 (247)
57785	00034228129	$2.02^{+0.02}_{-0.04}$	$0.09^{+0.07}_{-0.05}$	9.23 ± 0.15	0.97 (313)
57785	00034228130	$2.09^{+0.02}_{-0.03}$	$0.01^{+0.06}_{-0.01}$	8.00 ± 0.13	1.08 (288)
57785	00034228131	$2.08^{+0.03}_{-0.03}$	$0.18^{+0.06}_{-0.06}$	7.34 ± 0.12	1.09 (287)
57786	00034228132	$2.11^{+0.03}_{-0.03}$	$0.10^{+0.07}_{-0.07}$	9.05 ± 0.19	1.02 (270)
57786	00034228133	$2.36^{+0.05}_{-0.05}$	$0.06^{+0.11}_{-0.06}$	3.31 ± 0.09	1.08 (184)
57788	00034228134	$1.91^{+0.02}_{-0.03}$	$0.00^{+0.04}_{-0.00}$	9.83 ± 0.19	1.07 (290)
57790	00034228135	$2.21^{+0.03}_{-0.03}$	$0.04^{+0.07}_{-0.04}$	6.06 ± 0.11	1.00 (260)
57792	00034228136	$2.46^{+0.03}_{-0.05}$	$0.00^{+0.09}_{-0.00}$	3.61 ± 0.07	1.21 (196)
57801	00034228137	$2.29^{+0.04}_{-0.04}$	$0.13^{+0.09}_{-0.09}$	4.16 ± 0.09	1.12 (204)
57803	00034228138	$2.22^{+0.02}_{-0.04}$	$0.00^{+0.07}_{-0.00}$	6.06 ± 0.12	0.93 (252)

^a Fluxes given in $10^{-10}\text{ erg cm}^{-2}\text{ s}^{-1}$. For continuation of the table see next page.

Table B.1.: continued

ObsMJD	ObsID	α	β	$F_{(0.5-10)\text{ keV}}^a$	C_{red} (dof)
57805	00034228139	$2.19^{+0.03}_{-0.03}$	$0.08^{+0.06}_{-0.07}$	7.99 ± 0.14	1.07 (274)
57807	00034228141	$2.23^{+0.03}_{-0.03}$	$0.19^{+0.06}_{-0.06}$	6.88 ± 0.11	1.01 (272)
57810	00034228143	$2.16^{+0.03}_{-0.03}$	$0.13^{+0.07}_{-0.07}$	6.81 ± 0.12	1.07 (266)
57813	00034228147	$2.05^{+0.43}_{-0.51}$	$0.27^{+1.64}_{-1.11}$	8.21 ± 4.32	0.42 (5)
57819	00034228156	$2.18^{+0.02}_{-0.03}$	$0.00^{+0.05}_{-0.00}$	6.50 ± 0.10	1.09 (263)
57827	00034228159	$2.15^{+0.03}_{-0.03}$	$0.14^{+0.06}_{-0.06}$	7.45 ± 0.13	1.05 (281)
57829	00034228160	$2.13^{+0.03}_{-0.03}$	$0.04^{+0.06}_{-0.04}$	8.32 ± 0.14	0.99 (298)
57831	00034228161	$2.08^{+0.03}_{-0.03}$	$0.11^{+0.06}_{-0.06}$	9.69 ± 0.15	0.98 (308)
57833	00034228163	$2.15^{+0.04}_{-0.04}$	$0.23^{+0.09}_{-0.09}$	7.84 ± 0.19	1.08 (205)
57835	00034228164	$2.41^{+0.04}_{-0.04}$	$0.12^{+0.08}_{-0.09}$	4.75 ± 0.09	1.02 (222)
57838	00034228165	$2.56^{+0.04}_{-0.04}$	$0.13^{+0.11}_{-0.11}$	3.29 ± 0.08	1.05 (180)
57840	00034228166	$2.49^{+0.04}_{-0.04}$	$0.15^{+0.10}_{-0.10}$	2.94 ± 0.06	1.19 (193)
57840	00034228167	$2.43^{+0.04}_{-0.04}$	$0.08^{+0.09}_{-0.08}$	3.16 ± 0.07	0.93 (209)
57840	00034228168	$2.60^{+0.03}_{-0.04}$	$0.00^{+0.12}_{-0.00}$	3.08 ± 0.08	0.94 (170)
57840	00034228169	$2.53^{+0.05}_{-0.05}$	$0.05^{+0.12}_{-0.05}$	3.13 ± 0.08	0.94 (167)
57840	00034228170	$2.49^{+0.04}_{-0.02}$	$0.00^{+0.08}_{-0.00}$	3.30 ± 0.06	1.01 (197)
57840	00034228172	$2.38^{+0.04}_{-0.04}$	$0.07^{+0.09}_{-0.07}$	3.72 ± 0.08	1.04 (211)
57841	00034228173	$2.25^{+0.04}_{-0.04}$	$0.06^{+0.07}_{-0.06}$	5.81 ± 0.11	1.04 (242)
57842	00034228174	$2.30^{+0.03}_{-0.05}$	$0.00^{+0.13}_{-0.00}$	4.28 ± 0.13	0.80 (156)
57844	00034228175	$2.30^{+0.04}_{-0.04}$	$0.04^{+0.09}_{-0.04}$	3.99 ± 0.10	1.02 (201)
57844	00034228176	$2.27^{+0.04}_{-0.04}$	$0.17^{+0.09}_{-0.09}$	3.67 ± 0.08	0.86 (213)
57846	00034228177	$2.38^{+0.04}_{-0.04}$	$0.11^{+0.09}_{-0.09}$	3.21 ± 0.07	1.06 (201)
57848	00034228178	$2.21^{+0.06}_{-0.06}$	$0.28^{+0.13}_{-0.13}$	3.77 ± 0.12	1.10 (158)
57364	00035014240	$2.92^{+0.06}_{-0.07}$	$0.00^{+0.16}_{-0.00}$	1.26 ± 0.03	0.94 (109)
57367	00035014241	$2.41^{+0.04}_{-0.04}$	$0.37^{+0.10}_{-0.10}$	4.19 ± 0.08	1.02 (200)
57370	00035014242	$2.14^{+0.02}_{-0.02}$	$0.41^{+0.05}_{-0.05}$	11.11 ± 0.14	0.99 (316)
57373	00035014243	$2.16^{+0.03}_{-0.03}$	$0.21^{+0.05}_{-0.06}$	10.05 ± 0.15	0.99 (309)
57374	00035014245	$2.27^{+0.01}_{-0.01}$	$0.17^{+0.03}_{-0.03}$	6.46 ± 0.05	1.08 (461)
57375	00035014246	$2.29^{+0.01}_{-0.01}$	$0.20^{+0.03}_{-0.03}$	6.15 ± 0.05	1.17 (433)
57376	00035014247	$2.35^{+0.02}_{-0.02}$	$0.16^{+0.03}_{-0.04}$	5.52 ± 0.05	1.15 (403)
57376	00035014249	$2.34^{+0.03}_{-0.03}$	$0.22^{+0.06}_{-0.06}$	5.44 ± 0.07	1.31 (287)
57379	00035014250	$2.36^{+0.03}_{-0.03}$	$0.23^{+0.07}_{-0.07}$	6.50 ± 0.11	0.93 (250)
57383	00035014251	$2.11^{+0.03}_{-0.03}$	$0.23^{+0.06}_{-0.06}$	9.80 ± 0.15	1.13 (301)
57385	00035014252	$2.29^{+0.03}_{-0.03}$	$0.19^{+0.07}_{-0.07}$	6.94 ± 0.12	1.03 (251)
57389	00035014253	$2.28^{+0.03}_{-0.03}$	$0.33^{+0.06}_{-0.06}$	9.04 ± 0.13	1.17 (266)
57392	00035014254	$2.21^{+0.02}_{-0.02}$	$0.33^{+0.05}_{-0.05}$	13.66 ± 0.16	1.19 (321)
57392	00035014255	$2.13^{+0.20}_{-0.22}$	$0.52^{+0.65}_{-0.46}$	11.95 ± 1.36	1.18 (17)

^a Fluxes given in $10^{-10}\text{ erg cm}^{-2}\text{ s}^{-1}$. For continuation of the table see next page.

Table B.1.: continued

ObsMJD	ObsID	α	β	$F_{(0.5-10)\text{ keV}}^a$	C_{red} (dof)
57785	00081926001	$2.01^{+0.03}_{-0.03}$	$0.08^{+0.06}_{-0.06}$	8.64 ± 0.14	1.18 (314)
57133	00092204001	$2.14^{+0.02}_{-0.03}$	$0.17^{+0.05}_{-0.05}$	11.50 ± 0.16	1.21 (324)
57140	00092204002	$2.30^{+0.03}_{-0.03}$	$0.24^{+0.07}_{-0.07}$	8.63 ± 0.14	1.00 (252)
57147	00092204003	$2.01^{+0.03}_{-0.03}$	$0.20^{+0.06}_{-0.06}$	9.17 ± 0.15	0.98 (306)
57162	00092204004	$2.13^{+0.03}_{-0.03}$	$0.21^{+0.07}_{-0.07}$	7.15 ± 0.13	1.08 (270)
57175	00092204006	$2.14^{+0.03}_{-0.03}$	$0.21^{+0.06}_{-0.06}$	9.70 ± 0.16	1.03 (283)
57182	00092204007	$2.32^{+0.05}_{-0.05}$	$0.07^{+0.11}_{-0.07}$	6.26 ± 0.18	1.07 (178)
57189	00092204008	$2.24^{+0.03}_{-0.03}$	$0.29^{+0.06}_{-0.06}$	12.30 ± 0.17	1.01 (293)
57500	00092399001	$2.44^{+0.12}_{-0.12}$	$0.10^{+0.39}_{-0.36}$	3.38 ± 0.31	1.11 (46)
57521	00092399002	$2.70^{+0.04}_{-0.04}$	$0.25^{+0.13}_{-0.12}$	2.98 ± 0.07	0.84 (163)
57528	00092399003	$2.14^{+0.04}_{-0.04}$	$0.23^{+0.09}_{-0.09}$	4.97 ± 0.11	1.16 (218)
57535	00092399004	$1.90^{+0.02}_{-0.02}$	$0.22^{+0.05}_{-0.05}$	13.69 ± 0.18	1.21 (390)
57541	00092399005	$2.10^{+0.03}_{-0.03}$	$0.16^{+0.06}_{-0.06}$	8.17 ± 0.14	1.06 (285)
57548	00092399006	$1.79^{+0.02}_{-0.02}$	$0.34^{+0.04}_{-0.04}$	25.35 ± 0.26	1.39 (453)
57555	00092399007	$2.15^{+0.03}_{-0.03}$	$0.13^{+0.07}_{-0.07}$	7.91 ± 0.14	0.89 (274)
57745	00092399008	$2.40^{+0.04}_{-0.04}$	$0.19^{+0.08}_{-0.11}$	3.63 ± 0.07	1.14 (204)
57867	00092412001	$1.99^{+0.03}_{-0.03}$	$0.21^{+0.06}_{-0.06}$	10.46 ± 0.17	0.94 (300)
57874	00092412002	$2.03^{+0.03}_{-0.03}$	$0.15^{+0.06}_{-0.06}$	9.24 ± 0.15	0.87 (309)
57880	00092412003	$2.23^{+0.03}_{-0.03}$	$0.16^{+0.06}_{-0.06}$	6.87 ± 0.10	1.22 (286)
57868	00093249001	$2.06^{+0.03}_{-0.03}$	$0.20^{+0.05}_{-0.06}$	8.55 ± 0.15	1.14 (323)
57869	00093249002	$2.08^{+0.04}_{-0.04}$	$0.11^{+0.07}_{-0.07}$	9.49 ± 0.19	0.99 (266)
57870	00093249003	$2.19^{+0.05}_{-0.05}$	$0.21^{+0.11}_{-0.11}$	8.30 ± 0.23	0.99 (182)
57871	00093249004	$2.09^{+0.03}_{-0.03}$	$0.24^{+0.06}_{-0.06}$	7.06 ± 0.12	0.93 (283)
57874	00093249005	$2.04^{+0.03}_{-0.03}$	$0.17^{+0.06}_{-0.06}$	10.37 ± 0.16	1.12 (316)

^a Fluxes given in $10^{-10}\text{erg cm}^{-2}\text{s}^{-1}$.

B.2. Complementary multiwavelength light curves

A comparison of the DCF for T1 and T2 of the first visibility window shows that the UV emission is not or only tentatively correlated with the *Fermi*-LAT light curve in the outburst in January 2016. In this case the UV data lags the γ -ray emission by ~ 13 days. Furthermore, for the same time range (T1), The *Fermi*-LAT light curve is not correlated with the TeV emission. This supports the observations, that the first TeV outburst seen by FACT is not detected in γ -rays by *Fermi*-LAT. Both light curves are correlated during the second half of the visibility window (T2) which implies that the outbursts in these two time ranges have different physical origin. However, the first TeV flare in December 2015 is not an orphan flare, as it is also detected in X-rays and the later is strongly correlated with both the *Fermi*-LAT and FACT light curve. The fact that it correlates

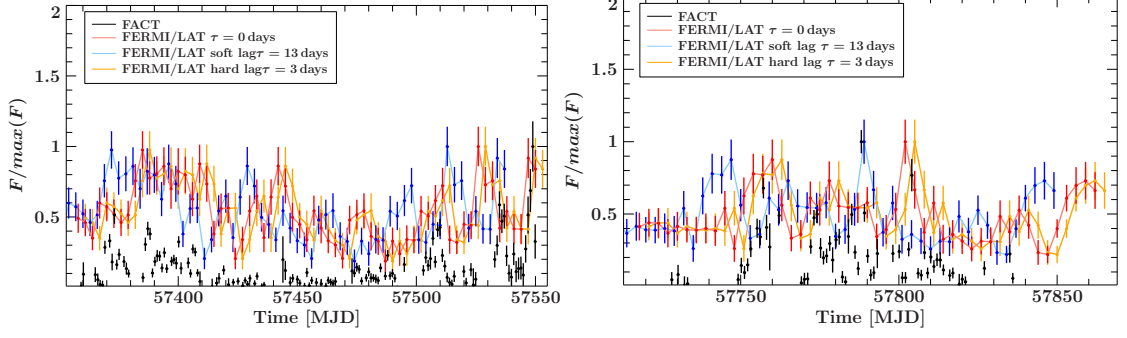


Figure B.1.: Comparison of FACT and *Fermi*-LAT light curves normalized to the maximum flux observed in the shown time range for visibility window 1 (*left*) and 2 (*right*).

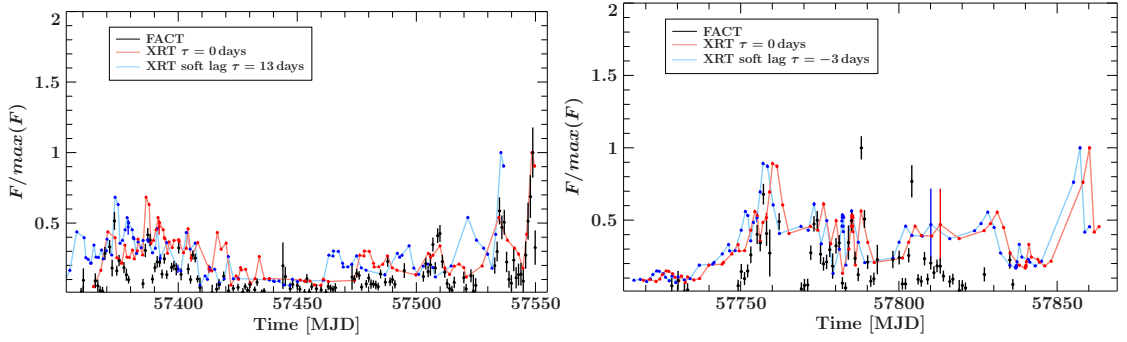


Figure B.2.: Comparison of FACT and *Swift*/XRT light curves normalized to the maximum flux observed in the shown time range for visibility window 1 (*left*) and 2 (*right*).

with both energy bands while there is no connection between those two may indicate, that the X-ray emission varies on different timescales at once, i.e. following the longterm variation observed in *Fermi*-LAT and UVOT, but also exhibiting strong variations on short time scales, correlated with TeV emission. T1 and T2 further also imply that the

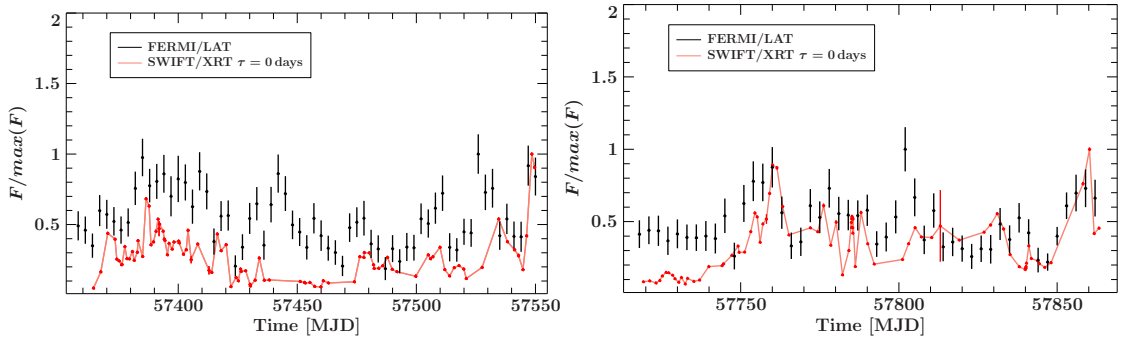


Figure B.3.: Comparison of *Fermi*-LAT and *Swift*/XRT light curves normalized to the maximum flux observed in the shown time range for visibility window 1 (*left*) and 2 (*right*).

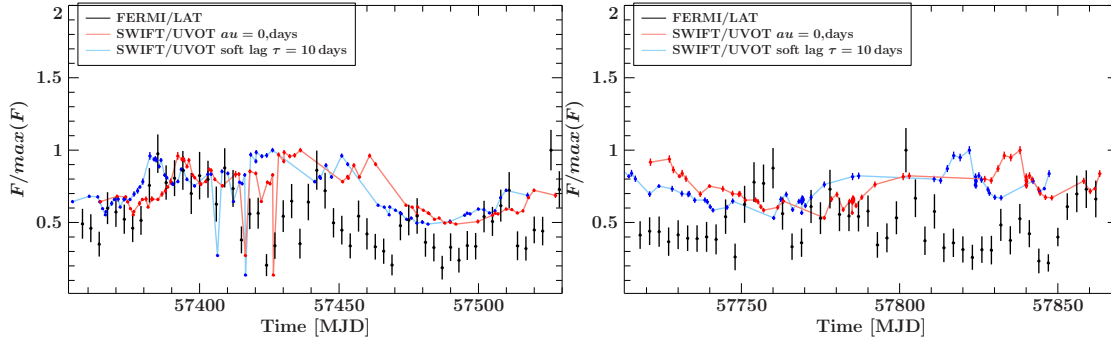


Figure B.4.: Comparison of *Fermi*-LAT and *Swift*/UVOT light curves normalized to the maximum flux observed in the shown time range for visibility window 1 (*left*) and 2 (*right*).

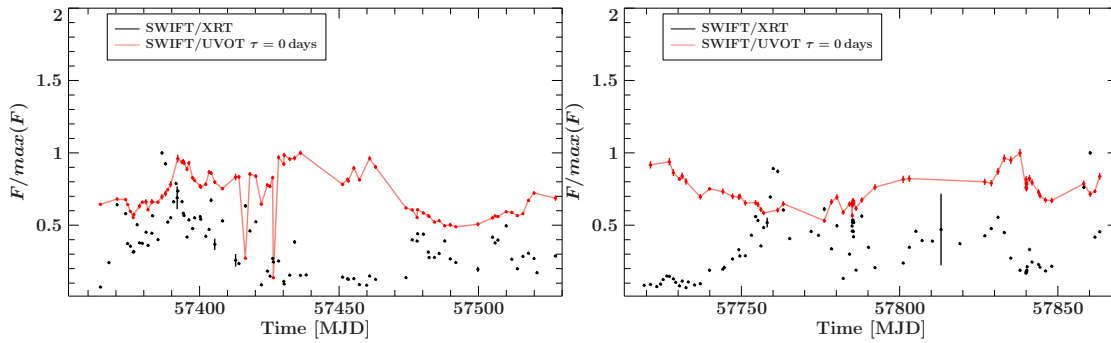


Figure B.5.: Comparison of *Swift*/XRT and *Swift*/UVOT light curves normalized to the maximum flux observed in the shown time range for visibility window 1 (*left*) and 2 (*right*).

second peak in the DCF between XRT and FACT is caused by the high sampling of both light curves and the two subsequent outbursts in Dec 2015 and Jan 2016 within only two weeks.

The DCF on shorter time scales shows:

- (T1) The UV emission seems marginally correlated with the γ -ray emission with the UV lagging the γ -rays by $dt = 13 \pm 3$ days. No further correlation is found for the UV emission and other emission bands or time periods.
- (T1) X-ray emission is both correlated with γ -rays and TeV emission, with $dt = 0 \pm 1.5$ days in both cases. The second peak in the DCF between X-rays and TeV is much stronger on this short timescale.
- (T1) The DCF between Fermi and FACT shows a broad peak from -10 to 25 days. However, the correlation is only significant for $dt = 13 \pm 1.5$ days, with the γ -ray emission lagging the TeV emission. Judging from the light curve, this lag corresponds to the time separation between the first TeV outburst and the γ -ray flux increase.

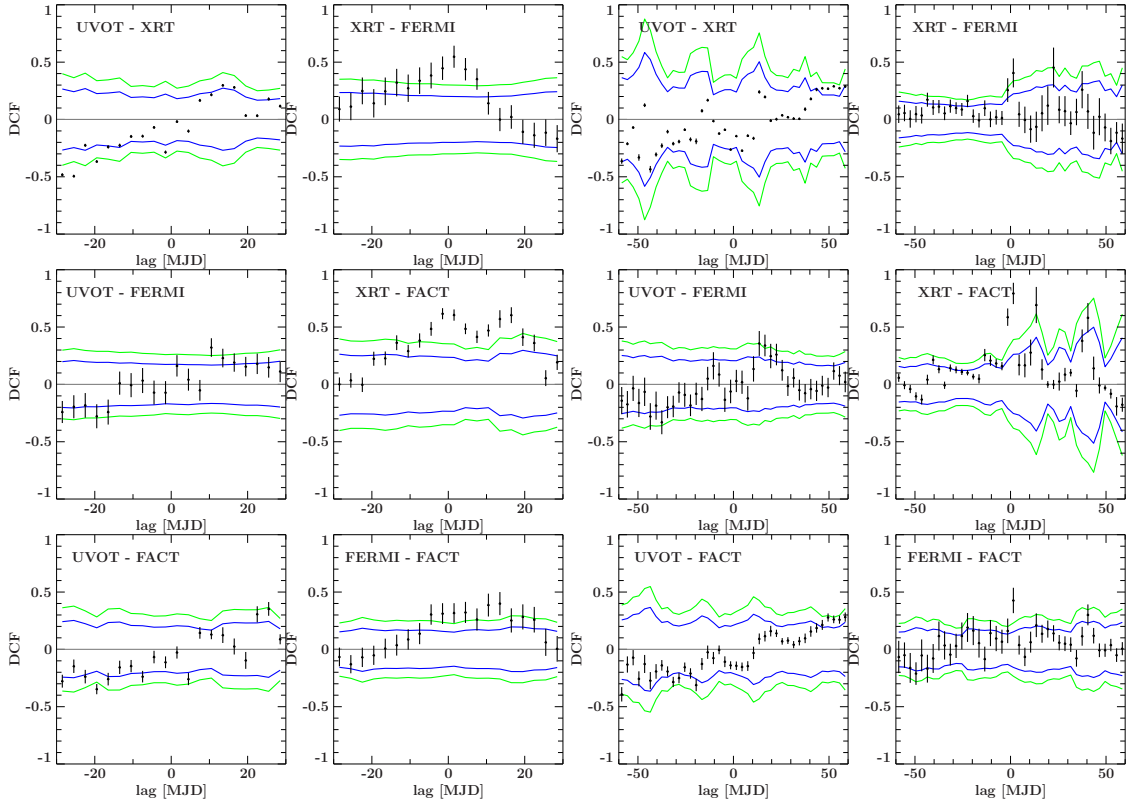


Figure B.6.: Results for the discrete cross-correlation function for observations period T1 MJD 57358-57500 (*left*) and period T2 MJD 57420-57550 (*right*).

(T2) No correlation between UV emission and any other energy band.

(T2) Tentative correlation between X-rays and γ -rays at zero time lag.

(T2) Significant correlation between XRT and FACT at zero time lag. The second peak is not significant anymore, supporting the hypothesis, that is stems from the two resolved outbursts in 2015.

(T2) Significant correlation with a sharp peak at zero time lag between FERMI and FACT. No further lags found.

(T3/4) Time ranges does not include enough data for DCF analysis. No significant features detected.

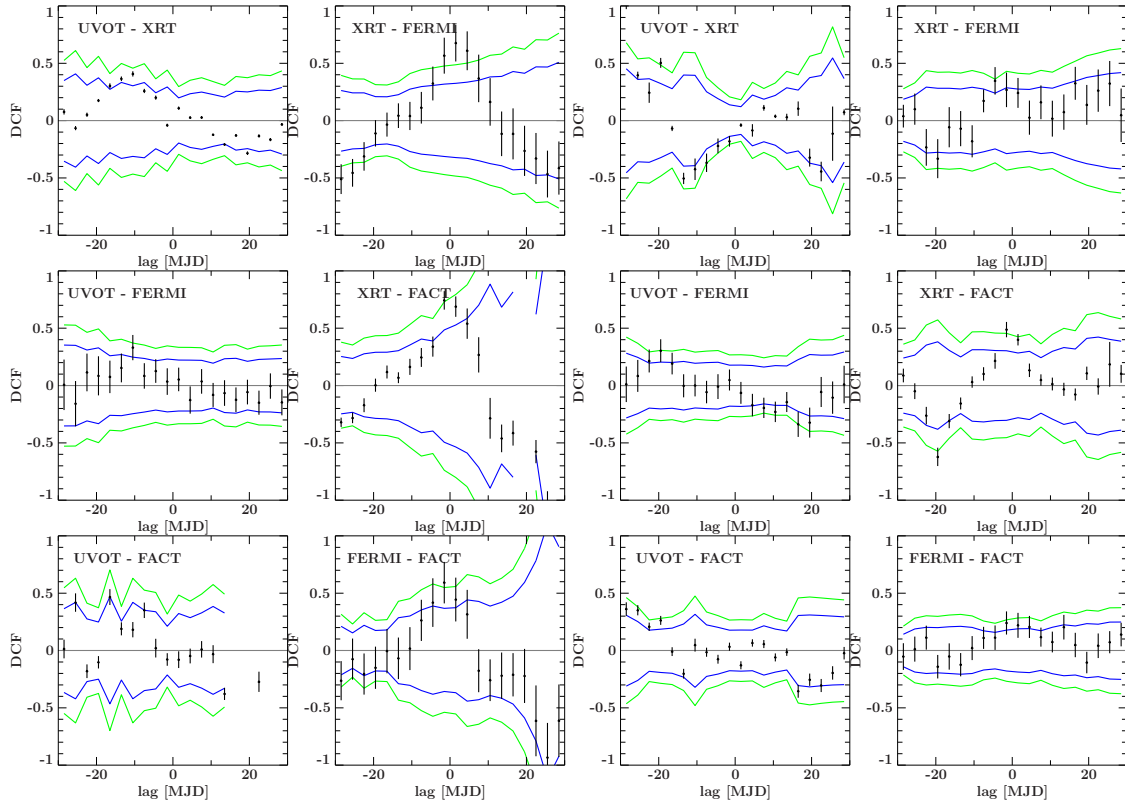


Figure B.7.: Results for the discrete cross-correlation function for observations period T3 MJD 57717-57770 and T4 MJD 57770-57864 (*right*).

B.3. Discussion: results in the context of hadronic jet scenarios

In Sect. 9.6.1, I have discussed the results of the spectral timing analysis of Mrk 421 with respect to the leptonic jet scenario. In this section, although valuable information of the VHE spectral evolution is yet missing, I briefly discuss the results in the framework of hadronic jet scenarios. In this case, a major contribution to the SED comes from relativistic protons through direct proton synchrotron radiation or secondary emission from hadronic cascades (e.g., from photopion production and the subsequent decay products) or Bethe-Heitler pair production. In the following, I will refer to the case, in which the SED is composed of proton induced emission only (i.e., synchrotron and emission by secondary processes) as *pure hadronic* and to the case, where radiation from primary relativistic electrons dominates at low energies, while the high-energy emission stems from a combination of proton synchrotron and hadronic cascade emission, as *lepto-hadronic*.

Stationary SEDs of Mrk 421 have been successfully fitted with one-zone lepto-hadronic models by various authors (e.g., Abdo et al. 2011b; Mastichiadis et al. 2013; Zech et al. 2017). A pure hadronic case was excluded due to a flat GeV spectrum. In these studies,

the low-energy hump was ascribed to synchrotron emission of primary electrons with small contribution of secondary emission from proton-photon interactions, mainly muon synchrotron emission. The high-energy hump was made up by multiple components of which the proton synchrotron emission dominated in the GeV and muon synchrotron emission peaked in the TeV range.

The strong correlation between VHE and X-ray light curves, observed in this as well as other studies, can be explained within both the pure and lepto-hadronic scenario. The former requires that primary leptons and protons are co-accelerated. If there is significant contribution of proton-photon interactions, which is correlated with the target photon field, the correlation implies that protons are co-spatial with soft synchrotron photons of electrons. Mastichiadis et al. (2013) have studied the expected TeV and X-ray flux-flux correlations between three different one-zone hadronic scenarios for Mrk 421 assuming variations of the injected particle luminosity or variations in the maximum particle energy γ_{max} . They distinguished between a pure hadronic (H) model and two lepto-hadronic ones, the pion-induced case (LH π) and proton synchrotron case (LHs). For the LHs case, they assume that the high-energy emission is dominated by proton synchrotron emission, while in the LH π case γ -rays are produced by a combination of secondary electrons from charged pion decay and photons from neutral pion decay. They find, that in all cases a strong correlation between these bands is observed. In particular, for the H and LH π case, where the later is similar to the best-fit model by Zech et al. (2017), a quadratic or steeper relation was observed between X-rays and VHE γ -rays. In the LHs case where proton synchrotron radiation dominated at TeV energies, the flux-flux relation is expected to be linear and may become even sub-linear at high fluxes due to $\gamma\gamma$ absorption (see Sect. 2.4.6). The steep observed correlation in our study (see Fig 9.6 and 9.7) is consistent with a scenario in which secondary emission from proton-photon interaction dominates at TeV emission. Interestingly, a linear to sub-linear flux-flux correlation is observed between GeV γ -rays and X-rays. This trend indicates that proton synchrotron emission dominates in the GeV band, consistent with spectral models from the literature. The observed correlation with synchrotron emission from primary electrons may then point to co-acceleration of primary protons and leptons.

The flux-flux relation between the UV band and observed emission at higher energies has not been well investigated yet. In the one-zone lepto-hadronic case, the low-energy hump is attributed to synchrotron emission of primary electrons with minor contribution from secondary electrons from hadronic processes. Judging from the steady-state spectrum by Zech et al. (2017), the low-energy hump is similar to the one-zone leptonic scenario as secondary cascade emission contributes only to a small fraction in the UV to X-ray band. The long-term monitoring suggests that this model is not adequate to explain the observed emission but we are missing an additional emission process that destroys an expected correlated emission between the UV and X-ray band. Zhang et al. (2016) studied the time-dependent signatures of a multizone pure hadronic model. They find that in the presence of a very strong magnetic field the low-energy emission does not respond to variations of γ -rays induced by enhanced stochastic acceleration (e.g., through turbulence in the jet plasma). While magnetic compression accelerates protons

to higher energy, leptons already cool efficiently via synchrotron radiation. The required magnetic fields are a factor ten to hundred times higher than what Zech et al. (2017) derived from lepto-hadronic model to the steady-state SED. Furthermore, the correlated emission at X-rays speaks against the saturated cooling of leptons.

C. Supplementary studies

Throughout my PhD studies I was involved in a number of investigations lead by colleagues. In this chapter, I give an overview of these studies in which I participated and which put my thesis in a broader context.

C.1. Extragalactic Neutrinos from jetted AGN

As described in Sect. 2 one of the most prevaillent questions in astronomy today is whether relativistic jets of AGN are sources of extragalactic neutrinos and cosmic rays and thus, whether the jets are powerful to accelerate hadrons to ultra-relativistic speed. In this context I have presented a monitoring program which aims at studying the emission processes and particle composition within those jets. Unambiguous evidence of hadronic processes could be provided by a direct association of a detected neutrino event with an AGN.

I was involved in the following studies that search for likely sources of extragalactic neutrinos: Krauß et al. (2014); ANTARES Collaboration et al. (2015); Krauß et al. (2016); Kadler et al. (2016). The following paragraphs summarize the four papers. The paragraphs are heavily based and partly taken verbatim from these publications.

The TANAMI program regularly monitors a sample of bright radio- and γ -ray-emitting AGN in the Southern Hemisphere. In an extensive study by Krauß et al. (2016), the spectral evolution between quiescent and flaring periods of 22 radio-loud AGN was studied through multiepoch, quasisimultaneous, broadband spectra.

For the study, I performed the UV and X-ray data acquisition, extraction, and model fitting for PKS 0308–611, PKS 0302–623, PKS 0235–618, and PMN 1717–3342. We retrieved all publicly available data of these sources. In case of PMN 1717-3342 no X-ray data were found. Therefore, I applied for a target-of-opportunity snapshot observation with the *Swift* satellite, which was performed for 4.5ks on 2014 January 30 (ObsID 00041526001). For all other sources there were archival *Swift* data. In addition, in case of PKS 0308-623 there were *XMM-Newton* data available. I have analyzed the *Swift* and *XMM-Newton* data with standard reduction methods (see sections 4.1.3 and 4.1.4). Model fitting of the X-ray spectra was performed using Cash statistics ?, except for the *XMM-Newton* data where the large number of spectral data counts per energy bin allowed the used of χ^2 -statistics. For each source each observation was first fit individually in the 0.3–10 keV energy band with an absorbed power-law model. Galactic absorptions were taken from the LAB survey ?. If the spectra of one source were consistent in normalization and shape, they were merged and re-fit again in order to increase the SNR

and reduce statistical uncertainties. None of the sources showed evidence for intrinsic X-ray absorption in excess to the Galactic value.

The X-ray and UVOT data of the complete sample provided valuable insights in the spectral evolution between the different spectral states and provided the infrastructure to quickly investigate a sample of TANAMI blazars in the context of IceCube neutrino detections. This infrastructure was used when the Icecube Collaboration discovered two extragalactic neutrino events at PeV energies in excess of the atmospheric background (Aartsen et al. 2013; IceCube Collaboration 2013), between May 2010 and May 2012. We found six blazars which were positionally coincident with the detected neutrino fields. The radio morphologies of the six blazars from the TANAMI VLBI data showed evidence for relativistic boosting at small angles to the line of sight, typical for γ -ray-emitting blazars. Based on our analysis of the SED catalog, we presented the multiwavelength SEDs of these six blazars from the TANAMI sample in Krauß et al. (2014). Assuming that the high-energy emission from X-rays to γ -ray originated from photo-pion production we calculated the integrated high-energy flux from the constructed non-simultaneous SEDs. In pion photo-pion production the neutrino flux is related to the bolometric high-energy electromagnetic flux. We found that, under this assumption, the maximum expected number of electron neutrino events from the six blazars in 662 days is 1.9 ± 0.4 .

Taking these results as an order-of-magnitude indication of the expected neutrino event rate, a follow-up study with higher-angular-resolution at lower neutrino energies was then performed using six years of data from the ANTARES neutrino telescope (ANTARES Collaboration et al. 2015; Ageron et al. 2011). ANTARES is an underwater neutrino telescope in the Mediterranean Sea off the coast of Toulon. It consists of an array of photomultiplier tubes which can record Cherenkov light from the passage of energetic particles in the water to infer the interaction of neutrinos. Similar to the IceCube experiment, ANTARES uses Earth's crust and the mediterranean sea water as effective detection volume. Thus, ANTARES is sensitive to up-going muon neutrinos from the Southern Hemisphere.

Among the sub-PeV Neutrino events that were detected by IceCube there were four more events that could be to be positionally associated with the six TANAMI blazars referred to above. While these events did not represent a significant excess above the atmospheric diffuse background, they may have originated from the bazars assuming a power-law energy distribution of neutrinos. Although it could not be ruled out that these events were background events, the ANTARES analysis (performed by the ANTARES collaboration) supported the results of Krauß et al. (2014), with the six TANAMI blazars being neutrino sources assuming their neutrino fluxes were proportional to their observed high-energy photon flux.

An important conclusion from these two studies is that a deciding quantity for possibility to observe a neutrino event of a blazar was a high fluence (i.e. the high-energy flux density integrated over time) of the respective object. We found relatively low maximum neutrino fluxes of the six individual TANAMI blazars owing to their low fluence built-up over two years, but the diffuse flux due to the integrated emission of all blazars in the fields was found to be sufficiently high to expect up to two events. While no con-

clusive association could be found, this result demonstrated the potential of identifying individual neutrino with high-fluence blazars.

Such a tentative association was found for the third detected PeV neutrino and published in Kadler et al. (2016). Besides the two PeV events (dubbed IC 14 and IC20), a third PeV event (IC 35) was recorded in the third year of IceCube data on 2012 Dec 4. Following our earlier strategy of Krauß et al. (2014), we cross-matched this field with the second catalog of AGN detected by *Fermi*-LAT (2LAC), which is based on *Fermi*-LAT all-sky observations between 2008 Aug and 2010 Sep. We found a total of 20 γ -ray-bright AGN in the field of IC 35 of which 17 were blazars. The dominant blazar in the field is PKS B1424–418 at redshift $z = 1.52224$ and classified as an FSRQ. The source showed two γ -ray flares in 2009–2011 and is listed as a bright γ -ray source *Fermi*/LAT catalogs since the 2FGL and 2LAC.

We detected a high-fluence outburst in summer 2012 which lasted over more than a year and which coincided with the PeV neutrino event IC 35 both in position and in time. In this context I extracted and processed the *Swift*/UVOT data for several epochs to derive the source flux in the optical and UV bandpasses. Along with the very bright γ -ray emission, an increase in X-ray, optical/UV, and radio emission from PKS B1424–418 was found.

The unprecedented nature of the outburst of PKS B1424–418 and the PeV neutrino event, and the small probability for chance coincidence of about 5% suggested a physical association of the two events. This discovery marked the first tentative association of an extragalactic neutrino event with an AGN and suggested that blazars are sources of the high-energy astrophysical neutrino flux. A similar case was recently reported by IceCube Collaboration et al. (2018), who could associated the high-fluence blazar TXS 0506+056 as possible neutrino source for the event IceCube-170922A and found additional neutrino emission prior to this event.

C.2. X-ray emission from Young Radio Galaxies

An elusive class of γ -ray emitting AGN are those with jets that are oriented at larger angles to the line of sight, so-called *misaligned* AGN (e.g., radio galaxies, Sect 3.1.2). They are typically less dominated by beamed jet emission. A sub-class of such misaligned objects are compact symmetric objects (CSO, see Sect. 3.1.2). These objects, which may transition into larger radio galaxies, are a stepping stone to understanding AGN evolution. A direct link between Narrow Line Seyfert 1 galaxies (NLS1) and young AGNs (CSS and CSO) has been suggested by Caccianiga et al. (2014). So far, four γ -ray AGN have been proposed as CSO candidate sources: 4C+55.17 (McConville et al. 2011), PKS 1413+135 (Gugliucci et al. 2005), PKS 1718-469 (Tingay & de Kool 2003) and PMN J1603–4904 (Müller et al. 2016b). The first two have not been confirmed to be young radio galaxies.

C.2.1. The discovery of the new young radio galaxy PMN J1603–4904

In a study lead by Cornelia Müller, we discovered a new CSO and γ -ray-emitting young radio galaxy candidate within the TANAMI sample. In this section I summarize the investigation that was published in four papers Müller (2014), Müller et al. (2016b), Müller et al. (2016a), and Krauß et al. (2018), hereafter, Mue14, Mue16a, Mue16b, and Kr18, respectively. I was involved in the UV and X-ray analysis of Mue14, Mue16b, and Kr18. The following paragraphs are heavily based and partly taken verbatim from these papers.

The source PMN J1603–4904 has been part of the TANAMI sample since 2009 (Ojha et al. 2010). The radio source (PKS B 1600–489) had been classified as a low synchrotron peaked (LSP) BL Lac object (Nolan et al. 2012) and was located close to the Galactic plane ($l = 332^\circ.15$, $b = 2^\circ.57$). No redshift measurement had been reported (Shaw et al. 2013). It was associated with a bright, hard-spectrum γ -ray source detected by *Fermi*-LAT (2FGL J1603.8–4904, Ackermann et al. 2013b). The radio source lay well within the *Fermi*/LAT 95%-error radius (Nolan et al. 2012) and no further known radio source lay in the vicinity, making this a very high confidence association. Interestingly, the GeV emission which was monitored over three years by *Fermi*-LAT showed evidence for mild variability on longer timescales but no flaring on timescales of days to weeks (Ackermann et al. 2013b). Interestingly, the TANAMI 8.4 GHz VLBI structure of PMN J1603–4904 suggested a double-sided source like in FRI radio galaxies, but on smaller scales, i.e., a jet-counterjet system seen side-on combined with a low brightness temperature $T_B \leq 10^{10}$ K. To investigate the nature of this source we accumulated archival data to compute the broadband SED.

PMN J1603–4904 had been observed three times by the *Swift* satellite (Gehrels et al. 2004) between 2009 May and 2010 July. I have extracted the *Swift*/UVOT and *Swift*/XRT data following description in Sect. 4.1.4. The UVOT data only yielded upper limits on the flux at 3σ . But the simultaneous observations by *Swift*/XRT revealed a single, but faint, X-ray source which was positionally consistent with the radio source. No other archival X-ray observations were available. The combined low-snr spectrum was well described by a standard absorbed hard power law ($\Gamma \sim 1.65$). F. Krauss and C. Müller used the *Swift* data together with the radio data and published IR, optical, and *Fermi*-LAT γ -ray data to construct a non-simultaneous broadband SED from radio to γ -rays. The broadband spectral shape of PMN J1603–4904 resembled the typical double-humped SEDs of blazars but showed a striking Compton dominance; the high-energy emission hump was about two orders of magnitude above the synchrotron peak. The unusual lack of short-term flux variability over years and across the electromagnetic spectrum, the strong Compton-dominance in the broadband SED, and most importantly, the resolved and symmetric brightness distribution on milliarcsecond scales of the TANAMI VLBI observations put serious doubts on the BL lac classification of the source. Alternatively, we considered the case where PMN J1603–4904 is an edge-on jet system. The intrinsic symmetry of the radio structure and especially the compactness

with a small angular separation could indicate a young, not yet evolved, radio galaxy.

Further evidence for the alternative scenario was found in high spectral-resolution X-ray data from XMM-Newton and Suzaku. The following paragraphs are based on and partly taken verbatim from Mue16.

In order to determine the physical origin of the high-energy emission processes in PMN J1603–4904, we studied the X-ray spectrum in detail. The origin of the X-ray emission of radio-loud AGN can arise from Comptonization of seed photons from the accretion disc in the hot corona, synchrotron or inverse Compton emission, or a combination of these. In 2013 September, C. Müller acquired quasi-simultaneous X-ray observations of PMN J1603–4904 with *XMM-Newton* (ObsID 0724700101, performed 2013-09-17) and *Suzaku* (ObsID 708035010, performed 2013-09-13). I extracted the *XMM-Newton* spectra following Sect. 4.1.3, together with C. Müller, while the *Suzaku* data was processed by T. Beuchert. We then performed an independent model fit of the *XMM-Newton* and *Suzaku* data using an absorbed power law. This revealed no significant flux variability during the observed period which allowed for a simultaneous analysis of both spectra and improved the signal-to-noise ratio of the spectra. The combined *XMM-Newton*/PN, MOS 1, and *Suzaku*/XIS data were well modeled with an absorbed power-law component, and a Gaussian emission line. Interestingly, we significantly detected a strong emission line that could be modeled by a Gaussian component at 5.44 ± 0.05 keV with an equivalent width of $EW = 200 \pm 90$ eV. We considered the line to correspond to the neutral Fe K α which allowed us to constrain the redshift of the system to $z = 0.18 \pm 0.01$. The detection of an iron line is a clear indication of reprocessed radiation from matter in the vicinity of the primary X-ray source. Iron lines are common features in spectra of radio-quiet and radio-loud sources at larger jet angles to the line of sight (Bianchi et al. 2004). Since blazar X-ray spectra are dominated by beamed jet emission, they are generally featureless and can in most cases be modeled with a simple or broken power law (Chang 2010; Rivers et al. 2013). The strong iron line in the X-ray spectrum of PMN J1603–4904 therefore suggested a non-blazar nature and is compatible with GPS and CSS sources.

Kr18 analysed the possible misidentification of the X-ray source using new Chandra observations. The following paragraphs are based on and partly taken verbatim from Kr18, in which I only contributed to the interpretation of the X-ray data.

Assuming the emission line, that we detected in the high-snr X-ray data of PMN J1603–4904, we estimated a redshift of $z = 0.18 \pm 0.01$. Optical data resulted in the LSP BL Lac classification, were not sensitive enough to detect any lines. However, more recent optical spectroscopy observation with the VLT X-shooter telescope showed that our proposed redshift was incorrect and yielded a redshift measurement of $z = 0.2321 \pm 0.0004$ (Goldoni et al. 2016). Hence, the emission line is due to He-like Fe, emitted at a rest frame energy of 6.7 keV. This emission feature is not typically seen in AGN, where edge-on sources exhibit neutral or slightly ionized Fe K α emission, which is expected to originate in the accretion disks. This feature seems to be common for CSO

sources (Siemiginowska et al. 2016). Highly ionized Fe emission is also observed in the LINER galaxy M81 (Page et al. 2004), though the latter still exhibits neutral Fe $K\alpha$ emission while PMN J1603–4904 does not. It is unclear whether this suggests a complete lack of an accretion disk, a truncated accretion disk (which could likely achieve the high temperatures to ionize Fe) or a lack of neutral Fe.

Although, the radio source is consistent with the Fermi/LAT 95% 2FGL positional uncertainty, it is unclear if there are other possible counterparts within the uncertainty ellipse in either radio or X-ray wavelengths (Mue14). Optical data are unable to solve this problem, due to the large number of nearby stars and the strong extinction. F. Kraus examined recent *Chandra*/ACIS data, the highest angular resolution data available at high energies, to confirm or rule out source confusion for PMN J1603–4904. We took one *Chandra* observation of PMN J1603–4904 with the Advanced CCD Imaging Spectrometer (ACIS; observation ID 17106, 10.08 ksec) on 12 May 2016. We found three X-ray sources in the *Chandra*/ACIS image in the direct vicinity of the 2MASS coordinates of PMN J1603–4904. The X-ray source in the center (no. 2) matches the radio coordinates. We could exclude the eastern and western source (no. 3) as a counterpart due to their large angular distances of $\sim 20''$ and $\sim 11''$. Using *Chandra*/ACIS positions, fluxes, and spectra, in combination with *Fermi*-LAT data, we confirm the X-ray counterpart, rule out contributions from nearby X-ray sources, and confirm a high Compton dominance in the broadband SED of PMN J1603–4904. We therefore conclude that PMN J1603–4904 is likely one of only two known γ -ray emitting young radio galaxies and that its emission mechanisms and strong Compton dominance warrant further research.

Only a few γ -ray emitting misaligned AGN are known (Abdo et al. 2010c). The confirmed detection of a γ -ray bright CSO challenges current jet emission models attempting to explain the high-energy spectral component with high beaming factors and would help to determine the region from where γ -rays are emitted.

C.2.2. Disentangling the extended X-ray emission of PKS 1718–649

Just recently Beuchert et al. (2018) (hereafter B18) reported the first firm detection of the CSO PKS 1718–649 at γ -rays. The extended X-ray emission of this source was investigated in a study lead by Tobias Beuchert. I briefly present the data analysis and conclusions. The paragraphs are based and partly taken verbatim on B18.

PKS 1718–649 is one of the closest and young AGN. The VLBI and single-dish radio observations show a CSO structure and that it is still embedded in its host galaxy (Tingay & de Kool 2003; Ojha et al. 2010). A spectral turnover at 4 GHz classifies the source as a prominent representative of Gigahertz-peaked spectrum (GPS) source (Tingay & de Kool 2003). The inverted radio spectrum below a few gigahertz and the CSO morphology of PKS 1718–649 indicate that the AGN is embedded in a cocoon of ionized matter. Spectral variations of the radio continuum led Tingay et al. (2015) to argue for variable free-free absorbing (FFA) and ionized foreground material as opposed to synchrotron-self absorption (SSA) of jet-intrinsic plasma. In this case, both an inverted radio and photo-absorbed X-ray continuum are expected, when the line of sight is piercing this obscuring

matter. To test this hypothesis we made use of all available archival high-resolution X-ray data as well as new proposed *XMM-Newton* data in order to study the time-resolved X-ray spectrum of this new-born AGN.

Co-adding all (three) publicly available archival *Chandra* data and complementing these datasets with the large effective area of *XMM-Newton* in the low-energy band below 1 keV, we were able to study the detailed physics of the environment of this young AGN. The high spatial resolution of the *Chandra* images allowed us to quantify the extended and non-variable X-ray emission. Image analysis performed by T. Beuchert, showed that the bulk of the photons and in particular hard X-rays above ~ 1.5 keV are emitted from the unresolved core region with an excess of $\sim 60\%$ above the soft X-rays within a radius of $300''$. Our acquired XMM-Newton observation (ObsID:) then provided a sufficient amount of counts below 1 keV to investigate the nature of this extended and soft emission. Together with T. Beuchert, I fitted the *Chandra* spectra combined with recently acquired XMM-Newton data to unveil the origin of the extended emission (see Fig. 2). The hard-X-ray data follow a common power-law of constant photon index ($\Gamma = 1.78$) that is absorbed towards lower energies. In a detailed analysis, T. Beuchert detected two plasma emission components that are non-variable on the probed time-scales of years: One is photoionized by the incident continuum and the second dominates the soft emission and is best described as a collisionally ionized and hot gas. Besides the non-variable emission components, the only parameters that turn out to be variable (on time-scales of years) are the source-intrinsic column density and flux of the incident hard X-ray power law.

Thus, we are able to report, for the first time in the literature, on variable X-ray absorption and on the physics of the extended X-ray emission in the CSO PKS 1718–649 that is for the most part unrelated to nuclear feedback. The X-ray source may be a corona close to the accretion disk, the parsec-scale radio jet, or its jet base. The spatially resolved and extended environment beyond ~ 600 pc from the core, however, predominantly emits soft X-rays. Based on its low overall luminosity with $(2.5 \sim 5.4) \times 10^{41} \text{ erg s}^{-1}$, we concluded that this gas must be part of the extended and hot interstellar medium, spatially distinct from the photoionized gas phase traced by OVII.

C.3. Mapping X-ray absorption in AGN and the local ISM

Absorption is a critical component in the analysis of optical to X-ray spectra. The intrinsic emission spectrum interacts with either source intrinsic or foreground material which alters the shape of the observable photon flux spectrum. Absorption is typically expressed by the equivalent hydrogen column density N_{H} . Using the temporal or spatial changes of N_{H} can provide important information on the structure and location of the absorbing material.

C.3.1. Variable absorption in the radio-quiet AGN NGC 3227

Variable absorption has been found for a number of AGN including NGC 3227. These absorption events can be explained by transits of discrete clouds or clumps of gas across the line of sight to the central X-ray continuum source and support a new generation of "clumpy torus" models (Elitzur 2007; Nenkova et al. 2002, 2008a,b). Tobias Beuchert performed a study with the aim to map out the distribution of gas of the Seyfert galaxy NGC 3227. It was published in Beuchert et al. (2015). The Seyfert 1.5 AGN NGC 3227 was monitored with RXTE from 1999 Jan to 2005 Dec (Uttley & McHardy 2005). The monitoring revealed a usually unabsorbed AGN as well as two eclipse events: an ~ 80 -day event in 2000/2001 (Lamer et al. 2003) and a 2-7 day event in 2002 (Markowitz et al. 2014). The estimated distances from the central engine are tens of light days (ld).

We have studied data from a five-week-long *Suzaku* and Swift X-ray and UV monitoring campaign on the Sy 1.5 NGC 3227 in late 2008, which caught the source in an absorbed state. The X-ray data was used to perform time-resolved X-ray spectroscopy in order to untangle the various emission components, i.e., the coronal power law and ionized reflection as well as multiple ionized absorption components, and to isolate the time-dependent behavior of the dominant absorber in 2008. Together with T. Beuchert, I helped in the X-ray analysis with ISIS to derive a baseline model using two archival and previously published *XMM-Newton*/EPIC spectra. The baseline model was then used by T. Beuchert to fit simultaneously to six *Suzaku* and 12 *Swift* observations from 2008. The two *XMM-Newton* spectra revealed three differently ionized absorbers of different (low, moderate, and high) ionization. The moderately ionized component showed absorption variability of ≥ 35 d in 2008, while the other two remained constant. Assuming that the absorption event stems from a spherical cloud on a Keplerian orbit around the illuminating source, the distance of the absorbing medium to the central SMBH is between 0.017 pc and 0.65 pc. Our model for the 2008 event is consistent with past observations. Small inclination angles ($\leq 20 - 30^\circ$) of the putative clumpy torus that are measured by independent methods and orbiting absorbing clouds help to explain the predominant lack of absorption in NGC 3227 during past observations. NGC 3227 is a rare laboratory to study a range of physical processes that form and shape clouds or filaments.

C.3.2. A 3D map of the local ISM: a *Gaia* and *XMM-Newton* synergy

The following study of the equivalent N_{H} distribution in the Milky Way makes use of the extensive spectral fitting database to the 3XMM-DR6, that I performed in the framework of the EXTraS project (see Chpt. 7). It was published in Gattuzz et al. (2018).

Essentially all line-of-sights from the earth to any point in the sky show a certain degree of absorption due to the ISM in the Milky Way. The local interstellar medium (ISM) includes cold ($\leq 10^4$,K), warm (10^4 - 10^6 ,K) and hot ($\geq 10^6$ K) components, where neutral hydrogen is contained in the warm and cold neutral medium. The latter plays an important role in the Galactic evolution acting as a gas reservoir for star formation processes. Therefore, knowledge of the hydrogen spatial distribution along the Milky

Way is key to understanding the chemical evolution of our own Galaxy. X-ray emission allows for probing the hot ionized medium with the advantage that moderate resolution (X-ray) spectra can be analyzed fast, while providing a good measure of the equivalent N_{H} absorption. Moreover, compared with the angular resolution provided by the 21 cm all-sky surveys (~ 36 arcmin) the *XMM-Newton* angular resolution (about 5 arcsec FWHM) allows a study of the small-scale ISM structure. The project was led by Efrain Gatzuz and made use of the unprecedented synergy of *Gaia* and *XMM-Newton*. Thus, it combines the analysis of small-scale structures in the cold ISM with *XMM-Newton* with parallax measurements for 2.5 million sources by *Gaia*.

The N_{H} values are provided by my model fits of the 3XMM-DR6 X-ray data, which I performed for the EXTraS project (see Chpt. 7) as well as the preliminary results for the source classification. For each EXTraS source that was classified as star at a confidence value of $\geq 1\sigma$, accurate parallax and distance measurements were obtained through positional cross-matches with the first *Gaia* Data Release using the angular distance separation. For the final data sample we used those stars that have $\leq 20\%$ of distance uncertainties, $\Delta N_{\text{H}} \leq 50\%$, given a reliable goodness-of-fit.

The most probable distribution of the N_{H} at any arbitrary point, even for lines-of-sight along which there are no initial observation, was predicted by E. Gatzuz, using a Bayesian method. The resulting maps (see Fig. C.1) show a local region with distances below 600 pc. This study marked the first time such a map has been created using X-ray spectral fits. Such X-ray density maps provide more information about the N_{H} distribution than 21 cm surveys because X-ray photons can trace not only the atomic ISM component but also the ionized gas, molecules and solids.

Strikingly, comparing the X-ray column densities $N_{\text{H,X}}$ with those derived from the 21 cm lines ($N_{\text{H,21}}$) we found an unexpected significant fraction of the sources ($\sim 65\%$) with $N_{\text{H,X}} > N_{\text{H,21}}$. A similar result has been described by Willingale et al. (2013), who studied the absorption in the afterglows of gamma ray bursts from the *Swift* satellite.

Possible explanations for this disagreement include:

- absorption which is intrinsic to the sources
- systematic errors in the X-ray fitting procedure
- the existence of absorbing structures in the ISM which are smaller than the angular resolution of the 21 cm survey beam and which are rare enough to not skew the net 21 cm emission significantly;
- the existence of ionized absorbers which only affects the X-ray absorption.

Because systematic uncertainties due to the N_{H} dependence on the continuum fitting model and the source identifications, the present maps should be considered qualitatively at this point. A similar analysis is currently under development using the much more complete and accurate *Gaia* DR2, which we will be feature in a future publication.

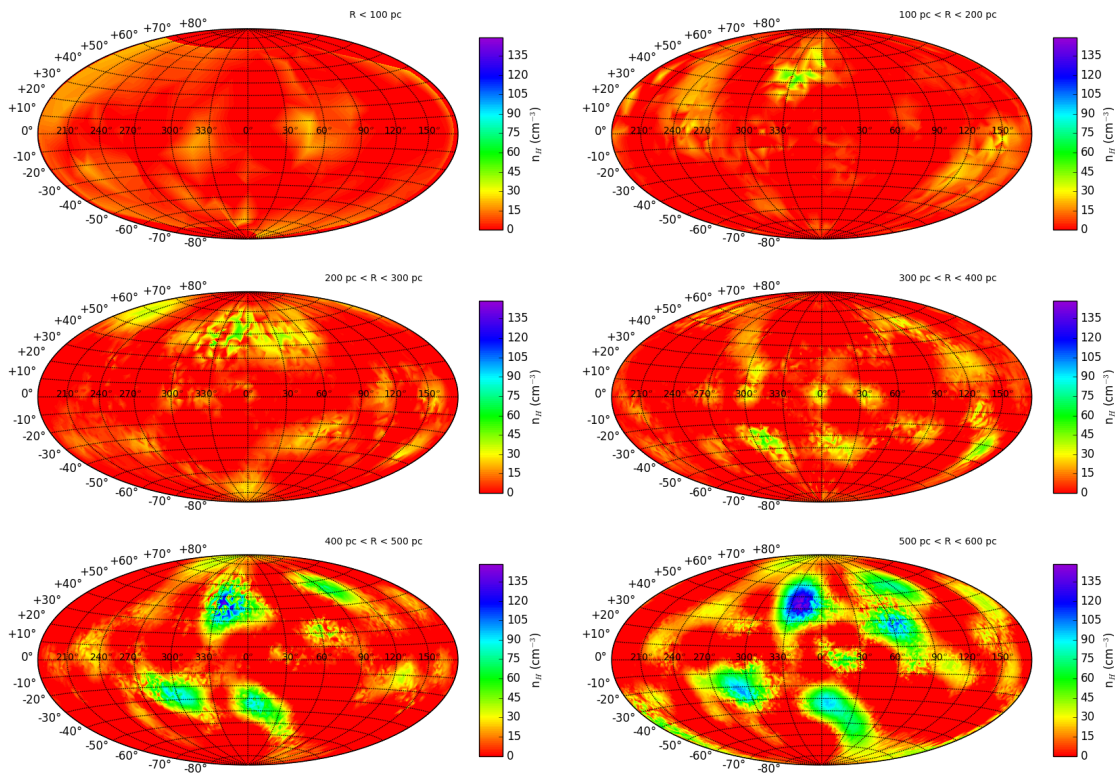


Figure C.1.: Full-sky 2D map of the density distribution. The map is an Aitoff projection covering distances from 0 to 600 pc.

References

- Aartsen M.G., Abbasi R., Ackermann M., et al., 2013, *Phys. Rev. D*, 88, 112008
- Aartsen M.G., Abraham K., Ackermann M., et al., 2017, *ApJ*, 835, 151
- Aartsen M.G., Ackermann M., Adams J., et al., 2014, *ApJ*, 796, 109
- Abbasi R., Abdou Y., Abu-Zayyad T., et al., 2009, *Physical Review Letters*, 103, 221102
- Abdo A.A., Ackermann M., Ajello M., et al., 2010a, *ApJ*, 188, 405
- Abdo A.A., Ackermann M., Ajello M., et al., 2011a, *Science*, 331, 739
- Abdo A.A., Ackermann M., Ajello M., et al., 2010b, *Science*, 329, 817
- Abdo A.A., Ackermann M., Ajello M., et al., 2009a, *ApJ*, 707, 727
- Abdo A.A., Ackermann M., Ajello M., et al., 2010c, *ApJ*, 720, 912
- Abdo A.A., Ackermann M., Ajello M., et al., 2009b, *ApJ*, 707, L142
- Abdo A.A., Ackermann M., Ajello M., et al., 2009c, *ApJ*, 707, L142
- Abdo A.A., Ackermann M., Ajello M., et al., 2011b, *ApJ*, 736, 131
- Abdo A.A., Ajello M., Antolini E., et al., 2010d, *ApJ*, 720, 26
- Abdollahi S., Ackermann M., Ajello M., et al., 2017, *ApJ*, 846, 34
- Abraham J., Abreu P., Aglietta M., et al., 2010, *Physics Letters B*, 685, 239
- Abreu P., Aglietta M., Ahn E.J., et al., 2010, *Astroparticle Physics*, 34, 314
- Acciari V.A., Aliu E., Arlen T., et al., 2011a, *ApJ*, 738, 25
- Acciari V.A., Aliu E., Arlen T., et al., 2011b, *ApJ*, 738, 169
- Acciari V.A., Aliu E., Arlen T., et al., 2009a, *Science*, 325, 444
- Acciari V.A., Aliu E., Aune T., et al., 2009b, *ApJ*, 703, 169
- Acciari V.A., Arlen T., Aune T., et al., 2011c, *ApJ*, 729, 2
- Acciari V.A., Beilicke M., Blaylock G., et al., 2008, *ApJ*, 679, 397
- Acero F., Ackermann M., Ajello M., et al., 2015, *ApJ*, 218, 23
- Acero F., Donato D., Ojha R., et al., 2013, *ApJ*, 779, 133
- Ackermann M., Ajello M., Albert A., et al., 2013a, *ApJ*, 771, 57
- Ackermann M., Ajello M., Albert A., et al., 2012a, *ApJS*, 203, 4
- Ackermann M., Ajello M., Allafort A., et al., 2011a, *ApJ*, 741, 30
- Ackermann M., Ajello M., Allafort A., et al., 2011b, *ApJ*, 743, 171
- Ackermann M., Ajello M., Allafort A., et al., 2012b, *ApJ*, 753, 83
- Ackermann M., Ajello M., Allafort A., et al., 2013b, *ApJS*, 209, 34
- Ackermann M., Ajello M., Atwood W.B., et al., 2015, *ApJ*, 810, 14
- Ackermann M., Ajello M., Atwood W.B., et al., 2016, *ApJS*, 222, 5
- Ackermann M., Ajello M., Atwood W.B., et al., 2012c, *ApJ*, 750, 3
- Ageron M., Aguilar J.A., Al Samarai I., et al., 2011, *Nuclear Instruments and Methods in Physics Research A*, 656, 11
- Agrawal A., Viktor H., Paquet E., 2015, In: 7th IC3K, IEEE Xplore 2016
- Aharonian F., Akhperjanian A.G., Aye K.M., et al., 2005a, *Science*, 309, 746
- Aharonian F., Akhperjanian A.G., Aye K.M., et al., 2005b, *A&A*, 437, 95
- Aharonian F., Akhperjanian A.G., Barres de Almeida U., et al., 2009, *A&A*, 495, 505
- Aharonian F., Akhperjanian A.G., Bazer-Bachi A.R., et al., 2007, *ApJ*, 664, L71
- Aharonian F., Akhperjanian A.G., Bazer-Bachi

- A.R., et al., 2006c, *Science*, 314, 1424
- Aharonian F., Akhperjanian A.G., Bazer-Bachi A.R., et al., 2006a, *A&A*, 460, 743
- Aharonian F., Akhperjanian A.G., Bazer-Bachi A.R., et al., 2006b, *A&A*, 460, 743
- Ahlers M., Halzen F., 2015, *Reports on Progress in Physics*, 78, 126901
- Ahnen M.L., Ansoldi S., Antonelli L.A., et al., 2016a, *A&A*, 593, A91
- Ahnen M.L., Ansoldi S., Antonelli L.A., et al., 2016b, *A&A*, 593, A91
- Ajello M., Atwood W.B., Baldini L., et al., 2017, *ApJS*, 232, 18
- Akiyama K., Kuramochi K., Ikeda S., et al., 2017, *ApJ*, 838, 1
- Akylas A., Georgantopoulos I., Ranalli P., et al., 2016, *A&A*, 594, A73
- Albert J., Aliu E., Anderhub H., et al., 2008, *ApJ*, 685, L23
- Albert J., Aliu E., Anderhub H., et al., 2006, *Science*, 312, 1771
- Albert J., Aliu E., Anderhub H., et al., 2007, *ApJ*, 669, 862
- Aleksić J., Ansoldi S., Antonelli L.A., et al., 2015a, *A&A*, 576, A126
- Aleksić J., Ansoldi S., Antonelli L.A., et al., 2015b, *A&A*, 578, A22
- Aleksić J., Ansoldi S., Antonelli L.A., et al., 2014a, *Science*, 346, 1080
- Aleksić J., Antonelli L.A., Antoranz P., et al., 2014b, *A&A*, 563, A91
- Alexander D.M., Chary R.R., Pope A., et al., 2008, *ApJ*, 687, 835
- Allen G.E., Keohane J.W., Gotthelf E.V., et al., 1997, *ApJ*, 487, L97
- Amit Y., Geman D., 1997, *Neural Computation*, 9, 1545–1588
- Anderhub H., Backes M., Biland A., et al., 2013a, *Journal of Instrumentation*, 8, P06008
- Anderhub H., Backes M., Biland A., et al., 2013b, *Journal of Instr.*, 8, 6008P
- Anderhub H., Backes M., Biland A., et al., 2011, *Nuc. Instr. Meth. Phys. R. A.*, 639, 58
- ANTARES Collaboration Adrián-Martínez S., Albert A., et al., 2015, *A&A*, 576, L8
- Antonucci R., 1993, *ARA&A*, 31, 473
- Arévalo P., Markowitz A., 2014, *ApJ*, 783, 82
- Asada K., Nakamura M., Doi A., et al., 2014, *ApJ*, 781, L2
- Atoyan A.M., Aharonian F.A., 1996, *Astronomy and Astrophysics Supplement Series*, 120, 453
- Atwood W.B., Abdo A.A., Ackermann M., et al., 2009, *ApJ*, 697, 1071
- Auchettl K., Slane P., Castro D., 2014, *ApJ*, 783, 32
- Bai X.N., Spitkovsky A., 2010, *ApJ*, 715, 1282
- Baldi R.D., Capetti A., Robinson A., et al., 2016, *MNRAS*, 458, L69
- Ball N.M., Brunner R.J., 2010, *International Journal of Modern Physics D*, 19, 1049
- Baloković M., Paneque D., Madejski G., et al., 2016, *ApJ*, 819, 156
- Bamba A., Koyama K., Tomida H., 2000, *PASJ*, 52, 1157
- Bartoli B., Bernardini P., Bi X.J., et al., 2016, *ApJS*, 222, 6
- Bednarek W., Bartosik M., 2003, *A&A*, 405, 689
- Bednarek W., Protheroe R.J., 1997, *MNRAS*, 292, 646
- Begelman M.C., Sikora M., Giommi P., et al., 1987, *ApJ*, 322, 650
- Benz A.O., Güdel M., 2010, *ARA&A*, 48, 241
- Berton M., Foschini L., Ciroi S., et al., 2015, *A&A*, 578, A28
- Best P.N., Heckman T.M., 2012, *MNRAS*, 421, 1569
- Beuchert T., 2017, Ph.D. thesis, Dr Remeis Observatory; ECAP/FAU
- Beuchert T., Markowitz A.G., Dauser T., et al., 2017, *A&A*, 603, A50
- Beuchert T., Markowitz A.G., Krauß F., et al., 2015, *A&A*, 584, A82
- Beuchert T., Rodríguez-Ardila A., Moss V.A., et al., 2018, *A&A*, 612, L4
- Bhattacharyya S., Bhatt H., Bhatt N., Singh K.K., 2014, *MNRAS*, 440, 106
- Bianchi S., Maiolino R., Risaliti G., 2012, *Advances in Astronomy*, 2012, 782030
- Bishop C.M., 2006, *Pattern Recognition and Machine Learning*, Springer
- Blandford R.D., 1972, *A&A*, 20, 135
- Blandford R.D., Königl A., 1979a, *ApJ*, 232, 34
- Blandford R.D., Königl A., 1979b, *ApJ*, 232, 34
- Blandford R.D., McKee C.F., 1982, *ApJ*, 255, 419

- Blandford R.D., Payne D.G., 1982, *MNRAS*, 199, 883
- Blandford R.D., Rees M.J., 1974, *MNRAS*, 169, 395
- Blandford R.D., Znajek R.L., 1977, *MNRAS*, 179, 433
- Blasi M.G., Lico R., Giroletti M., et al., 2013, *A&A*, 559, A75
- Bloom S.D., Marscher A.P., 1996, *ApJ*, 461, 657
- Boettcher M., 2010, ArXiv e-prints,
- Boettcher M., Harris D.E., Krawczynski H., 2012, *Relativistic Jets from Active Galactic Nuclei*
- Boller T., Freyberg M.J., Trümper J., et al., 2016, *A&A*, 588, A103
- Boroson T.A., Green R.F., 1992, *ApJ*, 80, 109
- Böttcher M., 2007, *Ap&SS*, 307, 69
- Böttcher M., Dermer C.D., 2010, *ApJ*, 711, 445
- Böttcher M., Reimer A., Sweeney K., Prakash A., 2013, *ApJ*, 768, 54
- Bradt H.V., Rothschild R.E., Swank J.H., 1993, *A&AS*, 97, 355
- Breiman L., 1996, *Machine Learning*, 26, 123
- Breiman L., 2001, *Machine Learning*, 45, 5
- Breiman L., Friedman R., Olshen R., Stone C., 1984, *Journal of the American Statistical Association*, 58, 415
- Bretz T., Anderhub H., Backes M., et al., 2013a, ArXiv e-prints,
- Bretz T., Biland A., Buß J., et al., 2014, ArXiv e-prints,
- Bretz T., Biland A., Buß J., et al., 2013b, ArXiv e-prints,
- Broos P.S., Townsley L.K., Feigelson E.D., et al., 2010, *ApJ*, 714, 1582
- Buckley J.H., Akerlof C.W., Biller S., et al., 1996, *ApJ*, 472, L9
- Budavári T., Szalay A.S., 2008, *ApJ*, 679, 301
- Bühler R., Blandford R., 2014, *Reports on Progress in Physics*, 77, 066901
- Burrows D.N., Hill J.E., Nousek J.A., et al., 2005, *SSR*, 120, 165
- Burtscher L., Davies R.I., Graciá-Carpio J., et al., 2016, *A&A*, 586, A28
- Bykov A.M., Chevalier R.A., Ellison D.C., Uvarov Y.A., 2000, *ApJ*, 538, 203
- Caccianiga A., Antón S., Ballo L., et al., 2014, *MNRAS*, 441, 172
- Calderone G., Ghisellini G., Colpi M., Dotti M., 2013, *MNRAS*, 431, 210
- Cardelli J.A., Clayton G.C., Mathis J.S., 1989, *ApJ*, 345, 245
- Carliles S., Budavári T., Heinis S., et al., 2010, *ApJ*, 712, 511
- Caruana R., Niculescu-Mizil A., 2006, In: *Proceedings of the 23rd international conference on Machine learning*, Association for Computing Machinery, New York, NY, USA, 512, ACM, 161
- Cash W., 1979, *ApJ*, 228, 939
- Cavaliere A., Fusco-Femiano R., 1976, *A&A*, 49, 137
- Celotti A., Ghisellini G., Fabian A.C., 2007, *MNRAS*, 375, 417
- Chang C.S., 2010, Ph.D. thesis, Universität zu Köln
- Charlot P., Gabuzda D.C., Sol H., et al., 2006, *A&A*, 457, 455
- Chawla N.V., Bowyer K.W., Hall L.O., Kegelmeyer W.P., 2002, *Journal of Artificial Intelligence Research*, 16, 321–357
- Chen L., 2017, ArXiv e-prints,
- Chen X., Fossati G., Liang E.P., Böttcher M., 2011, *MNRAS*, 416, 2368
- Chiaberge M., Marconi A., 2011, *MNRAS*, 416, 917
- Cohen M.H., Lister M.L., Homan D.C., et al., 2007, *ApJ*, 658, 232
- Cohn H.N., Lugger P.M., Couch S.M., et al., 2010, *ApJ*, 722, 20
- Congiu E., Contini M., Ciroi S., et al., 2017, *MNRAS*, 471, 562
- Cool A.M., Grindlay J.E., Cohn H.N., et al., 1995, *ApJ*, 439, 695
- Corral A., Georgantopoulos I., Watson M.G., et al., 2015, *A&A*, 576, A61
- Crocker R.M., Aharonian F., 2011, *Physical Review Letters*, 106, 101102
- Croton D.J., Springel V., White S.D.M., et al., 2006, *MNRAS*, 365, 11
- Crummy J., Fabian A.C., Gallo L., Ross R.R., 2006, *MNRAS*, 365, 1067
- Dai B.Z., Zhang L., 2003, *PASJ*, 55, 939
- D’Ammando F., Larsson J., Orienti M., et al., 2014a, *MNRAS*, 438, 3521
- D’Ammando F., Larsson J., Orienti M., et al., 2014b, *MNRAS*, 438, 3521

- D'Ammando F., Orienti M., Doi A., et al., 2013a, MNRAS, 433, 952
- D'Ammando F., Orienti M., Finke J., et al., 2013b, MNRAS, 436, 191
- D'Ammando F., Orienti M., Finke J., et al., 2012, MNRAS, 426, 317
- Dauser T., García J., Wilms J., 2016, *Astronomische Nachrichten*, 337, 362
- Dauser T., Garcia J., Wilms J., et al., 2013, MNRAS, 430, 1694
- Davis J.E., 2001a, ApJ, 562, 575
- Davis J.E., 2001b, ApJ, 548, 1010
- de Ruiter H.R., Willis A.G., Arp H.C., 1977, A&AS, 28, 211
- Dermer C.D., Schlickeiser R., 1993, ApJ, 416, 458
- Dermer C.D., Schlickeiser R., 1994, ApJS, 90, 945
- Dermer C.D., Schlickeiser R., Mastichiadis A., 1992, A&A, 256, L27
- Di Matteo T., Springel V., Hernquist L., 2005, Nature, 433, 604
- Dietterich T.G., 2000, Machine Learning, 40, 139
- Diltz C., Böttcher M., Fossati G., 2015, ApJ, 802, 133
- Doeleman S., Agol E., Backer D., et al., 2009, In: astro2010: The Astronomy and Astrophysics Decadal Survey, ArXiv Astrophysics e-prints, 2010
- Doeleman S.S., Fish V.L., Schenck D.E., et al., 2012, Science, 338, 355
- Done C., Davis S.W., Jin C., et al., 2012, MNRAS, 420, 1848
- Dove J.B., Wilms J., Maisack M., Begelman M.C., 1997, ApJ, 487, 759
- Drinkwater M.J., Webster R.L., Francis P.J., et al., 1997, MNRAS, 284, 85
- Dubath P., Rimoldini L., Süveges M., et al., 2011, MNRAS, 414, 2602
- Dutka M.S., Ojha R., Pottschmidt K., et al., 2013, ApJ, 779, 174
- Dwek E., Krennrich F., 2013, Astroparticle Physics, 43, 112
- Edelson R., Turner T.J., Pounds K., et al., 2002a, ApJ, 568, 610
- Edelson R., Turner T.J., Pounds K., et al., 2002b, ApJ, 568, 610
- Edelson R.A., Krolik J.H., 1988, ApJ, 333, 646
- Elitzur M., Ho L.C., 2009, ApJ, 701, L91
- Elitzur M., Shlosman I., 2006, ApJ, 648, L101
- Elvis M., Wilkes B.J., McDowell J.C., et al., 1994, ApJS, 95, 1
- Evans I.N., Tsvetanov Z., Kriss G.A., et al., 1993, ApJ, 417, 82
- Fabian A.C., 2012, ARA&A, 50, 455
- Fabian A.C., Vaughan S., 2003, MNRAS, 340, L28
- Fan J.H., Yang J.H., Yuan Y.H., et al., 2012, ApJ, 761, 125
- Fanaroff B.L., Riley J.M., 1974, MNRAS, 167, 31P
- Fanti C., Fanti R., Zanichelli A., et al., 2011, A&A, 528, A110
- Farrell S.A., Murphy T., Lo K.K., 2015, ApJ, 813, 28
- Feldman G.J., Cousins R.D., 1998, PRD, 57, 3873
- Finke J.D., 2013, ApJ, 763, 134
- Fitzpatrick E.L., 1999, PASP, 111, 63
- Fleishman G.D., Bietenholz M.F., 2007, MNRAS, 376, 625
- Foschini L., 2011, In: Narrow-Line Seyfert 1 Galaxies and their Place in the Universe
- Foschini L., 2012, In: PoS, "Nuclei of Seyfert galaxies and QSOs - Central engine and conditions of star formation", 010
- Foschini L., Berton M., Caccianiga A., et al., 2015, A&A, 575, A13
- Fossati G., Buckley J.H., Bond I.H., et al., 2008, ApJ, 677, 906
- Fossati G., Maraschi L., Celotti A., et al., 1998, MNRAS, 299, 433
- Fuhrmeister B., Schmitt J.H.M.M., 2003, A&A, 403, 247
- Fukazawa Y., Hiragi K., Mizuno M., et al., 2011, ApJ, 727, 19
- Funk S., 2015, Annual Review of Nuclear and Particle Science, 65, 245
- Gaidos J.A., Akerlof C.W., Biller S., et al., 1996, Nature, 383, 319
- Gallo L.C., Edwards P.G., Ferrero E., et al., 2006, MNRAS, 370, 245
- Gaspari M., Brighenti F., Temi P., 2012, MNRAS, 424, 190
- Gatuzz E., Rezaei K.S., Kallman T.R., et al., 2018, MNRAS, 479, 3715
- Gehrels N., 1986, ApJ, 303, 336

- Georganopoulos M., Kazanas D., 2003, *ApJ*, 594, L27
- Getman K.V., Feigelson E.D., Broos P.S., et al., 2010, *ApJ*, 708, 1760
- Ghisellini G., Celotti A., Fossati G., et al., 1998, *MNRAS*, 301, 451
- Ghisellini G., Madau P., 1996, *MNRAS*, 280, 67
- Ghisellini G., Maraschi L., Tavecchio F., 2009, *MNRAS*, 396, L105
- Ghisellini G., Tavecchio F., Chiaberge M., 2005, *A&A*, 432, 401
- Ghisellini G., Tavecchio F., Foschini L., et al., 2010a, *MNRAS*, 402, 497
- Ghisellini G., Tavecchio F., Foschini L., et al., 2010b, *MNRAS*, 402, 497
- Giannios D., Uzdensky D.A., Begelman M.C., 2010, *MNRAS*, 402, 1649
- Giebels B., Dubus G., Khélifi B., 2007, *A&A*, 462, 29
- Giommi P., Padovani P., Polenta G., et al., 2012a, *MNRAS*, 420, 2899
- Giommi P., Polenta G., Lähteenmäki A., et al., 2012b, *A&A*, 541, A160
- Gonzalez A.G., Wilkins D.R., Gallo L.C., 2017, *MNRAS*, 472, 1932
- Gordovskyy M., Browning P.K., Vekstein G.E., 2010, *ApJ*, 720, 1603
- Gorenstein P., Gursky H., Garmire G., 1968, *ApJ*, 153, 885
- Green A.R., McHardy I.M., Lehto H.J., 1993, *MNRAS*, 265, 664
- Grier C.J., Pancoast A., Barth A.J., et al., 2017, *ApJ*, 849, 146
- Grupe D., 2004, *AJ*, 127, 1799
- Grupe D., Komossa S., Leighly K.M., Page K.L., 2010, *ApJs*, 187, 64
- Guainazzi M., Matt G., Perola G.C., 2005, *A&A*, 444, 119
- Güdel M., 2004, *A&A Rev.*, 12, 71
- Gugliucci N.E., Taylor G.B., Peck A.B., Giroletti M., 2005, *ApJ*, 622, 136
- Guo H., Viktor H.L., 2004, *SIGKDD Explor. Newsl.*, 6, 30
- H. E. S. S. Collaboration Abdalla H., Abramowski A., et al., 2018, *A&A*, 612, A9
- Ha T.M., Bunke H., 1997, Off-line, Handwritten Numeral Recognition by Perturbation Method. *Pattern Analysis and Machine Intelligence*, 19/5, 535–539., 19/5, 535–539
- Haardt F., Maraschi L., 1993a, *ApJ*, 413, 507
- Haardt F., Maraschi L., 1993b, *ApJ*, 413, 507
- Haberl F., Sturm R., 2016, *A&A*, 586, A81
- Halzen F., Zas E., 1997a, *ApJ*, 488, 669
- Halzen F., Zas E., 1997b, *ApJ*, 488, 669
- Hambrick D.C., Ostriker J.P., Naab T., Johansson P.H., 2011, *ApJ*, 738, 16
- Harris D.E., Krawczynski H., 2006, *ARA&A*, 44, 463
- Harris D.E., Krawczynski H., Taylor G.B., 2002, *ApJ*, 578, 60
- Harrison F.A., Craig W.W., Christensen F.E., et al., 2013, *ApJ*, 770, 103
- Hastie T., Tibshirani R., Friedman J., 2001, *The Elements of Statistical Learning*, Springer Series in Statistics, Springer New York Inc.
- Hayashida M., Nalewajko K., Madejski G.M., et al., 2015, *ApJ*, 807, 79
- He H., Bai Y., Garcia E.A., Li S., 2008, In: 2008 IEEE International Joint Conference on Neural Networks (IEEE World Congress on Computational Intelligence), 1322
- Heckman T.M., Best P.N., 2014, *ARA&A*, 52, 589
- Henri G., Saugé L., 2006, *ApJ*, 640, 185
- Hillas A.M., 2006, *ArXiv Astrophysics e-prints*,
- Hinton J.A., Hofmann W., 2009, *ARA&A*, 47, 523
- Houck J.C., Denicola L.A., 2000, In: Manset N., Veillet C., Crabtree D. (eds.) *Astronomical Data Analysis Software and Systems IX*, Astronomical Society of the Pacific Conference Series, 216, 591
- Howard E.M., 2016, In: Taylor A.R., Rosolowsky E. (eds.) *Astronomical Data Analysis Software and Systems XXV (ADASS XXV)*, Astronomical Society of the Pacific Conference Series, 512, 245–248
- IceCube Collaboration 2013, *Science*, 342, 1242856
- IceCube Collaboration Aartsen M.G., Ackermann M., et al., 2018, *Science*, 361, 147
- Ingram A., van der Klis M., 2013, *MNRAS*, 434, 1476
- Jackson J.D., Gove H.E., Schwitters R.F., 1981, *Annual Review of Nuclear and Particle Science*. Volume 31.

- Jaffe W., Meisenheimer K., Röttgering H.J.A., et al., 2004, *Nature*, 429, 47
- Jansen F., Lumb D., Altieri B., et al., 2001, *A&A* p, 365, L1
- Järvelä E., Lähteenmäki A., Lietzen H., et al., 2017, *A&A*, 606, A9
- Joshi M., Böttcher M., 2011, *ApJ*, 727, 21
- Junor W., Biretta J.A., 1995, *AJ*, 109, 500
- Kadler M., Krauß F., Mannheim K., et al., 2016, *Nature Physics*, 12, 807
- Kalberla P.M.W., Burton W.B., Hartmann D., et al., 2005, *A&A*, 440, 775
- Kammoun E.S., Nardini E., Risaliti G., et al., 2017, *ArXiv e-prints*,
- Kapanadze B., Dorner D., Vercellone S., et al., 2016, *MNRAS*, 461, L26
- Kara E., Fabian A.C., Cackett E.M., et al., 2013, *MNRAS*, 434, 1129
- Karamanavis V., Angelakis E., Komossa S., et al., 2017, In: *Proceedings of the IAU Symposium No. 324: New Frontiers in Black Hole Astrophysics*
- Kaspi S., Smith P.S., Netzer H., et al., 2000, *ApJ*, 533, 631
- Kataoka J., Stawarz Ł., Aharonian F., et al., 2006, *ApJ*, 641, 158
- Kaufman J., Blaes O.M., Hirose S., 2018, *MNRAS*, 476, 5548
- Kellermann K.I., Condon J.J., Kimball A.E., et al., 2016, *ApJ*, 831, 168
- Kellermann K.I., Sramek R., Schmidt M., et al., 1989, *AJ*, 98, 1195
- Kikuchi S., Mikami Y., 1987, *PASJ*, 39, 237
- Kirk J.G., Giacinti G., 2017, *Physical Review Letters*, 119, 211101
- Kistler M.D., Stanev T., Yüksel H., 2014, *Phys. Rev. D*, 90, 123006
- Komissarov S.S., 2001, *MNRAS*, 326, L41
- Komissarov S.S., 2005, *MNRAS*, 359, 801
- Komossa S., Voges W., Xu D., et al., 2006, *AJ*, 132, 531
- Kotera K., Olinto A.V., 2011, *ARA&A*, 49, 119
- Kovalev Y.Y., Lister M.L., Homan D.C., Kellermann K.I., 2007, *ApJ*, 668, L27
- Krauss F., 2016, Ph.D. thesis, Dr Remeis Observatory; [ECAP/FAU <EMAIL>Felicia.Krauss@fau.de</EMAIL>](mailto:Felicia.Krauss@fau.de)
- Krauß F., Kadler M., Mannheim K., et al., 2014, *A&A*, 566, L7
- Krauß F., Kreter M., Müller C., et al., 2018, *A&A*, 610, L8
- Krauß F., Müller C., Kadler M., et al., 2013, In: *Conference Proceedings, "11th European VLBI Network Symposium & Users Meeting"*, arXiv:1301.5198
- Krauß F., Wilms J., Kadler M., et al., 2016, *A&A*, 591, A130
- Krawczynski H., Hughes S.B., Horan D., et al., 2004, *ApJ*, 601, 151
- Kreikenbohm A., 2013, *Master's thesis*, Julius-Maximilians University Würzburg
- Kreikenbohm A., Schulz R., Kadler M., et al., 2016, *A&A*, 585, A91
- Krivonos R., Tsygankov S., Revnivtsev M., et al., 2010, *A&A*, 523, A61
- Krolik J.H., 2007, *ApJ*, 661, 52
- Krumpe M., Lamer G., Corral A., et al., 2008, *A&A*, 483, 415
- Kunert-Bajraszewska M., Labiano A., Siemiginowska A., Guainazzi M., 2014, *MNRAS*, 437, 3063
- Laor A., 2000, *ApJ*, 543, L111
- Larsson J., D'Ammando F., Falocco S., et al., 2018, *MNRAS*, 476, 43
- Lawrence A., 1991, *MNRAS*, 252, 586
- Lawrence A., 2012, *MNRAS*, 423, 451
- Liaw A., Wiener M., 2002, *R News*, 2/3, 18
- Lister M.L., Aller M.F., Aller H.D., et al., 2018, *ApJS*, 234, 12
- Lister M.L., Aller M.F., Aller H.D., et al., 2013, *AJ*, 146, 120
- Lister M.L., Aller M.F., Aller H.D., et al., 2016, *ApJ*, 152, 12
- Lister M.L., Homan D.C., 2005, *AJ*, 130, 1389
- Liu Q.Z., van Paradijs J., van den Heuvel E.P.J., 2006, *A&A*, 455, 1165
- Liu Q.Z., van Paradijs J., van den Heuvel E.P.J., 2007, *A&A*, 469, 807
- Lo K.K., Farrell S., Murphy T., Gaensler B.M., 2014, *ApJ*, 786, 20
- Longair M.S., 2011, *High Energy Astrophysics*
- Lu F.J., Aschenbach B., 2000, *A&A*, 362, 1083
- Lucarelli F., Pittori C., Verrecchia F., et al., 2017, *ApJ*, 846, 121
- Lusso E., Risaliti G., 2016, *ApJ*, 819, 154
- Lyubarskii Y.E., 1997, *MNRAS*, 292, 679
- Lyubarsky Y., 2011, *Phys. Rev. E*, 83, 016302
- Lyutikov M., Blandford R., 2003, *ArXiv Astro-*

- physics e-prints,
 Lyutikov M., Komissarov S., Sironi L., 2018, *Journal of Plasma Physics*, 84, 635840201
 Lyutikov M., Lister M., 2010, *ApJ*, 722, 197
 Magnelli B., Lutz D., Santini P., et al., 2012, *A&A*, 539, A155
 Mannheim K., 1993, *AAP*, 269, 67
 Mannheim K., 1995, *Astroparticle Physics*, 3, 295
 Maraschi L., Fossati G., Tavecchio F., et al., 1999, *ApJ*, 526, L81
 Maraschi L., Ghisellini G., Celotti A., 1992a, *ApJl*, 397, L5
 Maraschi L., Ghisellini G., Celotti A., 1992b, *ApJ*, 397, L5
 Markowitz A., Edelson R., Vaughan S., et al., 2003, *ApJ*, 593, 96
 Markowitz A.G., Krumpke M., Nikutta R., 2014, *MNRAS*, 439, 1403
 Markowitz A.G., Reeves J.N., 2009, *ApJ*, 705, 496
 Marscher A.P., 2006, *Astronomische Nachrichten*, 327, 217
 Marscher A.P., 2014, *ApJ*, 780, 87
 Marscher A.P., Gear W.K., 1985, *ApJ*, 298, 114
 Marscher A.P., Jorstad S.G., Larionov V.M., et al., 2010, *ApJl*, 710, L126
 Marscher, A. P. in Belloni T., 2009, *Lect. Notes Phys.*, 794
 Martín J., Torres D.F., Rea N., 2012, *MNRAS*, 427, 415
 Massaro E., Perri M., Giommi P., Nesci R., 2004a, *A&A*, 413, 489
 Massaro E., Perri M., Giommi P., et al., 2004b, *A&A*, 422, 103
 Massaro E., Tramacere A., Perri M., et al., 2006, *A&A*, 448, 861
 Massaro F., D’Abrusco R., Paggi A., et al., 2013, *ApJS*, 209, 10
 Mastichiadis A., Petropoulou M., Dimitrakoudis S., 2013, *MNRAS*, 434, 2684
 Mastroserio G., Ingram A., van der Klis M., 2018, *MNRAS*, 475, 4027
 Mathur S., 2000, *MNRAS*, 314, L17
 Matt G., Perola G.C., Piro L., 1991, *A&A*, 247, 25
 Mattox J.R., Bertsch D.L., Chiang J., et al., 1996, *ApJ*, 461, 396
 Mattox J.R., Schachter J., Molnar L., et al., 1997, *ApJ*, 481, 95
 McConville W., Ostorero L., Moderski R., et al., 2011, *ApJ*, 738, 148
 McKinney J.C., 2006, *MNRAS*, 368, 1561
 McKinney J.C., Tchekhovskoy A., Blandford R.D., 2012, *MNRAS*, 423, 3083
 Mehdipour M., Branduardi-Raymont G., Kaastra J.S., et al., 2011, *A&A p*, 534, A39
 Meier D.L., 2012, *Black Hole Astrophysics: The Engine Paradigm*
 Migliori G., Siemiginowska A., Sobolewska M., et al., 2016, *ApJ*, 821, L31
 Mirabal N., Frías-Martinez V., Hassan T., Frías-Martinez E., 2012, *MNRAS*, 424, L64
 Mirabel I.F., Rodríguez L.F., 1994, *Nature*, 371, 46
 Mirabel I.F., Rodríguez L.F., 1999, *Annual Review of Astronomy and Astrophysics*, 37, 409
 Mitsuda K., Bautz M., Inoue H., et al., 2007, *PASJ*, 59, S1
 Mücke A., Protheroe R.J., Engel R., et al., 2003a, *Astroparticle Physics*, 18, 593
 Mücke A., Protheroe R.J., Engel R., et al., 2003b, *Astroparticle Physics*, 18, 593
 Mukai K., 2017, *PASP*, 129, 062001
 Müller C., 2014, *Ph.D. thesis, PhD Thesis, Friedrich-Alexander-Universität Erlangen-Nürnberg*, 2014
 Müller C., Burd P.R., Schulz R., et al., 2016a, *A&A p*, 593, L19
 Müller C., Burd P.R., Schulz R., et al., 2016b, *A&A*, 593, L19
 Müller C., Kadler M., Ojha R., et al., 2018, *A&A*, 610, A1
 Müller C., Kadler M., Ojha R., et al., 2011, *A&A*, 530, L11
 Müller C., Krauß F., Dauser T., et al., 2015, *A&A p*, 574, A117
 Nandra K., George I.M., Mushotzky R.F., et al., 1997, *ApJ*, 476, 70
 Narayan R., Yi I., 1995a, *ApJ*, 444, 231
 Narayan R., Yi I., 1995b, *ApJ*, 452, 710
 Neeser M.J., Eales S.A., Law-Green J.D., et al., 1995, *ApJ*, 451, 76
 Neininger N., 1992, *A&A*, 263, 30
 Neronov A., Semikoz D., Taylor A.M., 2012, *A&A*, 541, A31
 Netzer H., 2015, *ARA&A*, 53, 365
 Nolan P.L., Abdo A.A., Ackermann M., et al.,

- 2012, *ApJs*, 199, 31
- Nowak M.A., Wilms J., Heinz S., et al., 2005, *ApJ*, 626, 1006
- O’Dea C.P., 1998, *PASP*, 110, 493
- Ohm S., Hoischen C., 2018, *MNRAS*, 474, 1335
- Ojha R., Kadler M., Böck M., et al., 2010, *A&A*, 519, A45
- Oshlack A.Y.K.N., Webster R.L., Whiting M.T., 2001, *ApJ*, 558, 578
- Osterbrock D.E., Pogge R.W., 1985, *ApJ*, 297, 166
- Padovani P., Alexander D.M., Assef R.J., et al., 2017, *A&A Rev.*, 25, 2
- Padovani P., Ghisellini G., Fabian A.C., Celotti A., 1993, *MNRAS*, 260, L21
- Padovani P., Giommi P., Resconi E., et al., 2018, *MNRAS*, 480, 192
- Padovani P., Resconi E., 2014, *MNRAS*, 443, 474
- Paerels F.B.S., Kahn S.M., 2003, *ARA&A*, 41, 291
- Paliya V.S., Ajello M., Rakshit S., et al., 2018, *ApJ*, 853, L2
- Paliya V.S., Sahayanathan S., Parker M.L., et al., 2014, *ApJ*, 789, 143
- Paliya V.S., Stalin C.S., Shukla A., Sahayanathan S., 2013, *ApJ*, 768, 52
- Papitto A., Torres D.F., Li J., 2014, *MNRAS*, 438, 2105
- Paradijs J.v., Kouveliotou C., Wijers R.A.M.J., 2000, *Annual Review of Astronomy and Astrophysics*, 38, 379
- Pelletier G., Pudritz R.E., 1992, *ApJ*, 394, 117
- Penrose R., 1969, *Nuovo Cimento Rivista Serie*, 1
- Peterson B.M., 2009, In: Cepa J. (ed.) *The Emission-Line Universe*, 138
- Peterson B.M., Ferrarese L., Gilbert K.M., et al., 2004, *ApJ*, 613, 682
- Peterson B.M., Wandel A., 2000, *ApJ*, 540, L13
- Petropoulou M., Coenders S., Dimitrakoudis S., 2016, *Astroparticle Physics*, 80, 115
- Petropoulou M., Dimitrakoudis S., Padovani P., et al., 2015, *MNRAS*, 448, 2412
- Petrov L., Mahony E.K., Edwards P.G., et al., 2013, *MNRAS*, 432, 1294
- Pian E., Tuerler M., Fiacchi M., et al., 2013, *ArXiv e-print:1307.0558*, in press *A&A*,
- Pian E., Türler M., Fiacchi M., et al., 2014, *A&A*, 570, A77
- Piner B.G., Edwards P.G., 2005, *ApJ*, 622, 168
- Piner B.G., Pant N., Edwards P.G., 2010, *ApJ*, 723, 1150
- Piner B.G., Unwin S.C., Wehrle A.E., et al., 1999, *New A Rev.*, 43, 711
- Piran T., 2004, *Reviews of Modern Physics*, 76, 1143
- Pires A.M., Motch C., Turolla R., et al., 2015, *A&A*, 583, A117
- Planck CollaborationAbergel A., Ade P.A.R., et al., 2014, *ApJ*, 571, A11
- Potter W.J., 2018, *MNRAS*, 473, 4107
- Punch M., Akerlof C.W., Cawley M.F., et al., 1992, *Nature*, 358, 477
- Punsly B., 2001, *Black hole gravitohydrodynamics*
- Randall K.E., Hopkins A.M., Norris R.P., Edwards P.G., 2011, *MNRAS*, 416, 1135
- Rani B., Krichbaum T.P., Fuhrmann L., et al., 2013, *A&A*, 552, A11
- Ray P.S., Abdo A.A., Parent D., et al., 2012, *ArXiv e-prints*,
- Read A.M., Guainazzi M., Sembay S., 2014, *A&A*, 564, A75
- Rees M.J., 1966, *Nature*, 211, 468
- Rees M.J., Gunn J.E., 1974, *MNRAS*, 167, 1
- Reimer A., 2012, *Int. J. Mod. Phys. Conf. S.*, 355, 012011
- Reynolds S.P., 2008, *Annual Review of Astronomy and Astrophysics*, 46, 89
- Richards J.W., Starr D.L., Butler N.R., et al., 2011, *ApJ*, 733, 10
- Richter S., Spanier F., 2016, *ApJ*, 829, 56
- Rivers E., Markowitz A., Duro R., Rothschild R., 2012, *ApJ*, 759, 63
- Rivers E., Markowitz A., Rothschild R., 2013, *ApJ*, 772, 114
- Roming P.W.A., Kennedy T.E., Mason K.O., et al., 2005, *SSR*, 120, 95
- Rosen S.R., Webb N.A., Watson M.G., et al., 2016, *A&A*, 590, A1
- Rybicki G.B., Lightman A.P., 1986, *Radiative Processes in Astrophysics*
- Sahakyan N., Baghmanyan V., Zargaryan D., 2018, *ArXiv e-prints*,
- Saito S., Stawarz L., Tanaka Y.T., et al., 2013, *ApJ*, 766, L11
- Salamon M.H., Stecker F.W., 1994, *ApJ*, 430,

- L21
- Salpeter E.E., 1964, *ApJ*, 140, 796
- Salvato M., Buchner J., Budavári T., et al., 2018, *MNRAS*, 473, 4937
- Sambruna R.M., Gambill J.K., Maraschi L., et al., 2004, *ApJ*, 608, 698
- Schlegel D.J., Finkbeiner D.P., Davis M., 1998, *ApJ*, 500, 525
- Schmitt H.R., Donley J.L., Antonucci R.R.J., et al., 2003, *ApJ*, 597, 768
- Schulz R., Kreikenbohm A., Kadler M., et al., 2016, *A&A*, 588, A146
- Seward F.D., Charles P.A., 2010, *Exploring the X-ray Universe*
- Seyfert C.K., 1943, *ApJ*, 97, 28
- Shakura N.I., Sunyaev R.A., 1973, *A&A*, 24, 337
- Shang Z., Brotherton M.S., Green R.F., et al., 2005, *ApJ*, 619, 41
- Shen Y., Ho L.C., 2014, *Nature*, 513, 210
- Shi Y., Helou G., Armus L., 2013, *ApJ*, 777, 6
- Shibata K., Uchida Y., 1985, *PASJ*, 37, 31
- Shukla A., Chitnis V.R., Vishwanath P.R., et al., 2012, *A&A*, 541, A140
- Shukla A., Mannheim K., Patel S.R., et al., 2018, *ApJ*, 854, L26
- Siemiginowska A., LaMassa S., Aldcroft T.L., et al., 2008, *ApJ*, 684, 811
- Siemiginowska A., Sobolewska M., Migliori G., et al., 2016, *ApJ*, 823, 57
- Sikora M., Begelman M.C., Rees M.J., 1994, *ApJ*, 421, 153
- Simpson C., 2005, *MNRAS*, 360, 565
- Sin J., 2017, Bachelor thesis, Julius-Maximilians-Universität Würzburg
- Sinha A., Shukla A., Misra R., et al., 2015, *A&A*, 580, A100
- Snowden S.L., Freyberg M.J., Plucinsky P.P., et al., 1995, *ApJ*, 454, 643
- Sobolewska M.A., Siemiginowska A., Kelly B.C., Nalewajko K., 2014, *ApJ*, 786, 143
- Sobolewska M.A., Siemiginowska A., Życki P.T., 2004, *ApJ*, 617, 102
- Spada M., Ghisellini G., Lazzati D., Celotti A., 2001, *MNRAS*, 325, 1559
- Stanev T., 2004, *High energy cosmic rays*
- Stanghellini C., 2003, *PASA*, 20, 118
- Steffen A.T., Strateva I., Brandt W.N., et al., 2006, *AJ*, 131, 2826
- Stetson P.B., 1996, *PASP*, 108, 851
- Strohmer T.E., Watts A.L., 2005, *ApJ*, 632, L111
- Strohmer T.E., Zhang W., Swank J.H., et al., 1996, *ApJ*, 469, L9
- Su M., Slatyer T.R., Finkbeiner D.P., 2010, *ApJ*, 724, 1044
- Sulentic J.W., Zamfir S., Marziani P., et al., 2003, *ApJL*, 597, L17
- Sutherland W., Saunders W., 1992, *MNRAS*, 259, 413
- Takata J., Li K.L., Leung G.C.K., et al., 2014, *ApJ*, 785, 131
- Tanihata C., Takahashi T., Kataoka J., Madejski G.M., 2003, *ApJ*, 584, 153
- Tavani M., Barbiellini G., Argan A., et al., 2008, *Nuclear Instruments and Methods in Physics Research A*, 588, 52
- Tavani M., Bulgarelli A., Piano G., et al., 2009, *Nature*, 462, 620
- Tavecchio F., Ghisellini G., 2008, *MNRAS*, 385, L98
- Tavecchio F., Ghisellini G., 2015, *MNRAS*, 451, 1502
- Tavecchio F., Ghisellini G., Bonnoli G., Ghirlanda G., 2010, *MNRAS*, 405, L94
- Taylor G.B., Healey S.E., Helmboldt J.F., et al., 2007, *ApJ*, 671, 1355
- Tchekhovskoy A., Narayan R., McKinney J.C., 2010, *ApJ*, 711, 50
- Tchekhovskoy A., Narayan R., McKinney J.C., 2011, *MNRAS*, 418, L79
- Thompson D.J., 2010, *Astrophysics and Space Sciences Transactions*, 6, 59
- Tingay S.J., de Kool M., 2003, *AJ*, 126, 723
- Titarchuk L., 1994, *ApJ*, 434, 570
- Tombesi F., Sambruna R.M., Marscher A.P., et al., 2012, *MNRAS*, 424, 754
- Torres D.F., Reucroft S., Reimer O., Anchordoqui L.A., 2003, *ApJ*, 595, L13
- Tramacere A., Giommi P., Perri M., et al., 2009, *A&A*, 501, 879
- Tramacere A., Massaro F., Cavaliere A., 2007, *A&A*, 466, 521
- Treister E., Urry C.M., Virani S., 2009, *ApJ*, 696, 110
- Turner T.J., Romano P., George I.M., et al., 2001, *ApJ*, 561, 131
- Uchida Y., Shibata K., 1985, *PASJ*, 37, 515

- Ulmer A., 1999, *ApJ*, 514, 180
- Ulrich M.H., Kinman T.D., Lynds C.R., et al., 1975, *ApJ*, 198, 261
- Urry C.M., Padovani P., 1995, *PASP*, 107, 803
- Uttley P., Cackett E.M., Fabian A.C., et al., 2014, *A&A Rev.*, 22, 72
- Uttley P., McHardy I.M., Papadakis I.E., 2002, *MNRAS*, 332, 231
- Vaughan S., Edelson R., Warwick R.S., Uttley P., 2003a, *MNRAS*, 345, 1271
- Vaughan S., Fabian A.C., Nandra K., 2003b, *MNRAS*, 339, 1237
- Vaughan S., Reeves J., Warwick R., Edelson R., 1999, *MNRAS*, 309, 113
- Vermeulen R.C., Ogle P.M., Tran H.D., et al., 1995, *ApJ*, 452, L5
- Verner D.A., Ferland G.J., Korista K.T., Yakovlev D.G., 1996, *ApJ*, 465, 487
- Véron-Cetty M.P., Véron P., 2010, *A&A*, 518, A10
- Vink J., 2012, *A&A Rev.*, 20, 49
- Voges W., Aschenbach B., Boller T., et al., 1999, *A&A*, 349, 389
- Wagner S.J., Witzel A., 1995a, *ARA&A*, 33, 163
- Wagner S.J., Witzel A., 1995b, *Annu. Rev. Astron. Astrophys.*, 33, 163
- Wang J., 2015, *New A*, 37, 15
- Wang J.M., Luo B., Ho L.C., 2004, *ApJ*, 615, L9
- Weekes T.C., 2003, Very high energy gamma-ray astronomy
- Weekes T.C., Cawley M.F., Fegan D.J., et al., 1989, *ApJ*, 342, 379
- Weidinger M., Spanier F., 2015, *A&A*, 573, A7
- Weisskopf M.C., Brinkman B., Canizares C., et al., 2002, *PASP*, 114, 1
- White N.E., Zhang W., 1997, *ApJ*, 490, L87
- Wilms J., Allen A., McCray R., 2000, *ApJ*, 542, 914
- Winkler C., Courvoisier T.J.L., Di Cocco G., et al., 2003, *A&A*, 411, L1
- Wolter H., 1952, *Annalen der Physik*, 445, 94
- Wright A., Otrupcek R., 1990, In: *PKS Catalog (1990)*
- Yamazaki R., Ioka K., Nakamura T., 2004, *ApJ*, 607, L103
- Yao S., Yuan W., Zhou H., et al., 2015, *MNRAS*, 454, L16
- Yuan W., Zhou H.Y., Komossa S., et al., 2008, *ApJ*, 685, 801
- Zatsepin G.T., Kuz'min V.A., 1966, *Soviet Journal of Experimental and Theoretical Physics Letters*, 4, 78
- Zech A., Cerruti M., Mazin D., 2017, *A&A*, 602, A25
- Zhang H., Diltz C., Böttcher M., 2016, *ApJ*, 829, 69
- Zhou H., Wang T., Yuan W., et al., 2007, *ApJ*, 658, L13
- Zhou H.Y., Wang T.G., Dong X.B., et al., 2003, *ApJ*, 584, 147
- Zhou X.L., Zhang S.N., 2010, *ApJ*, 713, L11
- Zhu Q., Yan D., Zhang P., et al., 2016, *MNRAS*, 463, 4481
- Zhu Z., Stone J.M., 2018, *ApJ*, 857, 34

List of Figures

1.1.	Cosmic ray particle spectrum (Kotera & Olinto 2011). The spectrum covers more than 8 orders of magnitude in energy and more than 24 orders of flux. A transition from Galactic to extragalactic cosmic rays is thought to be somewhere between $(10^{15} - 10^{18})$ eV.	6
2.1.	Sky map of X-ray sources in Galactic coordinates and Hammer-Aitoff projection as observed by the <i>ROSAT</i> all-sky survey in the (0.1-2.4) keV range. <i>Top</i> : Distribution of diffuse emission (Credit: X-ray group at MPE, Germany). Colors represent the spectral shape from red (soft spectra) to blue (hard spectra). <i>Bottom</i> : Distribution of point sources in the Second <i>ROSAT</i> X-ray Source Catalog (2RXS, Boller et al. 2016). Color-code as in the top panel. The size of the point source symbols corresponds to the count rate. A large number of bright individual sources with hard spectra are found in the Galactic plane, indicating that at least part of the hard diffuse emission is induced by unresolved point sources (e.g., XRB). A large number of hard but faint sources are spread isotropically across the entire sky, produced by extragalactic objects (e.g., AGN). See text for more information.	11
2.2.	ROSAT image of two supernova remnants: the larger one is the Vela SNR at a distance of roughly 1,500 light years, and a smaller one, the Puppis SNR which is farther away from the sun and is visible as bright spot in the upper right corner. Image credit: Max-Planck-Institute for extraterrestrial physics (MPE), Germany.	12
2.3.	Full sky maps of the γ -ray sky observed with <i>Fermi</i> -LAT averaged over 7 years. Colors represent the photon flux from blue (low) to yellow (high). <i>Top panel</i> : shows the photon distribution for energies above 10 GeV (Ajello et al. 2017). <i>Bottom panel</i> : shows the same for hard energies between 50 GeV – 2 TeV (Ackermann et al. 2016).	13
2.4.	Full sky map of γ -ray sources in the Third <i>Fermi</i> -LAT source catalog (3FGL, Acero et al. 2015). See text for more information.	14
2.5.	Full sky map of VHE sources in the TeV catalog (TeVCat). See text for more information.	15
2.6.	Pulse profiles of the <i>Fermi</i> -LAT sources PSR J1709–4429 (top) and PSR J1952+3252 (bottom) for the full energy band above 0.1 GeV (Abdo et al. 2010d). Two pulsar rotation cycles are shown, and the fitting functions (thick solid lines) are superimposed on the light curves in the first cycle.	18

-
- 2.7. First nova explosion detected at γ -rays from the symbiotic system V407 Cyg Abdo et al. (2010b). *Left panel:* γ -ray, optical R and V band, and X-ray light curves. The vertical lines marks the epoch of the optical nova detection. Correlated variability between the γ -ray and optical band confirmed the nova counterpart which was prior found via positional coincidence. *Middle panel:* *Fermi*-LAT 0.2–100 GeV spectrum of the γ -ray flare. The spectrum can be π^0 decay due to proton-proton interaction of shocked gas in the dense ambient medium or inverse Compton emission of electrons with the radiation of the companion star. X-rays are interpreted as thermal emission as a reaction to shock heating of the ambient medium. *Right panel:* *Fermi*-LAT γ -ray count map of the region around V407 Cyg averaged over 19 days after the nova optical explosion. The 'x' marks the position of V407 Cyg. The closest known γ -ray source is marked with a circle in an angular distance of $\sim 1.5^\circ$ 19
- 3.1. Schematic picture of an AGN. The scheme is highly simplified and relative sizes of individual components are not to scale. A SMBH in the center is surrounded by a rotating accretion disk. The combination of these components can launch a relativistic jets which is highly collimated. An X-ray corona, BLR, and NLR clouds are located above the disk, although their structure and distribution are still debated. A cold dense distribution of dust called torus obscures the central engine with large covering factors. Emission from the central regions can be reprocessed through scattering and Compton reflection. See text for more information on each component and the unified model of AGN. 32
- 3.2. The optical HST image of the radio galaxy Centaurus A. The overlay of the radio emission shows a two-sided kpc scale structure of a powerful relativistic jet. Very long baseline interferometry allows to study jets on milliarcsecond resolution. The radio-structure of the highly collimated subparsec-scale jet of Cen A is shown in the inset images (Müller et al. 2011). 34
- 3.3. The blazar sequence refers to a correlation of the bolometric luminosity and synchrotron peak frequencies in the stationary broadband SED of blazars (Fossati et al. 1998). Also shown are three SEDs of γ -ray emitting non-blazars, Centaurus A, M 87, and NGC 6251, which show a similar spectral shape of their jet emission. The image taken from Ghisellini et al. (2005). 35
- 3.4. Radio loudness as a function of AGN black hole mass. *Left panel* shows a sample of broad-line AGN (Laor 2000). The parameter space occupied by NLS1 is shown in the *right panel* (Järvelä et al. 2017). 36
- 3.5. Illustration of emission component in the spectral energy distribution (SED) of jetted and non-jetted AGN. From Padovani et al. (2017), Fig. 1. 40

3.6.	Multiwavelength behaviour of the FSRQ PKS 2142–75 observed in 2011 (Dutka et al. 2013). <i>Left:</i> Long-term light curve in γ -ray and optical bands as observed with <i>Fermi</i> -LAT and SMARTS. The highlighted regions mark two γ -ray flaring events and one quiescent state showing different patterns of correlated emission. <i>Right:</i> Spectral energy distributions show very distinct shapes during the two γ -ray flaring states (blue and black points) and quiescent (red) periods.	43
3.7.	Timing signatures from an internal shock model in blazars (Böttcher & Dermer 2010). The leptonic model includes synchrotron and SSC emission. High-energy photons are generated by IC scattering of relativistic photons with an external photon field. <i>Left:</i> Snapshot SEDs of the blazar flare at different time-steps. Solid curves show the SED resulting from averaging over an integration time of 30 ksec, representative of typical deep X-ray observation of a blazar. Dotted vertical lines indicate frequencies (R-band, 1 keV, 1 MeV, 100 MeV) at which light curves were extracted. <i>Right:</i> Light curves of the blazar flares at various energies resulting from the internal shock model. Images taken from Böttcher & Dermer (2010)	46
3.8.	Example of the density structure in a turbulent thin accretion disk with a net vertical magnetic field from MHD simulations for CVs or proto-planetary disks (Zhu & Stone 2018). Magnetic flux diffusion and turbulence cause a filamentation of the disk surface and are capable of launching disk winds above the accretion disk corona.	47
3.9.	GRMHD simulations by Tchekhovskoy et al. (2011) of a magnetically launched relativistic jet for a maximally rotating SMBH. <i>Panels a–d:</i> equatorial ($z = 0$, top rows) and meridional ($y = 0$, bottom rows) snapshots of the accretion flow at different points in time. The rest-mass density is indicated with color (red for high and blue for low values). Filled black circles shows the BH horizon, and black lines show magnetic field lines in the image plane. <i>Panels e–g:</i> time-evolution of the accretion rate (e), magnetic flux (f), and energy outflow efficiency μ (g). red circles indicate time at which snapshots were taken.	48
4.1.	Comparison of the effective area for different X-ray satellite and instruments. Image credit: Beuchert (2017)	52
4.2.	Sky image observed with the EPIC pn camera. Objects at large angular distance from the optical axis are distorted.	54
4.3.	Light path of X-ray photons within the <i>XMM-Newton</i> satellite. Nested Wolter I mirrors focus X-ray photons via total reflection with a critical reflection index below $\sim 1^\circ$. Image credit: ESA / AOES Medialab	55

4.4.	<i>Left panel (a)</i> : Principle of the coded mask methods. A mask of opaque material (e.g., led) with a pattern of openings is placed in the aperture of the instrument. Gamma-ray photons that pass through the hole project a unique shadow on the detector plane. <i>Right panels</i> show examples of the different masks used for the spectrometer (<i>b</i>) and imager (<i>c</i>) on board the <i>INTEGRAL</i> satellite. Image credits: ISDC/M. Türler, SPI/IBIS Team.	57
4.5.	The FACT telescope at 2,200 m altitude on La Palma. The 9.5 m ² mirror area focuses the Cherenkov light of air shower particles in the camera with G-APD photo sensors. Image from Anderhub et al. (2013a).	61
5.1.	Simulated time series (<i>left</i>) and corresponding periodograms (<i>right</i>) by Vaughan et al. (2003a). <i>Upper panels</i> show an example of a flickering noise dominated light curve. The PSD is flat with larger power in short-term variability (high frequencies). <i>Lower panels</i> show a random walk time series (red noise term). These time series have steeper PSD with larger power in long-term variability (small frequencies). In general, the periodogram exhibits larger scatter for short-term variability.	66
6.1.	Schematic visualization of popular supervised machine learning algorithms. See Table 6.1 for further information about the algorithm.	72
6.2.	Schematic view of the training process of the supervised random forest algorithm.	74
6.3.	Generation of synthesized attribute vector in the multidimensional attribute space with the <i>k-nearest neighbour</i> method: for a given object of the minority class (blue point), five nearest neighbours (black points) are determined. The a synthetic object (red point) is generated by scaling one of the difference vectors. See text for further description.	78
7.1.	Sky distribution of <i>XMM-Newton</i> observations during pointed (green fields) and slew (blue lines) observations in Galactic coordinates. Image credit: A. Read, private communication.	84
7.2.	Distribution of the sources of the unbalanced 3XMM training (<i>left</i>) and testing (<i>right</i>) sample in Galactic coordinates.	86
7.3.	Distribution of background-subtracted spectral data counts in the 3XMM catalogue for the final training (<i>left</i>) and test sample (<i>right</i>) and divided with respect to their Galactic latitude.	88
7.4.	Unfolded example EPIC PN (black) and MOS 1 & 2 (gray) spectra for best-fits for each model. Solid lines are the best-fit model to the PN (red line) and MOS (yellow line) spectra.	90
7.5.	Importance of different source properties on the source classification using hardness ratios, spectral, and multiwavelength information with true Galactic coordinates of each detection (<i>left</i>) and with randomized positions (<i>right</i>).	94

7.6.	Histogram of Galactic source positions for the sources in the training sample. The true distributions are shown as black solid line, while the blue histogram depicts the redistributed positions of each source (see text for explanation).	95
7.7.	Histogram of Galactic source positions for each detection in the training sample. The true distributions are shown as black solid line, while the blue histogram depicts the redistributed positions of each detection drawn from the distribution of unique sources.	96
7.8.	Importance of classification features. <i>Left:</i> Training with hardness ratios only. <i>Right:</i> Training with spectral feature. All runs include source extension and Galactic coordinates.	99
7.9.	Importance of classification features. <i>Left:</i> Training with spectral and multiwavelength features. <i>Right:</i> Training with spectral, multiwavelength, and timing features. All runs include source extension and Galactic coordinates.	100
7.10.	Distribution of highest class probabilities from the spectral (blue) and timing (red) classification model. The classification results between spectral and timing model differs in a fraction of $\sim 40\%$ of sources. See Fig. 7.11 for an overview.	103
7.11.	Distribution of highest class probabilities from sources classified with the spectral model that differ from the timing model such as they either switched source type (7%, blue) or were not classified (33.5%, red). Most sources that switched source type had class probabilities only marginally higher than the second best class.	103
7.12.	Distribution of the predicted source types of 3XMM sources for spectral model in Galactic coordinates.	105
7.13.	Distribution of the predicted source types of 3XMM sources for timing model in Galactic coordinates.	105
7.14.	Background subtracted spectral data counts for EXTraS transient sources in the (0.2–12). keV energy band.	106
7.15.	Distribution of the classified transient sources in Galactic coordinates for the spectral (<i>top</i>) and timing (<i>bottom</i>) model.	109
8.1.	<i>XMM-Newton</i> spectrum and best-fit results of X-2004-04-11X-2012-05-01 (<i>left</i>) and X-2012-10-18 (<i>right</i>). <i>Upper panel:</i> EPIC pn (blue) and MOS (lightblue) data, as well as corresponding best fits for an absorbed power law evaluated over (0.5–10) keV (black solid line) and (2–10) keV (black dashed-dotted line). <i>Mid panel:</i> Data-to-model ratio for the best fit over the whole (0.5–10) keV energy range. <i>Lower panel:</i> Respective residuals for fitting the (2–10) keV energy range alone, extrapolated to lower energies. The red shaded region marks the region of a tentative soft excess in X-2004-04-11.	119

-
- 8.2. Comparison of the EPIC pn background spectra of all three *XMM-Newton* observations. No significant variation is observed that could mimic or contribute to a soft excess. 121
- 8.3. *XMM-Newton* spectrum of X-2004-04-11 with blackbody component. *Upper panel*: EPIC pn (blue) and MOS (lightblue) data, total model for an absorbed power law plus blackbody (black solid line) model components (black dashed line). *Mid panel* Data-to-model ratio for the best fit. 121
- 8.4. *XMM-Newton* spectrum of X-2012-05-01 (top) and X-2012-10-18 (bottom) with blackbody component. *Upper panel* EPIC pn (blue) and MOS (lightblue) data, total model for an absorbed power law plus blackbody (black solid line) model components (black dashed line). *Mid panel* Data-to-model ratio for the best fit. 122
- 8.5. *XMM-Newton* ratio of the *XMM-Newton* EPIC PN difference spectra to a power-law model. Difference spectra were created by subtracting the background-subtracted spectra of X-2012-05-01 (blue) and X-2012-10-18 (black) from the one of X-2004-04-11. Simple power-law fits were performed on the energy ranges (0.5–7) keV and (2.0–7) keV, where the fit to the later band was then extrapolated to lower energies. 122
- 8.6. *XMM-Newton* EPIC PN light curves for the source and background region and energies between (0.2–12) keV. Light blue and gray points depict count rates without filtering for flaring particle background. Flaring-corrected count rates are shown in blue (source region) and black (background region). Horizontal blue lines show the mean count rate of the source region (solid line) with 3σ uncertainties (dashed lines). 126
- 8.7. Long-term variation of the total absorption-corrected 0.5–10 keV flux. The gray-shaded background denotes the multiwavelength monitoring period. *XMM-Newton* data are shown as black points, *Swift* data are plotted as open blue triangles. Horizontal dashed-lines denote thresholds for the low, medium and high flux ranges. 127
- 8.8. Hardness-intensity diagram (HID): Hardness ratios $(S1-H1)/(S1+H1)$ (*top*) and $(S2-H2)/(S2+H2)$ (*bottom*) as a function of background-subtracted source count rates in the full energy band. Error bars correspond to 1-sigma uncertainties. *Left*: Results from *Swift* observations. Individual observations are shown as lightblue open symbols, while filled blue symbols denote results from merged data sets. *Right*: HID of the *XMM-Newton* data. 128

- 8.9. Hard- versus soft-band diagram (HSD): Comparison of the count rates in the soft (0.2–2) keV and hard (2–10) keV band. Error bars correspond to 1-sigma uncertainties. *Left*: Results from *Swift* observations. Individual observations are shown as lightblue open symbols, while filled blue symbols denote results from merged data sets. *Right*: HSD of the *XMM-Newton* data. Both panels show the best-fit linear regressions for low-SNR *swift* (dashed-dotted), merged high-SNR *Swift* (dashed), and *XMM-Newton* (solid) data. The combined 1σ uncertainties of all three fits are shown as orange-shaded region. 129
- 8.10. HSD derived from simulated *Swift* spectra with 5 ks exposure and power-law fluxes between $(10^{-17}\text{--}10^{-12})\text{ erg cm}^{-2}\text{ s}^{-1}$. Solid lines denote linear regressions. See text for more detailed explanation. 130
- 8.11. 68%- (red), 90%- (green), and 99%- (blue) confidence contours of the soft excess flux and the photon index of the power law continuum for the *XMM-Newton* observation in 2004. *Left panel*: Using only *XMM-Newton*/EPIC pn spectrum, the excess emission cannot be detected significantly within the sensitivity flux limit of $2 \times 10^{-15}\text{ erg s}^{-1}\text{ cm}^2$ ($\log F_{\text{SX}} = -14.7$) for the derived net exposure time of 35 ks in 2004 (*XMM-Newton* User Handbook). *Right panel*: A fit to the combined simulated *XMM-Newton* and *NuSTAR* spectra for 50 ks yields a significant detection of the soft excess component. 133
- 8.12. Spectrum of ATCA monitoring between 5.5 GHz and 40 GHz from 2011 Nov 08 to 2016 May 31. Dashed lines represent power-law fits to simultaneous observations. 134
- 8.13. Multiwavelength light curves from γ -rays (*top*) to radio (*bottom*) from 2010 until 2017. Instruments are *Fermi*-LAT, *Swift*/XRT and *XMM-Newton*/EPIC, *XMM-Newton*/OM & *Swift*/UVOT (UV filters), *XMM-Newton*/OM & *Swift*/UVOT (optical filters). Shaded regions were used for quasi-simultaneous SEDs (see text for more information). *Fermi*-LAT light curve is binned to 30 days with a significance threshold of $TS = 9$. Upper limits are shown as downward arrows. Radio, optical/UV, and X-ray data points correspond to single observations. Note that the y-axes are in logarithmic scale. 135
- 8.14. Quasi-simultaneous observed SED of PKS 2004–447 for different observing periods (see Text). Black symbols denote observed data. Gray symbols are absorption-corrected data. We also show the broadband data used by G06 in red symbols and the *Swift*/BAT upper limit (blue arrow). The SEDs are described by hand with a combination of two logarithmic parabolas affected by absorption extinction by the ISM. See table 8.8 for model parameters. The panel at the bottom right compares the used models to described the SED in each state. 138

-
- 8.15. *Left panel:* X-ray luminosity L_X in the (0.3–10) keV band as a function of photon index for γ -NLS1 galaxies in this paper (black filled symbols) and the MOJAVE 1 sample (open symbols). *Right panel:* Comparison of (0.3–10) keV X-ray luminosity L_X as a function of redshift z for the MOJAVE 1 sample (open symbols) and γ -NLS1 sources (black filled symbols) discussed in this paper. 143
- 8.16. Comparison of (0.3–10) keV X-ray luminosity L_X as a function (0.1–100) GeV luminosity L_γ of the MOJAVE 1 sample (open symbols) and γ -NLS1 sources (black filled symbols) discussed in this paper. 144
- 9.1. Schematic overview of the multiwavelength ToO program. During the combined FACT and *INTEGRAL* visibility windows, a target’s state is monitored by FACT (nightly), *Fermi*-LAT (continuously), and *Swift* (weekly). As soon as the FACT event rate exceeds the trigger threshold (red vertical line) trigger alerts are sent to *Swift*, *XMM-Newton* and *INTEGRAL*. *Swift* snapshots of 1 ks to 2 ks serve as bridge between trigger and the start of high-sensitivity observations, as well as follow-up to study the source evolution over a period of 25 days. Deep high-sensitivity pointings are performed by *XMM-Newton* and *INTEGRAL*. The combined observations from optical to TeV energies cover both the low and high-energy hump of the target’s SED. 151
- 9.2. Parsec-scale radio jet structure of Mrk 421 (Blasi et al. 2013). *Left:* VLBA image at 43 GHz from November 2011. The flux contours correspond to $(-1, 1, \sqrt{2}, 2, \dots) \times 0.55$ mJy/beam. *Right:* VLBA image from July 2011 at 43 GHz, contoured at $(-1, 1, 10, 100) \times 0.4$ mJy/beam. Overplotted are emission components (red) derived through fitting 2D Gaussian components to the data. By comparing model-fit of different observing epoch, the authors derived subluminal apparent component speeds between 0.02 c and 0.24 c. 152
- 9.3. Temporal evolution of best-fit parameters for all *Swift*/XRT observations. Color gradient depict temporal evolution (see Fig. 9.4). The color gradient encode the time information of the observation from red in 2015 to blue in 2017. 157
- 9.4. Long-term broadband light curve of Mrk 421 from December 2015 until May 2017, involving monitoring data by FACT, *Fermi*-LAT, *Swift*/BAT, *Swift*/XRT, and *Swift*/UVOT (from top to bottom panel). 158
- 9.5. Fractional variability amplitude for different energy bands calculated for the duration of the whole monitoring with *Swift*/UVOT at 2600 Å(circle), *Swift*/XRT (points) for the (0.5-2) keV (red), (2-10) keV (blue), and (0.5-10) keV energy range (black), *Fermi*-LAT (square) for (0.1-300) GeV, and FACT (left-to-right arrow) for energies above 750 GeV. 159

9.6.	Flux-flux correlations of UV (2600 Å), X-ray (0.5-10) keV, γ -ray (0.1-300) GeV, and TeV emission for visibility window VW1 (<i>left panels</i>) and visibility window VW2 (<i>right panels</i>). Color gradient depict temporal evolution (see Fig. 9.4).	161
9.7.	<i>Panels (a-f)</i> : Results for the discrete cross-correlation function for observations period MJD 57358-57550. <i>Panels (g-l)</i> : Results for the discrete cross-correlation function for observations period MJD 57717-57864.	163
9.8.	Observed light curves normalized by the maximum flux observed in a given band during the complete monitoring period. <i>Left panels</i> : zoom in on the activity in 2015 and beginning of 2016. <i>Right panels</i> : zoom in on the activity in the beginning of 2017. Shaded regions mark time frames for which simultaneous SEDs were assembled.	164
9.9.	Time-resolved SEDs from the outbursts in 2015 (S1 – S6, in red) . UV and X-ray data have been corrected for Galactic extinction and photo-absorption. Solid lines depict best-fits of a log parabolic model fitted to the UV and X-ray data.	167
9.10.	Time-resolved SEDs from the outbursts in 2017 (S7 – S11, in blue). UV and X-ray data have been corrected for Galactic extinction and photo-absorption. Solid lines depict best-fits of a log parabolic model fitted to the UV and X-ray data.	168
9.11.	Synchrotron peak position derived from the time-resolved SED fitting against the best-fit synchrotron peak flux (<i>left panel</i>), normalized fluxes in the TeV and GeV γ -ray band (<i>mid panel</i>), as well as normalized fluxes in the UV and X-ray band (<i>right band</i>). Results for the time SEDs S1 – S6 are shown in red/gray, while blue/black correspond to results of SED sets S7 – S9.	168
A.1.	Exemplary scheme of the fit process for the absorbed power-law model.	182
A.2.	Hardness diagrams for the sources of the training sample that are close to ($ b \leq 20^\circ$, top row) or farther away ($ b > 20^\circ$, bottom row) from the Galactic plane. The symbols for the sources are the same as in Fig. 7.2: AGN (red circle), CV (purple square), S1 (orange triangle top), S2 (green triangle down), STAR (grey dot), ULX (black diamonds), LMXRB (blue triangle left), HMXRB (cyan triangle right), NA/not classified (beige star).	190
A.3.	Correlation of various spectral parameters for the sources of the training sample for sources that are close ($ b \leq 20^\circ$) or farther away ($ b > 20^\circ$) from the Galactic plane. The symbols for the sources are the same as in Fig. 7.2. Plotted parameters are: EP8 flux provided by the 3XMM, flux (PL Flux) and photon index Γ of the simple power law (PL) in the (0.5–10) keV band, absorbing hydrogen column density N_{H} , backbody temperature k_{B} of the simple (BB) and complex (BB+PL) model , power law photon index of the complex models (PLPL and APPL).	191

A.4.	Multiwavelength indices as a function of the X-ray flux for the sources of the training sample that are close ($ b \leq 20^\circ$) or farther away ($ b > 20^\circ$) from the Galactic plane. The symbols for the sources are the same as in Fig. 7.2: AGN (red circle), CV (purple square), S1 (orange triangle top), S2 (green triangle down), STAR (grey dot), ULX (black diamonds), LMXRB (blue triangle left), HMXRB (cyan triangle right), NA/not classified (beige star).	192
A.5.	Correlation of various timing parameters for periodic and aperiodic variability (from WP2 and WP3) for the sources of the training sample for sources that are close ($ b \leq 20^\circ$) or farther away ($ b \geq 20^\circ$) from the Galactic plane. The symbols for the sources are the same as in Fig. 7.2.	193
A.6.	Correlation of various hardness ratios for the sources of the test sample for sources that are close ($ b \leq 20^\circ$) or farther away ($ b \geq 20^\circ$) from the Galactic plane. The classification run involves spectral information of the X-ray and broadband spectrum as well as parameters describing aperiodic and periodic variability. Information of longterm variability is not included. The symbols for the sources are the same as in Fig. 7.2.	194
A.7.	Correlation of various spectral parameters for the sources of the test sample for sources that are close ($ b \leq 20^\circ$) or farther away ($ b \geq 20^\circ$) from the Galactic plane. The classification run involves spectral information of the X-ray and broadband spectrum as well as parameters describing aperiodic and periodic variability. Information of longterm variability is not included. The symbols for the sources are the same as in Fig. 7.2.	195
A.8.	Correlation of various timing parameters (from WP2 and WP3) for the sources of the test sample for sources that are close ($ b \leq 20^\circ$) or farther away ($ b \geq 20^\circ$) from the Galactic plane. The classification run involves spectral information of the X-ray and broadband spectrum as well as parameters describing aperiodic and periodic variability. Information of longterm variability is not included. The symbols for the sources are the same as in Fig. 7.2.	196
A.9.	Hardness diagrams for transient sources. The symbols for the sources are the same as in Fig. 7.2.	196
A.10.	Correlation of various spectral parameters for transient sources. The symbols for the sources are the same as in Fig. 7.2.	197
A.11.	Correlation of the fractional variability amplitude and average count rate for transient sources. The symbols for the sources are the same as in Fig. 7.2.	197
B.1.	Comparison of FACT and <i>Fermi</i> -LAT light curves normalized to the maximum flux observed in the shown time range for visibility window 1 (<i>left</i>) and 2 (<i>right</i>).	213
B.2.	Comparison of FACT and <i>Swift</i> /XRT light curves normalized to the maximum flux observed in the shown time range for visibility window 1 (<i>left</i>) and 2 (<i>right</i>).	213

B.3.	Comparison of <i>Fermi</i> -LAT and <i>Swift</i> /XRT light curves normalized to the maximum flux observed in the shown time range for visibility window 1 (<i>left</i>) and 2 (<i>right</i>).	213
B.4.	Comparison of <i>Fermi</i> -LAT and <i>Swift</i> /UVOT light curves normalized to the maximum flux observed in the shown time range for visibility window 1 (<i>left</i>) and 2 (<i>right</i>).	214
B.5.	Comparison of <i>Swift</i> /XRT and <i>Swift</i> /UVOT light curves normalized to the maximum flux observed in the shown time range for visibility window 1 (<i>left</i>) and 2 (<i>right</i>).	214
B.6.	Results for the discrete cross-correlation function for observations period T1 MJD 57358-57500 (<i>left</i>) and period T2 MJD 57420-57550 (<i>right</i>).	215
B.7.	Results for the discrete cross-correlation function for observations period T3 MJD 57717-57770 and T4 MJD 57770-57864 (<i>right</i>).	216
C.1.	Full-sky 2D map of the density distribution. The map is an Aitoff projection covering distances from 0 to 600 pc.	228

List of Tables

2.1. List of most commonly detected high-energy source types divided in galactic and extragalactic origin.	20
3.1. The AGN zoo: list of AGN types.	39
6.1. Basic description of popular algorithms in supervised machine learning . .	71
6.2. Data set for example classification of X-ray spectra in absorbed AGN. . .	75
6.3. G_{ini} indices splitting the example data set	76
7.1. Break down of the training sample.	86
7.2. Break down of the balanced training sample.	87
7.3. Energy bands of the 3XMM-DR6 hardness ratio	88
7.4. Spectral models used for automated fitting.	89
7.5. Specification of the multiwavelength indices.	92
7.6. Final list of classification features.	98
7.7. Confusion matrix for different training runs.	101
7.8. Class prediction for the test sample using the spectral model.	102
7.9. Class prediction for the test sample using the timing model.	104
7.10. Difference matrix for classification with and without timing features. . .	104
7.11. Distribution of transients per class and classification model.	107
7.12. List of predicted class probabilities from the timing model, for EXTraS transients euqally classified in the spectral and timing model.	107
7.12. continued	108
7.13. Difference matrix for classification with spectral and timing model. . . .	110
8.1. Details of all <i>XMM-Newton</i> and <i>Swift</i> observations of PKS 2004–447. . .	117
8.2. Best-fit results of the absorbed power-law model for <i>XMM-Newton</i> and <i>Swift</i> spectra.	123
8.3. Results of the absorbed broken power-law model for <i>XMM-Newton</i> spec- tra.	124
8.4. Results of the black body and power-law model for <i>XMM-Newton</i> spectra. . .	124
8.5. Power-law fit of the <i>XMM-Newton</i> EPIC PN difference spectra.	124
8.6. Results from the linear regression to the HSD.	131
8.7. Fractional variability amplitude for different frequency bands	137
8.8. SED model parameters* of PKS 2004–447	140
8.9. Overview of X-ray spectral properties of γ -ray emitting and radio-loud NLS1 galaxies.	145

9.1. Combined visibility windows of FACT, <i>INTEGRAL</i> and <i>Swift</i> for all targets.	149
9.2. Overview of accepted proposals for the blazar monitoring program	149
9.3. Power-law fits to <i>Fermi</i> -LAT (0.1-300) GeV spectra	155
9.4. Overview of different time interval selections.	160
9.5. Flux-Flux Correlation Coefficients	162
9.6. Best-fit of the time-resolved UV to X-ray SEDs.	166
A.1. Spectral models used for automated fitting.	183
A.2. Initial parameter values for the absorbed power-law model.	183
A.3. Initial parameter values for the absorbed blackbody model.	184
A.4. Initial parameter values for the absorbed thermal model.	185
A.5. List of all classification features extracted in this analysis.	186
A.5. continued	187
A.5. continued	188
A.5. continued	189
A.6. Properties of EXTraS transient sources.	198
A.6. continued	199
A.6. continued	200
A.6. continued	201
A.6. continued	202
A.6. continued	203
A.7. List of predicted class probabilities from the spectral model, for EXTraS transients with unreliable timing properties.	204
A.7. continued	205
A.8. Differences between classified EXTraS transients between the spectral and timing model prediction.	205
A.8. continued	206
B.1. Best-fit results for a log parabolic model for <i>Swift</i> /XRT observations. . .	207
B.1. continued	208
B.1. continued	209
B.1. continued	210
B.1. continued	211
B.1. continued	212

Acknowledgement

Over the course of my PhD, there were many people that supported me in one way or the other. I am thankful for any direct or indirect support and company which has led to this thesis. First of all, my sincere thanks go to my supervisors Prof. Dr. Matthias Kadler at Würzburg University and Prof. Dr. Jörn Wilms at Remeis Observatory Bamberg (Erlangen-Nürnberg University), who offered me the opportunity to do my PhD in their groups, to present my work at various international conferences and workshops and who shared their fascination with science with me. It has been a great pleasure for me to be part of their groups.

I also want to thank Prof. Dr. Karl Mannheim (Würzburg University) for his support and advice since my first days during my masters when I started working in the Chair of Astronomy. I am also grateful for his support for my traineeship at the European Space Agency which introduce me to numerous inspiring persons working in science and the space industry.

I am very happy to have had such a wonderful mentor Dr. Maria Diaz-Trigo during the career program »women in science«. Special thanks for the inspiring discussions and insights in both science and science operations at ESO and ESAC.

It has been a great pleasure to learn from Prof. Dr. Manel Perucho who shared his theoretical knowledge and Spanish coolness during various summers at our institute. At this point I would also like to thank Dr. Alex Markowitz for this patience and support during my first project. The discussions and advice in X-ray spectroscopy were invaluable to me. Thanks to Dr. Daniela Dorner for the collaboration with FACT and to Mirjam Örtel for the collaboration on EXTraS. It was an inspiring challenge to work on the EXTraS project and I thank Prof. Jörn Wilms and the project coordinator Dr. Andrea De Luca (INAF/IASF Milano) for this opportunity.

During my masters and PhD I was very lucky to have been part of a group of scientist at Remeis and Würzburg that became friends rather than colleagues. It was an immense pleasure to work with these wonderful people. Thank you Dr. Tobias Beuchert, Dr. Thomas Dauser, Dr. Cornelia Müller, Dr. Robert Schulz, Marcus Langejahn, and Katha Leiter for proof reading parts of this thesis and all the scientific discussions, questions, doubts, and discoveries that we shared during the last few years. Thanks to Dr. Felicia Krauss, Dr. Matthias Bissinger, Dr. Thomas Dauser, and Dr. Tobias Beuchert for helping me on any kind of software-related problem. Also, this work would not have been possible without the people providing and maintaining the IT-infrastructure at both institutes. My thanks to the official and unofficial admins, Dr. Ingo Kreykenbohm, Dr. Thomas Dauser, Dr. Matthias Bissinger, Alexander Kappes, and Paul R Burd.

I feel very honored to have visited and worked at the inspiring and historic institutions European Space Agency, ESA, the European Southern Observatory, ESO, and the

NASA. Thanks to Dr. Roopesh Ojha and Dr. Elizabeth Hays for hosting me at NASA GSFC. My visit to Goddard was also such an unforgettable time thanks to Dr. Katja Pottschmidt who showed me around. Thanks to Dr. Vincenzo Mainieri, for hosting me at the European Southern Observatory and introducing me to optical line spectroscopy. Also, I am very grateful for his support on the ESO FORS2 proposal. Furthermore, thanks to Dr. Matteo Guainazzi for the opportunity to make my first scientific experience at ESA during my master degree.

As I said in the beginning, there were many people who indirectly supported me during my journey as a scientist. I want to thank those strangers as well as friends, who kept asking me questions about the universe. These moments and conversations always (re-)ignite my own curiosity about astronomy and make me proud to be part of this community.

My dear friends, who accompanied me during this journey, during moments of frustration and excitement, thank you for being part of my life. Mr. Crane, Mr. Racocon, Sherlock, my dear office mates you have saved the office day more than once. Thanks to the Schere 13 (in any form) and the Capo Gang who sometimes helped to reset my mind and focus. It is wonderful to be around people who are as crazy, active and intelligent as you are! Tobi, we have shared a long journey together, from the base of a volcano to the summit of a glaciers. It has been and continues to be a pleasure discovering Earth with you! Katha, thank you for all the cross-checks and nights of scripting, for working under the highest pressure and still find the time to clown around. The rides with Bolle will remain as a joyful memory.

Last but not least, I want to thank my family from the depth of my heart for their strength, guidance, great heart, and much more than I can name here. Their support has been invaluable to me. I am very grateful that you gave me the chance to study my passion and learn a powerful tool to model and describe the universe.

Mein herzlichster Dank gilt meiner Familie. Danke, dass ihr zu jederzeit für mich da seid, mich mit Rat und Tat unterstützt und meinen Weg begleitet. Ich bin sehr dankbar dafür, dass ihr mir die Möglichkeit gegeben habt meine Faszination zu studieren und ein Werkzeug zu erlernen, dass es mir ermöglicht unser Universum zu beschreiben. In mir steckt ein Teil von jedem von euch!

As a child, I once stood in our garden and watched the night sky. I was fascinated by the idea, that I was actually staring into the past, for every starlight that I saw has been emitted years ago. Last year, I stood in the Brazilian jungle and watched the night sky. I was overwhelmed by the idea, that I stood on this little planet within the plane of the Milky Way, staring at the center of our galaxy, knowing that there is a black hole several thousand times heavier than our sun that was eating small gas clouds.

This work was partly funded by Deutsche Forschungsgemeinschaft grant 50 OR 1303. This research has made use of the Interactive Spectral Interpretation System (ISIS) (Houck & Denicola 2000). This research has made use of a collection of ISIS scripts provided by the Dr. Karl Remeis observatory, Bamberg, Germany at <http://www.sternwarte.uni-erlangen.de/isis/>. This work has made use of data provided by the multi-wavelength monitoring program TANAMI and its participating facilities. The Very Long Baseline Array (VLBA) is an instrument of the National Radio Astronomy Observatory (NRAO). NRAO is a facility of the National Science Foundation, operated by Associated Universities Inc. The Australian Long Baseline Array and the Australia Telescope Compact Array are part of the Australia Telescope National Facility which is funded by the Commonwealth of Australia for operation as a National Facility managed by CSIRO. This study makes use of 43 GHz VLBA data from the Boston University gamma-ray blazar monitoring program (<http://www.bu.edu/blazars/VLBAproject.html>), funded by NASA through the Fermi Guest Investigator Program. This research has made use of data from the MOJAVE database that is maintained by the MOJAVE team (Lister et al., 2009, AJ, 137, 3718). This research has made use of the NASA/IPAC Extragalactic Database (NED) which is operated by the Jet Propulsion Laboratory, California Institute of Technology, under contract with the National Aeronautics and Space Administration. This research has made use of the VizieR catalogue access tool, CDS, Strasbourg, France. This research makes use of data obtained by *XMM-Newton*, an ESA science mission funded by ESA Member States and the USA (NASA), and *Swift*, a NASA mission with international participation.